frontiers | Research Topics

Advances in drug discovery and quality evaluation, 2nd edition

Edited by
Xuetao Xu, Xi Zheng and Xiping Cui

Published in
Frontiers in Chemistry

ISSN 1664-8714
ISBN 978-2-8325-7306-8
DOI 10.3389/978-2-8325-7306-8

Generative AI statement
Any alternative text (Alt text) provided alongside figures in the articles in this ebook has been generated by Frontiers with the support of artificial intelligence and reasonable efforts have been made to ensure accuracy, including review by the authors wherever possible. If you identify any issues, please contact us.

About Frontiers

Frontiers is more than just an open access publisher of scholarly articles: it is a pioneering approach to the world of academia, radically improving the way scholarly research is managed. The grand vision of Frontiers is a world where all people have an equal opportunity to seek, share and generate knowledge. Frontiers provides immediate and permanent online open access to all its publications, but this alone is not enough to realize our grand goals.

Frontiers journal series

The Frontiers journal series is a multi-tier and interdisciplinary set of open-access, online journals, promising a paradigm shift from the current review, selection and dissemination processes in academic publishing. All Frontiers journals are driven by researchers for researchers; therefore, they constitute a service to the scholarly community. At the same time, the *Frontiers journal series* operates on a revolutionary invention, the tiered publishing system, initially addressing specific communities of scholars, and gradually climbing up to broader public understanding, thus serving the interests of the lay society, too.

Dedication to quality

Each Frontiers article is a landmark of the highest quality, thanks to genuinely collaborative interactions between authors and review editors, who include some of the world's best academicians. Research must be certified by peers before entering a stream of knowledge that may eventually reach the public - and shape society; therefore, Frontiers only applies the most rigorous and unbiased reviews. Frontiers revolutionizes research publishing by freely delivering the most outstanding research, evaluated with no bias from both the academic and social point of view. By applying the most advanced information technologies, Frontiers is catapulting scholarly publishing into a new generation.

What are Frontiers Research Topics?

Frontiers Research Topics are very popular trademarks of the *Frontiers journals series*: they are collections of at least ten articles, all centered on a particular subject. With their unique mix of varied contributions from Original Research to Review Articles, Frontiers Research Topics unify the most influential researchers, the latest key findings and historical advances in a hot research area.

Find out more on how to host your own Frontiers Research Topic or contribute to one as an author by contacting the Frontiers editorial office: frontiersin.org/about/contact

Advances in drug discovery and quality evaluation, 2nd edition

Topic editors

Xuetao Xu — Wuyi University, China

Xi Zheng — Rutgers, The State University of New Jersey, United States

Xiping Cui — Guangdong University of Technology, China

Citation

Xu, X., Zheng, X., Cui, X., eds. (2025). *Advances in drug discovery and quality evaluation, 2nd edition*. Lausanne: Frontiers Media SA.

doi: 10.3389/978-2-8325-7306-8

Publisher's note: This is a 2nd edition due to an article retraction.

Table of contents

frontiers | Frontiers in Chemistry

TYPE Original Research
PUBLISHED 10 October 2022
DOI 10.3389/fchem.2022.1019663

OPEN ACCESS

EDITED BY
Xuetao Xu,
Wuyi University, China

REVIEWED BY
Jie Chen,
Shaoguan University, China
Danying Huang,
Guangdong University of Petrochemical Technology, China

*CORRESPONDENCE
Tongjun Liu,
liutongjunjn@163.com

SPECIALTY SECTION
This article was submitted to Medicinal and Pharmaceutical Chemistry, a section of the journal Frontiers in Chemistry

RECEIVED 15 August 2022
ACCEPTED 07 September 2022
PUBLISHED 10 October 2022

CITATION
Meng D, Wang Y and Liu T (2022), Protective effects of silibinin on LPS-induced inflammation in human periodontal ligament cells.
Front. Chem. 10:1019663.
doi: 10.3389/fchem.2022.1019663

Protective effects of silibinin on LPS-induced inflammation in human periodontal ligament cells

Di Meng[1], Yuling Wang[1,2] and Tongjun Liu[1]*

[1]Department of Stomatology, The Central Hospital Affilliated to Shandong First Medical University, Jinan, China, [2]Department of Stomatology, Shandong Qianfoshan Hospital, Jinan, China

Clinically, periodontitis is a chronic nonspecific inflammation that leads to damaged teeth and their supporting gum tissues. Although many studies on periodontitis have been conducted, therapy with natural products is still rare. Silibinin has been proven to have anti-inflammatory and antioxidant activities. However, the effects of silibinin on lipopolyssacharide (LPS)-induced inflammation in periodontal ligaments (PDLs) have not yet been investigated. In this study, the PDLs were treated with silibinin (10, 20, and 40 μM) in the presence of LPS. The results showed that silibinin treatment reduced the levels of NO, PGE_2, IL-6, TNF-α, MMP-1, and MMP-3 and enhanced the activities of superoxide dismutase (SOD) and glutathione (GSH). Moreover, silibinin treatment downregulated RANKL levels and upregulated OPG and ALP levels. In summary, silibinin protected PDLs against LPS-induced inflammation, oxidative stress, and osteogenic differentiation.

KEYWORDS

silibinin, inflammation, protective effects, LPS-induced, human periodontal ligament cells

Introduction

Periodontitis is a chronic nonspecific inflammation caused by periodontal pathogenic bacteria (Seo et al., 2004; Nagatomo et al., 2006; Yamamoto et al., 2006). In the early stages of periodontitis, only the gums are inflamed, and bleed (Choi et al., 2012; Jun et al., 2012). However, with continuous stimulation of pathogenic microorganisms and their metabolites, the periodontal tissue produces immune responses, resulting in the secretion of a large number of inflammatory factors (Kim et al., 2009; Lee et al., 2012; Lei et al., 2014). These factors damage the periodontal supporting tissue, loosening the teeth, ultimately leading to tooth loss. The periodontal ligament (PDL) is an important periodontal tissue that connects the alveolar bone and root (Grzesik and Narayanan, 2002; Choi et al., 2012; Shin et al., 2015). PDL cells, the base units of PDLs, maintain periodontal health by secreting various inflammatory factors and osteoblast/osteoclast regulators (Abiko et al., 1998; Miura et al., 2000; Gyawali and Bhattarai, 2017).

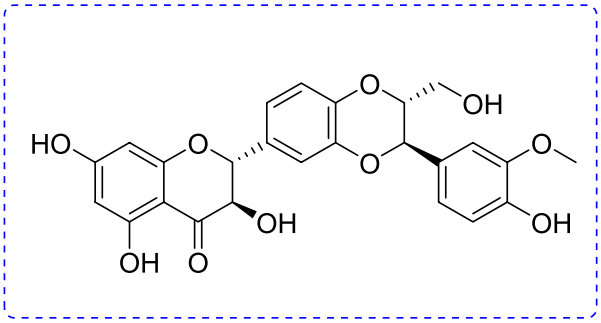

FIGURE 1
Chemical structure of SB.

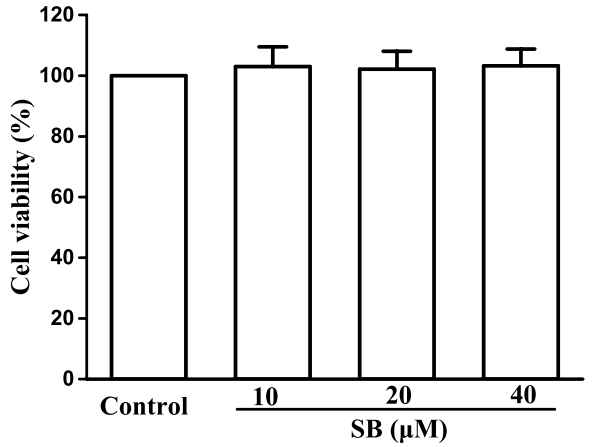

FIGURE 2
Cytotoxicity assay of SB.

Periodontitis is mainly caused by the imbalance between host's defense and accumulating bacteria (Slots et al., 1986; Birkedal-Hansen, 1993). Lipopolysaccharides (LPS) are bacterial membrane proteins that are present in most subgingival Gram-negative organisms (Aznar et al., 1990; Nair et al., 1996). LPS is a stimulant that induces vascular dilatation and edema of periodontal tissues. In addition, sustained LPS stimulation damages periodontal tissue by producing harmful pro-inflammatory mediators, including IL-1β, IL-6, and TNF-α (Gowen et al., 1983; Boyce et al., 1989; Milica et al., 2017). Moreover, LPS stimulation increases the receptor activator of the nuclear factor kappa-B (NF-κB) ligand (RANKL) and reduces osteoprotegerin (OPG). These mediators further stimulate periodontitis (Belibasakis et al., 2007). Thence, clearing inflammation had been recognized as an effective method for improving disease.

Phytoconstituents have been used as beneficial and therapeutic agents since ancient times owing to their low toxicity and biological benefits. Some of them have beneficial therapeutic effects in the treatment of periodontitis. Silibinin (SB) is an important polyphenol found in *Silybum marianum L.* (Kim et al., 2003; Esmaeil et al., 2017; Amato et al., 2019) (Figure 1). Natural products and their derivatives play increasing roles in disease prevention (Cheng et al., 2022; Zhang et al., 2022). SB has been confirmed to have stimulating health benefits and shows promising biological activities, including anti-inflammatory, antioxidant, anti-tumor, and anti-fibrotic effects (Raina et al., 2013; Federico et al., 2017; Zheng et al., 2017). As a reliever of inflammation, SB reportedly ameliorates silica-induced pulmonary fibrosis by reducing the pro-inflammatory mediators (IL-1β, IL-6, and TNF-α) and collagen deposition (Ali et al., 2021). SB is effective against LPS-induced inflammation in PBMCs in horses (Gugliandolo et al., 2020). SB also ameliorates hepatotoxicity by inhibiting inflammation and oxidative stress (Saxena et al., 2022). Moreover, SB can enhance anti-inflammatory activity when combined with thymol (Chen et al., 2020), while it is also used as a beneficial dietary supplement to maintain body health and treat liver disorders.

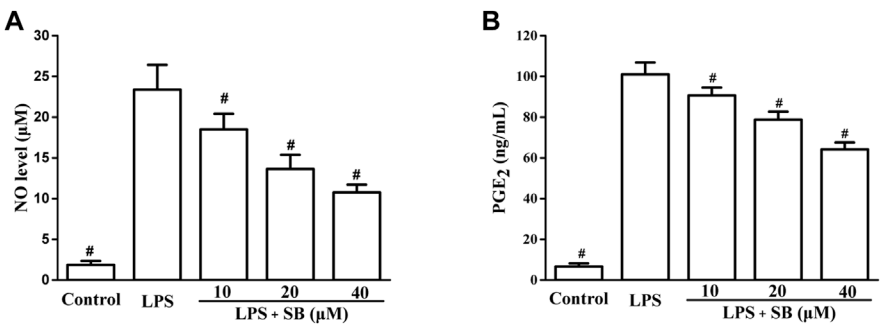

FIGURE 3
SB treatment reduced LPS-induced NO **(A)** and PGE_2 **(B)** in hPDLs. $^{\#}p < 0.05$, compared to the LPS group.

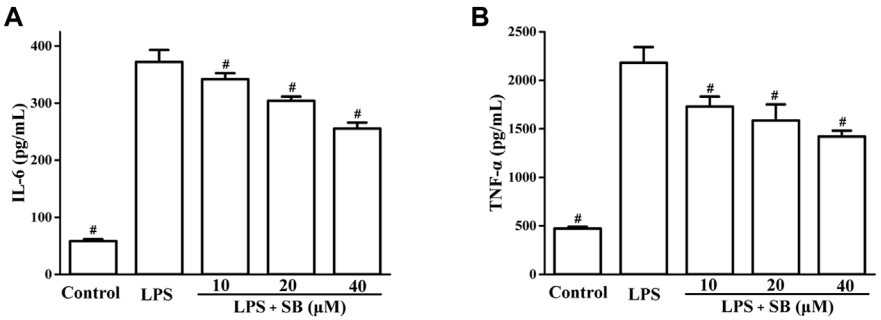

FIGURE 4
SB treatment inhibited LPS-induced IL-6 **(A)** and TNF-α **(B)** in hPDLs. $^{\#}p < 0.05$, compared to the LPS group.

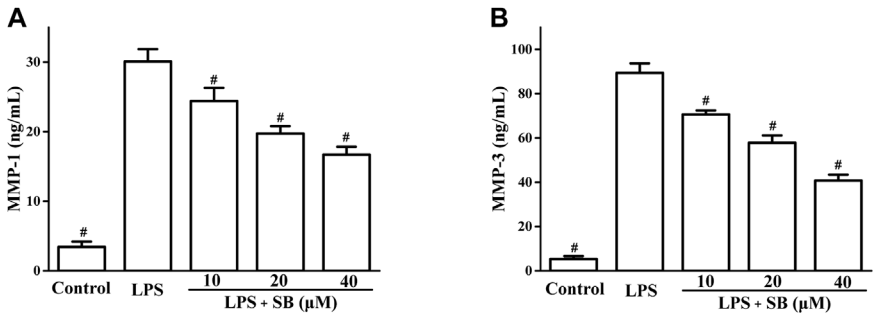

FIGURE 5
SB treatment inhibited LPS-induced MMP-1 **(A)** and MMP-3 **(B)** in hPDLs. $^{\#}p < 0.05$, compared to the LPS group.

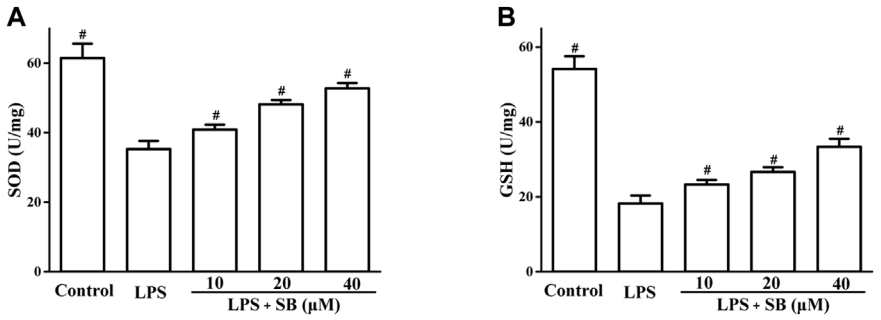

FIGURE 6
SB treatment regulated LPS-induced SOD **(A)** and GSH **(B)** in hPDLs. $^{\#}p < 0.05$, compared to the LPS group.

The aforementioned evidence suggested that SB has good anti-inflammatory activity. Similarly, many studies have shown that periodontitis can be improved by inhibiting inflammatory responses. We designed and evaluated the anti-inflammatory effects of SB on LPS-induced hPDLCs.

Results and discussion

Cytotoxicity assay of SB

To evaluate the cytotoxicity of SB on hPDLs, we exposed hPDLs to various concentrations of SB (10, 20, and 40 μM) for

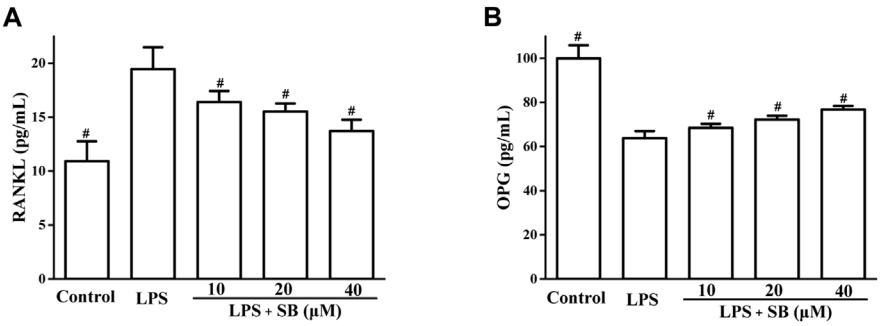

FIGURE 7
SB treatment regulated LPS-induced SOD **(A)** and GSH **(B)** in hPDLs. $^{\#}p < 0.05$, compared to the LPS group.

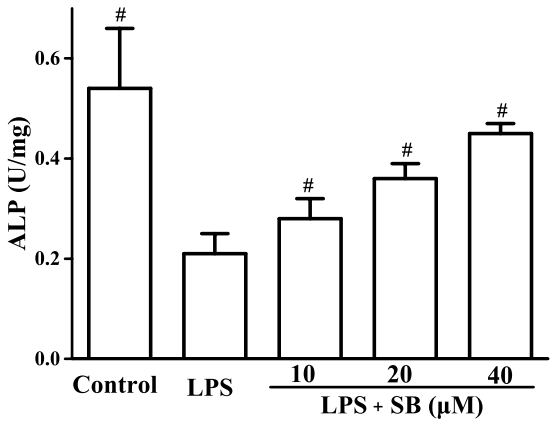

FIGURE 8
SB treatment regulated LPS-induced ALP in hPDLs. $^{\#}p < 0.05$, compared to the LPS group.

24 h and tested cell viability using the MTT method. Based on the MTT assay results (Figure 2), SB was found to have no effect on the cell viability, indicating non-cytotoxicity to hPDLs at the tested concentrations (10–40 μM).

SB reduce LPS-induced NO and PGE_2

NO and PGE_2 are two inflammatory mediators produced by the induction of iNOS and COX-2, respectively (Jeong et al., 2009; Jeong et al., 2011). They can effectively influence inflammation and are classical markers of inflammation. Inhibition of NO and PGE_2 is considered an effective strategy for the treatment of inflammation. The effects of SB on NO and PGE_2 levels were assayed in LPS-induced hPDLs. From Figure 3A, it could be seen that LPS treatment significantly increased the NO level to 23.37 ± 3.04 μM compared to the control group. However, the elevated LPS-induced NO levels decreased by treatment with SB in a dose-dependent manner.

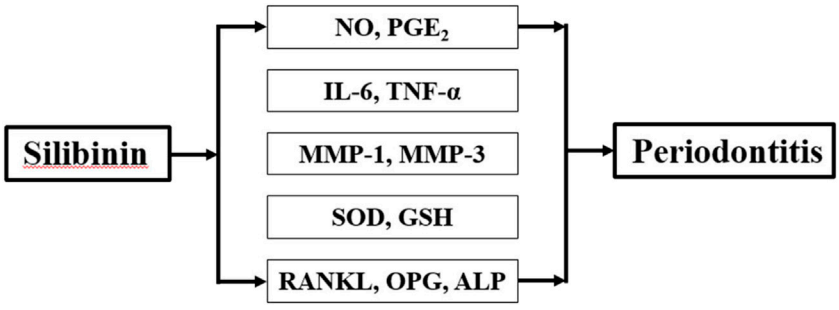

FIGURE 9
Effect of SB on LPS-induced hPDLs.

The NO level reduced to 10.75 ± 0.96 μM, when treated with SB at 40 μM. Similarly, SB (40 μM) treatment inhibited the abnormally elevated PGE_2 level induced by LPS stimulation to 64.12 ± 3.43 ng/ml (Figure 3B).

SB inhibit LPS-induced IL-6 and TNF-α

Next, the effects of SB on LPS-induced IL-6 and TNF-α levels were examined by ELISA. It is well known that the overexpression of pro-inflammatory cytokines is closely related to various inflammatory processes (Lee et al., 2020; Tan et al., 2021). The release of pro-inflammatory cytokines results in the elimination of foreign pathogens. Therefore, reduction in pro-inflammatory cytokines is very important for the treatment of inflammation. As shown in Figure 4, LPS stimulation visibly increased IL-6 (up to 371.88 ± 21.13 pg/ml) and TNF-α (2,180.74 ± 160.30 pg/ml) levels compared to the control group. SB pre-treatment could significantly decrease the IL-6 level to 255.26 ± 10.39 pg/ml at 40 μM compared to the LPS-induced group (Figure 4A). Moreover, pre-treatment with 40 μM SB also reduced the TNF-α level to 1,419.61 ± 59.69 pg/ml (Figure 4B).

SB inhibit LPS-induced MMP-1 and MMP-3

Matrix metalloproteases (MMPs) are the major proteases of ECM metabolism and are involved in the destruction of periodontal tissues (Hosokawa et al., 2021). MMP-1 progresses and damages periodontal soft tissues by degrading type 1 collagen of periodontal tissues. MMP-3 is also reported to be involved in soft tissue destruction through the activation of pro-MMP-1. Hence, regulation of MMP-1 and MMP-3 leads to the improvement of periodontitis. SB treatment decreased LPS-induced MMP-1 and MMP-3 production in a dose-dependent manner (Figure 5). SB (40 μM) treatment reduced the MMP-1 and MMP-3 levels to 16.71 ± 1.12 and 40.72 ± 2.72 ng/ml, respectively, compared to the LPS group (30.09 ± 1.76 and 89.41 ± 4.23 ng/mL pg/ml, respectively).

SB regulate LPS-induced SOD and GSH

It has been revealed that the inflammatory response involves cross-talk with oxidative stress in the defense against pathogenic microorganisms (Chang et al., 2014; Wang et al., 2019). The effects of SB on superoxide dismutase (SOD) and glutathione (GSH) levels, which are important indicators of oxidative stress, were assayed. The results in Figure 6 showed that LPS stimulation could obviously reduce SB on SOD levels in hPDLs, which could be increased by SB treatment (Figure 5A). Similarly, treatment with SB (Figure 6A) significantly increased GSH reduction following LPS stimulation (Figure 6B).

SB regulate LPS-induced RANKL and OPG

RANKL and OPG have been reported to play important roles in bone resorption. RANKL regulates osteoclast differentiation (Shu et al., 2008). OPG is a decoy receptor that binds to RANKL to regulate its activity (Bae et al., 2018). We evaluated the effects of SB on LPS-induced RANKL and OPG expressions. As shown in Figure 7A, SB treatment clearly downregulated the unusually high RANKL expression induced by LPS. However, treatment with SB enhanced the unusually low OPG levels induced by LPS (Figure 7B).

SB regulate LPS-induced ALP

Alkaline phosphatase (ALP) is an important marker of osteoblast differentiation and plays a key role in connective tissue calcification and mineral deposits (Li and Peng, 2019). Studies have shown that LPS can inhibit ALP activity, cell metabolism, and viability in osteoblasts. Our results (Figure 8) showed that LPS treatment significantly inhibited ALP activity compared with the control group. However, the reduced ALP activity induced by LPS treatment was effectively reversed by treatment with SB.

Conclusion

We treated PDLs with silibinin (10, 20, and 40 μM) in the presence of LPS to investigate the protective effects of silibinin against periodontitis. Our findings revealed that silibinin treatment reduced the levels of NO, PGE_2, IL-6, TNF-α, MMP-1, and MMP-3 and enhanced the activities of SOD and GSH. Moreover, silibinin treatment downregulated RANKL levels and upregulated OPG and ALP levels. Our results indicate that silibinin could affect inflammation, oxidative stress, and osteogenic differentiation capacity against LPS (Figure 9) and could be used as an effective agent for the treatment of periodontitis.

Experimental

Cell culture and treatment

hPDLCs were prepared using previously reported methods (Blufstein et al., 2021) and cultured in α-MEM

with 10% FBS, 100 U/mL penicillin, and 100 μg/ml. The cells were divided into five groups: control group (no agent), LPS group (treatment with 1 μg/ml LPS), and three SB groups (treatment with 10, 20, and 40 μM SB, before 1 μg/ml LPS treatment).

Cytotoxicity assay

The cytotoxicity of SB on hPDLCs was assayed using the MTT assay. hPDLCs were seeded into 96-well plates for 24 h and then treated with SB (10, 20, and 40 μM) for another 24 h. The MTT reagent (0.5 mg/ml) was added to each well and incubated for 4 h. DMSO was used to dissolve the resulting crystals, followed by absorbance measurement at 570 nm.

Determination of NO

The hPDLCs were treated with SB (10, 20, and 40 μM) for 2 h, followed by exposure to LPS (1 μg/ml) for 24 h. The NO level in the supernatant was then determined using the Griess reagent. An equal volume of the Griess reagent was added to the culture supernatant and incubated for 10 min. The absorbance was then measured at 540 nm.

Determination of PGE_2

After hPDLCs were treated for 24 h, the culture supernatant was harvested. PGE2 levels in each group were measured using an EIA kit according to the manufacturer's instructions.

Determination of IL-6, TNF-α, MMP-1, MMP-3, and OPG

After hPDLCs were treated for 24 h, IL-6 and TNF-α levels were measured in the harvested culture supernatant using the corresponding IL-6, TNF-α, MMP-1, MMP-3, or OPG ELISA assay kits.

Determination of SOD and GSH

After hPDLCs were treated for 24 h, SOD and GSH levels were measured in the harvested cells using the corresponding commercial kits.

Determination of RANKL

After hPDLCs were treated for 24 h, the cells were harvested and lysed and RANKL levels were measured using RANKL ELISA kits.

Determination of ALP activity

After hPDLCs were treated for 7 days, the harvested cells were lysed using 1% Triton X-100. After centrifugation, ALP activity of the supernatant was detected the ALP activity using an ALP assay kit.

Data availability statement

The datasets presented in this study can be found in online repositories. The names of the repository/repositories and accession number(s) can be found in the article/ Supplementary Material.

Author contributions

DM carried out the experiments, YW collected the data, and TL supervised the work.

Conflict of interest

The authors declare that the research was conducted in the absence of any commercial or financial relationships that could be construed as a potential conflict of interest.

Publisher's note

Supplementary material

The Supplementary Material for this article can be found online at: https://www.frontiersin.org/articles/10.3389/fchem.2022.1019663/full#supplementary-material

References

Abiko, Y., Shimizu, N., Yamaguchi, M., Suzuki, H., and Takiguchi, H. (1998). Effect of aging on functional changes of periodontal tissue cells. *Ann. Periodontol.* 3, 350–369. doi:10.1902/annals.1998.3.1.350

Ali, S. A., Saifi, M. A., Godugu, C., and Talla, V. (2021). Silibinin alleviates silica-induced pulmonary fibrosis: Potential role in modulating inflammation and epithelial-mesenchymal transition. *Phytotherapy Res.* 35, 5290–5304. doi:10.1002/ptr.7210

Amato, A., Terzo, S., and Mule, F. (2019). Natural compounds as beneficial antioxidant agents in neurodegenerative disorders: A focus on alzheimer's disease. *Antioxidants* 8, 608. doi:10.3390/antiox8120608

Aznar, C., Fitting, C., and Cavaillon, J. M. (1990). Lipopolysaccharide-induced production of cytokines by bone marrow-derived macrophages: Dissociation between intracellular interleukin 1 production and interleukin 1 release. *Cytokine* 2, 259–265. doi:10.1016/1043-4666(90)90026-p

Bae, W. J., Park, J. S., Kang, S. K., Kwon, I. K., and Kim, E. C. (2018). Effects of melatonin and its underlying mechanism on ethanol-stimulated senescence and osteoclastic differentiation in human periodontal ligament cells and cementoblasts. *Int. J. Mol. Sci.* 19, 1742. doi:10.3390/ijms19061742

Belibasakis, G. N., Bostanci, N., Hashim, A., Johansson, A., Aduse-Opoku, J., Curtis, M. A., et al. (2007). Regulation of RANKL and OPG gene expression in human gingival fibroblasts and periodontal ligament cells by porphyromonas gingivalis: A putative role of the arg-gingipains. *Microb. Pathog.* 43, 46–53. doi:10.1016/j.micpath.2007.03.001

Birkedal-Hansen, H. (1993). Role of cytokines and inflammatory mediators in tissue destruction. *J. Periodontal Res.* 28, 500–510. doi:10.1111/j.1600-0765.1993.tb02113.x

Blufstein, A., Behm, C., Kubin, B., Gahn, J., Rausch-Fan, X., Moritz1, A., et al. (2021). Effect of vitamin D3 on the osteogenic differentiation of human periodontal ligament stromal cells under inflammatory conditions. *J. Periodont. Res.* 56, 579–588. doi:10.1111/jre.12858

Boyce, B. F., Aufdemorte, T. B., Garrett, I. R., Yates, A. J., and Mundy, G. R. (1989). Effects of interleukin-1 on bone turnover in normal mice. *Endocrinology* 125, 1142–1150. doi:10.1210/endo-125-3-1142

Chang, Y. C., Chang, W. C., Hung, K. H., Yang, D. M., Cheng, Y. H., Liao, Y. W., et al. (2014). The generation of induced pluripotent stem cells for macular degeneration as a drug screening platform: Identification of curcumin as a protective agent for retinal pigment epithelial cells against oxidative stress. *Front. Aging Neurosci.* 6, 191. doi:10.3389/fnagi.2014.00191

Chen, J., Li, D., Xie, L., Ma, Y., Wu, P., Li, C., et al. (2020). Synergistic anti-inflammatory effects of silibinin and thymol combination on LPS-induced RAW264.7 cells by inhibition of NF-κB and MAPK activation. *Phytomedicine* 78, 153309. doi:10.1016/j.phymed.2020.153309

Cheng, F., Duan, D. S., Jiang, L. M., Li, B. S., Wang, J. X., Zhou, Y. J., et al. (2022). Copper-catalyzed asymmetric ring-opening reaction of cyclic diaryliodonium salts with imides. *Org. Lett.* 24, 1394–1399. doi:10.1021/acs.orglett.2c00247

Choi, E. Y., Jin, J. Y., Lee, J. Y., Choi, J. I., Choi, I. S., and Kim, S. J. (2012). Anti-inflammatory effects and the underlying mechanisms of action of daidzein in murine macrophages stimulated with Prevotella intermedia lipopolysaccharide. *J. Periodontal Res.* 47, 204–211. doi:10.1111/j.1600-0765.2011.01422.x

Esmaeil, N., Anaraki, S. B., Gharagozloo, M., and Moayedi, B. (2017). Silymarin impacts on immune system as an immunomodulator: One key for many locks. *Int. Immunopharmacol.* 50, 194–201. doi:10.1016/j.intimp.2017.06.030

Federico, A., Dallio, M., and Loguercio, C. (2017). Silymarin/silybin and chronic liver disease: A marriage of many years. *Molecules* 22, 191. doi:10.3390/molecules22020191

Gowen, M., Wood, D. D., Ihrie, E. J., McGuire, M. K., and Russell, R. G. (1983). An interleukin 1 like factor stimulates bone resorption *in vitro*. *Nature* 306, 378–380. doi:10.1038/306378a0

Grzesik, W. J., and Narayanan, A. S. (2002). Cementum and periodontal wound healing and regeneration. *Crit. Rev. Oral Biol. Med.* 13, 474–484. doi:10.1177/154411130201300605

Gugliandolo, E., Crupi, R., Biondi, V., Licata, P., Cuzzocrea, S., and Passantino, A. (2020). Protective effect of silibinin on lipopolysaccharide-induced inflammatory responses in equine peripheral blood mononuclear cells, an *in vitro* study. *Animals* 10, 2022. doi:10.3390/ani10112022

Gyawali, R., and Bhattarai, B. (2017). Orthodontic management in aggressive periodontitis. *Int. Sch. Res. Not.* 2017, 8098154. doi:10.1155/2017/8098154

Hosokawa, Y., Hosokawa, I., Ozaki, K., and Matsuo, T. (2021). Nobiletin inhibits inflammatory reaction in interleukin-1β-stimulated human periodontal ligament cells. *Pharmaceutics* 13, 667. doi:10.3390/pharmaceutics13050667

Jeong, G. S., Lee, D. S., Li, B., Kim, J. J., Kim, E. C., and Kim, Y. C. (2011). Anti-inflammatory effects of lindenenyl acetate via heme oxygenase-1 and AMPK in human periodontal ligament cells. *Eur. J. Pharmacol.* 670, 295–303. doi:10.1016/j.ejphar.2011.08.008

Jeong, G. S., Lee, S. H., Jeong, S. N., Kim, Y. C., and Kim, E. C. (2009). Anti-inflammatory effects of apigenin on nicotine- and lipopolysaccharide-stimulated human periodontal ligament cells via heme oxygenase-1. *Int. Immunopharmacol.* 9, 1374–1380. doi:10.1016/j.intimp.2009.08.015

Jun, I. H., Lee, D. E., Yun, J. H., Cho, A. R., Kim, C. S., You, Y. J., et al. (2012). Anti-inflammatory effect of (−)-epigallocatechin- 3-gallate on *Porphyromonas gingivalis* lipopolysaccharide-stimulated fibroblasts and stem cells derived from human periodontal ligament. *J. Periodontal Implant Sci.* 42, 185–195. doi:10.5051/jpis.2012.42.6.185

Kim, N. C., Graf, T. N., Sparacino, C. M., Wani, M. C., and Wall, M. E. (2003). Complete isolation and characterization of silybins and isosilybins from milk thistle (Silybum marianum)electronic supplementary information (ESI) available: HPLC chromatograms of isolates and extracts. *Org. Biomol. Chem.* 1, 1684–1689. doi:10.1039/b300099k

Kim, Y. S., Pi, S. H., Lee, Y. M., Lee, S. I., and Kim, E. C. (2009). The anti-inflammatory role of heme oxygenase-1 in lipopolysaccharide and cytokine-stimulated inducible nitric oxide synthase and nitric oxide production in human periodontal ligament cells. *J. Periodontol.* 80, 2045–2055. doi:10.1902/jop.2009.090145

Lee, S. A., Park, B. R., Moon, S. M., Shin, S. H., Kim, J. S., Kim, D. K., et al. (2020). Cynaroside protects human periodontal ligament cells from lipopolysaccharide-induced damage and inflammation through suppression of NF-κB activation. *Arch. Oral Biol.* 120, 104944. doi:10.1016/j.archoralbio.2020.104944

Lee, S. I., Park, K. H., Kim, S. J., Kang, Y. G., Lee, Y. M., and Kim, E. C. (2012). Mechanical stress-activated immune response genes *via* Sirtuin 1 expression in human periodontal ligament cells. *Clin. Exp. Immunol.* 168, 113–124. doi:10.1111/j.1365-2249.2011.04549.x

Lei, M., Li, K., Li, B., Gao, L. N., Chen, F. M., and Jin, Y. (2014). Mesenchymal stem cell characteristics of dental pulp and periodontal ligament stem cells after *in vivo* transplantation. *Biomaterials* 35, 6332–6343. doi:10.1016/j.biomaterials.2014.04.071

Li, J., and Peng, Y. J. (2019). Effect of puerarin on osteogenic differentiation of human periodontal ligament stem cells. *J. Int. Med. Res.* 48, 030006051985164–11. doi:10.1177/0300060519851641

Milica, K., Dušanka, K., Milica, B. P., Tatjana, J. S., Marko, J., Aleksandar, P., et al. (2017). Anti-inflammatory effect of the *Salvia sclarea L.* ethanolic extract on lipopolysaccharide-induced periodontitis in rats. *J. Ethnopharmacol.* 199, 52–59. doi:10.1016/j.jep.2017.01.020

Miura, S., Yamaguchi, M., Shimizu, N., and Abiko, Y. (2000). Mechanical stress enhances expression and production of plasminogen activator in aging human periodontal ligament cells. *Mech. Ageing Dev.* 112, 217–231. doi:10.1016/s0047-6374(99)00095-0

Nagatomo, K., Komaki, M., Sekiya, I., Sakaguchi, Y., Noguchi, K., Oda, S., et al. (2006). Stem cell properties of human periodontal ligament cells. *J. Periodontal Res.* 41, 303–310. doi:10.1111/j.1600-0765.2006.00870.x

Nair, S. P., Meghji, S., Wilson, M., Reddi, K., White, P., and Henderson, B. (1996). Bacterially induced bone destruction: Mechanisms and misconceptions. *Infect. Immun.* 64, 2371–2380. doi:10.1128/iai.64.7.2371-2380.1996

Raina, K., Agarwal, C., and Agarwal, R. (2013). Effect of silibinin in human colorectal cancer cells: Targeting the activation of NF-κB signaling. *Mol. Carcinog.* 52, 195–206. doi:10.1002/mc.21843

Saxena, N., Dhaked, R. K., and Nagar, D. P. (2022). Silibinin ameliorates abrin induced hepatotoxicity by attenuating oxidative stress, inflammation and inhibiting Fas pathway. *Environ. Toxicol. Pharmacol.* 93, 103868. doi:10.1016/j.etap.2022.103868

Seo, B. M., Miura, M., Gronthos, S., Bartold, P. M., Batouli, S., Brahim, J., et al. (2004). Investigation of multipotent postnatal stem cells from human periodontal ligament. *Lancet* 364, 149–155. doi:10.1016/s0140-6736(04)16627-0

Shin, S. Y., Kim, Y. S., Lee, S. Y., Bae, W. J., Park, Y. D., Hyun, Y. C., et al. (2015). Expression of phospholipase D in periodontitis and its Role in the Inflammatory and osteoclastic response by nicotine and Lipopolysaccharide-stimulated human periodontal ligament cells. *J. Periodontol.* 86, 1405–1416. doi:10.1902/jop.2015.150123

Shu, L., Guan, S. M., Fu, S. M., Guo, T., Cao, M., and Ding, Y. (2008). Estrogen modulates cytokine expression in human periodontal ligament cells. *J. Dent. Res.* 87, 142–147. doi:10.1177/154405910808700214

Slots, J., Bragd, L., Wikstrom, M., and Dahlen, G. (1986). The occurrence of Actinobacillus actinomycetemcomitans, Bacteroides gingivalis and Bacteroides intermedius in destructive periodontal disease in adults. *J. Clin. Periodontol.* 13, 570–577. doi:10.1111/j.1600-051x.1986.tb00849.x

Tan, L., Cao, Z., Chen, H., Xie, Y., Yu, L., Fu, C., et al. (2021). Curcumin reduces apoptosis and promotes osteogenesis of human periodontal ligament stem cells under oxidative stress *in vitro* and. *Life Sci.* 270, 119125. doi:10.1016/j.lfs.2021.119125

Wang, Y., Zhang, Y., Yang, L., Yuan, J., Jia, J., and Yang, S. (2019). SOD2 mediates curcumin-induced protection against oxygen-glucose deprivation/reoxygenation injury in HT22 cells. *Evidence-Based Complementary Altern. Med.* 2019, 1–14. doi:10.1155/2019/2160642

Yamamoto, T., Kita, M., Oseko, F., Nakamura, T., Imanishi, J., and Kanamura, N. (2006). Cytokine production in human periodontal ligament cells stimulated with Porphyromonas gingivalis. *J. Periodontal Res.* 41, 554–559. doi:10.1111/j.1600-0765.2006.00905.x

Zhang, X., Zheng, Y. Y., Hu, C. M., Wu, X. Z., Lin, J., Xiong, Z., et al. (2022). Synthesis and biological evaluation of coumarin derivatives containing oxime ester as α-glucosidase inhibitors. *Arab. J. Chem.* 15, 104072. doi:10.1016/j.arabjc.2022.104072

Zheng, W., Feng, Z., Lou, Y., Chen, C., Zhang, C., Tao, Z., et al. (2017). Silibinin protects against osteoarthritis through inhibiting the inflammatory response and cartilage matrix degradation *in vitro* and *in vivo*. *Oncotarget* 8, 99649–99665. doi:10.18632/oncotarget.20587

frontiers | Frontiers in Chemistry

TYPE Review
PUBLISHED 28 October 2022
DOI 10.3389/fchem.2022.1040333

OPEN ACCESS

EDITED BY
Xi Zheng,
Rutgers, The State University of New Jersey, United States

REVIEWED BY
Hadia Almahli,
University of Cambridge, United Kingdom
Farhad Eisvand,
Mashhad University of Medical Sciences, Iran

*CORRESPONDENCE
Chao Wang,
wangchao20086925@126.com
Dongming Xing,
xdm_tsinghua@163.com

†These authors share first authorship

SPECIALTY SECTION
This article was submitted to Medicinal and Pharmaceutical Chemistry, a section of the journal Frontiers in Chemistry

RECEIVED 09 September 2022
ACCEPTED 10 October 2022
PUBLISHED 28 October 2022

CITATION
Wang C, Chang J, Yang S, Shi L, Zhang Y, Liu W, Meng J, Zeng J, Zhang R and Xing D (2022), Advances in antitumor research of CA-4 analogs carrying quinoline scaffold.
Front. Chem. 10:1040333.
doi: 10.3389/fchem.2022.1040333

Advances in antitumor research of CA-4 analogs carrying quinoline scaffold

Chao Wang[1,2*†], Jing Chang[1,2†], Shanbo Yang[1,2], Lingyu Shi[1,2], Yujing Zhang[3], Wenjing Liu[1,2], Jingsen Meng[1,2], Jun Zeng[1,2], Renshuai Zhang[1,2] and Dongming Xing[1,4*]

[1]Cancer Institute, The Affiliated Hospital of Qingdao University, Qingdao University, Qingdao, China, [2]Qingdao Cancer Institute, Qingdao University, Qingdao, China, [3]The Affiliated Cardiovascular Hospital of Qingdao University, Qingdao University, Qingdao, China, [4]School of Life Sciences, Tsinghua University, Beijing, China

Combretastatin A-4 (CA-4) is a potent inhibitor of tubulin polymerization and a colchicine binding site inhibitor (CBSI). The structure-activity relationship study of CA-4 showed that the *cis* double bond configuration and the 3,4,5-trimethoxy group on the A ring were important factors to maintain the activity of CA-4. Therefore, starting from this condition, chemists modified the double bond and also substituted 3,4,5-trimethoxyphenyl with various heterocycles, resulting in a new generation of CA-4 analogs such as chalcone, Flavonoid derivatives, indole, imidazole, etc. Quinoline derivatives have strong biological activity and have been sought after by major researchers for their antitumor activity in recent years. This article reviews the research progress of novel CA-4 containing quinoline analogs in anti-tumor from 1992 to 2022 and expounds on the pharmacological mechanisms of these effective compounds, including but not limited to apoptosis, cell cycle, tubulin polymerization inhibition, immune Fluorescence experiments, etc., which lay the foundation for the subsequent development of CA-4 containing quinoline analogs for clinical use.

KEYWORDS

inhibitor of tubulin polymerization, CA-4, CBSI, quinoline, antitumor

1 Introduction

Microtubules, a key building block of the cytoskeleton, are dynamic polymers of tubulin that form an ordered network of polarized tubules (Honore et al., 2005). Microtubules are formed by combining α and β heterodimers, which are important components of the eukaryotic cytoskeleton, and they have played important roles in mitosis and cytokinesis (Lu et al., 2012). The vast majority of these molecules act by binding to a heterodimer of the protein microtubulin (α, β) that forms the microtubule core (Wang et al., 2021). The microtubulin heterodimer contains six binding sites (Pryor et al., 2002): Pironetin, Taxane, Laulimalide/Peloruside, Vinca, Maytansine, and Colchicine binding sites. Targeted drugs that act on microtubules and exert anti-

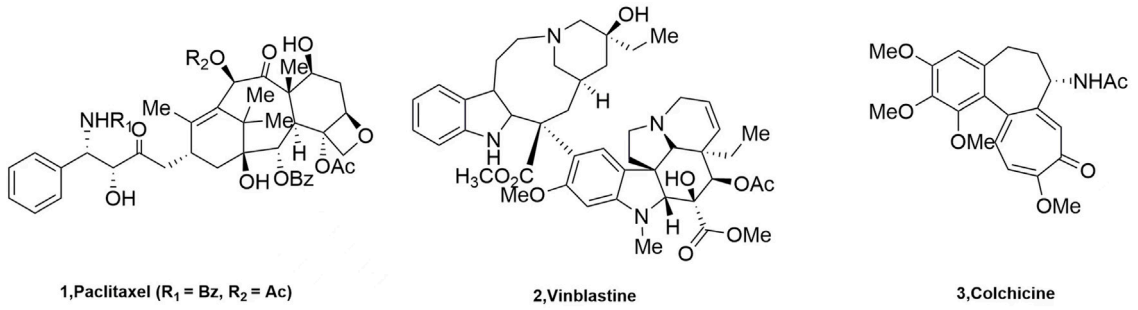

FIGURE 1
The structure of tubulin inhibitors.

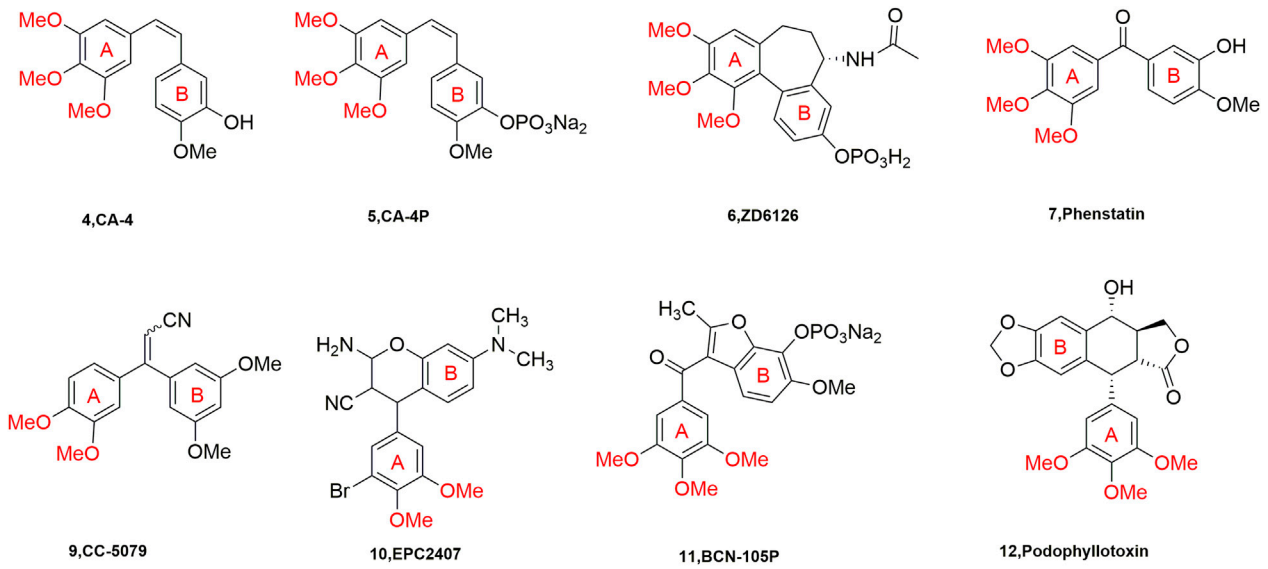

FIGURE 2
Chemical structures of some CBSIs (currently in clinical trials).

tumor effects by inhibiting microtubule proteins are called microtubule protein inhibitors. They were classified into two categories according to their mechanism of action on microtubules: microtubule protein depolymerization inhibitors, such as Paclitaxel (**1**, Figure 1), and microtubule protein polymerization inhibitors, such as Vinblastine (**2**, Figure 1) and Colchicine (**3**, Figure 1).

Current studies show that there are many drugs used in clinical oncology that act on the paclitaxel and vincristine binding sites. These drugs are very effective but have complex structures due to their large molecular weights, which makes the major researchers discouraged. However, the compounds acting on CBSI have the characteristics of small molecular weight, simple structure, diverse molecules, and easy synthesis and transformation, which are sought after by major researchers (Gigant et al., 2005). A number of representative tubulin inhibitors (currently in clinical trials) targeting the colchicine binding site have emerged (Figure 2).

It is well known that quinoline was isolated in the 19th century and since then more and more related natural products have been isolated and identified. Derivatives containing quinoline show great advantages due to nitrogen atoms, such as can increase the basicity of molecules, because of its basic properties and the possibility of nitrogen atoms forming strong hydrogen bonds with the target. Another important property is polarity, which can be used as a means to reduce lipophilicity and

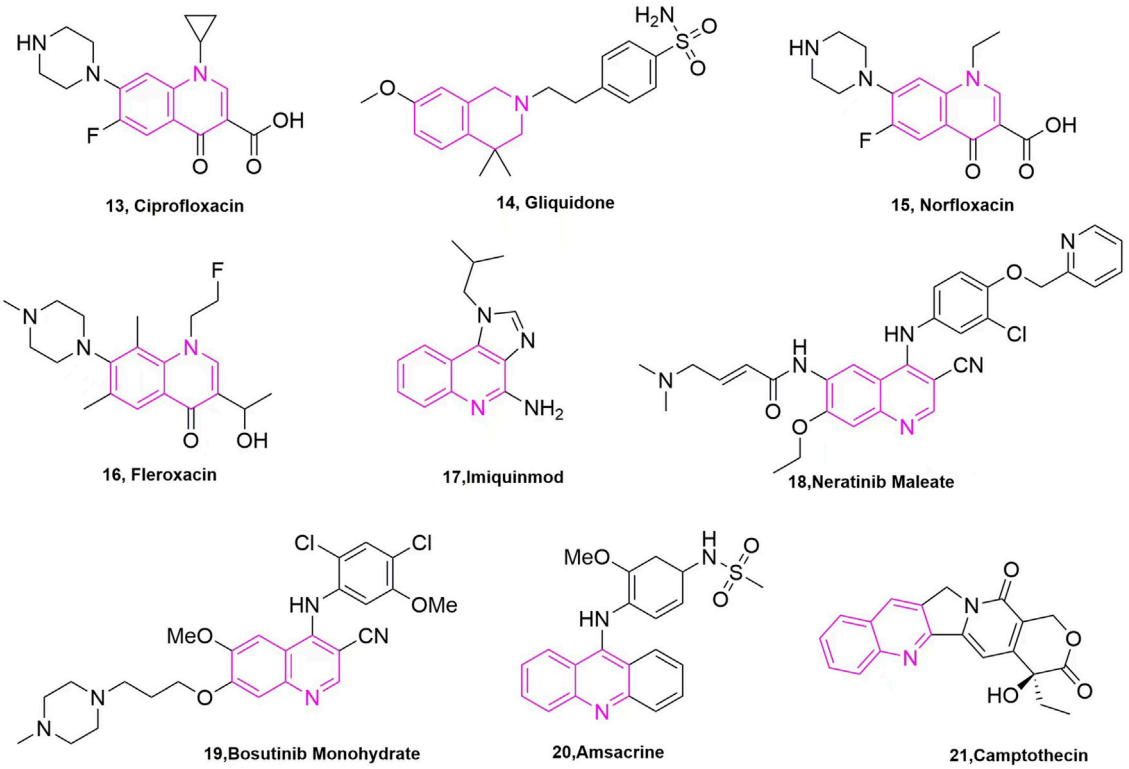

FIGURE 3
The marketed drugs carrying quinoline's structure.

improve water solubility and oral absorption (Alvarez et al., 2016). Quinoline groups are often present in natural alkaloids with a wide range of biological activities and there are many drugs that carry quinoline on the market (Figure 3). Molecules containing quinoline scaffolds can even enhance the cytotoxicity of doxorubicin against multidrug-resistant cancer cell lines at non-toxic concentrations (Chen et al., 2014). Quinoline analogues have also shown anticancer activity by different mechanisms, including alkylating agents, tyrosine kinase inhibitors, and microtubulin inhibitors (Kaur et al., 2010).

Meanwhile, extensive structure-activity relationship (SAR) studies were performed on CA-4, which demonstrated the 3,4,5-trimethoxy substitution pattern on the A-ring, 4-methoxy-substituted B-ring and cis-configuration double bond as the basis for the polymerization-inhibiting activity of microtubulin (Stefanski et al., 2018). We have mapped the mechanism of action of these compounds (CA-4 analogs) based on the SAR of CA-4 (Figure 4). Among the modifications of the CA-4 structure, some researchers have modified it using quinoline and *iso*-quinoline structures. Their study also further demonstrates that the quinoline fraction may be an alternative to the conventional 3,4,5-trimethoxyphenyl fraction when bound to the colchicine site (Li et al., 2019). In addition, the use of other heterocycles to replace the B-ring has been pursued by various researchers (Solomon et al., 2019). They designed and synthesized some derivatives that carry CA-4 quinoline analogues and interact with the colchicine binding site. The results showed that the successfully modified compounds had comparable activity to CA-4, and some had higher activity than CA-4. In addition, we searched PubMed, Web of science and Scoups for 30 related articles published between 1992 and 2022 (Figure 5). This paper mainly reviews the design, synthesis and validation of pharmacological activities of quinoline fragment-containing CA-4 derivatives in these articles, including the experiments involved and the corresponding experimental results. Finally, the similarities and differences among these articles are pointed out, and the outlook is proposed.

2 CA-4 analogues carrying quinoline scaffold

2.1 Modification of CA-4

2.1.1 Modification of A-ring

Kuo et al. (1993) started with a tricyclic chemical structural pattern, which was the first and similar to CA-4 analogues carrying quinoline scaffold. They designed and synthesized a

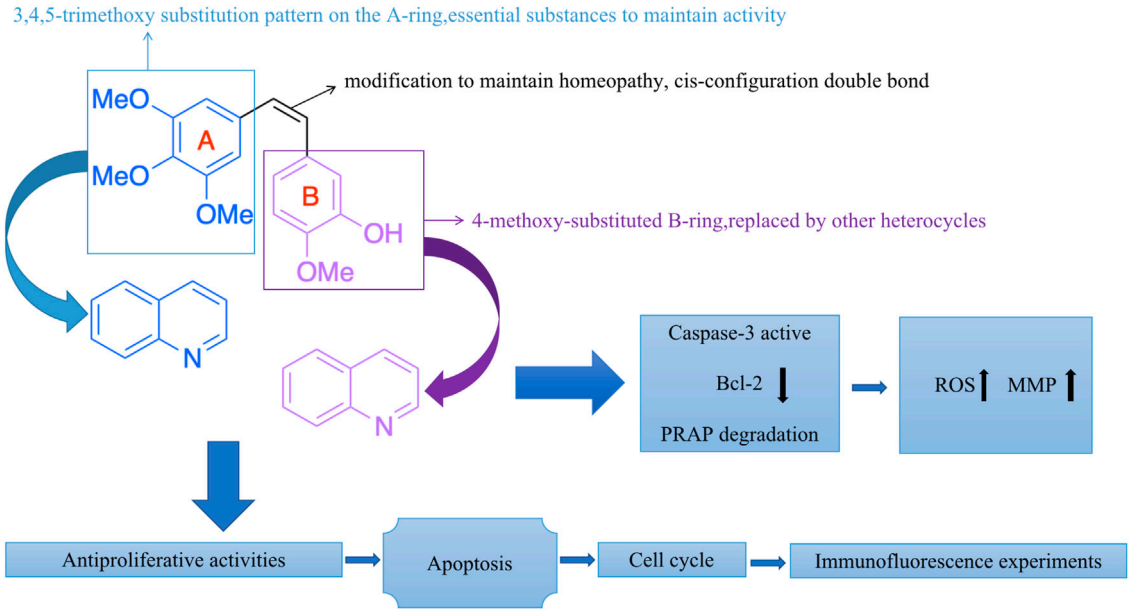

FIGURE 4
The mechanism of action of these compounds (CA-4 analogs).

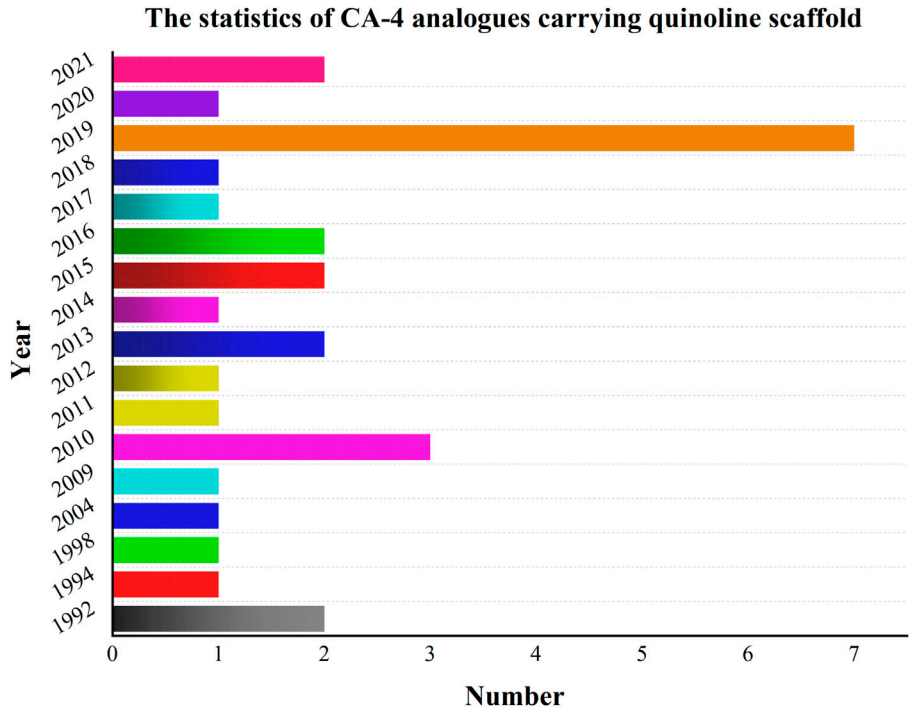

FIGURE 5
Relevant articles have been published from 1992 to 2022.

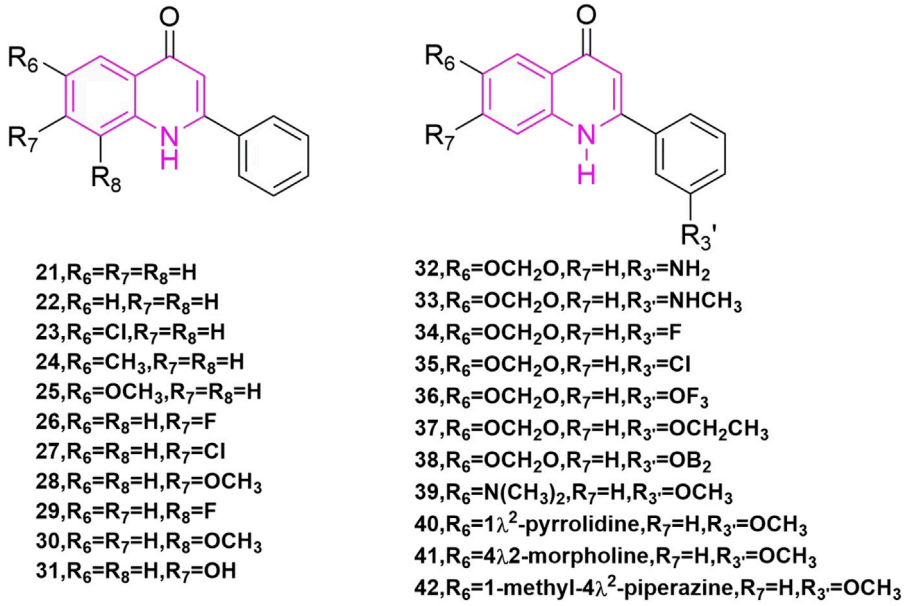

FIGURE 6
The structures of the compounds designed by Kuo et al. (1993) and Li et al. (1994b).

series of 1,6,7,8-substituted 2-(4′-substituted phenyl)-4-quinolones, which had been evaluated as cytotoxic compounds and as antimitotic agents that interact with tubulin. These compounds were assayed for their cytotoxicity *in vitro* against six tumor cell lines, which included human lung carcinoma cell lines (A-549), ileocecal carcinoma cell lines (HCT-8), and melanoma cell lines (RPMI-7951), and epidermoid carcinoma of the nasopharynx cell lines (KB) and two murine leukaemia cell lines (P-388 and L1210). In these compounds, compound **23** (Figure 6), compound **25** (Figure 6), and compound **26** (Figure 6) showed potent cytotoxicity (Monks et al., 1991), with EC_{50} values < 1.0 μg/ml in all cancer lines. They then tested the effects of these three compounds on tubulin interactions, which used the COMPARE algorithm (Bai et al., 1991) assay and compound **25** showed the best with an IC_{50} value of 2.7 ± 0.04 μM. In addition, these compounds could inhibit the binding of radiolabelled colchicine to tubulin, compared to colchicine, podophyllotoxin, and CA-4, and compound **25** showed the best of them. Even so, the three compounds were not as potent as natural products.

Li et al. (1994b) is a continuation of Kuo et al., they began studying 2-phen-yl-quinolones and designing and synthesizing a new series of compounds, which illustrated strong inhibitory effects against a variety of human tumor cell lines, including those derived from solid tumors. Compound **28** (Figure 6) illustrated great activity and also inhibited tubulin polymerization (Li et al., 1994a), with activity comparable to those of the potent antimitotic natural products colchicine, podophyllotoxin, and CA-4. Compounds **21**, **23**, **24**, **27**–**29**, **33**, **40**, and **41** (Figure 6) demonstrated strong cytotoxic effects to most of the tumor cell lines with GI_{50} values in the micromolar to nanomolar range. Also, compounds **42** are just to enrich the structure of quinoline compounds.

Xia et al. (1998) designed and synthesized a novel series of 6,7,2′,3′,4-substituted-1,2,3,4-tetrahydro-2-phenyl-4-quinolones based on the structure of natural anti-mitotic drugs. They evaluated cytotoxicity (Rubinstein et al., 1990) in six cancer cell lines, including HCT-8, breast cancer cell lines (MCF-7), A-549, KB, renal cancer cell lines (CAKI-1), and melanoma cancer cell lines (SKMEL-2). In these compounds, compounds **43**, and **44**, **45** (Figure 7) illustrated great cytotoxic effects with ED_{50} values in the nanomolar or sub nanomolar range. Compound **44** demonstrated the best activity, pyrrolidinylrrolinyl ring at the 6-position, similar with Li's research before.

2.1.2 Modification of B-ring and *cis*-double bond

By studying the conformational relationship of CA-4, Perez-Melero et al. (2004) proposed using 2-naphthyl moiety to replace the 3-hydroxy-4-methoxyphenyl ring of CA-4, which could not observably reduce cytotoxicity and inhibit tubulin polymerization activity. Then they came up with using 6- or 7-quinolyl systems to substitute 3-hydroxy-4-methoxyphenyl ring, keeping the 3,4,5-trimethoxyphenyl moiety as A-ring at the same time (**46a**, **46b**, Figure 7), getting a new family of analogues of CA-4. Compound **46a** was highly cytotoxic but did

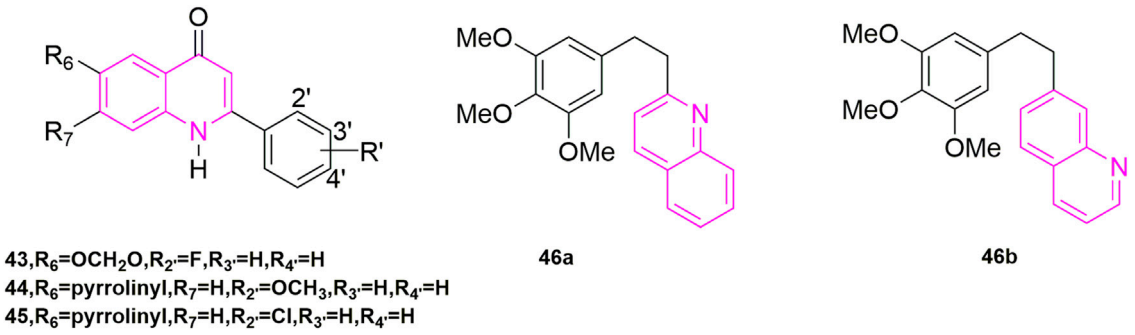

FIGURE 7
The structures of the compounds designed by Xia et al. (1998) and Perez-Melero et al. (2004).

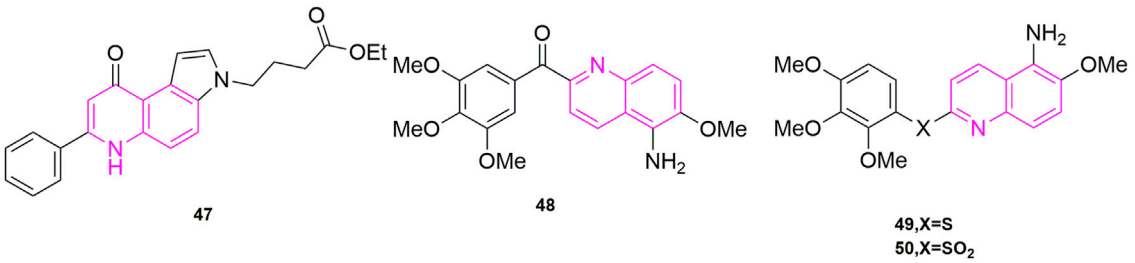

FIGURE 8
The structures of the compounds designed by Ferlin et al. (2010), Nien et al. (2010), and Lee et al. (2011).

not inhibit tubulin polymerization. While compound **46b** was similar to the naphthalene-containing compound previously described and had powerful cytotoxicity [−log (IC_{50}) M = 6.8] and tubulin inhibition ability. Other compounds demonstrated weak inhibition of tubulin compared to CA-4. In addition, the presence of N atoms also made these compounds more water-soluble than CA-4, which pointed out the way to solve the water-soluble problem of CA-4.

Ferlin et al. (2010) designed and synthesized a series of new substituted 7-phenyl-3*H*-pyrrolo [3,2-f] quinolin-9-ones, which starting from the study of the antiproliferative activity (Gasparotto et al., 2007) of this structure of pyrroloquinoline. By evaluating its antiproliferative activities, the best active compound **47** (Figure 8) was found to be highly selective for human leukaemia cells (GI_{50} = 0.45 ± 0.10 μM), and it also blocked Jurkat cells in the G2/M phase in a concentration-dependent manner. At a concentration of 0.06 μM for 24 h compared to the control the number of G2/M cells increased from 9.4% to 77% in the control group. G1 cells decreased from 47% to 3% in the control group, while S-phase cells decreased from 43% to 20% (Gasparotto et al., 2007). Such results were reflected in the other compounds as well. To verify that subsequent experiments were relevant, apoptosis experiments were conducted, in which they selected Jurkat cells treated with compound **47** for 24 h and 48 h to observe the extent of apoptosis (Martin et al., 1995; Vermes et al., 1995). The effectiveness led them to further investigate the mechanism of apoptosis, so they carried out mitochondrial depolarization experiments and confirmed that compound **47** could dose-dependently increase the mitochondrial transmembrane potential. To investigate the relationship between mitochondrial depolarization and reactive oxygen species, they used compound **47** to treat cells to see if reactive oxygen species production increased, and the results confirmed that it was as expected and induced reactive oxygen species (ROS) production in the cells (Zamzami et al., 1995). This was the same increase in mitochondrial transmembrane potential as in the mitochondrial depolarization assay. Finally, they found that Jurket cells treated with compound **47** activated caspase-3 in a concentration-dependent manner *in vitro*, while an increase in Poly ADP-ribose polymerase (PARP) fragments and a decrease in Bcl-2 protein were also observed in Western blot experiments. In their experiments, compound **47** induced apoptosis by activating caspase-3, cleavage PARP, and downregulating Bcl-2 protein (Earnshaw et al., 1999; Denault and Salvesen, 2002).

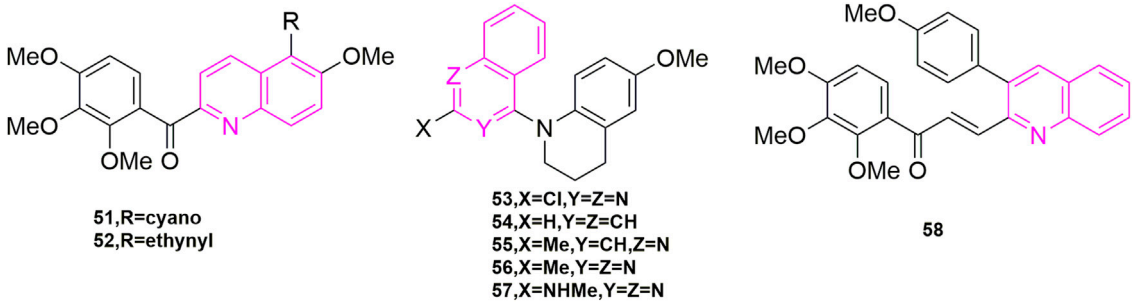

FIGURE 9
The structures of the compounds designed by Lee et al. (2012), Wang et al. (2013b), and Tseng et al. (2015).

Nien et al. (2010) designed and synthesized a series of new aryl quinoline derivatives by coupling the quinoline nucleus with 3,4,5-trimethoxybenzoyl from the pharmacological activity of the parent quinoline nucleus and combining it with CA-4 conformational relationship. *In vitro*, antiproliferative activityexperiments were also performed, and five cells were selected, including KB, non-small-cell lung carcinoma cell lines (H460), human colorectal carcinoma cell lines (HT29), and human gastric cancer cell lines (MKN45), as well as the MDR-positive cancer cell lines, KB-vin10 cells, that overexpressed P-GP 170/MDR. Compound **48** (Figure 8), which contained 5-amino-2-aroylquinolines, was shown to be the most potent of the five cells (IC_{50} = 0.2–0.7 nM), surpassing CA-4. To further understand its potentially active structure, molecular docking was performed, and the results showed that the presence of hydrogen bonds increased the potential of compound **48** and contributed to its effectiveness. To investigate the anti-microtubule protein activity and the ability of compound 36 to compete for colchicine binding sites (Kuo et al., 2004), CA-4 was selected as a control, and compound **48** was effective in inhibiting microtubule aggregation (IC_{50} = 1.6 μM) compared to CA-4 (IC_{50} = 2.1 μM), which was positively correlated with its anti-proliferative activity. The results of the [^{3}H]-colchicine binding assay showed that compound **48** bound tightly to the colchicine binding domain with a binding affinity comparable to that of CA-4.

Lee et al. (2011) used amine, sulphide, and sulfone group substitution of compound carbonyls from compound **48** (Figure 8) based on Nien's study. The results showed that compounds **49** (mean IC_{50} = 42 nM) and **50** (mean IC_{50} = 12 nM) (Figure 9) containing sulfide and sulfone groups between 3,4,5-trimethoxyphenyl ring and 5-amino-6-methoxyquinoline showed significant antiproliferative activity against KB, HT29 and MKN45 cells. Compound **49** inhibited microtubulin polymerization (Kuo et al., 2004; Liou et al., 2004) (IC_{50} = 2.0 μM), similar to CA-4. They went on to study the C-5 substituent of the 3′,4′,5′-trimethoxybenzoyl-6-methoxyquinoline derivative and confirmed that compound **49** containing the hydroxyl group had excellent antiproliferative activity (IC_{50} = 3.4 nM) and microtubule-stabilizing potency of 1.5 μM, greater than that of CA-4 (IC_{50} = 1.9 μM). It also blocked blood vessels and when HUVECs were treated with compound **49** at 15, 30, 60, and 120 nM, compound **49** was able to destroy the formed capillaries in a concentration-dependent manner. In addition, compounds **49** and **50** showed significant efficacy against MDR/MRP-related drug-resistant cell lines (KB-vin10, KB-S1, and KB-7D) with mean IC_{50} values of 2.6–6.7 nM, respectively.

Lee et al. (2012) continued his previous studies, also starting with compound **49**, and continued to investigate the C-5 substituents of 3,4′,5′-trimethoxybenzoyl-6-methoxyquinoline derivatives, choosing cyano, acetylenic and various aryl groups that are less used by major chemists to design and synthesize a new series of new aryl quinoline derivatives. Three human cancer cell lines, KB, HT29, and MKN45 cells were assayed for antiproliferative activity. Compound **51** and compound **52** (Figure 9) exhibited significant antiproliferative activity with mean IC_{50} values of 30 and 57 nM, comparing to colchicine. Interestingly, when they attempted to validate the anti-microtubulin activity and colchicine binding activity of compounds **51** and **52** using colchicine and CA-4 as controls, the binding affinity of cyano **51** and alkyne **52** to the colchicine binding site (Nien et al., 2010) was introduced at 47% and 44% respectively with a 2-fold reduction in activity compared to CA-4, suggesting that both compounds may be bound to another binding site of colchicine binding. In addition, compound **51** and compound **52** were selected to observe the anti-microtubulin activity at concentrations of 1.25, 2.5, 5, 10, and 20 μM, respectively, and showed complete inhibition of microtubulin activity at a concentration of 10 μM. Then they each also inhibited MAP-rich microtubulin aggregation in a concentration-dependent manner. Finally, the reason whether the introduction of cyano and alkyne groups is related to the mode of microtubule protein interactions is unclear at present.

Wang et al. (2013b) also continued his previous research by exploring three design options using methyl 6-chloro-2-(N-(4-

methoxyphenyl)-N-methyl) amino nicotinate as the lead compound. The first was that they wanted to explore how to affect the growth inhibitory activity of tumor cells through some specific modifications, the second was that they opted for a conformational restriction strategy that explored feasible binding conformations and possible ligand-target interactions, and the third was to enhance the affinity to the binding site on microtubule proteins to produce good antitumor activity. A total of 24 new compounds were designed and synthesized using these three strategies, of which compound **53** (Figure 9) was the most active and showed high cytotoxicity (Perez-Sayans et al., 2010; Hung et al., 2012) (GI_{50} = 1.5–1.7 nM), especially against P-gp-expressing multidrug-resistant cell lines (vincristine-resistant KB) (KB-vin), in antiproliferative activity against four human tumor cell lines [A549, KB, KB-vin, and prostate cancer (DU145)] using paclitaxel as control (GI_{50}). Analogues **54**, **55**, **56**, and **57** (Figure 9) were also comparable [GI_{50} = (0.011–0.19 μM)]. In further studies, the active compounds **55–57** significantly inhibited microtubulin polymerization (IC_{50} = 0.92–1.0 μM) and strongly inhibited colchicine binding to microtubulin (75%–99%), using CA-4 (IC_{50} = 0.96 μM) as a control. In contrast to the previously designed pharmacological mechanism studies, they involved the study of drug solubility (Log P parameter) and *in vivo* metabolic stability (Roehm et al., 1991; Sun et al., 2012), in which five compounds, compounds **54**, **55**, **56** (3.21–7.67 μg/ml) exhibited better water solubility than the other two compounds (1.0 μg/ml), while with propranolol ($t_{1/2}$ = 3–5 h) and terfenadine ($t_{1/2}$ = 3 h) were used as positive controls to further assess the metabolic stability of compounds **54–56** by *in vitro* human liver microsomal culture assays. Compound **54** ($t_{1/2}$ = 7.89 min) and compound **53** ($t_{1/2}$ = 10.59 min) were unstable and rapid metabolism may help to reduce drug toxicity *in vivo* and could be used as novel anticancer candidates.

Tseng et al. (2015) designed and synthesized a series of novel 3-phenylquinolinone derivatives against breast cancer and performed antiproliferative activities *in vitro* on three breast cancer cell lines (MCF-7, MDA-MB-231, and SKBR-3) and one non-cancerous normal epithelial cell line (H184B5F5/M10). Among them, (*E*)-3-[3-(4-methoxyphenyl) qui-nolin-2-yl]-1-(3,4,5-trimethoxyphenyl) prop-2-en-1-one (compound **58**, Figure 9) showed anti-proliferative activity against MCF-7 (IC_{50} = 1.05 μM), MDA-MB-231 (IC_{50} = 0.75 μM) and SKBR-3 (IC_{50} = 0.78 μM) with growth inhibitory activity and no significant cytotoxicity against normal H184B5F5/M10 cell lines (IC_{50} > 10 μM). Therefore, a series of pharmacological mechanism studies were subsequently performed. MDA-MB-231 cells were selected for cell cycle experiments and compound **58** at 1, 5, and 10 μM concentrations, with CIL-102 used as a positive control, were treated together for 12, 24, and 36 h. As shown, 28% and 36% of cells were arrested in the G2/M phase when treated with 1 μM and 5 μM compound **58**, respectively, indicating that the induced cell cycle was concentration and time-dependent. Western blot experiments showed, downregulation of CDC25c, CDK1, and the cell cycle protein cyclin B1 in cells treated with compound **58**. To further investigate the mechanism, they selected CLI-102 as a control (10 μM) and selected the same concentration of compound **58** as in the cell cycle experiments (1, 5, and 10 μM), performed immunofluorescence experiments, and they found that the cells exhibited filamentous structures and a reduced round tube state in the cytoplasm. In addition, they went on to perform Western blot experiments to observe the microtubulin polymerization inhibition assay, and as shown, the microtubulin polymer form showed a concentration-dependent decrease, indication inhibition of microtubulin polymerization. They concluded that the inhibition of cell growth by compound **58** was due to apoptosis and they analysed the effect of compound **58** on the anti-apoptotic protein Bcl-2 and the pro-apoptotic proteins Bad and Bax. Compound **58** had no significant effect on the expression of apoptotic protein Bad, but upregulated apoptotic protein Bax and downregulated anti-apoptotic protein Bcl-2. In parallel they also evaluated caspase-3, caspase-8 and PARP in compound **58** treated MDA-MB-231 cells by Western blot assay. From this experiment they confirmed that compound **58** induces cell cycle arrest in the G2/M phase of PARP by activating caspase-3, caspase-8, which leads to cell death.

Chaudhary et al. (2016) started with the structure of CA-4 to ensure that the A and B ring remain *Z*-form. Like other chemists, they also considered various linkers to replace the double bond. Among their considerations, they selected the 2-aminoimidazole backbone, a backbone that is also a valuable molecular motif in medicinal chemistry. They designed and synthesized a series of 4,5-diaryl-2-aminoimidazoles and in performing experimental studies for antiproliferative activities, they found that compound **59** (Figure 12) showed good activity against five types of human cancer cells, which are MCF-7 (IC_{50} = 3 ± 2 nM), HeLa (IC_{50} = 10 ± 1 nM), hepatocellular carcinoma (HuH-7, IC_{50} = 335 ± 10 nM), MDA-MB-231(IC_{50} = 96 ± 13 nM) and drug-resistant mouse breast cancer (EMT6/AR1, IC_{50} = 350 ± 7 nM). In these cells, compound **59** was more potent than CA-4 (IC_{50} = 18 ± 2, 25 ± 2, 430 ± 9, 332 ± 32, and 495 ± 11 nM), and they speculated that it might be that the quinoline ring played a role in addition to the 2-aminoimidazole backbone. It might be due to the biological target—the N-/NH and C2-amine functional groups of the 2-aminoimidazole and quinoline N rings in the ligand play the role of hydrogen bonding to stabilize the ligand. Immunofluorescence experiments were performed immediately after and they found that compound **59** mildly depolymerized microtubules at a concentration of 5 nM and strongly depolymerized MCF-7 cells at 10 nM, which found that the compound blocked the single-stage spindle in mitosis. Meanwhile, they performed cell cycle experiments using MCF-7 cells using CA-4 as a control, and 40% and 74% of the cells were in the G2/M phase at 5 and 10 nM of compound **59** concentrations, which compared to CA-4 (20%

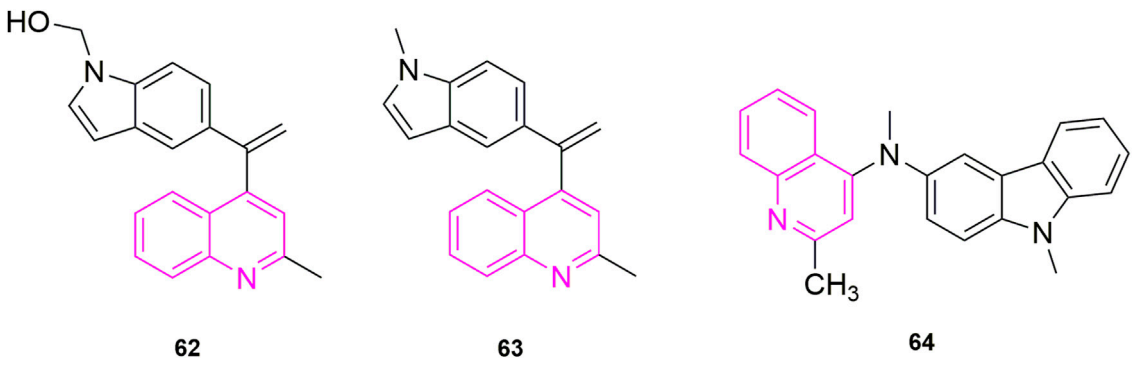

FIGURE 10
The structures of the compounds designed by Li et al. (2019) and Khelifi et al. (2017).

and 60%). To verify the reliability of the results, they stained the cells with Ser-10, which showed a concentration-dependent increase in the number of staining group proteins compared to the carrier cells. They evaluated the effect of compound **59** on MDA-MB-231 wound healing in migrating tumour cells, using CA-4, a well-known antivascular agent, as an example. Cells in the Control group had complete wound closure after 18 h. The results showed that compound **59** strongly inhibited the migration of MDA-MB-231 (50 and 150 nM, 56% ± 3% and 52% ± 4% inhibition) cells compared to CA-4 (50 nM, 8% ± 1% inhibition). Finally, they verified that the compound **59** is bound to the colchicine binding site (Cortese et al., 1977; Sackett, 1993) of microtubulin by measuring the fluorescence intensity of compound **59**, selected from CA-4 mycotoxin, paclitaxel, and vincristine.

Kumari et al. (2019) wanted to further elucidate the specific molecular mechanism and antitumor activity of compound **59** (Figure 10) based on the previous study by Chaudhary. Fibroblasts (L929) and non-tumorigenic mammary epithelial cells (MCF-10A) with IC_{50} values of 147 ± 45, 136 ± 30, and 3,316 ± 493 nM, respectively. In addition, they performed EB1 gene transfection and EB1 comet number calculations and they found that compound **59** strongly depolymerized microtubules of HeLa cells in interphase and mitotic cells, and also observed that reduction in the number of comets in cells treated with 5, 10, and 20 nM compound **59**. To further clarify the mechanism, they investigated the binding of compound **59** to EB1 with microtubules *in vitro*, and the results were due to a reduction in the number of comet cells due to a reduction in the number of microtubules in the cell body, not due to a reduction in EB1 binding to intracellular microtubules. They concluded not only that compound **59** inhibited intermediate microtubule dynamics in HeLa cells, but also that it could also interfere with mitotic spindle dynamics in the cells. They also evaluated chromosomes by examining the effect of compound **59** on chromosome movement by time-lapse imaging of live HeLa cells expressing histone 2B, using cells treated with a concentration of 10 and 20 nM, which showed that the compound **59** inhibited chromosome movement and that these chromosomes could not be aligned on tumid phase plate, and even an increase in chromosome consistency index (CI) was also observed as well as mitotic defects and chromosome misalignment, which could be responsible for the diminished microtubule dynamics. Subsequently, to investigate whether misaligned chromosomes activate the spindle assembly checkpoint (SAC), SAC activation was next examined after compound **59** treatment, which showed that cells treated with compound **59** were blocked at mid mitosis and were unable to enter the ate phase due to SAC activation, and in addition, they observed that compound **59** inhibited mitotic spindle assembly and induced multistage spindle formation. It is known that there are two ways of SAC activation, one is cell slippage through mitosis and the other is apoptosis. To confirm apoptosis, they did Western blot experiments with HeLa cell-associated proteins and showed that compound **59** can activate caspase-3 and caspase-9 to induce cleavage of PREP-1, which is consistent with the previously observed apoptosis. In addition, they also did mitochondrial membrane potential experiments and found that the compound could cause apoptosis by causing a decrease in mitochondrial membrane potential. These two forms of apoptosis will be of further value for subsequent studies. Finally, they were also the third study to perform animal experiments. They used NOD-SCID mice and according to Chaudhary's study, which used compound **59** and selected MCF-7 cells to determine the effect of xenografts in mice. The results of the study showed 49% reduction in tumor volume in mice treated with compound **59** compared to the control group, with no significant effect on body weight, suggesting a lesser side effect and a worthwhile candidate to investigate for the treatment of cancer.

Ibrahim et al. (2020) started from the analysis of the structure of CA-4 and proposed the same idea as major chemists to use

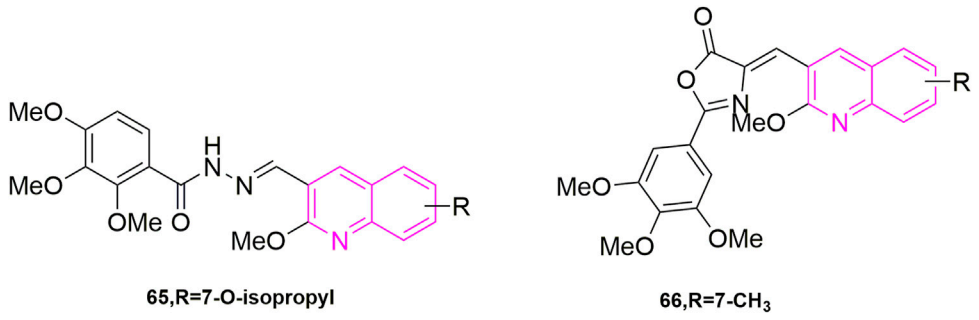

FIGURE 11
The structures of the compounds designed by Ibrahim et al. (2020, 2021).

heterocycles to replace the unstable double-built structure in CA-4, for example. Some chemists used quinoline to replace the B ring showing compounds with 10 times more powerful activity than CA-4. So, they designed two models of compounds, the first model was synthesized using the 3,4,5-trimethoxyphenyl fraction and the anthraquinone fraction as various electronic substituents for bioelectronic isomeric substitution of the B ring of CA-4. The second model is to add structural rigidity by introducing a C-ring (a hydrazone open linker and its cyclic form) to replace the carbene bond, and this prevents CA-4 from isomerizing *in vivo*. These compounds were subsequently tested for anti-value-added activity in four human cancer cells: MCF-7, human leukaemia cells (HL-60), HCT-116, and HeLa. Most of the compounds showed significant antiproliferative activity in the sub-micromolar range, with the most potent compound being compound **65** (Figure 11) (7-tert-butyl-substituted quinoline) (IC_{50} = 0.02–0.04 μM), and they later did antiproliferative activity assays (IC_{50} > 35 μM) in MCF-10A, showing that the compound against MCF-7 cells with good selectivity. Then they further did *in vitro* microtubulin polymerization inhibition assay and colchicine binding site assay, and the results were as expected, compound **65** effectively inhibited microtubulin polymerization and inhibited the colchicine binding site. With the results from the previous step, they continued with the cell cycle assay, selecting compound **65** at a concentration of 50 and 250 nM to treat MCF-7 cells, and the percentage of cells in the G2/M phase increased to 23.7% and 35.6% within 48 h compared to the control, a trend that further increased as time progressed. It indicates that compound **65** can induce MCF-7 cells blocked in the G2/M phase in a concentration-dependent manner. At the same time, they also did an apoptosis assay and MCF-7 cells treated with 50 nM and 250 nM significantly increased to 15% and 29% compared to the control (0.8%), indicating that the sub-compound can induce apoptosis in a concentration-dependent manner. The above results make compound **65** worthies of further investigation as an effective chemotherapeutic agent for targeting microtubulin.

Another study was carried out by Ibrahim et al. (2021), who further optimized CA-4 from its structure by inserting rigid oxazolones and imidazolines between the A and B ring to maintain *cis*-activity, and then maintained 3,4,5-trimethoxyphenyl by altering the electron group substitution effect. The designed compounds were subjected to antiproliferative activity assays against four MCF-7, HL-60, HCT-116, HeLa) using CA-4 as a control, where compound **66** (Figure 11) stood out with the optimal effect (IC_{50} = 0.019–0.042 μM), and more excitingly the compound was selective for cancer cells by verifying that MCF-10A (IC_{50} > 50 μM), compared to an IC_{50} value of 6.1 μM for CA-4. They have since performed more detailed mechanistic studies, such as the next microtubulin polymerization inhibition assay, where they used CA-4 as a control (IC_{50} = 2.17 μM) and found that compound **66** (IC_{50} = 1.21 μM) strongly inhibited microtubulin polymerization. They then proceeded to use compound **66** concentrations at 1 and 10 μM on the ability of colchicine to compete with microtubulin, using CA-4 as a control (86% and 97%), with 79% and 87% inhibition of compound **66**, this result suggests that the odd compound is involved in microtubulin polymerization inhibition *via* the colchicine binding site. After that they continued with cell cycle experiments, wanting to understand the potential anti-value-added activity of compound **66**, and selected 50 and 250 nM to observe the extent of cell block in the G2/M phase at 0, 24, 48, and 72 h. After 48 h, the percentage of the G2/M phase was 28.4% and 38.3% compared to the control (9.2%). After 72 h it was 33% and 40.8%. In addition, they found that the compound also induced phase apoptosis, they also looked at the percentage of apoptosis in cells at 24, 48, and 72 h. They mainly looked at apoptosis at 0 and 250 nM and CA-4 at 50 nM with an increase of 15%, 21%, and 29% respectively, in that order, compared to the control (1%). They then performed Western blot experiments and confirmed that the compound triggered apoptosis in MCF-7 cells by down-regulating the expression level of the anti-apoptotic protein Bcl-2 and up-regulating the expression of

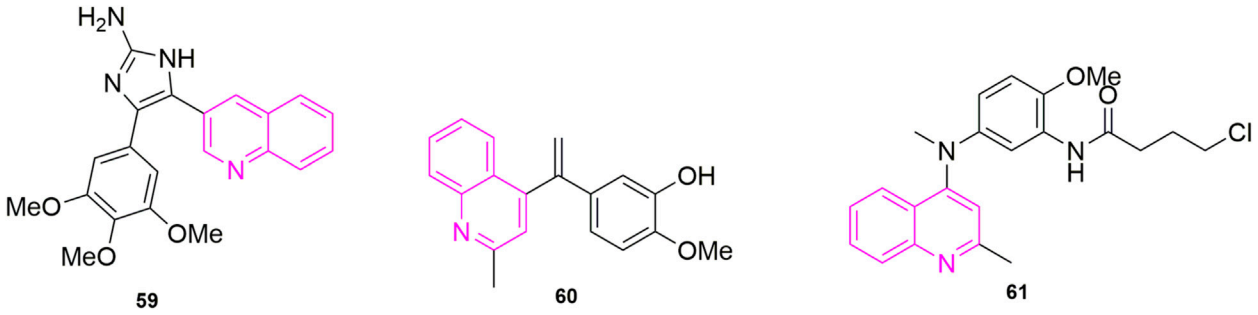

FIGURE 12
The structures of the compounds designed by Chaudhary et al. (2016), Khelifi et al. (2017), and Tseng et al. (2015).

the pro-apoptotic protein Bax, while activating caspase-9 and could participate in the mitochondrial apoptotic pathway, causing changes in mitochondrial membrane potential. The final cell scratching assay also confirmed that the compound could effectively inhibit cancer cell migration. In conclusion, this compound **66** is a drug worthy of further investigation for development as a microtubulin inhibitor.

2.2 Modification of *iso*-CA-4

Khelifi et al. (2017) study found that compounds using a quinoline ring to replace *iso*-CA-4 and 3,4,5-trimethoxy (A ring) in CA-4, while containing 3-hydroxy-4-methoxy on the B ring were the best actor. They tested five human cancer cell lines (IC_{50} < 10 nM), namely human astrocytoma cell lines (U87), acute phase chronic myeloid leukaemia cell lines (K562), Adriamycin-resistant K562 (K562R), A-549 and human colon cancer cells (HCT-116). To further investigate the mechanism, they continued to do immunofluorescence experiments using A549 cells, after treating the cells with compound **60** (Figure 12) for 24 h, mitotic spindle formation was disrupted at 1 nM concentration, and at 5 nM concentration, the microtubule system had been severely disrupted and even multinucleated cells appeared. They performed further cell cycle experiments, selecting compound **60** at concentrations of 0.5, 1, 5, and 10 nM, using dimethyl sulfoxide (DMSO) as a control. It can be observed that the compound **60** blocked the A549 cells in the G2/M phase in a concentration-dependent manner, with a 10 nM concentration blocking the entire population of A549 in G2/M phase (Provot et al., 2013). The final molecular docking showed that when compound **60** was bound to microtubulin, the nitrogen atom of the quinoline A ring could form a hydrogen bond with the Cys241 residue of the B subunit of microtubulin, which was noted that the colchicine binding site to microtubulin showed a binding pattern comparable to that previously used with the quinazoline analogues (*iso*-CoQ) and *iso*-CA-4.

Zhou et al. (2017) resynthesized a series of novel 4-anilinoquinoline derivatives based on their original synthesis of 4-anilino cyclic coumarin derivatives by replacing the coumarin ring with a quinoline ring and performed antiproliferative activity (Sri Ramya et al., 2017) studies in the human colon, lung, ovarian and breast cancer cells, where compound **61** (Figure 12) exhibited potent cytotoxicity (IC_{50} = 1.5–3.9 nM). In addition, they performed cell cycle assays, immunofluorescence assays, microtubule kinetic analysis and colchicine binding site competition assays sequentially to verify the pharmacological mechanism of the antitumor activity of the compound, which were also the first to study the antitumor activity of quinoline analogues in animal models. In the cell cycle assay, compound **61** was selected at a concentration of 3, 10, and 30 nM, the cells present in the G2/M phase (Wang et al., 2015) increased from 15.34% to 80.67%. In immunofluorescence experiments, they chose colchicine and paclitaxel as controls and treated with human ovarian cancer (A27280) cells with 5 nM and 50 nM of compound **61**, and it was seen that the compound **61** significantly disrupted microtubule formation at 50 nM, which was similar to the colchicine effect and even more targeted to microtubule proteins. In the microtubule kinetic analysis assay, compound **61** was taken at a concentration of 0.4, 2, and 10 μM and the control sample was chosen to be colchicine. Compound **61** inhibited microtubule protein polymerizations in a concentration-dependent manner, at 10 μM being significantly stronger than colchicine. In the colchicine binding site (Fortin et al., 2010) competition assay, compound **61** was selected at a concentration of 1, 5, and 25 μM, in Human hepatocellular carcinomas cell lines (HepG2), a dose-dependent inhibition of β-duct formation, leading to the disappearance of the adduct bands, which could be observed by Western blot experiments. Finally, they established an HCT-116 xenograft model in nude mice and selected 5-fluorouracil as a positive control drug (Wang et al., 2013a). They found that compound **61** significantly inhibited tumor growth, with an average inhibition rate of 54.3% already at day 18. The above

results laid the clinical foundation for compound **61** to become an anti-tumor drug.

Starting from the structure of *iso*-CA-4, Li et al. (2019) designed and synthesized a new series of quinoline-indole derivatives by replacing the 3,4,5- trimethoxyphenyl and isovanillin in the structure with quinoline and indole rings, respectively, and selected five human cancer cells for evaluation of antiproliferative activity, which were HepG2, KB, HCT-8, MDA-MB-231, and mouse hepatocellular carcinoma cells (H22). The best activities were compound **62** (Figure 10) and compound **63** (Figure 10) (IC_{50} = 2 nM–11 nM), which were more active than CA-4 (IC_{50} = 11 nM–14 nM). To elucidate whether compound **63**, the best active compound, targeted the microtubule protein-microscopic system, they went on to evaluate the effect of the compound on microtubule dynamics in K562 cells, using paclitaxel and colchicine as control, which found that compound 50 had 90.5% binding to colchicine at 5 μM. Further, they evaluated whether the compound **63** can disrupt the cell cycle distribution performed cell cycle experiments, using DMSO as control, the cell stays in G2/M phase increased to 23.21% compared to the control (10.51%). While they performed apoptosis experiments, selected compound **63** concentration at 1, 2, and 4 nM concentration, which was the first time in quinoline analogues to use Flow cytometry to analyse the article of apoptosis. The result that the percentage of apoptotic cells in the control group was 5.96% and after 48 h the total number of apoptotic cells reached 25.7%, 54.9%, and 72.8% respectively, indicating that compound **63** induced apoptosis in K562 cells in a concentration-dependent manner. Furthermore, to further understand whether the compound-induced apoptosis was involved in mitochondrial membrane integrity disruption, JC-1 assay was performed. Again, the concentration of compound **63** was selected as 1, 2, and 4 nM concentration and it was observed from the result that the collapse of mitochondrial membrane potential increased from 6.17% to 28.99%, 45.10%, and 73.55% respectively. This confirmed that apoptosis could disrupt mitochondrial membrane potential integrity. Later they performed immunofluorescence analysis to investigate whether the compound could disrupt microtubule dynamics in the cells, and after treatment of K562 cells with compound **62** at a concentration of 1, 2, and 4 nM for 24 h, which was evident that the microtubule network in the cells was disrupted, and these results indicated that compound **62** could disrupt the microtubule network. Based on the unique anti-vascular activity of CA-4, they then evaluated the anti-vascular activity of compound **62** in human umbilical vein endothelial cells (HUVEC) by performing cell scratching experiments, which could observe that compound **62** could inhibit HUVEC cord formation in a concentration-dependent manner. They designed the compound **62** as the second person to perform animal experiments in quinoline compound design, and they evaluated the antitumor activity of compound **62** and compound **63** by inoculating H22 cells into the right side of mice to establish a mouse model of hepatocellular carcinoma xenograft. They chose paclitaxel, CA-4, and CA-4P as positive controls, and both compounds at a dose of 20 mg/kg/day showed 57.3% and 63.7% tumor reduction at 21 days after treatment, even more than CA-4 (51%) and CA-4P (62.7%), and neither compound **62** and **63** had a significant effect on the body weight of the mice compared to the control drug.

Khelifi et al. (2019) based on the previous design of replacing the 3,4,5-trimethoxyphenyl in CA-4 or *iso*-CA-4 with a quinoline or quinazoline ring to maintain good antitumor activity, designed a new series of compounds based on this by replacing the B ring with a carbazole or indole ring, and they first performed antiproliferative activity assay, in which compound **64** (Figure 10) showed the strongest activity (IC_{50} = 70 pM). Thereafter, antiproliferative activity assays were performed in six more cells, which were A2780, cisplatin-resistant human ovarian tumor (A2780R), human pancreatic cancer (MiaPaca2), K562R, K562R and breast cancer cells (JIM-T1) continued evaluation, which found that the activity of compound **64** was all located within sub-nanomolar levels. Thereafter they performed cell cycle experiments and selected compound **64** at concentrations of 1/5/10 nM, compared to the control DMSO (23%), which blocked the HCT-116 cell cycle at G2/M by 25%, 80%, and 82%, respectively. Somewhat similar to previous methods, they assessed the ability of compound **64** to induce apoptosis by a specific apoptosis assay that cleaved pro-cysteine aspartate to active cysteine aspartate. HCT-116 cells were incubated with 0.5, 1, 5, and 10 nm of compound **64** for 24 h. The activity of caspase-3 and caspase-7 was assessed using a standard cysteines assay, using DMSO as a control. The proteolytic activity of cystoplasties was significantly increased in HCT-116 cells treated with compound **64**, implying that compound **64** induced apoptosis at a low concentration of 5 nM. Finally, they did *in vitro* antiproliferative activity assays, in which flattened endothelial cell aggregates form a reticular vascular network consisting of capillary-like vessels when grown on a stromal gel. After 2, 3, and 5 h, compound **64** was added to the tubular structure at a concentration of 10 nM, and it was observed that compound **64** rapidly disrupted the integrity of the vascular network. Their results also revealed a highly cytotoxic HUVEC showing antiproliferative activity at extended times (72 h) with a GI_{50} value of 3.23 ± 0.28 nM. This did not correlate with the disruption of the vasculature observed in its short time, suggesting that this compound is expected to be further screened as an anti-vascular active drug.

3 Similarities and differences in pharmacological experiments

The introduction of quinoline heterocycles, and the insertion of rigid heterocycles between the A and B rings seem to be a common interest of all major researchers in all designed quinoline compounds. By observing the designed compounds, it is found that the double bond is substituted with a heterocyclic

10.3389/fchem.2022.1040333

	Kuo	Li	Xia	Mara	Nien	Lee	Wang	Tseng	Chaudary	Khelfia	Zhou	Kumari	Ibrahim	
Total	6	6	5	1	5	3	4	5	3	4	1	8	5	Total
A549	1		1				1							3
HCT-18	1													1
RPMI-7951	1													1
KB	1	1			1	1	1							5
P-388	1													1
L1210	1													1
HCT-8		1	1											2
MCF-7			1					1					1	3
CAKI-1			1											1
SKMEL-2			1											1
Jurket				1										1
HT-29					1	1								2
MKN45					1	1								2
MDR-positive					1									1
KB-vin10					1		1							2
P-gp170/MDR					1									1
DU145							1	1						2
MDA-MB-231		1						1						2
SKBR-3								1						1
HeLa									1			1	1	3
HuH-7									1					1
MDR-EMT6/AR1									1					1
U87										1				1
K562		1								1				2
K562R										1				1
HCT-116										1	1		1	3
HepG2		1												1
H22		1												1
A2780												1		1
A2780R												1		1
MiaPaca2												1		1
JIM-T1												1		1
WI-38												1		1
L929												1		1
H184B5F5/M10								1						1
MCF-10A												1	1	2
HL-60													1	1

FIGURE 13
The researchers used all cell lines.

ring, and the B ring is substituted with a quinoline ring to obtain a compound with higher activity, such as compound **47** (MCF-7, IC_{50} = 3 ± 2 nM). Some of them also modify the compounds designed by their predecessors, including the substitution of substituents or modification of linkage bonds, all to more active compounds, such as compound **53** and **57**, which had mentioned above.

Among the compounds they designed, the human cancer cells they used the most were KB, which was used by five investigators, followed by MCF-7, HCT-116, and HeLa, which were used by three investigators each (Figure 13). Of course, after the antiproliferative activity assay in the human cancer cells they selected, they continued to select the compound with the best activity for the next mechanistic study. Their mechanistic studies included cell cycle assays, immunofluorescence assays, apoptosis assays, microtubulin polymerization inhibition assays, competitive colchicine binding assays, mitochondrial machine reactive oxygen mechanism assays, Western blot assays, cell scratching assays, and cell colony assays as well as molecular docking assays. In their pharmacological experiments, tubulin polymerization inhibition experiments were involved, indicating that this pharmacological mechanism experiment is an important means to prove the effective activity of the compounds. Some experiments have explored deeper pharmacological mechanisms, such as EB1 gene transfection and EB1 comet count, as well as the alteration of a series of apoptosis induced after SAG activation, such as compound **47**.

In most cell cycle experiments, the compound with the best quinoline derivative activity blocked the selected cancer cells in the G2/M phase in a concentration-dependent manner. Similarly in apoptosis experiments, the percentage of apoptotic cells increases with increasing compound concentration. In immunofluorescence experiments, the microtubule state disrupted by the compounds is usually seen, even with multinucleation. In microtubule protein polymerization inhibition assays, most quinoline compounds exhibit inhibition of microtubule proteins, some even beyond CA-4. In mitochondrial mechanism assays, compounds cause a collapse of the mitochondrial membrane potential, which leads to apoptosis. In Western blot experiments, compounds triggered apoptosis in cancer cells by downregulating the expression level

of the anti-apoptotic protein Bcl-2 and upregulating the expression of the pro-apoptotic protein Bax, while activating caspase-9 also triggered apoptosis. Cell scratching experiments also illustrated that quinoline-like microtubulin inhibitors can inhibit the migration of cancer cells. For the selected derivatives with activity beyond CA-4, the researchers further conducted animal experiments, taking subcutaneous inoculation of cancer cells and observing the size of tumor cells in mice after drug treatment, as well as observing changes in body weight of mice, and they found that most of the drugs with good activity had a manageable effect on body weight of mice. These pharmacological experiments can provide strong evidence for the follow-up research on these drugs.

4 Concluding remarks

This paper reviews all the designed and synthesized CA-4 analogues containing quinoline structures from 1992 to 2022, from the beginning of design to synthesis to pharmacological activity studies. Among these numerous quinoline-based derivatives, several good compounds deserve further push, such as compound **46**, which has been studied in detail from design to synthesis and then *in vitro*, and the results of the study are in line with expectations and are ready to be studied for consideration to enter the clinical study part. In addition, we did statistics on quinoline derivatives and found that the most used cell in the antiproliferative activity assay was the KB. Therefore, we suggest that the future design of quinoline derivatives can be considered to use this cell for the study. One point worth mentioning is that various researchers have only made modifications to the structure and stability, including modifications to the A and B ring, insertion of rigid thickened heterocyclic quinolines or indoles between the A and B ring, and substitution of 3,4,5-trimethoxyphenyl for other heterocycles. Fortunately, the modified derivatives have maintained better activity, and some even surpassed CA-4. However, for the modified toxicity of the compounds, only three investigators have conducted experiments on two non-human cells and confirmed the high selectivity of their designed compounds. Therefore, we suggest that the selectivity for normal cells can be improved on the existing basis. We encourage other researchers to also select potent compounds from mechanistic studies beyond the other mechanistic pathways studied above, not limited to apoptosis. For example, we propose the use of potent compounds in combination with cell signaling pathways for deeper studies. Finally, these quinoline-containing derivatives enrich the diversity of tubulin inhibitors, and also lay a foundation for the druggability of these compounds to go to the clinic.

Author contributions

CW; writing—original draft preparation, CW and JC; writing—review and editing, SY, LS, and YZ; supervision, Figure, JM, JZ, RZ; Table, DX; All authors have read and agreed to the published version of the manuscript.

Funding

This work was supported by grants from the Natural Science Foundation of Shandong (ZR2021QH156) and the Medical and Health Science and Technology Development Plan Project of Shandong (202113051140).

Conflict of interest

The authors declare that they have no known competing financial interests or personal relationships that could have appeared to influence the work reported in this paper.

Publisher's note

All claims expressed in this article are solely those of the authors and do not necessarily represent those of their affiliated organizations, or those of the publisher, the editors and the reviewers. Any product that may be evaluated in this article, or claim that may be made by its manufacturer, is not guaranteed or endorsed by the publisher.

Supplementary material

The Supplementary Material for this article can be found online at: https://www.frontiersin.org/articles/10.3389/fchem.2022.1040333/full#supplementary-material

References

Alvarez, R., Aramburu, L., Puebla, P., Caballero, E., Gonzalez, M., Vicente, A., et al. (2016). Pyridine based antitumour compounds acting at the colchicine site. *Curr. Med. Chem.* 23 (11), 1100–1130. doi:10.2174/0929867323111604201048 23

Bai, R. L., Paull, K. D., Herald, C. L., Malspeis, L., Pettit, G. R., and Hamel, E. (1991). Halichondrin B and homohalichondrin B, marine natural products binding in the vinca domain of tubulin. Discovery of tubulin-based mechanism of action by analysis of differential cytotoxicity data. *J. Biol. Chem.* 266 (24), 15882–15889. doi:10.1016/s0021-9258(18)98491-7

Chaudhary, V., Venghateri, J. B., Dhaked, H. P., Bhoyar, A. S., Guchhait, S. K., and Panda, D. (2016). Novel combretastatin-2-aminoimidazole analogues as potent

tubulin assembly inhibitors: Exploration of unique pharmacophoric impact of bridging skeleton and aryl moiety. *J. Med. Chem.* 59 (7), 3439–3451. doi:10.1021/acs.jmedchem.6b00101

Chen, M., Chen, H., Ma, J., Liu, X., and Zhang, S. (2014). Synthesis and anticancer activity of novel quinoline-docetaxel analogues. *Bioorg. Med. Chem. Lett.* 24 (13), 2867–2870. doi:10.1016/j.bmcl.2014.04.091

Cortese, F., Bhattacharyya, B., and Wolff, J. (1977). Podophyllotoxin as a probe for the colchicine binding site of tubulin. *J. Biol. Chem.* 252 (4), 1134–1140. doi:10.1016/s0021-9258(17)40631-4

Denault, J. B., and Salvesen, G. S. (2002). Caspases: Keys in the ignition of cell death. *Chem. Rev.* 102 (12), 4489–4500. doi:10.1021/cr010183n

Earnshaw, W. C., Martins, L. M., and Kaufmann, S. H. (1999). Mammalian caspases: Structure, activation, substrates, and functions during apoptosis. *Annu. Rev. Biochem.* 68, 383–424. doi:10.1146/annurev.biochem.68.1.383

Ferlin, M. G., Bortolozzi, R., Brun, P., Castagliuolo, I., Hamel, E., Basso, G., et al. (2010). Synthesis and *in vitro* evaluation of 3h-pyrrolo[3, 2-f]-quinolin-9-one derivatives that show potent and selective anti-leukemic activity. *ChemMedChem* 5 (8), 1373–1385. doi:10.1002/cmdc.201000180

Fortin, S., Lacroix, J., Cote, M. F., Moreau, E., Petitclerc, E., and René, C. G. (2010). Quick and simple detection technique to assess the binding of antimicrotubule agents to the colchicine-binding site. *Biol. Proced. Online* 12 (1), 113–117. doi:10.1007/s12575-010-9029-5

Gasparotto, V., Castagliuolo, I., and Ferlin, M. G. (2007). 3-substituted 7-phenyl-pyrroloquinolinones show potent cytotoxic activity in human cancer cell lines. *J. Med. Chem.* 50 (22), 5509–5513. doi:10.1021/jm070534b

Gigant, B., Wang, C., Ravelli, R. B., Roussi, F., Steinmetz, M. O., Curmi, P. A., et al. (2005). Structural basis for the regulation of tubulin by vinblastine. *Nature* 435 (7041), 519–522. doi:10.1038/nature03566

Honore, S., Pasquier, E., and Braguer, D. (2005). Understanding microtubule dynamics for improved cancer therapy. *Cell. Mol. Life Sci.* 62 (24), 3039–3056. doi:10.1007/s00018-005-5330-x

Hung, H. Y., Ohkoshi, E., Goto, M., Bastow, K. F., Nakagawa-Goto, K., and Lee, K. H. (2012). Antitumor agents. 293. Nontoxic dimethyl-4, 4'-dimethoxy-5, 6, 5', 6'-dimethylenedioxybiphenyl-2, 2'-dicarboxylate (DDB) analogues chemosensitize multidrug-resistant cancer cells to clinical anticancer drugs. *J. Med. Chem.* 55 (11), 5413–5424. doi:10.1021/jm300378k

Ibrahim, T. S., Hawwas, M. M., Malebari, A. M., Taher, E. S., Omar, A. M., Neamatallah, T., et al. (2021). Discovery of novel quinoline-based analogues of combretastatin A-4 as tubulin polymerisation inhibitors with apoptosis inducing activity and potent anticancer effect. *J. Enzyme Inhib. Med. Chem.* 36 (1), 802–818. doi:10.1080/14756366.2021.1899168

Ibrahim, T. S., Hawwas, M. M., Malebari, A. M., Taher, E. S., Omar, A. M., O'Boyle, N. M., et al. (2020). Potent quinoline-containing combretastatin A-4 analogues: Design, synthesis, antiproliferative, and anti-tubulin activity. *Pharm. (Basel)* 13 (11), 393. doi:10.3390/ph13110393

Kaur, K., Jain, M., Reddy, R. P., and Jain, R. (2010). Quinolines and structurally related heterocycles as antimalarials. *Eur. J. Med. Chem.* 45 (8), 3245–3264. doi:10.1016/j.ejmech.2010.04.011

Khelifi, I., Naret, T., Hamze, A., Bignon, J., Levaique, H., Garcia Alvarez, M. C., et al. (2019). N, N-bis-heteroaryl methylamines: Potent anti-mitotic and highly cytotoxic agents. *Eur. J. Med. Chem.* 168, 176–188. doi:10.1016/j.ejmech.2019.02.038

Khelifi, I., Naret, T., Renko, D., Hamze, A., Bernadat, G., Bignon, J., et al. (2017). Design, synthesis and anticancer properties of IsoCombretaQuinolines as potent tubulin assembly inhibitors. *Eur. J. Med. Chem.* 127, 1025–1034. doi:10.1016/j.ejmech.2016.11.012

Kumari, A., Srivastava, S., Manne, R. K., Sisodiya, S., Santra, M. K., Guchhait, S. K., et al. (2019). C12, a combretastatin-A4 analog, exerts anticancer activity by targeting microtubules. *Biochem. Pharmacol.* 170, 113663. doi:10.1016/j.bcp.2019.113663

Kuo, C. C., Hsieh, H. P., Pan, W. Y., Chen, C. P., Liou, J. P., Lee, S. J., et al. (2004). BPR0L075, a novel synthetic indole compound with antimitotic activity in human cancer cells, exerts effective antitumoral activity ***in vivo***. *Cancer Res.* 64 (13), 4621–4628. doi:10.1158/0008-5472.CAN-03-3474

Kuo, S. C., Lee, H. Z., Juang, J. P., Lin, Y. T., Wu, T. S., Chang, J. J., et al. (1993). Synthesis and cytotoxicity of 1, 6, 7, 8-substituted 2-(4'-substituted phenyl)-4-quinolones and related compounds: Identification as antimitotic agents interacting with tubulin. *J. Med. Chem.* 36 (9), 1146–1156. doi:10.1021/jm00061a005

Lee, H. Y., Chang, J. Y., Nien, C. Y., Kuo, C. C., Shih, K. H., Wu, C. H., et al. (2011). 5-Amino-2-aroylquinolines as highly potent tubulin polymerization inhibitors. Part 2. The impact of bridging groups at position C-2. *J. Med. Chem.* 54 (24), 8517–8525. doi:10.1021/jm201031f

Lee, H. Y., Lee, L. W., Nien, C. Y., Kuo, C. C., Lin, P. Y., Chang, C. Y., et al. (2012). Application of Suzuki arylation, Sonogashira ethynylation and Rosenmund-von Braun cyanation in the exploration of substitution effects on the anticancer activity of 2-aroylquinolines. *Org. Biomol. Chem.* 10 (48), 9593–9600. doi:10.1039/c2ob26614h

Li, L., Wang, H. K., Kuo, S. C., Wu, T. S., Lednicer, D., Lin, C. M., et al. (1994a). Antitumor agents. 150. 2', 3', 4', 5', 6, 7-substituted 2-phenyl-4-quinolones and related compounds: Their synthesis, cytotoxicity, and inhibition of tubulin polymerization. *J. Med. Chem.* 37 (8), 1126–1135. doi:10.1021/jm00034a010

Li, L., Wang, H. K., Kuo, S. C., Wu, T. S., Mauger, A., Lin, C. M., et al. (1994b). Antitumor agents. 155. Synthesis and biological evaluation of 3', 6, 7-substituted 2-phenyl-4-quinolones as antimicrotubule agents. *J. Med. Chem.* 37 (20), 3400–3407. doi:10.1021/jm00046a025

Li, W., Shuai, W., Sun, H., Xu, F., Bi, Y., Xu, J., et al. (2019). Design, synthesis and biological evaluation of quinoline-indole derivatives as anti-tubulin agents targeting the colchicine binding site. *Eur. J. Med. Chem.* 163, 428–442. doi:10.1016/j.ejmech.2018.11.070

Liou, J. P., Chang, J. Y., Chang, C. W., Chang, C. Y., Mahindroo, N., Kuo, F. M., et al. (2004). Synthesis and structure-activity relationships of 3-aminobenzophenones as antimitotic agents. *J. Med. Chem.* 47 (11), 2897–2905. doi:10.1021/jm0305974

Lu, Y., Chen, J., Xiao, M., Li, W., and Miller, D. D. (2012). An overview of tubulin inhibitors that interact with the colchicine binding site. *Pharm. Res.* 29 (11), 2943–2971. doi:10.1007/s11095-012-0828-z

Martin, S. J., Reutelingsperger, C. P., McGahon, A. J., Rader, J. A., van Schie, R. C., LaFace, D. M., et al. (1995). Early redistribution of plasma membrane phosphatidylserine is a general feature of apoptosis regardless of the initiating stimulus: Inhibition by overexpression of bcl-2 and abl. *J. Exp. Med.* 182 (5), 1545–1556. doi:10.1084/jem.182.5.1545

Monks, A., Scudiero, D., Skehan, P., Shoemaker, R., Paull, K., Vistica, D., et al. (1991). Feasibility of a high-flux anticancer drug screen using a diverse panel of cultured human tumor cell lines. *JNCI J. Natl. Cancer Inst.* 83 (11), 757–766. doi:10.1093/jnci/83.11.757

Nien, C. Y., Chen, Y. C., Kuo, C. C., Hsieh, H. P., Chang, C. Y., Wu, J. S., et al. (2010). 5-Amino-2-aroylquinolines as highly potent tubulin polymerization inhibitors. *J. Med. Chem.* 53 (5), 2309–2313. doi:10.1021/jm900685y

Perez-Melero, C., Maya, A. B., del Rey, B., Pelaez, R., Caballero, E., and Medarde, M. (2004). A new family of quinoline and quinoxaline analogues of combretastatins. *Bioorg. Med. Chem. Lett.* 14 (14), 3771–3774. doi:10.1016/j.bmcl.2004.04.098

Perez-Sayans, M., Somoza-Martin, J. M., Barros-Angueira, F., Diz, P. G., Rey, J. M., and Garcia-Garcia, A. (2010). Multidrug resistance in oral squamous cell carcinoma: The role of vacuolar ATPases. *Cancer Lett.* 295 (2), 135–143. doi:10.1016/j.canlet.2010.03.019

Provot, O., Hamze, A., Peyrat, J. F., Brion, J. D., and Alami, M. (2013). Discovery and hit to lead optimization of novel combretastatin A-4 analogues: Dependence of C-linker length and hybridization. *Anticancer. Agents Med. Chem.* 13 (10), 1614–1635. doi:10.2174/18715206131013120616230 2

Pryor, D. E., O'Brate, A., Bilcer, G., Diaz, J. F., Wang, Y., Wang, Y., et al. (2002). The microtubule stabilizing agent laulimalide does not bind in the taxoid site, kills cells resistant to paclitaxel and epothilones, and may not require its epoxide moiety for activity. *Biochemistry* 41 (29), 9109–9115. doi:10.1021/bi020211b

Roehm, N. W., Rodgers, G. H., Hatfield, S. M., and Glasebrook, A. L. (1991). An improved colorimetric assay for cell proliferation and viability utilizing the tetrazolium salt XTT. *J. Immunol. Methods* 142 (2), 257–265. doi:10.1016/0022-1759(91)90114-u

Rubinstein, L. V., Shoemaker, R. H., Paull, K. D., Simon, R. M., Tosini, S., Skehan, P., et al. (1990). Comparison of *in vitro* anticancer-drug-screening data generated with a tetrazolium assay versus a protein assay against a diverse panel of human tumor cell lines. *JNCI J. Natl. Cancer Inst.* 82 (13), 1113–1117. doi:10.1093/jnci/82.13.1113

Sackett, D. L. (1993). Podophyllotoxin, steganacin and combretastatin: Natural products that bind at the colchicine site of tubulin. *Pharmacol. Ther.* 59 (2), 163–228. doi:10.1016/0163-7258(93)90044-e

Solomon, V. R., Pundir, S., and Lee, H. (2019). Examination of novel 4-aminoquinoline derivatives designed and synthesized by a hybrid pharmacophore approach to enhance their anticancer activities. *Sci. Rep.* 9 (1), 6315. doi:10.1038/s41598-019-42816-4

Sri Ramya, P. V., Angapelly, S., Guntuku, L., Singh Digwal, C., Nagendra Babu, B., Naidu, V. G. M., et al. (2017). Synthesis and biological evaluation of curcumin inspired indole analogues as tubulin polymerization inhibitors. *Eur. J. Med. Chem.* 127, 100–114. doi:10.1016/j.ejmech.2016.12.043

Stefanski, T., Mikstacka, R., Kurczab, R., Dutkiewicz, Z., Kucinska, M., Murias, M., et al. (2018). Design, synthesis, and biological evaluation of novel

combretastatin A-4 thio derivatives as microtubule targeting agents. *Eur. J. Med. Chem.* 144, 797–816. doi:10.1016/j.ejmech.2017.11.050

Sun, L. Q., Zhu, L., Qian, K., Qin, B., Huang, L., Chen, C. H., et al. (2012). Design, synthesis, and preclinical evaluations of novel 4-substituted 1, 5-diarylanilines as potent HIV-1 non-nucleoside reverse transcriptase inhibitor (NNRTI) drug candidates. *J. Med. Chem.* 55 (16), 7219–7229. doi:10.1021/jm3007678

Tseng, C. H., Tzeng, C. C., Hsu, C. Y., Cheng, C. M., Yang, C. N., and Chen, Y. L. (2015). Discovery of 3-phenylquinolinylchalcone derivatives as potent and selective anticancer agents against breast cancers. *Eur. J. Med. Chem.* 97, 306–319. doi:10.1016/j.ejmech.2015.04.054

Vermes, I., Haanen, C., Steffens-Nakken, H., and Reutelingsperger, C. (1995). A novel assay for apoptosis. Flow cytometric detection of phosphatidylserine expression on early apoptotic cells using fluorescein labelled Annexin V. *J. Immunol. Methods* 184 (1), 39–51. doi:10.1016/0022-1759(95)00072-i

Wang, C., Zhang, Y., Wu, Y., and Xing, D. (2021). Developments of CRBN-based PROTACs as potential therapeutic agents. *Eur. J. Med. Chem.* 225, 113749. doi:10.1016/j.ejmech.2021.113749

Wang, G., Peng, F., Cao, D., Yang, Z., Han, X., Liu, J., et al. (2013a). Design, synthesis and biological evaluation of millepachine derivatives as a new class of tubulin polymerization inhibitors. *Bioorg. Med. Chem.* 21 (21), 6844–6854. doi:10.1016/j.bmc.2013.02.002

Wang, S., Fang, K., Dong, G., Chen, S., Liu, N., Miao, Z., et al. (2015). Scaffold diversity inspired by the natural product evodiamine: Discovery of highly potent and multitargeting antitumor agents. *J. Med. Chem.* 58 (16), 6678–6696. doi:10.1021/acs.jmedchem.5b00910

Wang, X. F., Wang, S. B., Ohkoshi, E., Wang, L. T., Hamel, E., Qian, K., et al. (2013b). N-aryl-6-methoxy-1, 2, 3, 4-tetrahydroquinolines: A novel class of antitumor agents targeting the colchicine site on tubulin. *Eur. J. Med. Chem.* 67, 196–207. doi:10.1016/j.ejmech.2013.06.041

Xia, Y., Yang, Z. Y., Xia, P., Bastow, K. F., Tachibana, Y., Kuo, S. C., et al. (1998). Antitumor agents. 181. Synthesis and biological evaluation of 6, 7, 2', 3', 4'-substituted-1, 2, 3, 4-tetrahydro-2-phenyl-4-quinolones as a new class of antimitotic antitumor agents. *J. Med. Chem.* 41 (7), 1155–1162. doi:10.1021/jm9707479

Zamzami, N., Marchetti, P., Castedo, M., Decaudin, D., Macho, A., Hirsch, T., et al. (1995). Sequential reduction of mitochondrial transmembrane potential and generation of reactive oxygen species in early programmed cell death. *J. Exp. Med.* 182 (2), 367–377. doi:10.1084/jem.182.2.367

Zhou, Y., Yan, W., Cao, D., Shao, M., Li, D., Wang, F., et al. (2017). Design, synthesis and biological evaluation of 4-anilinoquinoline derivatives as novel potent tubulin depolymerization agents. *Eur. J. Med. Chem.* 138, 1114–1125. doi:10.1016/j.ejmech.2017.07.040

Glossary

CA-4 Combretastatin A-4

CBSI Colchicine binding site inhibitor

A-549 Human lung carcinoma cell lines

HCT-8 Ileocecal carcinoma cell lines

RPMI-7951 Melanoma cell lines

KB Oral epidermoid carcinoma cells

P-388 and L1210 Two murine leukaemia cell lines

MCF-7 Breast cancer cell lines

CAKI-1 Renal cancer cell lines

SKMEL-2 Melanoma cancer cell lines

ROS Reactive oxygen species

PRAP Poly ADP-ribose polymerase

HT-29 Human colorectal carcinoma cell lines

MKN45 Human gastric cancer cell lines

H460 Non-small-cell lung carcinoma cell lines

MDR Multiple drug resistance

MRP Multi-drug resistant protein

KB-vin P-gp-expressing multidrug-resistant cell lines (vincristine-resistant KB)

DU145 Prostate cancer cell lines

H184B5F5/M10 Non-cancerous normal epithelial cell lines

MDA-MB-231 Breast cancer cell lines

SKBR-3 Breast cancer cell lines

CIL-102 A known inhibitor of tubulin polymerization

HuH-7 Hepatocellular carcinoma cell lines

EMT6/AR1 Drug-resistant mouse breast cancer cell lines

U87 Human astrocytoma cell lines

K562 Acute phase chronic myeloid leukaemia cell lines

HCT-116 Human colon cancer cells

A27280 Human ovarian cancer cell lines

HepG2 Human hepatocellular carcinomas cell lines

H22 Mouse hepatocellular carcinoma cell lines

HUVECs Human umbilical vein endothelial cell lines

A2780R Cisplatin-resistant human ovarian tumor cell lines

MiaPaca2 Human pancreatic cancer cell lines

JIM-T1 Breast cancer cell lines

L929 Fibroblasts cell lines

MCF-10A Non-tumorigenic mammary epithelial cell lines

CI Chromosome consistency index

SAC Spindle assembly checkpoint

frontiers | Frontiers in Chemistry

TYPE Original Research
PUBLISHED 15 November 2022
DOI 10.3389/fchem.2022.1041328

OPEN ACCESS

EDITED BY
Xi Zheng,
Rutgers, The State University of New Jersey, United States

REVIEWED BY
Ren Qinggang,
Guangdong University of Petrochemical Technology, China
Jie Zheng,
Shangrao Normal University, China

*CORRESPONDENCE
Xin Zhong,
zhuhua2006@163.com

SPECIALTY SECTION
This article was submitted to Medicinal and Pharmaceutical Chemistry, a section of the journal Frontiers in Chemistry

RECEIVED 10 September 2022
ACCEPTED 04 October 2022
PUBLISHED 15 November 2022

CITATION
Zhu H and Zhong X (2022), Synthesis of activity evaluation of flavonoid derivatives as α-glucosidase inhibitors. *Front. Chem.* 10:1041328. doi: 10.3389/fchem.2022.1041328

Synthesis of activity evaluation of flavonoid derivatives as α-glucosidase inhibitors

Hua Zhu[1] and Xin Zhong[2]*

[1]School of Chemistry and Chemical Engineering, Mianyang Teacher's College, Mianyang, China, [2]Dean's Office, Mianyang Teacher's College, Mianyang, China

Six flavonoid derivatives were synthesized and tested for anti-α-glucosidase activities. All derivatives were confirmed using NMR and HRMS and exhibited excellent inhibitory effects on α-glucosidase. Derivative **four** exhibited the highest anti-α-glucosidase activity (IC_{50}: 15.71 ± 0.21 μM). Structure-activity relationship results showed that bromine group would be the most beneficial group to anti-α-glucosidase activity. Inhibitory mechnism and inhibition kinetics results showed derivative **four** was a reversible and mixed-type inhibitor. Molecular docking revealed that derivative **four** was tightly bind to the amino acid residues of active pocket of α-glucosidase and formed hydrogen bond, π-π stacking, and Pi-Donor hydrogen with α-glucosidase. Moreover, the physicochemical parameters of all derivatives were assessed using SwissADME software. This results also showed that the hybridization of flavonoid and phenylpropionic acid would be a useful strategy for the development of α-glucosidase inhibitors.

KEYWORDS

α-glucosidase, inhibitor, synthesis, flavonoid, screen

1 Introduction

Diabetes mellitus is reported as a common chronic metabolic disorder with hyperglycemia. This hyperglycemia can cause microvascular complications such as cardiovascular, renal, and neurological problems (Forouhi and Wareham, 2014; Proenca et al., 2021). Numerous researches reveal that the hydrolysis of carbohydrates is the major inducement of hyperglycemia (Kokil et al., 2015; Kousaxidis et al., 2020). α-Glucosidase located in the small intestine is one important catalytic hydrolase, which can hydrolyze carbohydrates into absorbable glucose. The excess absorbed glucose causes postprandial hyperglycemia, resulting in diabetes (Ali et al., 2017; Proença et al., 2017; Tsoutsouki et al., 2020). Thence, inhibiting α-glucosidase activity might be an effective strategy for controlling postprandial hyperglycemia (Imran et al., 2015; Rasouli et al., 2017; Sohretoglu et al., 2018). Although lots of α-glucosidase inhibitors have been developed, only a few have been used as clinical drugs for the treatment of diabetes, including acarbose, voglibose, and miglitol (Figure 1). But they are reported to have some adverse reactions during the use (Santos et al., 2018; Hedrington and Davis, 2019). This encourages researchers to find more effective and safety α-glucosidase inhibitors.

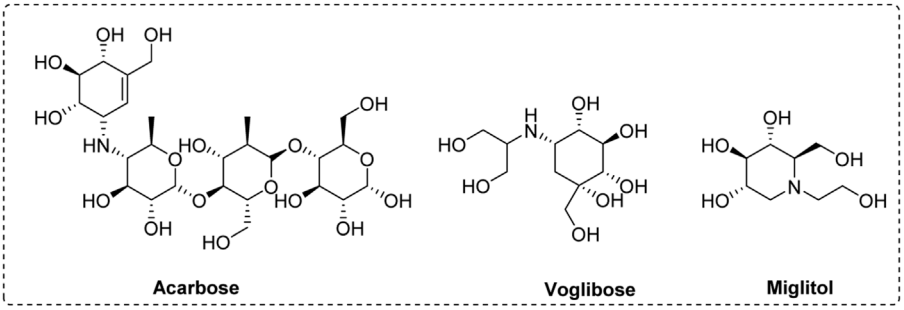

FIGURE 1
The chemical structure of acarbose, voglibose, and miglitol.

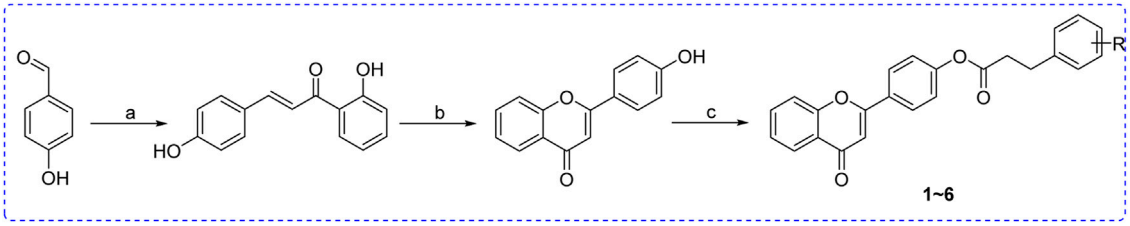

SCHEME 1
Synthesis of flavonoid derivatives **1**~**6**. Reagents and condition: **(A)** Piperdine, reflux, 160°C; **(B)** DMSO, I_2, 100°C; **(C)** Substituted phenylpropionic acid, DMSO, EDCI, DCM, rt.

TABLE 1 The anti-α-glucosidase activity of flavonoid derivatives.

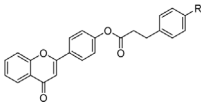

Compound	R	IC_{50} (μM)
1		42.06 ± 0.08*
2	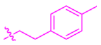	21.55 ± 0.13*
3	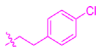	31.09 ± 0.10*
4	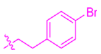	15.71 ± 0.21*
5		19.66 ± 0.04*
6	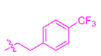	27.54 ± 0.02*
Acarbose		658.26 ± 11.48

Natural products are the important medicinal resources, and many clinical drugs are generated directly or indirectly from natural products (Şöhretoğlu and Sari, 2020; Proenca et al., 2021; Mo et al., 2022). Flavonoids present abundantly in natural products that are a class of compounds with biological and pharmacological activities (Dong et al., 2020; Qin et al., 2020; Wang et al., 2020). Besides, antioxidants, antibacterial, anti-inflammatory, anti-tumor, etc., their anti-α-glucosidase and anti-diabetic properties have gotten more and more attention recently (Amador et al., 2020; Liu et al., 2020; Tang et al., 2020). Now, lots of synthesized and isolated flavonoids were obtained as α-glucosidase inhibitors (Jia et al., 2019; Lu et al., 2020; Oueslati et al., 2020; Zhu et al., 2020).

On the other hand, the esterification modification of natural products is effective strategies to obtain better active compounds or ester prodrugs. Previous works revealed that the esterification modification of coumarin and honokiol produced a series of compounds with better anti-α-glucosidase activity (Sheng et al., 2018; Hu et al., 2021). Thence, in this work, flavonoid skeleton was modified with esterification by substituted phenylpropionic acid, followed by the screening of anti-α-glucosidase activity.

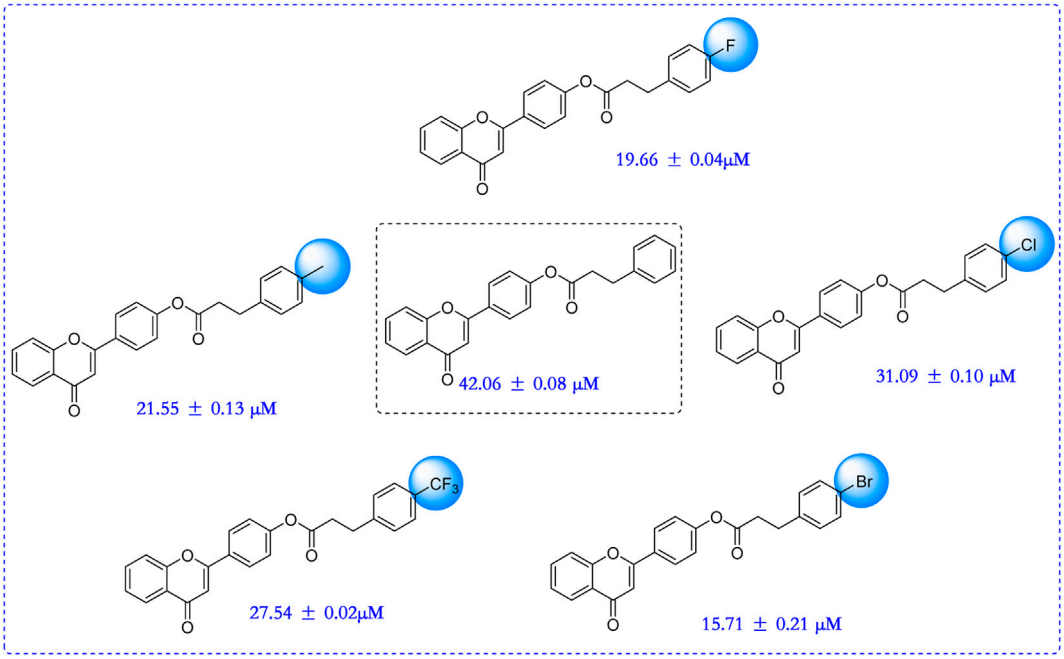

FIGURE 2
SAR analysis of synthesized six flavonoid derivatives.

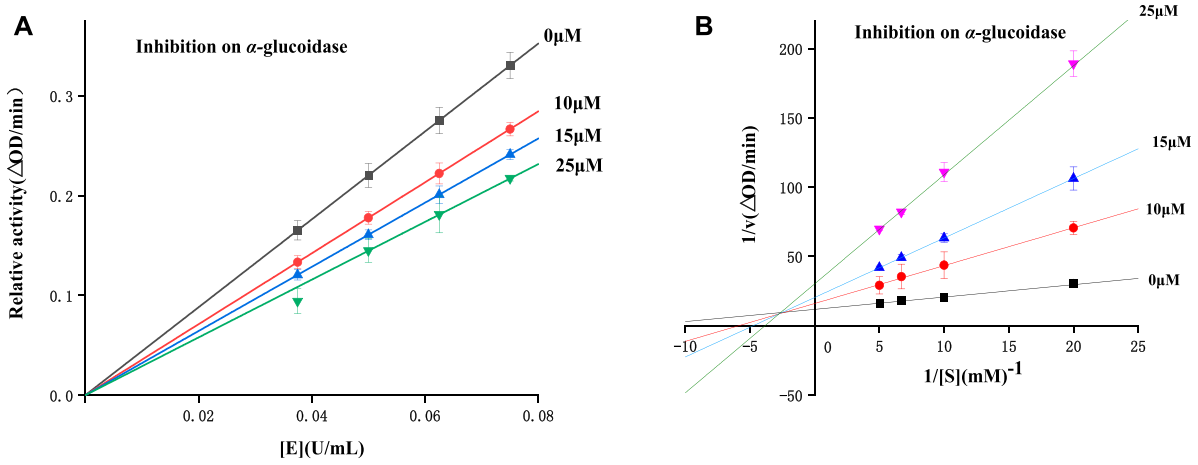

FIGURE 3
Inhibitory mechanism **(A)** and type assay **(B)** investigation.

2 Results and discussion

2.1 Chemistry

All flavonoid ester derivatives (**1~6**) were synthesized according to route outlined in Scheme 1. p-Hydroxybenzaldehyde and 2-Hydroxyacetophenone underwent Claisen-Schmidt condensation to yield 4,2′-dihydroxychalcone, followed by the cyclization reaction to produce 4′-hydroxyflavonoid which reacted with substituted phenylpropionic acid to generate flavonoid derivatives (**1~6**), respectively. All synthesized flavonoid ester derivatives were identified by ^{1}H NMR, ^{13}C NMR and HRMS.

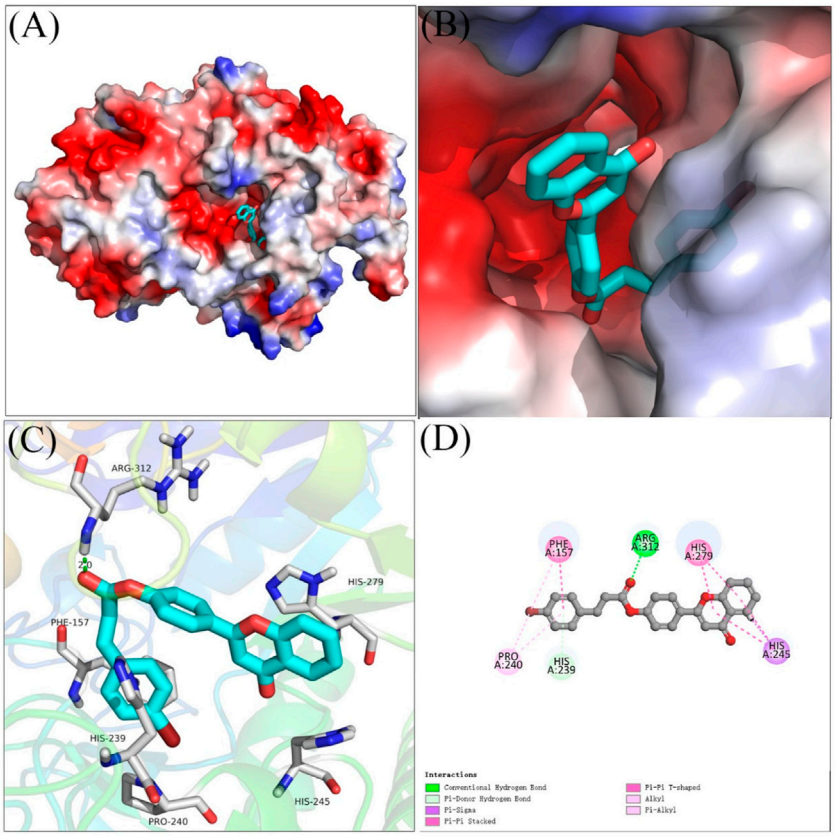

FIGURE 4
The molecular docking of compound 4 with α-glucosidase. **(A,B)** compound 4 in the active pocket. **(C,D)** detailed binding between compound 4 and enzyem.

TABLE 2 The physicochemical parameters of all derivatives.

Compound	MW (g/mol)	RB	HBA	HBD	TPSA (Å^2)	LogP$_{o/w}$	WS
1	370.4	6	4	0	56.51	4.6	Poorly soluble
2	384.42	6	4	0	56.51	4.92	Poorly soluble
3	404.84	6	4	0	56.51	5.12	Poorly soluble
4	449.29	6	4	0	56.51	5.16	Poorly soluble
5	388.39	6	5	0	56.51	4.92	Poorly soluble
6	438.4	7	7	0	56.51	5.65	Poorly soluble

2.2 α-Glucosidase inhibition assay and SAR analysis

All synthesized six flavonoids were screened for inhibitory activity against α-glucosidase and the results were listed in Table 1. The six flavonoid derivatives existed potential anti-α-glucosidase activity with IC_{50} range of 15.71 ± 0.21–42.06 ± 0.08 μM, which was stronger than that of acarbose (658.26 ± 11.48 μM). Among them, compound **4** showed the strongest inhibitory activity (IC_{50} = 15.71 ± 0.21 μM). The results showed that flavonoid derivatives could be used as potential α-glucosidase inhibitors. That also was said that hybridization of flavonoid skeleton and phenylpropionic acid would be an effective strategy to discover anti-α-glucosidase inhibitors.

Compared to acarbose, $^*p < 0.05$.

In order to better guide future derivatization, the structure-activity relationship (SAR) was analyzed. For all six derivatives, compound **1** with no substituent group at

phenylpropionic acid fraction was selected as template molecule, showing an IC_{50} value of 42.06 ± 0.08 μM. Introducing methyl group (compound **2**, IC_{50} = 21.55 ± 0.13 μM), chlorine group (compound **3**, IC_{50} = 31.09 ± 0.10 μM), bromine group (compound **4**, IC_{50} = 15.71 ± 0.21 μM), fluorine group (compound **5**, IC_{50} = 19.66 ± 0.04 μM), and trifluoromethyl group (compound **6**, IC_{50} = 27.54 ± 0.02 μM) on phenylpropionic acid fraction caused effective increase in inhibition activity. Thence, introducing substituents would enhance their anti-α-glucosidase activity and the sequence of substitute group was bromine, fluorine, methyl, trifluoromethyl, chlorine group, and hydrogen. (Figure 2).

2.3 Inhibitory mechanism and type assay

To study the inhibitory mechanisms of all derivatives on α-glucosidase, enzyme inhibitory mechnism was detected using compound **4** with the strongest inhibitory. Figure 3A illustrated the plots of enzyme activity vs. enzyme concentration. It could be seen that the plots with compound **4** (0–25 μM) all passed the origin, revealing compound **4** as a reversible inhibitor.

The kinetic type was also studied using Lineweaver-Burk plots. As shown in the Lineweaver-Burk plots of enzyme activity vs. substrate concentration (Figure 3B), all plots with compound **4** (0–25 μM) intersected at the second quadrant, indicating a mix-type inhibition.

2.4 Molecular docking

Molecular docking of compound **4** with *α*-glucosidase was simulated using SYBYL software, and the binding interactions were analyzed. As shown in Figures 4A–3B, compound **4** bind reliably with the active pocket, the flavonoid section of compound **4** located at entrance of the active pocket, and the bromophenylpropionic acid section located at the interior. Figures 3C,D were the detailed interactions in 3D view and 2D view, respectively. It was seen that the carbonyl moiety formed a hydrogen bond with Arg 312 (2.0 Å), benzene ring of bromophenylpropionic acid section formed a π-π stacking with Phe157 and Pi-Donor hydrogen bond with His239. Moreover, compound **4** also formed hydrophobic interactions with Pro240, His245, and His279.

2.5 Physicochemical parameters

The physicochemical parameters of all derivatives were analyzed using SwissADME software. The results showed (Table 2) that all derivatives presented favourable drug-likeness profile. The molecular weight, RB, HBA, HBD, and TPSA of derivatives basically met the standard.

3 Conclusion

In this study, we synthesized six flavonoid derivatives and tested their anti-*α*-glucosidase activities. All derivatives exhibited excellent inhibitory effects on *α*-glucosidase. Among them, derivative four exhibited the highest anti-*α*-glucosidase activity (IC_{50}: 15.71 ± 0.21 μM). Moreover, bromine group was the optimal substituent for activity. Inhibitory mechnism and inhibition kinetics results showed derivative four was a reversible and mixed-type inhibitor. Molecular docking revealed that derivative **four** was tightly bind to the amino acid residues of active pocket of α-glucosidase. Thence, the hybridization of flavonoid and phenylpropionic acid would be a useful strategy for the development of *α*-glucosidase inhibitors. In addition, derivative **four** would be used as a lead compound to develop hypoglycemic drugs.

4 Experimental

4.1 Materials and methods

α-Glucosidase from *Saccharomyces cerevisiae* (EC 3.2.1.20) and *p*-Nitrophenyl-*α*-D-galactopyranoside (*p*-NPG) were purchased from Sigma-Aldrich. All additional reagents and solvents were readily obtained from a commercial source. NMR spectra were obtained on 500 MHz equipment in $CDCl_3$. High-resolution mass spectral (HRMS) data was recorded on Apex II using the ESI technique.

4.2 General procedure for the synthesis of flavonoid derivatives 1–6

2-hydroxy acetophenone (0.01 M) and appropriate benzaldehydes (0.01 M) were added into piperidine (10 ml) and maintained at 160 C. After reaction was completed, the mixture was treated with ice-cold water and adjusted pH. Then this obtained precipitate was recrystallized in methanol to give 4,2′-dihydroxychalcone. Then, 4,2′-dihydroxychalcone (0.015 M) and iodine (0.015 M) were added into dimethyl sulfoxide, and stirred for 60 min at 140 C. After treated with 20% aqueous sodium thiosulfate, the mixture was extracted with DCM, followed by washing with brine, concentrating in a rotary evaporator, and subsequent recrystallization to obtain 4′-hydroxyflavonoid. 4′-hydroxyflavonoid (0.21 mmol), substituted phenylpropionic acid (0.32 mmol), DMAP (0.42 mmol) and EDCI (0.42 mmol) were added into 10 ml DCM and reacted at room temperature. Then the mixture was quenched by water, extracted with DCM, washed with

brine, dried by $MgSO_4$, removed solvent under vacuum, and subsequently purified using column chromatography to yield the corresponding flavonoid derivatives **1** ~ **6**. All ^1H NMR, ^{13}C NMR and HRMS data were summarized into SUPPORTING INFORMATION.

4.3 A-glucosidase inhibition and kinetics assay

The α-glucosidase inhibitory activity of compounds (**1** ~ **6**) was detected as described in previous reports (Adisakwattana et al., 2009; Adisakwattana et al., 2013; Zhang et al., 2022). 10 μl α-glucosidase solution, 10 μl compound were added into 80 μl phosphate buffer, and the mixture was incubated for 10 min. Then, 100 μl *p*-NPG solution was added into the mixture, followed by the absorbance change detection at 405 nm. The inhibition rate (%) = $[(OD_1 - OD_0)/OD_0] \times 100\%$, where OD_1 and OD_0 were the absorbance of tested compound and blank, respectively. The IC_{50} value was calculated from the plot of inhibition rate vs. compound concentration. Acarbose was used as a positive sample. All samples were repeated four times. The enzyme inhibitory mechnism and kinetic type were also determined according to previous reported reports (Adisakwattana et al., 2004; Song et al., 2016).

4.4 Molecular docking

Molecular docking of compound **4** with *α*-glucosidase was simulated using SYBYL software according to previous researches (Li et al., 2016; Xu et al., 2019). Compound **4** was constructed and energy minimized using software own programs. The *α*-glucosidase were prepared by hydrogenation and disability rehabilitation. Then, the docking between compound **4** and *α*-glucosidase was operated in the default format.

4.5 Statistical analysis

Data was presented as mean ± SD. One-way ANOVA was used to analyze the difference between groups. $p < 0.05$ was considered significant.

Data availability statement

The datasets presented in this study can be found in online repositories. The names of the repository/repositories and accession number(s) can be found in the article/Supplementary Material.

Author contributions

HZ carried out the investigation, and XZ was responsible for project design.

Funding

This work was financially supported by the Start Fund Project of Mianyang Teacher's College (Nos. QD 2020A01).

Conflict of interest

The authors declare that the research was conducted in the absence of any commercial or financial relationships that could be construed as a potential conflict of interest.

Publisher's note

All claims expressed in this article are solely those of the authors and do not necessarily represent those of their affiliated organizations, or those of the publisher, the editors and the reviewers. Any product that may be evaluated in this article, or claim that may be made by its manufacturer, is not guaranteed or endorsed by the publisher.

Supplementary material

The Supplementary Material for this article can be found online at: https://www.frontiersin.org/articles/10.3389/fchem.2022.1041328/full#supplementary-material

References

Adisakwattana, S., Chantarasinlapin, P., Thammarat, H., and Yibchok-Anun, S. (2009). A series of cinnamic acid derivatives and their inhibitory activity on intestinal alpha-glucosidase. *J. Enzyme Inhib. Med. Chem.* 24, 1194–1200. doi:10.1080/14756360902779326

Adisakwattana, S., Pongsuwan, J., Wungcharoen, C., and Yibchok-anun, S. (2013). *In vitro* effects of cinnamic acid derivatives on protein tyrosine phosphatase 1B. *J. Enzyme Inhib. Med. Chem.* 28, 1067–1072. doi:10.3109/14756366.2012.715286

Adisakwattana, S., Sookkongwaree, K., Roengsumran, S., Petsom, A., Ngamrojnavanich, N., Chavasiri, W., et al. (2004). Structure-activity relationships of trans-cinnamic acid derivatives on alpha-glucosidase inhibition. *Bioorg. Med. Chem. Lett.* 14, 2893–2896. doi:10.1016/j.bmcl.2004.03.037

Ali, F., Khan, K. M., Salar, U., Taha, M., Ismail, N. H., Wadood, A., et al. (2017). Hydrazinyl arylthiazole based pyridine scaffolds: Synthesis, structural characterization, *in vitro* α-glucosidase inhibitory activity, and *in silico* studies. *Eur. J. Med. Chem.* 138, 255–272. doi:10.1016/j.ejmech.2017.06.041

Amador, S., Nieto-Camacho, A., Ramírez-Apan, M. T., Martínez, M., and Maldonado, E. (2020). Cytotoxic, anti-inflammatory, and alpha-glucosidase inhibitory effects of flavonoids from Lippia graveolens (Mexican oregano). *Med. Chem. Res.* 29, 1497–1506. doi:10.1007/s00044-020-02569-6

Dong, Y., Yu, N., Li, X., Zhang, B., Xing, Y., Zhuang, C., et al. (2020). Dietary 5, 6, 7-Trihydroxy-flavonoid aglycones and 1-deoxynojirimycin synergistically inhibit the recombinant maltase-glucoamylase subunit of alpha-glucosidase and lower postprandial blood glucose. *J. Agric. Food Chem.* 68, 8774–8787. doi:10.1021/acs.jafc.0c01668

Forouhi, N. G., and Wareham, N. J. (2014). Epidemiology of diabetes. *Med. (Abingdon)* 42 (12), 698–702. doi:10.1016/j.mpmed.2014.09.007

Hedrington, M. S., and Davis, S. N. (2019). Considerations when using alpha-glucosidase inhibitors in the treatment of type 2 diabetes. *Expert Opin. Pharmacother.* 20, 2229–2235. doi:10.1080/14656566.2019.1672660

Hu, C., Wang, W., Na, Y., Kang, Y., Lin, J., Wu, P., et al. (2021). Novel cinnamic acid magnolol derivatives as potent α-glucosidase and α-amylase inhibitors: Synthesis, *in vitro* and *in silico* studies, Bioorg. *Chem* 116, 105291.

Imran, S., Taha, M., Ismail, N. H., Kashif, S. M., Rahim, F., Jamil, W., et al. (2015). Synthesis of novel flavone hydrazones: *In-vitro* evaluation of α-glucosidase inhibition, QSAR analysis and docking studies. *Eur. J. Med. Chem.* 105, 156–170. doi:10.1016/j.ejmech.2015.10.017

Jia, Y., Ma, Y., Cheng, G., Zhang, Y., and Cai, S. (2019). Comparative study of dietary flavonoids with different structures as alpha-glucosidase inhibitors and insulin sensitizers. *J. Agric. Food Chem.* 6, 10521–10533. doi:10.1021/acs.jafc.9b04943

Kokil, G. R., Veedu, R. N., Ramm, G. A., Prins, J. B., and Parekh, H. S. (2015). Type 2 diabetes mellitus: Limitations of conventional therapies and intervention with nucleic acid-based therapeutics. *Chem. Rev.* 115 (11), 4719–4743. doi:10.1021/cr5002832

Kousaxidis, A., Petrou, A., Lavrentaki, V., Fesatidou, M., Nicolaou, I., and Geronikaki, A. (2020). Aldose reductase and protein tyrosine phosphatase 1B inhibitors as a promising therapeutic approach for diabetes mellitus. *Eur. J. Med. Chem.* 207, 112742. doi:10.1016/j.ejmech.2020.112742

Li, Y., Yuan, X., Rong, X., Gao, Y., Qiu, Z., Zhang, Z., et al. (2016). Design, synthesis and biological evaluation of a hybrid compound of berberine and magnolol for improvement of glucose and lipid metabolism. *RSC Adv.* 6, 81924–81931. doi:10.1039/c6ra15100k

Liu, J., Kong, Y., Miao, J., Mei, X., Wu, S., Yan, Y., et al. (2020). Spectroscopy and molecular docking analysis reveal structural specificity of flavonoids in the inhibition of alpha-glucosidase activity. *Int. J. Biol. Macromol.* 152, 981–989. doi:10.1016/j.ijbiomac.2019.10.184

Lu, H., Qi, Y., Zhao, Y., and Jin, N. (2020). Effects of hydroxyl group on the interaction of carboxylated flavonoid derivatives with S. Cerevisiae alpha-glucosidase,. *Curr. Comput. Aided. Drug Des.* 16, 31–44. doi:10.2174/1573409914666181022142553

Mo, Q. G., Zhou, G., Zhu, W. D., Ge, L. L., and Wang, Y. W. (2022). Coumaroyl and feruloyl flavonoid glycosides from the male flowers of Ginkgo biloba L. and their inhibitory activity against alpha-glucosidase. *Nat. Prod. Res.* 36, 4365–4372. doi:10.1080/14786419.2021.1993216

Oueslati, M. H., Bouajila, J., Gurtat, A., Al-Gamdi, F., and Hichri, F. (2020). Cytotoxic, alpha-glucosidase, and antioxidant activities of flavonoid glycosides isolated from flowers of Lotus lanuginosus vent. (Fabaceae). *Pharmacogn. Mag.* 16, 22.

Proença, C., Freitas, M., Ribeiro, D., Oliveira, E. F., Sousa, J. L., Tomé, S. M., et al. (2017). α-Glucosidase inhibition by flavonoids: An *in vitro* and *in silico* structure-activity relationship study. *J. Enzyme Inhib. Med. Chem.* 32, 1216–1228. doi:10.1080/14756366.2017.1368503

Proenca, C., Ribeiro, D., Freitas, M., and Fernandes, E. (2021). Flavonoids as potential agents in the management of type 2 diabetes through the modulation of alpha-amylase and alpha-glucosidase activity: A review. *Crit. Rev. Food Sci. Nutr.* 62, 3137–3207. doi:10.1080/10408398.2020.1862755

Qin, Y., Chen, J., Li, C., Zhu, L., Zhu, X., Zhang, X., et al. (2020). Flavonoid glycosides from the fruits of Embelia ribes and their anti-oxidant and alpha-giucosidase inhibitory activities. *J. Asian Nat. Prod. Res.* 23, 724–730. doi:10.1080/10286020.2020.1776266

Rasouli, H., Hosseini-Ghazvini, S. M., Adibi, H., and Khodarahmi, R. (2017). Differential α-amylase/α-glucosidase inhibitory activities of plant-derived phenolic compounds: A virtual screening perspective for the treatment of obesity and diabetes. *Food Funct.* 8, 1942–1954. doi:10.1039/c7fo00220c

Santos, C. M. M., Freitas, M., and Fernandes, E. (2018). A comprehensive review on xanthone derivatives as alpha-glucosidase inhibitors. *Eur. J. Med. Chem.* 157, 1460–1479. doi:10.1016/j.ejmech.2018.07.073

Sheng, Z., Ge, S., Xu, X., Zhang, Y., Wu, P., Zhang, K., et al. (2018). Design, synthesis and evaluation of cinnamic acid ester derivatives as mushroom tyrosinase inhibitors. *Med. Chem. Commun.* 9, 853–861. doi:10.1039/c8md00099a

Sohretoglu, D., Sari, S., Barut, B., and Ozel, A. (2018). Discovery of potent alpha-glucosidase inhibitor flavonols: Insights into mechanism of action through inhibition kinetics and docking simulations. *Bioorg. Chem.* 79, 257–264. doi:10.1016/j.bioorg.2018.05.010

Şöhretoğlu, D., and Sari, S. (2020). Flavonoids as alpha-glucosidase inhibitors: Mechanistic approaches merged with enzyme kinetics and molecular modelling. *Phytochem. Rev.* 19, 1081–1092. doi:10.1007/s11101-019-09610-6

Song, Y. H., Kim, D. W., Curtis-Long, M. J., Park, C., Son, M., Kim, J. Y., et al. (2016). Cinnamic acid amides from Tribulus terrestris displaying uncompetitive alpha-glucosidase inhibition. *Eur. J. Med. Chem.* 114, 201–208. doi:10.1016/j.ejmech.2016.02.044

Tang, H., Huang, L., Sun, C., and Zhao, D. (2020). Exploring the structure-activity relationship and interaction mechanism of flavonoids and alpha-glucosidase based on experimental analysis and molecular docking studies. *Food Funct.* 4, 3332–3350. doi:10.1039/c9fo02806d

Tsoutsouki, J., Wunna, W., Chowdhury, A., and Chowdhury, T. A. (2020). Advances in the management of diabetes: Therapies for type 2 diabetes. *Postgrad. Med. J.* 96, 610–618. doi:10.1136/postgradmedj-2019-137404

Wang, H., Zhao, J., and Zhang, Y. (2020). The flavonoid-rich ethanolic extract from the green cocoon shell of silkworm has excellent antioxidation, glucosidase inhibition, and cell protective effects *in vitro*. *Food Nutr. Res.* 64, 1637. doi:10.29219/fnr.v64.1637

Xu, X. T., Deng, X. Y., Chen, J., Liang, Q. M., Zhang, K., Li, D. L., et al. (2019). Synthesis and biological evaluation of coumarin derivatives as alpha-glucosidase inhibitors. *Eur. J. Med. Chem.* 189, 112013. doi:10.1016/j.ejmech.2019.112013

Zhang, X., Zheng, Y. Y., Hu, C. M., Wu, X. Z., Lin, J., Xiong, Z., et al. (2022). Synthesis and biological evaluation of coumarin derivatives containing oxime ester as α-glucosidase inhibitors. *Arab. J. Chem.* 15, 104072. doi:10.1016/j.arabjc.2022.104072

Zhu, J., Chen, C., Zhang, B., and Huang, Q. (2020). The inhibitory effects of flavonoids on alpha-amylase and alpha-glucosidase. *Crit. Rev. Food Sci. Nutr.* 60, 695–708. doi:10.1080/10408398.2018.1548428

frontiers | Frontiers in Chemistry

TYPE Original Research
PUBLISHED 08 December 2022
DOI 10.3389/fchem.2022.1104249

OPEN ACCESS

EDITED BY
Xi Zheng,
Rutgers, The State University of New Jersey, United States

REVIEWED BY
Jie Gao,
Nankai University, China
Chong Qin,
Ocean University of China, China

*CORRESPONDENCE
Jinfei Yang,
jfyang@uor.edu.cn
Yuanyuan Zhang,
zyy@scu.edu.cn

SPECIALTY SECTION
This article was submitted to Medicinal and Pharmaceutical Chemistry, a section of the journal Frontiers in Chemistry

RECEIVED 21 November 2022
ACCEPTED 28 November 2022
PUBLISHED 08 December 2022

CITATION
Yang J, Yao W, Yang H, Shen Y and Zhang Y (2022), Design and synthesis of ERα agonists: Effectively reduce lipid accumulation.
Front. Chem. 10:1104249.
doi: 10.3389/fchem.2022.1104249

Design and synthesis of ERα agonists: Effectively reduce lipid accumulation

Jinfei Yang[1]*, Weiwei Yao[1], Huihui Yang[1], Yajing Shen[1] and Yuanyuan Zhang[2]*

[1]School of Health and Life Sciences, University of Health and Rehabilitation Sciences, Qingdao, China, [2]West China School of Pharmacy, Sichuan University, Chengdu, China

In recent years, the incidence of non-alcoholic fatty liver disease (NAFLD) has been increasing worldwide. Hepatic lipid deposition is a major feature of NAFLD, and insulin resistance is one of the most important causes of lipid deposition. Insulin resistance results in the disruption of lipid metabolism homeostasis characterized by increased lipogenesis and decreased lipolysis. Estrogen receptor α (ERα) has been widely reported to be closely related to lipid metabolism. Activating ERa may be a promising strategy to improve lipid metabolism. Here, we used computer-aided drug design technology to discover a highly active compound, YRL-03, which can effectively reduce lipid accumulation. Cellular experimental results showed that YRL-03 could effectively reduce lipid accumulation by targeting ERα, thereby achieving alleviation of insulin resistance. We believe this study provides meaningful guidance for future molecular development of drugs to prevent and treat NAFLD.

KEYWORDS

ERα, agonists, lipid accumulation, NAFLD, liver disease

1 Introduction

Non-alcoholic fatty liver disease (NAFLD) has become the most common chronic liver disease in the world (Li et al., 2018), affecting more than 30% of the general population in western countries, and its incidence continues to increase in other parts of the world (Asrih and Jornayvaz, 2015). NAFLD is a multifactorial disease triggered by interactions between environment, genetic background, and metabolic stress (Lonardo et al., 2017). Unlike alcoholic fatty liver disease, patients have no history of excessive alcohol consumption (Ahmed, 2015). The pathogenic mechanisms involved in NAFLD are complex and have not yet been fully elucidated (Xi and Li, 2020; Hrncir et al., 2021). Insulin resistance is one of the key factors in the development of steatosis (Alam et al., 2016), which leads to an imbalance between hepatic lipogenesis and metabolism, mainly manifested by increased *de novo* lipogenesis and decreased adipose tissue lipolysis (Saponaro et al., 2015). If NAFLD is not controlled, it will further develop into liver cirrhosis (Zhou et al., 2020), and may eventually develop into hepatocellular carcinoma, which seriously

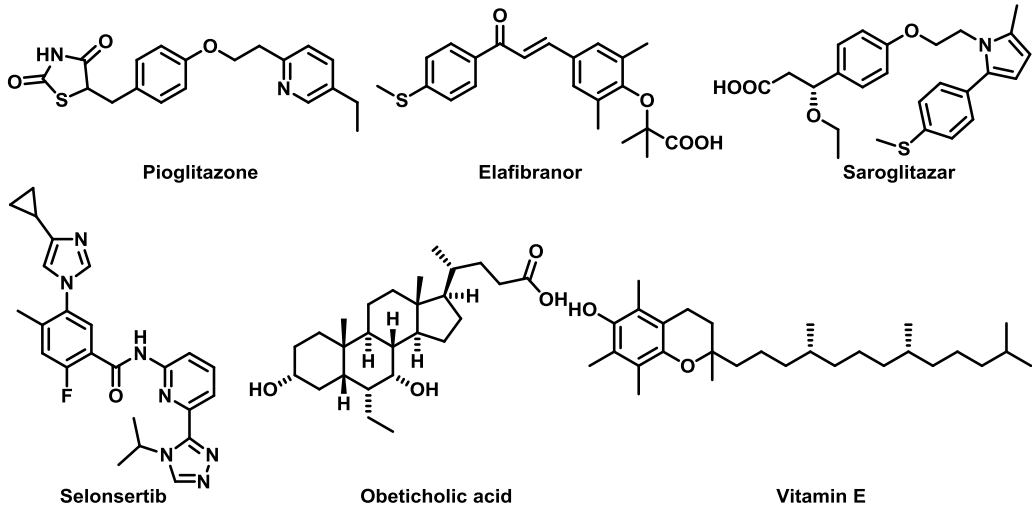

FIGURE 1
Drug molecules that have entered clinical phase III.

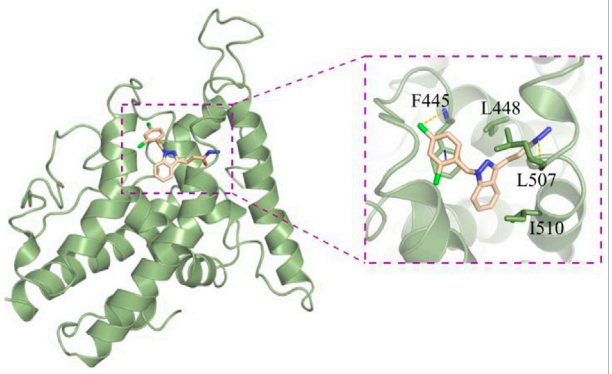

FIGURE 2
Computer-assisted molecular docking experiments (PDB: 5GS4).

threatens human health (Chrysavgis et al., 2022). However, there is no drug specifically for the treatment of NAFLD on the market so far (Ma et al., 2019; Wang et al., 2020). Some drugs that regulate metabolism, oxidative stress and anti-fibrosis are still in the clinical stage (Kumar et al., 2021), such as Pioglitazone (Della Pepa et al., 2021), Elafibranor (Boeckmans et al., 2022), Saroglitazar (Gawrieh et al., 2021), Obeticholic acid (Abenavoli et al., 2018; Malnick et al., 2020), Selonsertib (Reimer et al., 2020) and Vitamin E (Perumpail et al., 2018) (Figure 1). Therefore, there is an urgent need to develop novel drugs with high efficacy and minimal side effects for the treatment of NAFLD. Lipid metabolism plays a key role in the progression of NAFLD (Lai et al., 2016), and insulin resistance is one of the most important causes of lipid deposition. Insulin resistance results in the disruption of lipid metabolism homeostasis characterized by increased lipogenesis and decreased lipolysis (Yao et al., 2016). Estrogen receptor α (ERα) has been widely reported to be closely related to lipid metabolism, especially has an important impact on NAFLD (Meda et al., 2022). Studies have shown that the activation of ERα can effectively reduce the accumulation of liver lipids (Chen et al., 2020). Based on this, we plan to use computer-assisted drug design technology to develop an agonist of ERα, which can effectively reduce lipid accumulation by targeting ERα, thereby achieving the purpose of alleviating NAFLD.

2 Results and discussion

For the target of ERα, we used computer-aided drug design technology to discover a compound 3-(1-(2,4-dichlorobenzyl)-1H-indazol-3-yl)propanehydrazide (YRL-03) with strong interaction with ERα (Figure 2). Molecular docking experiments show that the chlorine atom on the benzene ring of YRL-03 has a strong electrophilic interaction with the amino group on the amino acid site F445 of ERα, and the nitrogen atom on the hydrazide of YRL-03 has a strong electrophilic interaction with the carbonyl group on the amino acid site L507. In addition, the benzene ring of YRL-03 has an arene-arene interaction with the benzene ring of F445.

Subsequently, starting from cheap and easily available indazole, we used the developed chemical synthesis route to rapidly synthesize the target molecule YRL-03 by a four-step reaction, and the total

10.3389/fchem.2022.1104249

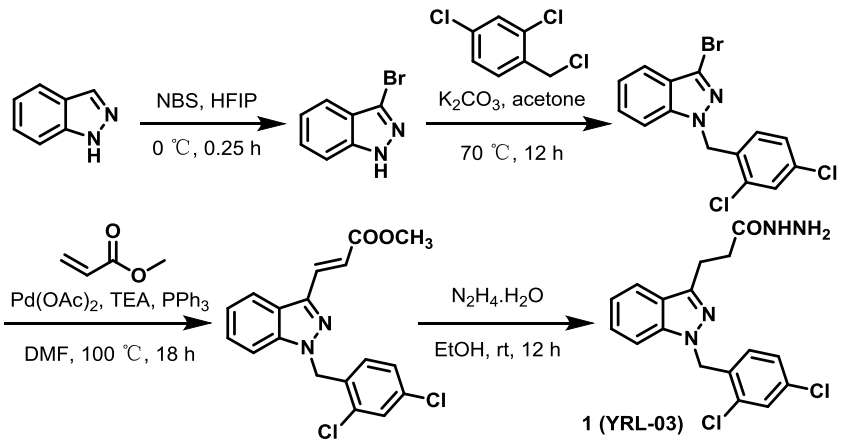

SCHEME 1
Chemical synthesis of YRL-03[a].

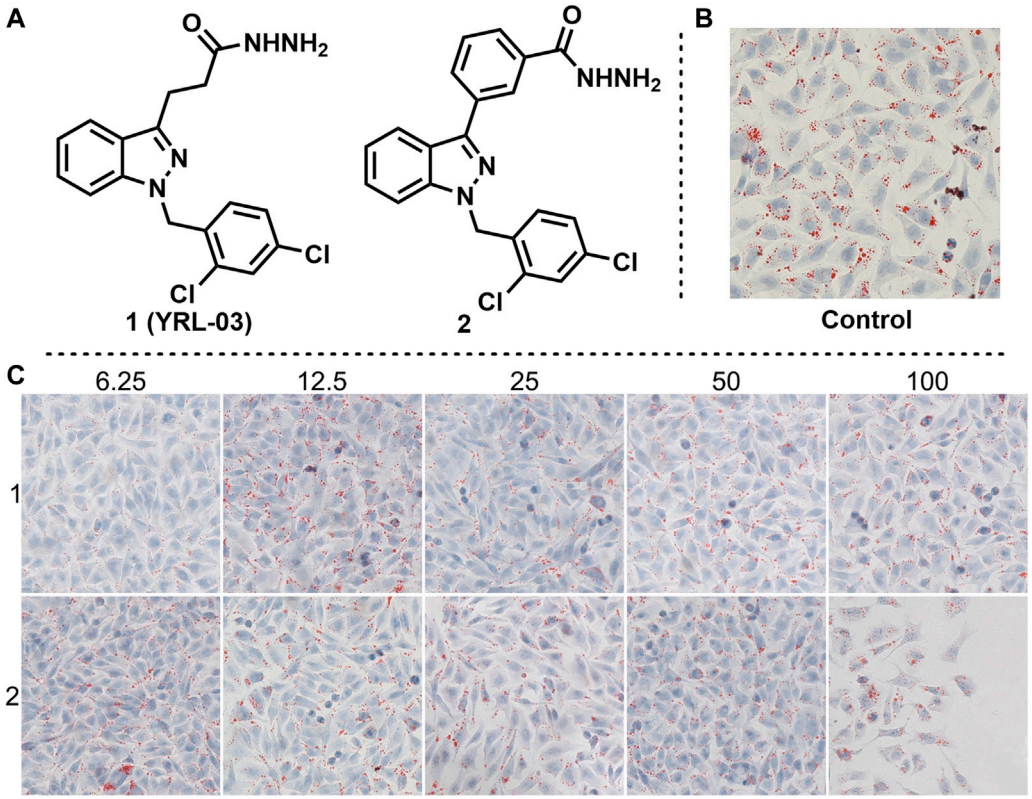

FIGURE 3
Effects of YRL-03 and compound 2 on lipid accumulation. **(A)** Chemical structure of YRL-03 and compound 2. **(B)** Control experiment. **(C)** Effects of different concentration gradients of YRL-03 and compound 2 on lipid accumulation.

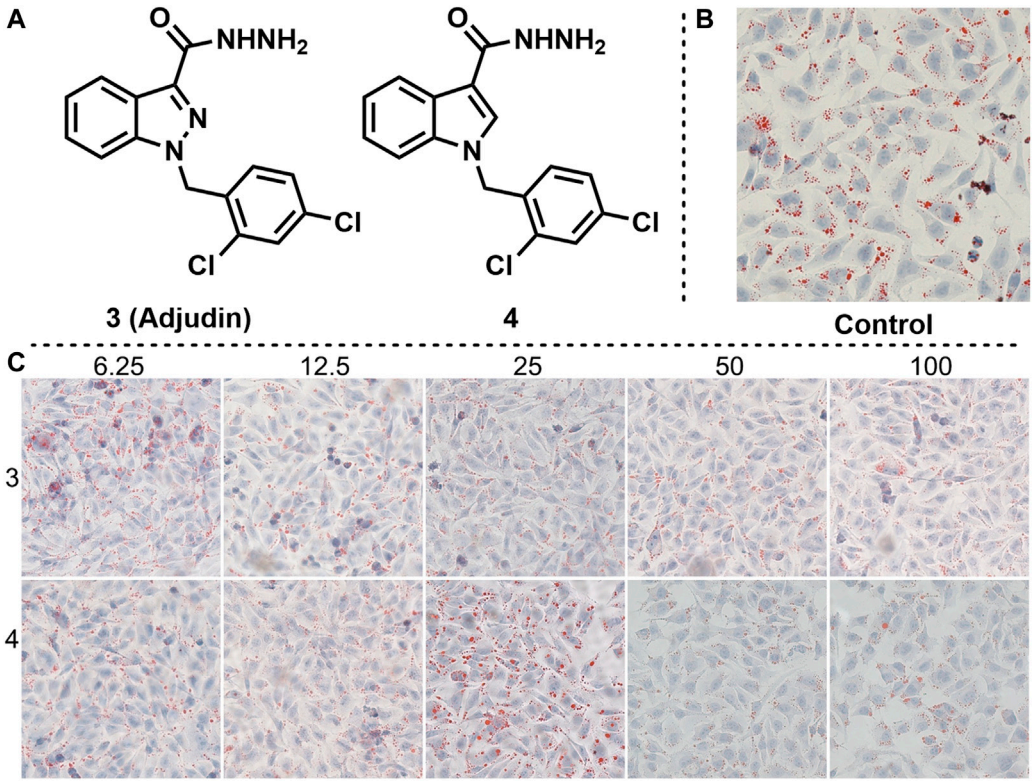

FIGURE 4
Effects of compounds 3 and 4 on lipid accumulation. **(A)** Chemical structure of compounds 3 and 4. **(B)** Control experiment. **(C)** Effects of different concentration gradients of compounds 3 and 4 on lipid accumulation.

yield of four-step reaction is 43.6% (Scheme 1). To our delight, the whole reaction process is mild, no nitrogen protection is required, and no hazardous reagents are used.

[a]Reaction conditions: (a) NBS, Hexafluoroisopropanol (HFIP), 0°C, 0.25 h; (b) 2,4-dichloro-1-(chloromethyl)benzene, K_2CO_3, acetone, 70°C, 12 h, 78% (two steps); (c) methyl acrylate, $Pd(OAc)_2$, TEA, PPh_3, DMF, 100°C, 18 h, 81%; (d)N_2H_4. H_2O, EtOH, rt, 12 h, 96%.

With the obtaining target molecule YRL-03 in hand, we began to try to verify whether this compound has the effect of reducing lipid accumulation. The cellular model is a model of lipid deposition in hepatocytes induced by oleic acid. First, hepatocytes were treated with 125 μm sodium oleate to induce lipid deposition, resulting in a uniform distribution of lipid droplets in hepatocytes without significant changes in cell morphology. Second, YRL-03 was formulated into five gradient concentrations of 6.25, 12.5, 25, 50, and 100 μm, respectively, to verify the effect of different gradient concentrations on lipid deposition. Cell experiments showed that lipid droplets were significantly reduced at 6.25 μm, but little change at 12.5, 25, 50, and 100 μm. It reveals that YRL-03 had a good effect of reducing lipid accumulation under the administration of 6.25 μm gradient concentration.

In order to find more excellent active compunds, we imagined that if the 3-position alkyl hydrazide of the indazole was changed to an aryl hydrazide, would it produce better results? Based on this hypothesis, we synthesized compound 2 by a similar synthetic method, and tested its effect on lipid accumulation. Regrettably, the test results showed that compound 2 did not show a good effect on reducing lipid accumulation. When the gradient concentration was 6.25 μm, lipid deposition did not decrease but increased. When the gradient concentration increased to 100 μm, the cell morphology changed significantly (Figure 3).

Adjudin is a potential non-hormonal male contraceptive under development (Mruk et al., 2006). We found that adjudin and its derivatives also have interaction with ER in previous studies, but the cell experiments showed that they had little inhibitory effect on estrogen receptors (Yao et al., 2022). Therefore, we envisioned whether they would have the opposite effect, being an estrogen receptor agonist. Based on this idea, we synthesized Adjudin and its derivative 4, and verified their effects on lipid deposition at different gradient concentrations (Figure 4, the same control used for compounds 1, 2, 3 and 4). The results of cell experiments showed that Adjudin did not reduce lipid deposition at low

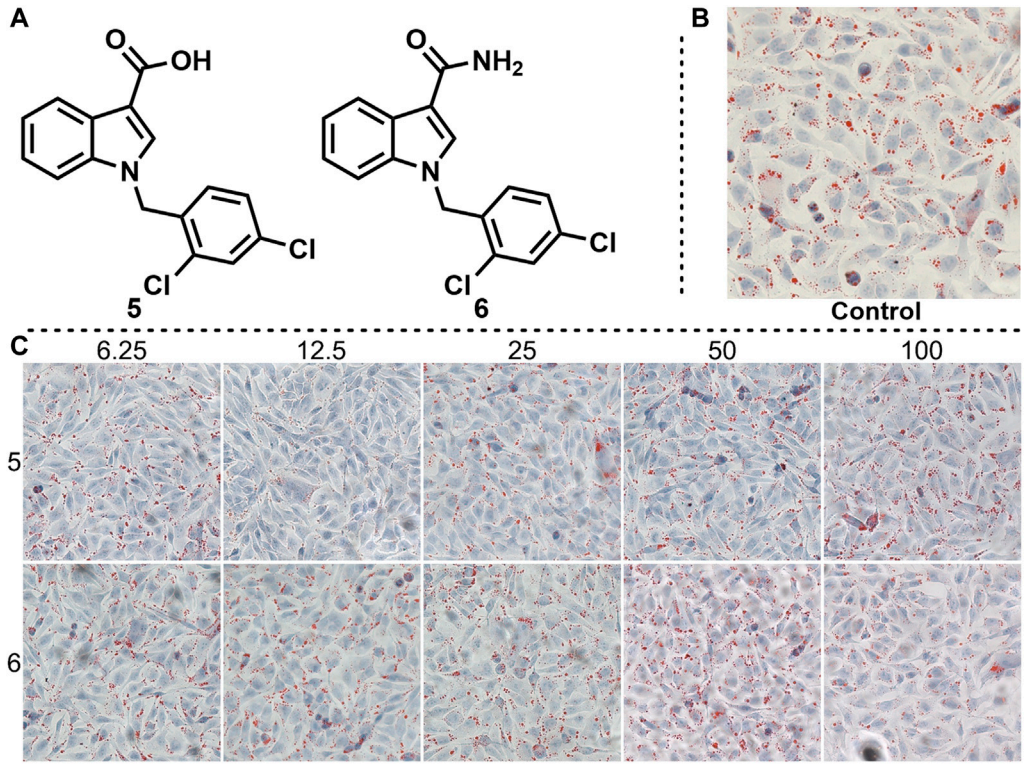

FIGURE 5
Effects of compounds 5 and 6 on lipid accumulation. **(A)** Chemical structure of compounds 5 and 6. **(B)** Control experiment. **(C)** Effects of different concentration gradients of compounds 5 and 6 on lipid accumulation.

concentrations. When the concentration was increased to 50 and 100 μm, it had a weak effect on reducing lipid deposition. The low concentration of compound 4 did not reduce lipid deposition, and when the concentration was increased to 50 and 100 μm, lipid droplets were reduced, but cell morphology was changed.

Given that compound 4 has a certain lipid-lowering effect at 50 and 100 μm, we imagined whether changing the hydrazide substituent on the indole backbone of compound 4 to carboxyl or amide could enhance its lipid-lowering effect. Based on this idea, we synthesized compounds 5 and 6, and tested their effects on fat accumulation (Figure 5). The cell experiments results showed that the two compounds had no effect on reducing fat accumulation. Even with increasing their concentration, lipid droplets are still present in abundance.

The position of the substituent has a strong correlation with the biological activity of the compound. Therefore, the biological activity may also change greatly when the position of the substituent changes. To improve the biological activity of ER-targeted agonists, we changed the hydrazide position on the adjudin indazole backbone from 3 to 5 or 6 to obtain compounds 7 and 8, and tested their effects on fat accumulation (Figure 6, the same control used for compounds 5, 6, 7 and 8), respectively. Unfortunately, it didn't end up as we expected. Cell experiments showed that compounds 7 and 8 did not reduce fat accumulation. When the gradient concentration of compound 8 was increased to 50 and 100 μM, the cell morphology changed significantly.

3 Conclusion

In conclusion, we developed an ERα-targeting agonist YRL-03 by computer-aided drug design technology, which was effective in reducing lipid accumulation at a concentration of 6.25 μm. Cell experiments showed that YRL-03 could effectively inhibit lipid accumulation. The specific interaction mode of YRL-03 and ERα given by molecular docking experiments is that the chlorine atom on the benzene ring of YRL-03 has a strong electrophilic interaction with the amino group on the amino acid site F445 of ERα, and the benzene ring of YRL-03 have aromatic-aromatic interactions with the benzene ring of F445, the nitrogen atom on the YRL-03 hydrazide has a strong electrophilic interaction with the carbonyl group on the amino acid site L507. Notably, the target compound can be obtained

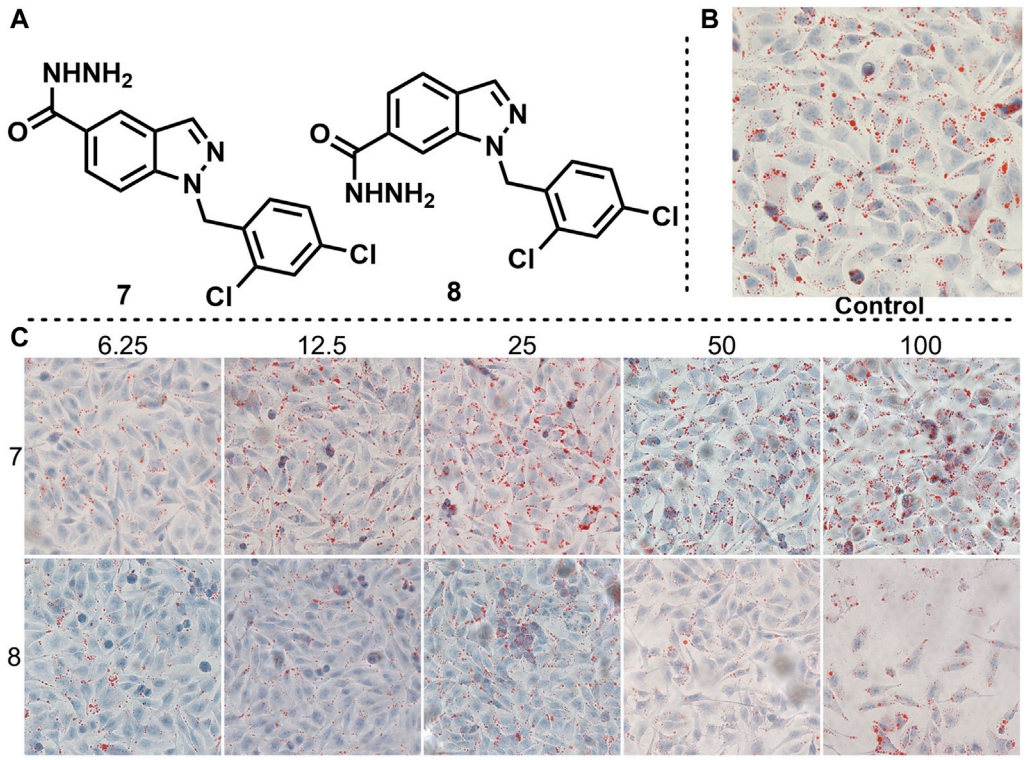

FIGURE 6
Effects of compounds 7 and 8 on lipid accumulation. **(A)** Chemical structure of compounds 7 and 8. **(B)** Control experiment. **(C)** Effects of different concentration gradients of compounds 7 and 8 on lipid accumulation.

from cheap and easily available indazole through four-step reactions, and the whole reaction process is simple to operate and does not need flammable and explosive dangerous reagents. Further molecular structure optimization and toxicology experiments are ongoing in our group. We believe that the results of this study will provide meaningful guidance for the future development of drugs that can effectively treat NAFLD.

4 Experimental section

General Information Unless stated otherwise, all reactions were conducted in pressure tubes under N_2. All solvents were received from commercial sources without further purification. Commercially available reagents were used as received. Non-commercially available substrates were synthesized following reported protocols. Thin-layer chromatography (TLC) was visualized using a combination of UV and potassium permanganate staining techniques. Silica gel (particle size 40–63 μm) was used for flash column chromatography. NMR spectra were recorded on Bruker AV 400 spectrometer at 400 MHz (^{1}H NMR), 100 MHz (^{13}C NMR). Proton and carbon chemical shifts are reported relative to the solvent used as an internal reference. The results of molecular docking experiments were completed using Schrödinger and Molecular Operating Environment (MOE).

Typical Procedure for Synthesis of Compund 1. Indazole (5 mmol) was added to a stirred mixture of NBS (5.5 mmol, 1.1 equiv.) in HFIP (15 ml). After 0.25 h at 0°C, the organic layer was washed successively with aq $NaHCO_3$, and brine, dried over anhydrous sodium sulphate, filtered, and evaporated *in vacuo*. Then the crude material was dissolved in acetone, and to the mixture 2,4-dichloro-1-(chloromethyl)benzene (5.5 mmol, 1.1 equiv.), K_2CO_3 (22 mmol, 4.4 equiv.) were added. The reaction mixture was refluxed overnight at 70°C. Then it was cooled to room temperature, filtered, and the residue was washed with acetone. The combined filtrate was concentrated under vacuum. The solid was dissolved in DCM and filtered to remove any undissolved solid. The residue was re-crystallized (DCM/hexane) to afford the pure product 3-bromo-1-(2,4-dichlorobenzyl)-1H-indazole as a white solid in 78% yield (two steps).

To a glass pressure tube were added 3-bromo-1-(2,4-dichlorobenzyl)-1H-indazole (0.5 mmol, 1.0 equiv.), Pd $(OAc)_2$ (0.05 mmol, 10 mol%), PPh_3 (0.1 mmol, 20 mol%) and anhydrous DMF (2 ml) under N_2. and then TEA (1.5 mmol, 3.0 equiv.) and methyl acrylate (5 mmol, 10.0 equiv.) were added. The resulting solution was stirred at 100°C for 18 h. Cool the reaction mixture and dilute with EA. Wash with waterand dry over Na_2SO_4. Evaporate and purify the residue by column chromatography to obtain the product methyl (E)-3-(1-(2,4-dichlorobenzyl)-1H-indazol-3-yl)acrylate in 81% yield.

To a solution of methyl (E)-3-(1-(2,4-dichlorobenzyl)-1H-indazol-3-yl)acrylate (1 mmol, 1.0 equiv.) in ethanol at room temperature was added hydrazine hydrate (50 mmol, 50.0 equiv.). The reaction mixture was stirred at room temperature over night. The volatiles were removed under reduced pressure and the crude mass was diluted with dichloromethane, washed with water, brine, dried over anhydrous sodium sulphate and the solvent was removed under reduced pressure to obtain the crude product. The residue was purified by column chromatography to afford the pure product 1 (YRL-03) as a white solid in 96% yield.

Cell Culture. Human hepatic L02 cells were obtained from the American Type Culture Collection, and cultured with Roswell Park Memorial Institute (RPMI) 1,640 medium (Hyclone, UT, United States) supplemented with 10% fetal bovine serum (Biological Industries, CT, United States) and 1% penicillin/streptomycin (Hyclone, UT, United States).

Oil red O staining. L02 cells were seeded in 24-well plates and induced with sodium oleate at 100 μm for 24 h when reaching 50% confluence. Then cells were treated with compounds at 6.25, 12.5, 25, 50, 100 μm for 24 h. Then cells were washed with phosphate buffer saline (PBS) and fixed with 4% paraformaldehyde (PFA, Sangon, Shanghai, China) for 20 min at room temperature, stained with freshly diluted oil red O staining solution (3 mg/ml) for 45 min, rinsed with PBS, and sealed with glycerin (Chu et al., 2019). Lipid droplets in cells were captured by an optical microscope (Zeiss).

3-(1-(2,4-dichlorobenzyl)-1H-indazol-3-yl)propanehydrazide (1). White solid (61% yield, four steps). ^{1}H NMR (400 MHz, $CDCl_3$) δ 7.72 (d, J = 8.0 Hz, 1 H), 7.42 (d, J = 2.0 Hz, 1 H), 7.40-7.35 (m, 1 H), 7.30-7.28 (m, 1 H), 7.18-7.14 (m, 2 H), 7.09 (dd, J = 8.0, 1.6 Hz, 1 H), 6.60 (d, J = 8.4 Hz, 1 H), 5.59 (s, 2 H), 3.83 (s, 2 H), 3.34 (t, J = 7.2 Hz, 2 H), 2.74 (t, J = 7.2 Hz, 2 H).^{13}C NMR (100 MHz, $CDCl_3$) δ 173.3, 144.8, 140.8, 134.0, 133.4, 133.0, 129.3, 129.3, 127.5, 127.1, 122.9, 120.6, 120.4, 109.1, 49.3, 33.0, 22.6.

3-(1-(2,4-dichlorobenzyl)-1H-indazol-3-yl)benzohydrazide (2).[23] White solid (77% yield, two steps). ^{1}H NMR (400 MHz, $CDCl_3$) δ 8.35 (t, J = 1.6 Hz, 1 H), 8.15 (dt, J = 7.6, 1.2 Hz, 1 H), 8.06 (d, J = 8.0 Hz, 1 H), 7.78 (dt, J = 8.0, 1.2 Hz, 1 H), 7.59 (t, J = 7.6 Hz, 1 H), 7.49 (s, 1 H), 7.44 (d, J = 2.4 Hz, 1 H), 7.42-7.37 (m, 2 H), 7.29-7.27 (m, 1 H), 7.09 (dd, J = 8.4, 2.4 Hz, 1 H), 6.73-6.71 (m, 1 H), 5.72 (s, 2 H), 4.14 (s, 2 H).^{13}C NMR (100 MHz, DMSO)δ 165.9, 142.9, 141.4, 134.2, 133.9, 133.3, 133.21, 133.16, 130.7, 129.6, 129.2, 129.1, 127.8, 127.0, 126.6, 125.5, 121.9, 121.2, 120.9, 110.3, 49.3.

Data availability statement

The original contributions presented in the study are included in the article/Supplementary Material, further inquiries can be directed to the corresponding authors.

Author contributions

JY is responsible for molecular docking experiments and writing this manuscript. WY is responsible for the synthesis of small molecular compounds. HY is responsible for collecting literature. YS is responsible for collecting literature. YZ is responsible for completing cell experiments and organizing cell experiment data.

Funding

We thank the National Key Research and Development Program of China (2022YFC2804400) and the Taishan Scholar Project of Shandong Province (tsqn202103108) for financial support.

Conflict of interest

The authors declare that the research was conducted in the absence of any commercial or financial relationships that could be construed as a potential conflict of interest.

Publisher's note

Supplementary material

The Supplementary Material for this article can be found online at: https://www.frontiersin.org/articles/10.3389/fchem.2022.1104249/full#supplementary-material

References

Abenavoli, L., Falalyeyeva, T., Boccuto, L., Tsyryuk, O., and Kobyliak, N. (2018). Obeticholic acid: A new era in the treatment of nonalcoholic fatty liver disease. *Pharmaceuticals* 11, 104. doi:10.3390/ph11040104

Ahmed, M. (2015). Non-alcoholic fatty liver disease in 2015. *World J. hepatology* 7, 1450. doi:10.4254/wjh.v7.i11.1450

Alam, S., Mustafa, G., Alam, M., and Ahmad, N. (2016). Insulin resistance in development and progression of nonalcoholic fatty liver disease. *World J. Gastrointest. Pathophysiol.* 7, 211. doi:10.4291/wjgp.v7.i2.211

Asrih, M., and Jornayvaz, F. R. (2015). Metabolic syndrome and nonalcoholic fatty liver disease: Is insulin resistance the link? *Mol. Cell. Endocrinol.* 418, 55–65. doi:10.1016/j.mce.2015.02.018

Boeckmans, J., Gatzios, A., Heymans, A., Rombaut, M., Rogiers, V., Kock, J. D. J., et al. (2022). Transcriptomics reveals discordant lipid metabolism effects between *in vitro* models exposed to elafibranor and liver samples of NAFLD patients after bariatric surgery. *Cells* 11, 893. doi:10.3390/cells11050893

Chen, Q., Chao, Y., Zhang, W., Zhang, Y., Bi, Y., Fu, Y., et al. (2020). Activation of estrogen receptor α (ERα) is required for Alisol B23-acetate to prevent post-menopausal atherosclerosis and reduced lipid accumulation. *Life Sci.* 258, 118030. doi:10.1016/j.lfs.2020.118030

Chrysavgis, L., Giannakodimos, I., Diamantopoulou, P., and Cholongitas, E. (2022). Non-alcoholic fatty liver disease and hepatocellular carcinoma: Clinical challenges of an intriguing link. *World J. Gastroenterology* 28, 310–331. doi:10.3748/wjg.v28.i3.310

Chu, Q., Zhang, S., Chen, M., Han, W., Jia, R., Chen, W., et al. (2019). Cherry anthocyanins regulate NAFLD by promoting autophagy pathway. *Oxid. Med. Cell. Longev.* 2019. doi:10.1155/2019/4825949

Della Pepa, G., Russo, M., Vitale, M., Carli, F., Vetrani, C., Masulli, M., et al. (2021). Pioglitazone even at low dosage improves NAFLD in type 2 diabetes: Clinical and pathophysiological insights from a subgroup of the TOSCA.IT randomised trial. *Diabetes Res. Clin. Pract.* 178, 108984. doi:10.1016/j.diabres.2021.108984

Gawrieh, S., Noureddin, M., Loo, N., Mohseni, R., Awasty, V., Cusi, K., et al. (2021). Saroglitazar, a PPAR-α/γ agonist, for treatment of NAFLD: A randomized controlled double-blind phase 2 trial. *Hepatology* 74, 1809–1824. doi:10.1002/hep.31843

Hrncir, T., Hrncirova, L., Kverka, M., Hromadka, R., Machova, V., Trckova, E., et al. (2021). Gut microbiota and NAFLD: Pathogenetic mechanisms, microbiota signatures, and therapeutic interventions. *Microorganisms* 9, 957. doi:10.3390/microorganisms9050957

Kumar, V., Xin, X., Ma, J., Tan, C., Osna, N., and Mahato, R. I. (2021). Therapeutic targets, novel drugs, and delivery systems for diabetes associated NAFLD and liver fibrosis. *Adv. Drug Deliv. Rev.* 176, 113888. doi:10.1016/j.addr.2021.113888

Lai, Y. S., Lee, W. C., Lin, Y. E., Ho, C. T., Lu, K. H., Lin, S. H., et al. (2016). Ginger essential oil ameliorates hepatic injury and lipid accumulation in high fat diet-induced nonalcoholic fatty liver disease. *J. Agric. Food Chem.* 64, 2062–2071. doi:10.1021/acs.jafc.5b06159

Li, B., Zhang, C., and Zhan, Y. T. (2018). Nonalcoholic fatty liver disease cirrhosis: A review of its epidemiology, risk factors, clinical presentation, diagnosis, management, and prognosis. *Can. J. Gastroenterology Hepatology* 2018, 1–8. doi:10.1155/2018/2784537

Lonardo, A., Nascimbeni, F., Targher, G., Bernardi, M., Bonino, F., Bugianesi, E., et al. (2017). AISF position paper on nonalcoholic fatty liver disease (NAFLD): Updates and future directions. *Dig. Liver Dis.* 49, 471–483. doi:10.1016/j.dld.2017.01.147

Ma, J., Yin, H., Li, M., Deng, Y., Ahmad, O., Qin, G., et al. (2019). A comprehensive study of high cholesterol diet-induced larval zebrafish model: A short-time *in vivo* screening method for non-alcoholic fatty liver disease drugs. *Int. J. Biol. Sci.* 15, 973–983. doi:10.7150/ijbs.30013

Malnick, S., Mildiner, S., and Neuman, M. G. (2020). Obeticholic acid for treatment of NAFLD—A drug in search of a disease. *GastroHep* 2, 133–137. doi:10.1002/ygh2.397

Meda, C., Dolce, A., Vegeto, E., Maggi, A., and Torre, S. D. (2022). Erα-dependent regulation of adropin predicts sex differences in liver homeostasis during high-fat diet. *Nutrients* 14, 3262. doi:10.3390/nu14163262

Mruk, D. D., Wong, C. H., Silvestrini, B., and Cheng, C. Y. (2006). A male contraceptive targeting germ cell adhesion. *Nat. Med.* 12, 1323–1328. doi:10.1038/nm1420

Perumpail, B. J., Li, A. A., John, N., Sallam, S., Shah, N. D., Kwong, W., et al. (2018). The role of Vitamin E in the treatment of NAFLD. *Diseases* 6, 86. doi:10.3390/diseases6040086

Reimer, K. C., Wree, A., Roderburg, C., and Tacke, F. (2020). New drugs for NAFLD: Lessons from basic models to the clinic. *Hepatol. Int.* 14, 8–23. doi:10.1007/s12072-019-10001-4

Saponaro, C., Gaggini, M., Carli, F., and Gastaldelli, A. (2015). The subtle balance between lipolysis and lipogenesis: A critical point in metabolic homeostasis. *Nutrients* 7, 9453–9474. doi:10.3390/nu7115475

Wang, C., Hu, N. H., Yu, L. Y., Gong, L. H., Dai, X. Y., Peng, C., et al. (2020). 2, 3, 5, 4'-tetrahydroxystilbence-2-O-β-D-glucoside attenuates hepatic steatosis via IKKβ/NF-κB and Keap1-Nrf2 pathways in larval zebrafish. *Biomed. Pharmacother.* 127, 110138. doi:10.1016/j.biopha.2020.110138

Xi, Y., and Li, H. (2020). Role of farnesoid X receptor in hepatic steatosis in nonalcoholic fatty liver disease. *Biomed. Pharmacother.* 121, 109609. doi:10.1016/j.biopha.2019.109609

Yao, H., Qiao, Y. J., Zhao, Y. L., Tao, X. F., Xu, L. N., Yin, L. H., et al. (2016). Herbal medicines and nonalcoholic fatty liver disease. *World J. Gastroenterology* 22, 6890. doi:10.3748/wjg.v22.i30.6890

Yao, W. W., Wang, P. R., Yang, H. H., Pu, X. H., and Yang, J. F. (2022). Development of potent ERα inhibitors: Effectively inhibit the growth of breast cancer cells. *ChemistrySelect* 7, e202201451. doi:10.1002/slct.202201451

Zhou, J., Zhou, F., Wang, W., Zhang, X.-J., Ji, Y.-X., Zhang, P., et al. (2020). Epidemiological features of NAFLD from 1999 to 2018 in China. *Hepatology* 71, 1851–1864. doi:10.1002/hep.31150

frontiers | Frontiers in Chemistry

TYPE Original Research
PUBLISHED 23 December 2022
DOI 10.3389/fchem.2022.1064518

OPEN ACCESS

EDITED BY
Xuetao Xu,
Wuyi University, China

REVIEWED BY
Sridhar Goud Nerella,
National Institutes of Health (NIH), United States
Carsten Höltke,
University Hospital Münster, Germany

*CORRESPONDENCE
Xinhui Su,
suxinhui@zju.edu.cn

†These authors have contributed equally to this work

SPECIALTY SECTION
This article was submitted to Medicinal and Pharmaceutical Chemistry, a section of the journal Frontiers in Chemistry

RECEIVED 08 October 2022
ACCEPTED 09 December 2022
PUBLISHED 23 December 2022

CITATION
Su X, Wang L, Yang R and Guo Z (2022), Longitudinal ^{18}F-VUIIS1008 PET imaging in a rat model of rheumatoid arthritis.
Front. Chem. 10:1064518.
doi: 10.3389/fchem.2022.1064518

Longitudinal ^{18}F-VUIIS1008 PET imaging in a rat model of rheumatoid arthritis

Xinhui Su[1,2,3*†], Liangliang Wang[2,3,4†], Rongshui Yang[3†] and Zhide Guo[5]

[1]Department of Nuclear Medicine, School of Medicine, The First Affiliated Hospital, Zhejiang University, Hangzhou, China, [2]The School of Clinical Medicine, Fujian Medical University, Fuzhou, China, [3]Department of Nuclear Medicine, Zhongshan Hospital Xiamen University, Xiamen, China, [4]Department of Nuclear Medicine, Linyi People's Hospital, Linyi, China, [5]Center for Molecular Imaging and Translational Medicine, Xiamen University, Xiamen, China

Macrophages have crucial roles in the pathogenesis of rheumatoid arthritis (RA). We aimed to elucidate the temporal profile of macrophage infiltration in synovitis in RA rat models using PET (positron emission tomography) imaging based a new generation of TSPO (Translocator protein, 18 kDa)-PET ligand, ^{18}F-VUIIS1008 {2-[5,7-Diethyl-2-{4-[2-(^{18}F)fluoroethoxy]phenyl} pyrazolo(1,5-a)pyri-midin-3-yl]-N, N-diethylacetamide}. *In vitro* and *in vivo* studies were conducted using RAW264.7 macrophage cells and a rat model of RA induced by Complete Freund's Adjuvant (CFA). Our results showed ^{18}F-VUIIS1008 showed excellent stability *in vitro* and binding specificity to RAW264.7 cells, and rapid accumulation in the left inflammatory ankles. PET studies revealed that ^{18}F-VUIIS1008 could clearly identify the left inflammatory ankles with good contrast at 30–120 min post-injection. The uptake of ^{18}F-VUIIS1008 of left inflammatory ankles was a wiggle trace with two peaks on day 7 and 29, and then, the highest peak uptake was seen on day 29 (3.00% ± 0.08%ID/g) at 60 min after injection. Tracer uptakes could be inhibited by PK11195 or VUIIS1008. Immunohistochemistry and immunofluorescence tests showed that elevated TSPO expression and infiltrated macrophages were found in the left inflammation ankles. ^{18}F-VUIIS1008 as a novel PET imaging agent showed great potential to identify temporal profile of macrophage infiltration in synovitis in RA, and deliver accurate non-invasive diagnosis and real-time monitoring of RA development.

KEYWORDS

18F-VUIIS1008, PET, rheumatoid arthritis, TSPO 18 kDa, macrophages

Abbreviations: RA, rheumatoid arthritis; TSPO, translocator protein, 18 kDa; PET, positron emission tomography; SPECT, single-photon emission computed tomography; VUIIS1008, 2-(5,7-diethyl-2-(4-(2-flfluoroethoxy)phenyl)pyrazolo[1,5-a]pyrimidin-3 -yl)-N,N-di- ethylacetamide); 18F, fluorine-18; CFA, Complete Freund's Adjuvant; DMSO, dimethyl sulfoxide; DMEM, Dulbecco's modifified Eagle's medium; RAW264.7, mouse macrophage cell lines; PBS, phosphate-buffered saline; LIA/M, the ratio of the left inflflammatory ankle to muscle; LIA/B, the ratio of the left inflammatory ankle to blood; ROI, regions of interest; %ID/g, percentage of the injected radioactivity per gram of tissue.

1 Introduction

Rheumatoid arthritis (RA) is a chronic systemic autoimmune inflammatory disease primarily characterized by chronic joint inflammation, cartilage destruction and bone erosion, leading to severe progressive joint damage, functional disability, morbidity, and increased mortality (Calabrò et al., 2016). RA is approximately three-times more common in women than in men and affects 0.5%–1.0% of the world's population (De Cata et al., 2014). The main objective of RA treatment is to stop inflammation, relieve symptoms, prevent joint and organ damage, improve physical function and reduce long-term complications (Jalil et al., 2016). The common treatment method is anti-inflammation early in the disease course as soon as the diagnostic has been established, suggesting that the early diagnosis is a key for the therapy and prognosis of RA.

Although the pathogenesis of RA is not yet completely understood, it is considered as a complex, multi-factorial etiology, including genetic sensitivity, and environment factors and autoimmune responses, which collectively trigger the onset and persistence of inflammatory circumstance (Firestein, 2003). Mounting data of evidence have shown that the degree of macrophage infiltration into the synovium is correlated with the degree of bone erosion in the affected joints in RA (Soler Palacios et al., 2015; Udalova et al., 2016), since pro-inflammatory cytokines from activated macrophage, such as tumor necrosis factor-α (TNF-α), interleukin-1 (IL-1), and interleukin-6 (IL-6), contribute to synovial inflammation in early stages of RA (Arthur and Ley, 2013). The abundance of synovial tissue macrophages is an early RA hallmark (Kurowska-Stolarska and Alivernini, 2022). Therefore, the imaging using a specific probe targeted activated macrophage possibly enable an earlier detection of RA. Recently, specific ligands targeting macrophage receptors such as CD20 receptor, interleukin-1 (IL-1) receptor, *etc.*, have been investigated in the patients with RA using ^{99m}Tc-anti-CD20, ^{123}I-IL-1ra and ^{124}I-anti-CD20 illustrating the interest for molecular imaging in this type of pathology (Barrera et al., 2000; Tran et al., 2011; Malviya et al., 2012). The drawbacks of probes with antibodies severely hamper their clinical applications due to their large size resulting in slow inflammation accumulation and slow clearance from the circulation (Su et al., 2015).

The translocator protein 18 kDa (TSPO), previously known as the peripheral-type benzodiazepine receptor (PBR), is located in the outer mitochondrial membrane, where involved in apoptosis, cell proliferation, anion transport, regulation of mitochondrial functions and immunomodulation (Papadopoulos et al., 2006). TSPO is a potential candidate for individualized approach to inflammation as its expression is enhanced in activated macrophage but it is low in the normal macrophage (Kanegawa et al., 2016). Thus, TSPO is regarded as a potential target for inflammatory diseases (Gatliff and CampanellaTSPO, 2016). It has been reported that positron emission tomography (PET) or single photon emission computed tomography (SPECT) study targeted TSPO probes, including ^{11}C-(R)-PK11195, ^{11}C-DPA-713, ^{18}F-DPA-714 or ^{99m}Tc-DTPA-CB86, can visualize RA (Gent et al., 2014a; Gent et al., 2014b; Liu et al., 2020). However, to our knowledge, few studies on TSPO imaging *in vivo* assessing the complete time course of joint inflammation during complete Freund's adjuvant (CFA)-induced RA have been reported. Establishing such data may be important for the subsequent development of image-guided anti-inflammation interventions. Compared with ^{11}C and ^{99m}Tc, ^{18}F may improve imaging of TSPO-expression and is more suitable for clinical application. In addition, a novel TSPO ligand (2-(5,7-diethyl-2-(4-(3-fluoro- 2-methylpropoxy)phenyl)pyrazolo[1,5-*a*] pyrimidin-3-yl)-*N*,*N*-diethylacetamide, VUI- IS1008), has been proved a 36-fold enhancement in binding affinity (K_i = 0.3 ± 0.14 nM) compared to DPA-714 (K_i = 10.9 ± 0.39 nM) (Tang et al., 2014). Furthermore, Kwon YD, et al., have reported that in a rat lipopolysaccharide (LPS)-induced neuroinflammation model, the uptake ratio of ^{18}F-VUIIS1008 between the neuroinflammation ipsilateral and contralateral regions in the brain was 18% higher than that of ^{18}F-DPA-714, suggesting that ^{18}F-VUIIS1008 has better PET imaging tracer's features for identifying neuroinflammation in brain than that of ^{18}F-DPA-714 (Kwon et al., 2018). Accordingly, in the present study, we aimed to elucidate the potential role of longitudinal ^{18}F-VUIIS1008 PET imaging in an experimental RA.

2 Materials and methods

2.1 General

VUIIS1008, a new TSPO agent, was presented by Professor Shoufa Han (College of Chemistry and Chemical Engineering, Xiamen University) according to the previous study by Kwon YD (Kwon et al., 2018). No-carrier-added ^{18}F-fluoride was kindly provided by the First Affiliated Hospital of Xiamen University. Freund's Adjuvant and anti-TSPO antibodies were purchased from Sigma-Aldrich Shanghai Trading Co Ltd. (Shanghai, China). Goat anti-mouse IgG antibody was from Santa Cruz Biotechnology Inc. (Santa Cruz, California, United States). WIZARD 2480 gamma counter from Perkin-Elmer Inc. (Waltham, MA, United States). CRC-25R Dose Calibrator from Capintec Inc. (Ramsey, New Jersey, United States). Mouse macrophage RAW264.7 cell lines were obtained from the Cell Culture Center of Institute of Basic Medical Sciences of Chinese

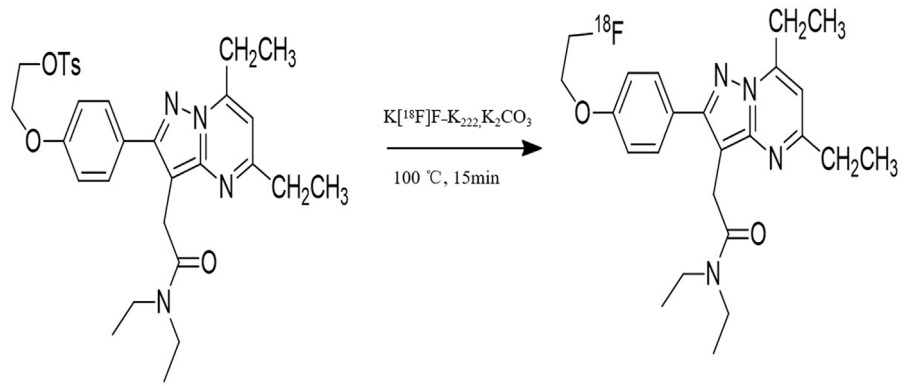

FIGURE 1
Synthetic scheme of ^{18}F-VUIIS1008.

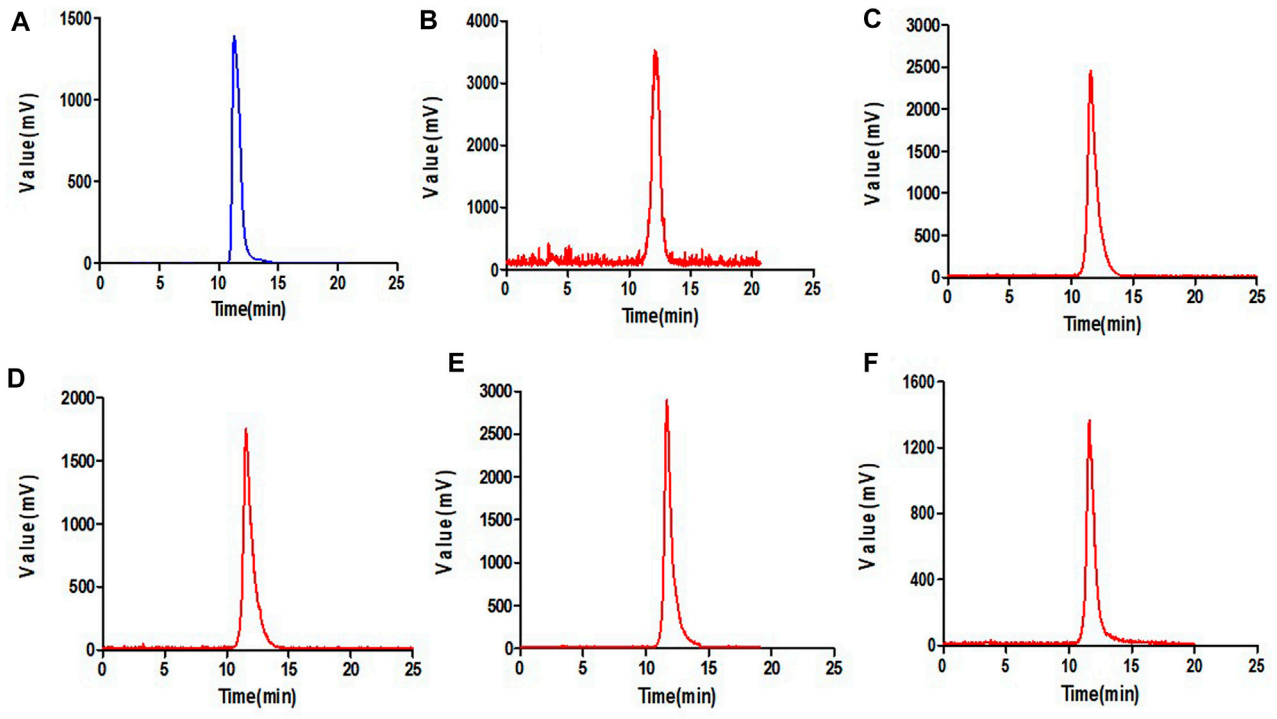

FIGURE 2
Prep-HPLC chromatogrm **(A)** and HPLC radiochromatograms of purified ^{18}F-VUIIS1008 **(B)** and radiola-beled probe after 30 min **(C)**, 60 min **(D)**, 120 min **(E)** and 240 min **(F)** of incubation with PBS.

Academy of Medical Sciences (Beijing, China). Male Wistar rats, aged 6–8 weeks (200–300 g), were purchased from the Experimental Animal Center of Xiamen University (Xiamen, China). Small animal PET/CT imaging studies were performed using a micro-PET/CT scanner (Inveon, Siemens Medical Solutions United States, Inc.).

2.2 Chemistry and radiochemistry

The synthesis of radiotracers 2-(5,7-diethyl-2-(4-(2-fluoroethoxy) phenyl) pyrazolo [1,5-a] pyrimidin-3-yl)-N, N-diethylacetamide (^{18}F-VUIIS1008) were prepared from its corresponding tosylate precursors *via* manual synthesis

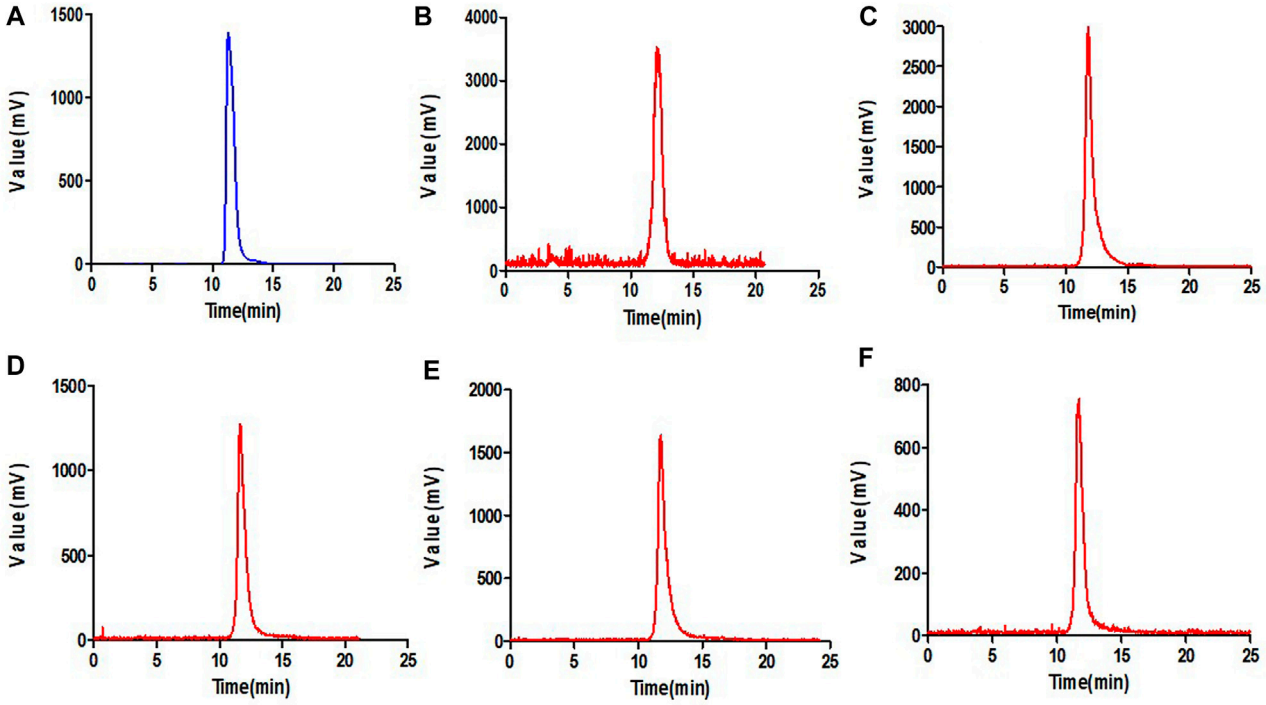

FIGURE 3
Prep-HPLC chromatogrm **(A)** and HPLC radiochromatograms of purified ^{18}F-VUIIS1008 **(B)** and radiola-beled probe after 30 min **(C)**, 60 min **(D)**, 120 min **(E)** and 240 min **(F)** of incubation with mouse serum.

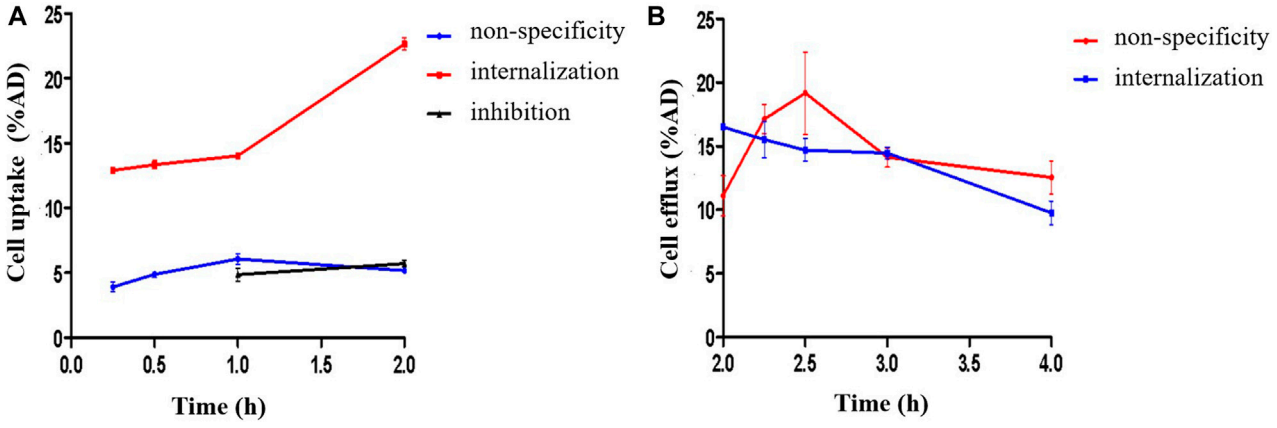

FIGURE 4
Uptake **(A)**, and efflux assay **(B)** of ^{18}F-VUIIS1008 in RAW264.7 cells.

according to previously reported procedures (Tang et al., 2013; Kwon et al., 2018). Briefly, aqueous ^{18}F-fluoride (5–15 mCi; 0.2~0.6 GBq) was eluted from the cartridge with a solution of Kryptofix K2.2.2 to form the complexation mixture. This complex was then reacted with appropriate tosylate precursor VUIIS1008 (4.0 mg) in dimethylsulfoxide (0.7 mL) at 100°C for 15min. The reaction crude was purified using semi-preparative HPLC (C18, Dynamax 250 × 10 mm; Varian), eluting with 10 mM NaH_2PO_4

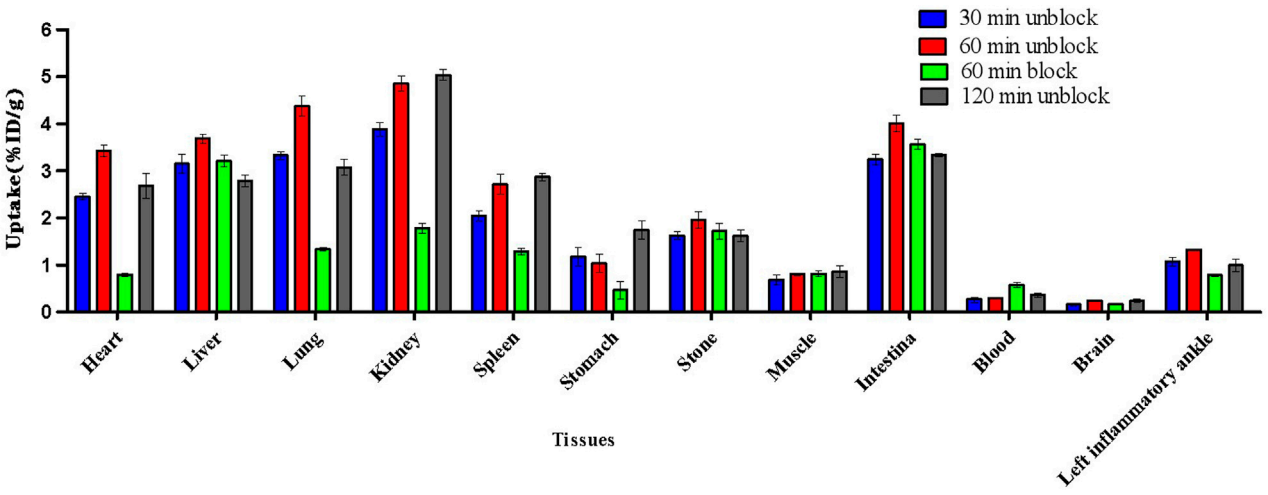

FIGURE 5
Biodistribution results for ^{18}F-VUIIS1008 on day 3 after CFA injection. Data are presented as %ID/g at various times post-injection of ^{18}F-VUIIS1008.

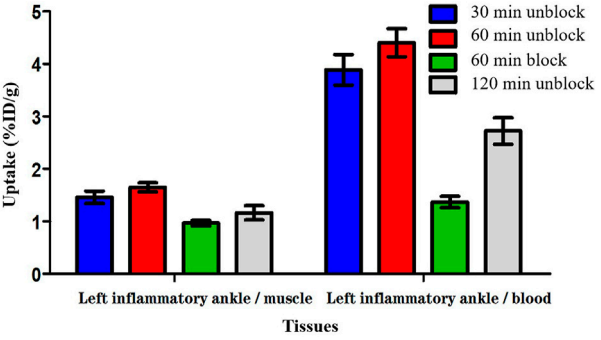

FIGURE 6
The radioactivity ratios of the left inflammatory ankle to blood (LIA/B) and the left inflammatory ankle to muscle (LIA/M) at various times post-injection based on biodistribution results of ^{18}F-VUIIS1008.

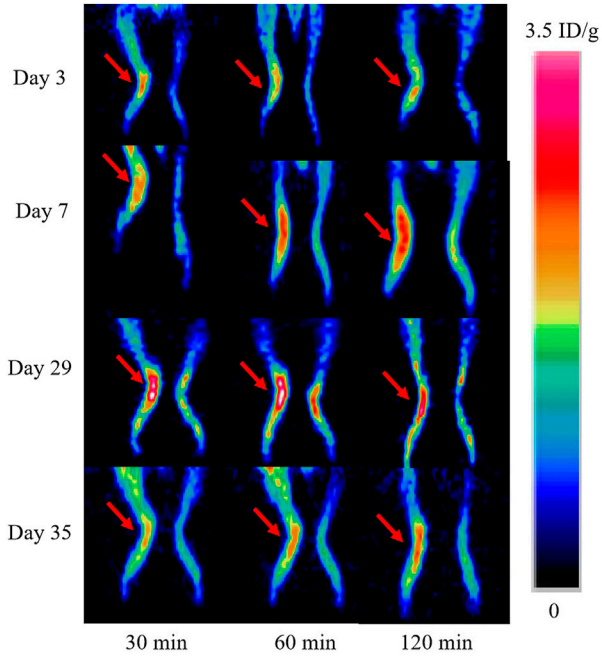

FIGURE 7
^{18}F-VUIIS1008 PET imaging of RA rat model at 30, 60, and 120 min post-injection on day 3, 7, 29, 35 after CFA injection. Red arrow indicate left inflammatory ankles.

buffer (pH 6.7) and methanol (30/70, v/v) at 3.0 mL/min. The product (^{18}F-VUIIS1008) was collected directly into 140 ml of water (deionized), passed through a C-18 September-Pak Plus (Waters, Milford, MA, United States of America), and eluted with 200 proof ethanol (1.0 mL) then saline (0.9%) into a sterile vial.

2.3 Lipophilicity test of ^{18}F-VUIIS1008

According to our previous report (Liu et al., 2020), the lipophilicity of ^{18}F-VUIIS1008 was analysed by the n-octanol/water mixture containing 200 μL ^{18}F-VUIIS1008 and 1 mL phosphate-buffered saline (pH = 7.4). The solution was centrifuged at 6,000 rpm for 5 min, and separated and then they were counted in a γ counter, respectively. The

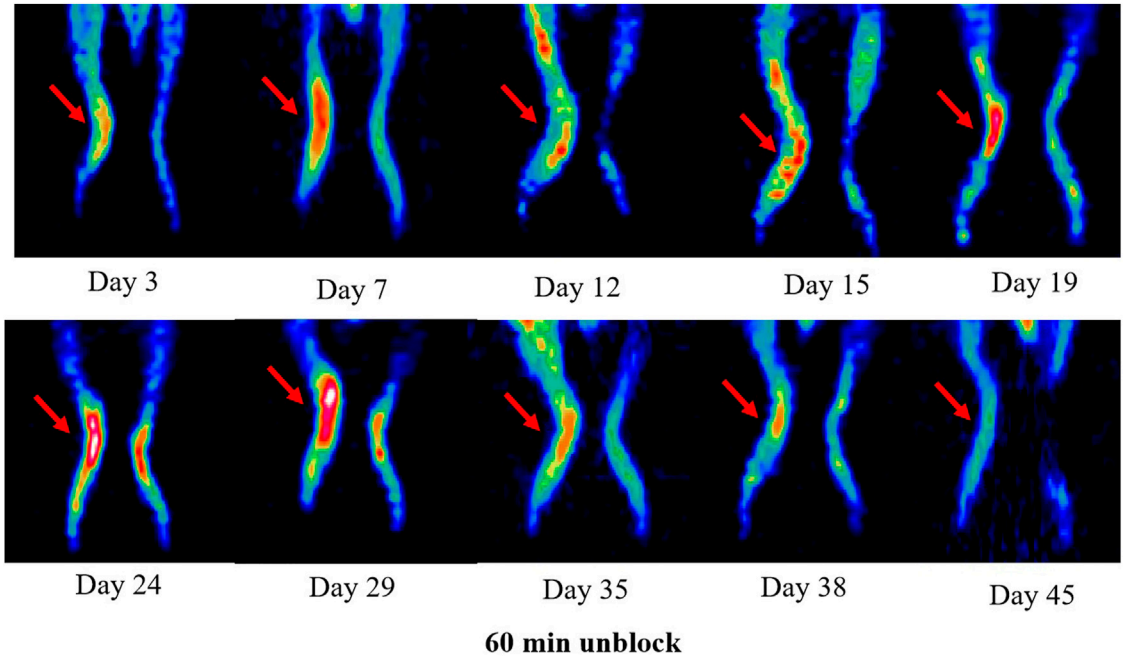

FIGURE 8
^{18}F-VUIIS1008 PET imaging of RA rat model at 60 min post-injection on day 3, 7, 12, 15, 19, 24, 29, 35, 38, and 45 after CFA injection. Red arrow indicate left inflammatory ankles.

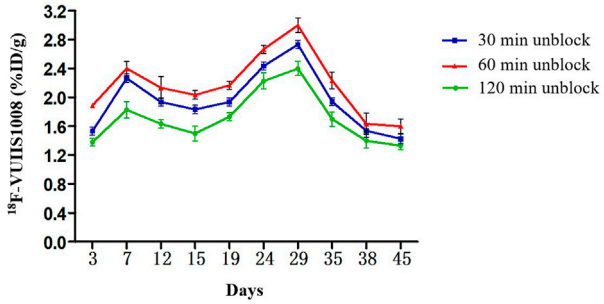

FIGURE 9
Quantitative analysis of ^{18}F-VUIIS1008 uptake in the left inflammatory ankles at different time post-injection on different day based on PET imaging. Peak uptake was found on day 29.

radioactivity were used to calculate the log *p* values. The lipophilicity of ^{18}F-VUIIS1008 was determined as (cpm in organic phase)/ (cpm in water phase).

2.4 Stability studies

Based on our previous report (Liu et al., 2020), the stability of the complex containing 500 μL (3.7 MBq) ^{18}F-VUIIS1008 and phosphate-buffered saline (PBS, pH = 7.4) or mouse serum was evaluated by performing the complex at 37°C for 30、60、120、and 240 min. The radioactivity of ^{18}F-VUIIS1008 was measured at various time points by a HPLC.

2.5 Cell tests

The RAW264.7 cell lines were conducted cell uptake, and efflux tests in accordance with our previous study (Liu et al., 2020).

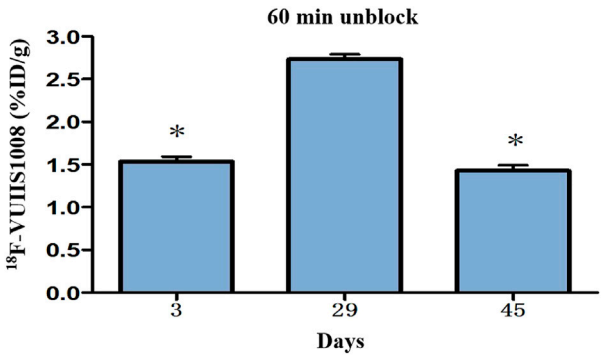

FIGURE 10
Quantitative analysis of ^{18}F-VUIIS1008 uptake in the left inflammatory ankles on day 3, 29, 45 based on PET imaging.

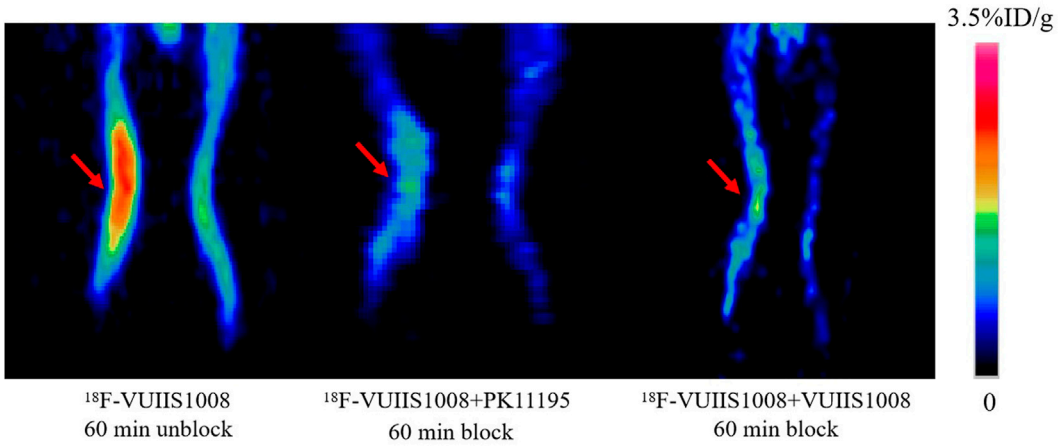

FIGURE 11
Representative PET images of ^{18}F-VUIIS1008 uptake in the left inflammatory ankles without and with cold PK11195 or VUIIS1008 blocking. Red arrow indicate left inflammatory ankles.

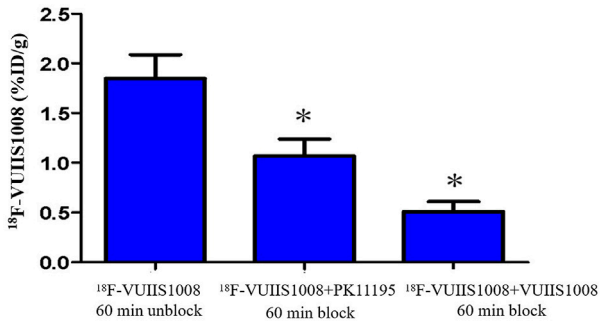

FIGURE 12
Quantification of ^{18}F-VUIIS1008 uptake in the left inflammatory ankles without and with cold PK11195 or VUIIS1008 blocking.

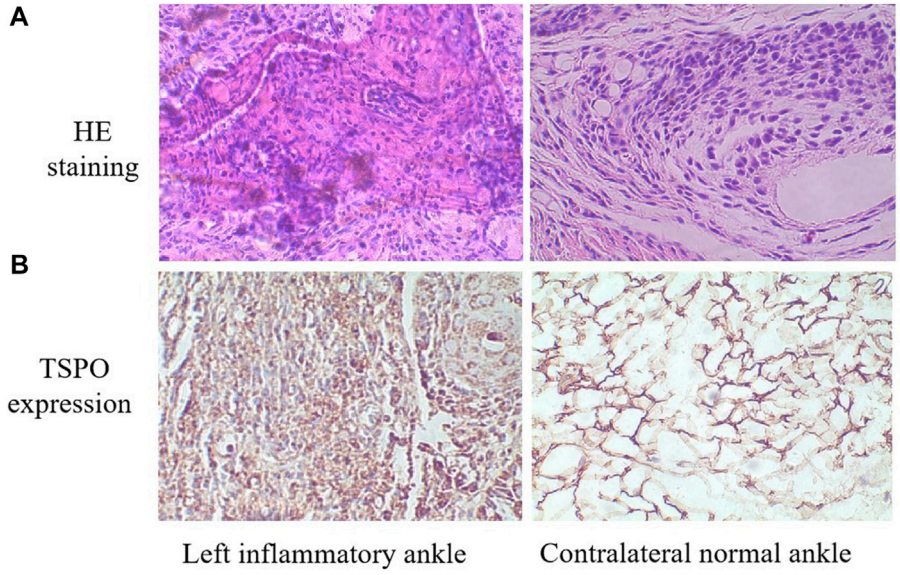

FIGURE 13
(A) HE staining of the left inflammatory ankles and contralateral normal ankles (×100). **(B)** The expression of TSPO on the left inflammatory ankles and contralateral normal ankles by immunohistochemical analysis (×100).

2.5.1 Cell uptake tests

The RAW264.7 cell lines were cultured at 37°C for 15, 30, 60 and 120 min in the complex containing 0.5 mL serum-free DMEM medium and 7.4×10^{-3} MBq 100 μL ^{18}F-VUIIS1008 with/without 10.0 μg unlabeled VUIIS1008, and then were lysed with 1 mL 1 M NaOH. The radioactivity of the lysates was measured at various time points by a γ counter.

2.5.2 Cell efflux tests

The RAW264.7 cells were cultured at 37°C for 120, 135, 150 and 180, 240 min in the culture medium with 1.11×10^{-2} MBq 100 μL ^{18}F-VUIIS1008 and then were lysed with 1 mL 1 M NaOH. The radioactivity of the lysates was measured at various time points by a γ counter.

2.6 Rat models with RA

The animal study protocol was carried out according to the principles outlines by the Institutional Animal Care and Use Committee of Zhongshan Hospital Xiamen University. The left inflammatory ankles were induced in male Wistar rats in accordance with our previous study (Liu et al., 2020). Briefly, 0.1 mL of Complete Freund's Adjuvant (CFA) with Mycobacterium butyricum 1% suspension in mineral oil was injected into the left ankle of each rat (day 0). The severity of RA was monitored daily by two observers. The left inflammatory ankles were estimated by the number swollen joints. When the left inflammatory ankles grew to swell in two to three joints, the RA rats were subject to *in vivo* biodistribution and PET studies.

2.7 Biodistribution analysis

The biodistribution analysis were induced on day 3 after CFA injection. RA rats were administrated with ^{18}F-VUIIS1008 (3.7 MBq, 100 μL) *via* tail vein. At 30, 60, and 120 min post-injection, the left inflammatory ankles and normal tissues of interest were removed and determined their radioactivity with a γ counter. For *in vivo* specificity study, RA rats were injected with ^{18}F-VUIIS1008 and unlabeled PK11195 (500 μg), and biodistribution studies were performed at 60 min post-injection. The radioactivity ratios of the left inflammatory ankle to blood (LIA/B) and the left inflammatory ankle to muscle (LIA/M) were calculated. Biodistribution data are expressed as %ID/g values by dividing counts per gram per minute by the injected dose.

2.8 Micro-PET studies

PET imaging studies were performed using a micro-PET scanner (Siemens Medical Solutions United States, Inc.). Static PET imaging was performed at 30, 60, and 120 min post-injection of 3.7 MBq 100 μL ^{18}F-VUIIS1008 *via* tail vein on day 3, 7, 12, 15, 19, 24, 29, 35, 38, and 45 after CFA injection.

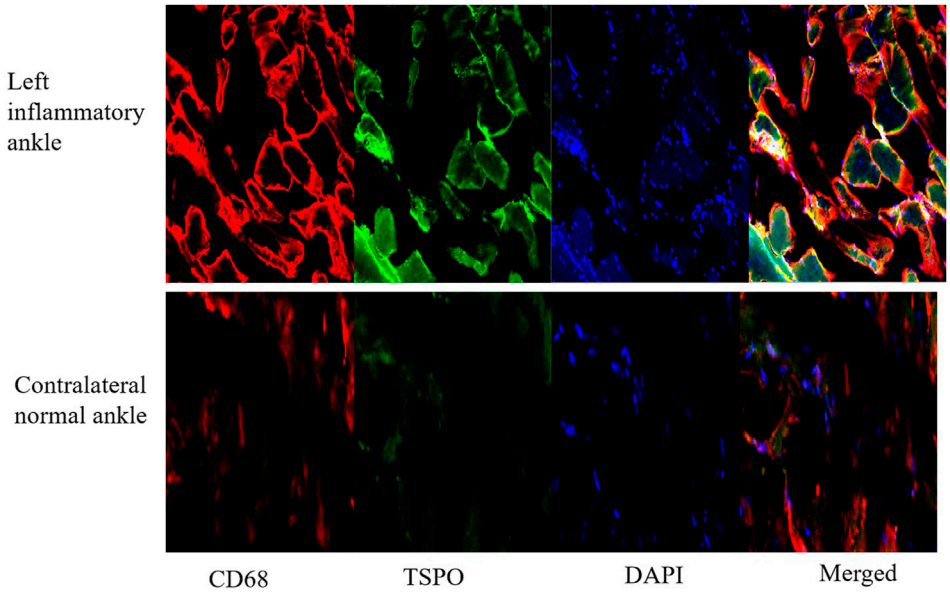

FIGURE 14
The expression of TSPO and CD68 on contralateral normal ankles by immunofluorescence staining (x100).

For blocking imaging, unlabeled PK11195 (500 μg) or VUIIS1008 (500 μg) was co-injected with ^{18}F-VUIIS1008 (3.7 MBq 100 μ) on day seven. The RA rat were anesthetized with 2% isoflurane and positioned prone in micro-PET bed. Micro-PET images were reconstructed using an 3D OSEM scatter corrected reconstruction algorithm. Regions of interest (ROIs) were placed on the left inflammatory ankles. Micro-PET data are expressed as %ID/g values by dividing counts per gram per minute by the injected dose.

2.9 Histological studies

According to routine protocols, Hematoxylin and Eosin (HE staining), immunohistochemistry (IHC) tests and immunofluorescence staining were carried out in the tissues of left inflammatory ankles, contralateral normal ankles on day 3 after CFA injection. For HE tests, 5 ?m longitudinal sections were stained with hematoxylin and Eosin solution for 5 and 3 min at 25°C, respectively, and then analysed using an Olympus BX53 fluorescence microscope (Tokyo, Japan). For immunohistochemical analyses, the slices successively incubated with rabbit anti-rat TSPO antibodies (1:100, Abcam) and goat anti-rat secondary antibodies (1:1,000; Sigma) for 2 h at 25°C, and then analysed using an Olympus BX53 fluorescence microscope. For immunofluorescence staining, according to a standard protocol (Capaccione et al., 2020). The slides successively incubated with rabbit anti-rat TSPO antibodies (1:100, Abcam), anti-mouse CB68 antibodies (1:100, Abcam), and goat anti-rat FITC-IgG secondary antibodies (1:200; Sigma), goat anti-mouse TRITC-IgG secondary antibodies (1:200; Sigma), respectively, for 2 h at 25°C, and then stained using 200–300 μL 10 μg/mL of DAPI. After then, These slides were analysed using an Olympus BX53 fluorescence microscope.

2.10 Statistical analysis

The experimental data are presented as mean ± standard deviation. Statistical calculations were determined using the Student's t-test and $p < .05$ was statistically significant.

3 Results and discussion

3.1 Radiosynthesis of ^{18}F-VUIIS1008 and log P determination

^{18}F-VUIIS1008 was successfully radiosynthesized (Figure1). Under radio-HPLC conditions described above, ^{18}F-VUIIS1008 displayed a retention time of 11.8 min. The radiochemical purity of the radiopharmaceutical exceeded 98.00%, and the specific activity of the purified ^{18}F-VUIIS1008 was 1.52 × 10^8 MBq/mmol. The lipid-water partition coefficient (log *P*) of ^{18}F-VUIIS1008 is 1.58 ± 0.03, indicating ^{18}F-VUIIS1008 is a fat-soluble compound.

3.2 Stability studies

^{18}F-VUIIS1008 displayed excellent stability in the PBS (Figure 2) or mouse serum (Figure 3). It showed that defluorination of ^{18}F-VUIIS1008 was not obviously found, and the percentage of intact probes remained more than 90% during 30–240 min of incubation in the PBS or mouse serum.

3.3 Cell assays

Cell uptake ratios of ^{18}F-VUIIS1008 were shown in Figure 4A. The level of ^{18}F-VUIIS1008 in RAW264.7 cells was 12.00 ± 0.10%, 13.00 ± 1.00%, 14.00 ± 0.30% and 23.00 ± 0.60% at 15, 30, 60, and 120 min, respectively. When the probe was incubated with large excesses of non-radioactive VUIIS1008, its uptake levels in RAW264.7cells was significantly inhibited (p <0.05) at all incubation time points. Moreover, cell efflux studies (Figure 4B) indicated ^{18}F-VUIIS1008 has excellent cell retention in RAW264.7 cells, which ^{18}F-VUIIS1008 efflux was 6.74% (reduction from 16.50 ± 0.002% to 9.76 ± 0.001% of total input radioactivity) from 120 min to 240 min incubation. In general, the results demonstrated that ^{18}F-VUIIS1008 maintained high affinity to TSPO to further study *in vivo* TSPOtargeted imaging.

3.4 Biodistribution studies

The biodistribution studies were conducted on day 3 after CFA injection. At 30, 60, and 120 min post-injection, the biodistribution characteristics of ^{18}F-VUIIS1008 was shown in Figure 5. ^{18}F-VUIIS1008 displayed high radioactivity uptake in the left inflammatory ankle. At 30, 60, and 120 min, the left inflammatory ankle uptake was 1.08% ± 0.08% ID/g, 1.33% ± 0.02% ID/g, 0.99% ± 0.1 3% ID/g, respectively, lower than that in the liver, kidney, intestine, stomach, lungs, bone, and spleen, whereas it was higher than blood, muscle, and brain. Furthermore, ^{18}F-VUIIS1008 showed high levels of the left inflammatory ankle to muscle (LIA/M) and left inflammatory ankle to blood (LIA/B) (Figure 6). At 60 min, the ratio of LIA/M and LIA/B was 1.65 ± 0.07 and 4.40 ± 0.22, respectively, and higher than that at 30 and 120 min.

In order to investigate the specificity of ^{18}F-VUIIS1008, an excess of PK11195 (500 μg) was coinjected with ^{18}F-VUIIS1008 into RA rats to saturate endogenous and overexpressed TSPO in some normal tissues. PK11195 decreased significantly the accumulations of ^{18}F-VUIIS1008 in the left inflammatory ankle and many tissues, such as liver, lung, heart, kidney, stomach, and intestine (p <.05), whereas it did not decreased those in the blood, muscle, and bone (p >.05).

3.5 Longitudinal PET/CT imaging studies

Longitudinal small animal PET/CT studies were performed at 30, 60, and 120 min after injection of ^{18}F-VUIIS1008 on day 3, 7, 12, 15, 19, 24, 29, 35, 38, and 45 after CFA injection. As shown in Figure 7, ^{18}F-VUIIS1008 highly accumulated in the left inflammatory ankles at 30 min compared with the collateral ankles, and exhibited a gradual increasing uptake during 60–120 min post-injection. The left inflammatory ankles were clearly visible with good inflammatory to background contrast. During day 3–45 after CFA injection, the uptake of left inflammatory ankles was a wiggle trace with two peaks on day 7 and 29, and then the uptake on day 29 was the highest (60 min (3.00% ± 0.08% ID/g) (p <.05) (Figures 8–10). Importantly, there was an inflection point on day 15, and after day 15, the uptake gradually increased along with time till day 29, then dropped slowly along with time till day 45, when the uptake was the lowest, and still higher than that in collateral muscle. Furthermore, when co-injected with unlabeled PK11195 (500 μg) or VUIIS1008 (500 μg), the left inflammatory ankles were barely visible on PET images at 60 min post-injection (Figure 11), while the contralateral normal muscle stayed at the low uptake level, affected slightly by PK11195 or VUIIS1008 injection. Regions of interest (ROIs) analysis of PET showed a high ratio of the left inflammatory ankle in RA rats injected unblocking dose compared to with 500 μg blocking dose at 60 min post-injection (Figure 12) (p <.05).

3.6 Histological results

For HE tests, it found that synovial hyperplasia and infiltration of inflammatory cells (such as lymphocaytes and macrophages) were identified in the left inflammatory ankles, while they were not observed in the normal contralateral ankles (Figure 13A). For immunohistochemistry (IHC) analysis, there found positive staining of TSPO in the left inflammatory ankles, while negative expression of TSPO in the normal contralateral normal ankles (Figure 13B). Moreover, for immunofluore-scence analysis, it showed the positive staining of TSPO and macrophage (CD68) could be detected in the left inflammatory ankles, whereas they were not found in the normal contralateral normal ankles (Figure 14).

4 Conclusion

In this study, we performed longitudinal ^{18}F-VUIIS1008 PET imaging to defined the temporal profile of macrophage infiltration in synovitis in rat models of rheumatoid arthritis. The results supported the feasibility of ^{18}F-VUIIS1008 PET imaging to identify the dynamics of macrophage activation and infiltration in different stages of synovitis in RA rat models, suggesting

^{18}F-VUIIS1008 PET imaging could be used to be a non-invasive imaging technique for clinical management of RA.

Data availability statement

The original contributions presented in the study are included in the article/Supplementary Materials, further inquiries can be directed to the corresponding author.

Ethics statement

The animal study was reviewed and approved by the animal procedures were performed according to a protocol approved by the Institutional Animal Care and Use Committee of Zhongshan Hospital Xiamen University.

Author contributions

XS designed, wrote, and funded the study, LW and RY conducted all the experiments and prepared the figures, ZG participated in the discussion. All authors approved the final version.

Funding

This work was supported by grants from the National Natural Science Foundation of China (NSFC) (82071965), Fujian medical innovation project (2019-CXB-32), National Natural Science Foundation of Fujian province (2020J011210), and Huadong Medicine Joint Funds of the Zhejiang Provincial Natural Science Foundation of China (LHDMZ22H300010).

Conflict of interest

The authors declare that the research was conducted in the absence of any commercial or financial relationships that could be construed as a potential conflict of interest.

Publisher's note

References

Arthur, J. S., and Ley, S. C. (2013). Mitogen-activated protein kinases in innate immunity. *Nat. Rev. Immunol.* 13 (9), 679–692. doi:10.1038/nri3495

Barrera, P., van der Laken, C. J., Boerman, O. C., Oyen, W. J., van de Ven, M. T., van Lent, P. L., et al. (2000). Radiolabelled interleukin-1 receptor antagonist for detection of synovitis in patients with rheumatoid arthritis. *Rheumatolog- (Oxford)* 39 (8), 870–874. doi:10.1093/rheumatology/39.8.870

Calabrò, A., Caterino, A. L., Elefante, E., Valentini, V., Vitale, A., Talarico, R., et al. (2016). One year in review 2016: Novelties in the treatment of rheumatoid arthritis.novelties in the treatment of rheumatoid arthritis. *Clin. Exp. Rheumatol.* 34 (3), 357–372.

Capaccione, K. M., Doubrovin, M., Bhatt, N., Mintz, A., and Molotkov, A. (2020). Granzyme B PET imaging of the innate immune response. *Molecules* 25 (13), 3102. doi:10.3390/molecules25133102

De Cata, A., D'Agruma, L., Tarquini, R., and Mazzoccoli, G. (2014). Rheumatoid arthritis and the biological clock. *Expert Rev. Clin. Immunol.* 10 (5), 687–695. doi:10.1586/1744666x.2014.899904

Firestein, G. S. (2003). Evolving concepts of rheumatoid arthritis. *Nature* 423 (6937), 356–361. doi:10.1038/nature01661

Gatliff, J., and CampanellaTSPO, M. (2016). Tspo: Kaleidoscopic 18-kDa amid biochemical pharmacology, control and targeting of mitochondria. *Biochem. J.* 473 (2), 107–121. doi:10.1042/bj20150899

Gent, Y. Y., Ahmadi, N., Voskuyl, A. E., Hoetjes, N., van Kuijk, C., Britsemmer, K., et al. (2014). Detection of subclinical syno- vitis with macrophage targeting and positron emission tomography in patients with rheumatoid arthritis without clinical arthritis. *J. Rheumatol.* 41 (11), 21 45–2152. doi:10.3899/jrheum.140059

Gent, Y. Y., Weijers, K., Molthoff, C. F., Windhorst, A. D., Huisman, M. C., Kassiou, M., et al. (2014). Promising potential of new genera- tion translocator protein tracers providing enhanced contrast of arthritis imag- ing by positron emission tomography in a rat model of arthritis. *Arthritis Res. Ther.* 16 (2), R70. doi:10.1186/ar4509

Jalil, S. F., Arshad, M., Bhatti, A., Ahmad, J., Akbar, F., Ali, S., et al. (2016). Rheumatoid arthritis: What have we learned about the causing factors? *Pak J. Pharm. Sci.* 29 (2), 629–645.

Kanegawa, N., Collste, K., Forsberg, A., Schain, M., Arakawa, R., Jucaite, A., et al. (2016). *In vivo* evidence of a functional association between immune cells in blood and brain in healthy human subjects. *Brain Behav. Immun.* 54, 149–157. doi:10.1016/j.bbi.2016.01.019

Kurowska-Stolarska, M., and Alivernini, S. (2022). Synovial tissue macrophages in joint homeostasis, rheumatoid arthritis and disease remission. *Nat. Rev. Rheumatol.* 18 (7), 384–397. doi:10.1038/s41584-022-00790-8

Kwon, Y. D., Kang, S., Park, H., Cheong, I. K., Chang, K. A., Lee, S. Y., et al. (2018). Novel potential pyrazolopyrimidine based translocator protein ligands for the evaluation of neuroinflammation with PET. *Eur. J. Med. Chem.* 159, 292–306. doi:10.1016/j.ejmech.2018.09.069

Liu, P., Wang, T., Yang, R., Dong, W., Wang, Q., Guo, Z., et al. (2020). Preclinical evaluation of a novel 99mTc-labeled CB86 for rheumatoid arthritis imaging. *ACS Omega* 5 (49), 31657–31664. doi:10.1021/acsomega.0c04066

Malviya, G., Anzola, K. L., Podestà, E., Laganà, B., Del Mastro, C., Dierckx, R. A., et al. (2012). (99m)Tc-labeled rituximab for imaging B lymphocyte infiltration in inflammatory autoimmune disease patients. *Mol. Imaging Biol.* 14 (5), 637–646. doi:10.1007/s11307-011-0527-x

Papadopoulos, V., Baraldi, M., Guilarte, T. R., Knudsen, T. B., Lacapère, J. J., Lindemann, P., et al. (2006). Translocator prot- ein (18kDa): New nomenclature for the peripheral-type benzodiazepine receptor based on its structure and molecular function. *Trends Pharmacol. Sci.* 27 (8), 402–409. doi:10.1016/j.tips.2006.06.005

Soler Palacios, B., Estrada-Capetillo, L., Izquierdo, E., Criado, G., Nieto, C., Municio, C., et al. (2015). Macrophages from the synovium of active rheumatoid arthritis exhibit an activin A-dependent pro-inflammatory profile. *J. Pathol.* 235 (3), 515–526. doi:10.1002/path.4466

Su, X., Cheng, K., Liu, Y., Hu, X., Meng, S., and Cheng, Z. (2015). PET imaging of insulin-like growth factor type 1 receptor expression with a 64Cu-labeled Affibody molecule. *Amino Acids* 47 (7), 1409–1419. doi:10.1007/s00726-015-1975-4

Tang, D., McKinley, E. T., Hight, M. R., Uddin, M. I., Harp, J. M., Fu, A., et al. (2013). Synthesis and structure-activity relationships of 5, 6, 7-subst- ituted pyrazolopyrimidines: Discovery of a novel TSPO PET ligand for cancer imaging. *J. Med. Chem.* 56 (8), 3429–3433. doi:10.1021/jm4001874

Tang, D., Nickels, M. L., Tantawy, M. N., Buck, J. R., and Manning, H. C. (2014). Preclinical imaging evaluation of novel TSPO-PET ligand 2-(5, 7-Diethyl-2-(4-(2-[(18)F]fluoroethoxy) phenyl)pyrazolo[1, 5-a]pyrimidin-3-yl)-N, N-diethylacetamide ([(18)F]VUIIS1008) in glioma. *Mol. Imaging Biol.* 16 (6), 813–820. doi:10.1007/s11307-014-0743-2

Tran, L., Huitema, A. D., van Rijswijk, M. H., Dinant, H. J., Baars, J. W., Beijnen, J. H., et al. (2011). CD20 antigen imaging with ^{124}I-rituximab PET/CT in patients with rheumatoid arthritis. *Hum. Antibodies* 20 (1-2), 29–35. doi:10.3233/hab-2011-0239

Udalova, I. A., Mantovani, A., and Feldmann, M. (2016). Macrophage heterogeneity in the con- text of rheumatoid arthritis. *Nat. Rev. Rheumatol.* 12 (8), 472–485. doi:10.1038/nrrheum.2016.91

frontiers | Frontiers in Chemistry

TYPE Original Research
PUBLISHED 06 January 2023
DOI 10.3389/fchem.2022.1094841

OPEN ACCESS

EDITED BY
Xiping Cui,
Guangdong University of Technology, China

REVIEWED BY
Mohammad Abrar Alam,
Arkansas State University, United States
Yaxian Wu,
Jiangnan University, China
Hui Zhang,
Bengbu Medical College, China

*CORRESPONDENCE
Panpan Wu,
wyuchemwpp@126.com
Weiqian David Hong,
davidhwq@liverpool.ac.uk
Song Ang,
jnuangsong@126.com

SPECIALTY SECTION
This article was submitted to Medicinal and Pharmaceutical Chemistry, a section of the journal Frontiers in Chemistry

RECEIVED 10 November 2022
ACCEPTED 19 December 2022
PUBLISHED 06 January 2023

CITATION
Zheng W, Tu B, Zhang Z, Li J, Yan Z, Su K, Deng D, Sun Y, Wang X, Zhang B, Zhang K, Wong W-L, Wu P, Hong WD and Ang S (2023), Ligand and structure-based approaches for the exploration of structure–activity relationships of fusidic acid derivatives as antibacterial agents. *Front. Chem.* 10:1094841. doi: 10.3389/fchem.2022.1094841

Ligand and structure-based approaches for the exploration of structure–activity relationships of fusidic acid derivatives as antibacterial agents

Wende Zheng[1,2], Borong Tu[1,2], Zhen Zhang[1,2], Jinxuan Li[1,2], Zhenping Yan[1,2], Kaize Su[1,2], Duanyu Deng[1,2], Ying Sun[1,2], Xu Wang[1,2], Bingjie Zhang[3], Kun Zhang[1,2], Wing-Leung Wong[4], Panpan Wu[1,2]*, Weiqian David Hong[1,2]* and Song Ang[1,2]*

[1]School of Biotechnology and Health Sciences, Wuyi University, Jiangmen, China, [2]International Healthcare Innovation Institute, Jiangmen, China, [3]School of Biomedicine and Pharmaceutical Sciences, Guangdong University of Technology, Guangzhou, China, [4]The State Key Laboratory of Chemical Biology and Drug Discovery, Department of Applied Biology and Chemical Technology, The Hong Kong Polytechnic University, Hung Hom, Kowloon, Hong Kong SAR, China

Introduction: Fusidic acid (**FA**) has been widely applied in the clinical prevention and treatment of bacterial infections. Nonetheless, its clinical application has been limited due to its narrow antimicrobial spectrum and some side effects.

Purpose: Therefore, it is necessary to explore the structure–activity relationships of **FA** derivatives as antibacterial agents to develop novel ones possessing a broad antimicrobial spectrum.

Methods and result: First, a pharmacophore model was established on the nineteen **FA** derivatives with remarkable antibacterial activities reported in previous studies. The common structural characteristics of the pharmacophore emerging from the **FA** derivatives were determined as those of six hydrophobic centers, two atom centers of the hydrogen bond acceptor, and a negative electron center around the C-21 field. Then, seven **FA** derivatives have been designed according to the reported structure–activity relationships and the pharmacophore characteristics. The designed **FA** derivatives were mapped on the pharmacophore model, and the Qfit values of all **FA** derivatives were over 50 and **FA-8** possessed the highest value of 82.66. The molecular docking studies of the partial target compounds were conducted with the elongation factor G (EF-G) of *S. aureus*. Furthermore, the designed **FA** derivatives have been prepared and their antibacterial activities were evaluated by the inhibition zone test and the minimum inhibitory concentration (MIC) test. The derivative **FA-7** with a chlorine group as the substituent group at C-25 of **FA** displayed the best antibacterial property with an MIC of 3.125 μM. Subsequently, 3D-QSAR was carried on all the derivatives by using the CoMSIA mode of SYBYL-X 2.0.

Conclusion: Hence, a computer-aided drug design model was developed for **FA**, which can be further used to optimize **FA** derivatives as highly potent antibacterial agents.

KEYWORDS

fusidic acid, derivatives, pharmacophore model, antibacterial, structure–activity relationships

1 Introduction

Fusidic acid (FA), a typical antibiotic with excellent bioactivity against *Staphylococcus aureus* including the strain that produced cross resistance with other antibiotics, has been applied in clinical therapy since the 1960s (Collignon and Turnidge, 1999; Turnidge, 1999). The study on the antibacterial mechanism of **FA** showed that the elongation factor G (EF-G) of the bacteria was interfered and the production of bacterial proteins was inhibited (Tanaka et al., 1968; Bodley et al., 1969). Accordingly, the relevant protein of the EF-G has always been implemented as a target acceptor in the development of **FA**-type antibiotics (Borg et al., 2015; Belardinelli and Rodnina, 2017; Lu et al., 2019). However, the narrow antibacterial spectrum of **FA**, which merely possessed the activity against Staphylococci, limited its practical application in extensive medical treatment (Petrosillo et al., 2018). Therefore, it became increasingly important to design and synthesize new **FA** derivatives to explore a broad range of relationships between structures and antibacterial activity. According to the literature, the structure–activity relationships (SARs) between **FA** derivatives and antibacterial activity have been studied (Godtfredsen et al., 1965; Von Daehne et al., 1979; Duvold et al., 2001). The reported SAR demonstrated that the hydroxyl group at C-3 played a crucial role in drug activity. As a recent study showed blocking the metabolic sites (21-COOH and 3-OH) of **FA** and its derivatives could maintain the antibacterial activity with a prolonged half-life (Lu et al., 2019). Moreover, it has been reported that the hydroxylation at C-27 of **FA** and its derivatives could significantly cause the vanishment of the antibacterial activity (Ragab et al., 2020). Hence, the further SARs of **FA** should be obtained through more designed derivatives and their bioassay tests.

Nowadays, computer-aided drug design (CADD) has become an integral component involving drug discovery and development since it has enormous leverage as an auxiliary tool to raise economic efficiency and reduce time costs (Cerqueira et al., 2015). Advanced rational design techniques combined with computational methodologies have been utilized to create more effective and creative medications (Fjell et al., 2012; Cardoso et al., 2019). The rational design of innovative pharmaceuticals, with the aim of creating pharmaceutical products with more specificity by calculated simulation, has emerged as a crucial aspect of medicinal chemistry (Mouchlis et al., 2020). Pharmacophore-based and docking-based screening are two classic CADD approaches, which were usually applied in virtual screening to select the potential bioactive derivatives (Niu et al., 2012; Sangeetha et al., 2017). Recently, the discovery of a novel drug has benefited greatly from the use of pharmacophore-based virtual screening (PBVS), especially when there is a lack of information regarding the three-dimensional structure of the desired protein target (Sharma et al., 2020; Zhu et al., 2020). In addition, the investigation of the comparison showed that the result of the pharmacophore-based method had higher accuracy than the docking-based method in the experiment (Chen et al., 2009; Talambedu et al., 2017).

In this study, a pharmacophore model has been constructed to design the **FA** derivatives and molecular docking was used to predict the interactions between **FA** derivatives and the target protein EF-G. The antibacterial activities of the **FA** derivatives were assessed by the inhibition zone test and the MIC assay. Furthermore, the quantitative structure–activity relationships (QSARs) of **FA** were investigated with a thorough inquiry according to biological test data. All in all, this study has provided a novel pharmacophore model to select antibacterial **FA** derivatives and studied the relationship between the structures and bioactivity.

2 Results and discussion

2.1 Establishment of a pharmacophore model

Based on a set of **FA** derivatives with remarkable antibacterial activity reported in previous studies (Godtfredsen et al., 1966; Riber et al., 2006; Lv et al., 2017; Kong et al., 2018; Salimova et al., 2018; Singh et al., 2020), a pharmacophore model was established to gain an insight into the necessary features for designing antibacterial agents. A total of 19 **FA** derivatives selected from the literature reports were aligned by using the GALAHAD module of SYBYL-X 2.0. The assessment parameters generated by two similar models are shown in Table 1, including data of specificity, N-hits, feats, energy, sterics, H-bond, and Mo-Qry. The specificity data of the model, which is a logarithmic indicator of the expected discrimination of each query, are determined by the number of features they contain and the extent of dissociation. Identical specificity values of 5.70 indicated that the two models could come to an anticipant result. Moreover, the model had nine pharmacophore features, i.e., six hydrophobic centers (HYs), two H-bond acceptors, and a negative center (NC) (Figure 1). The hydrophobic centers were distributed in the indole ring and the FA skeleton frame aromatic ring, two H-bond acceptors were found in the carbonyl group and the ester group, and the negative center was distributed in the carboxyl group of the FA derivatives at C-21, which sketched the common structural characteristics of pharmacophore emerging from the FA derivatives with antibacterial activity.

2.2 Design and validation of the derivatives

Seven **FA** derivatives were conceived according to the reported structure–activity relationships and the characteristics of the pharmacophore model by modifying the C-3, C-21, and C-25 positions of **FA**. The designed **FA** derivatives were validated by

TABLE 1 Assessment parameters of the pharmacophore theory produced by the GALAHAD module.

Model	Specificity	N-hits	Feats	Energy	Sterics	H-bond	Mo-Qry
1	5.70	19	9	21.28	24,609.90	741.20	169.84
2	5.70	19	9	21.28	24,609.90	741.20	169.84

N-hits, actual number hit; feats, total number of features in the model query; energy: the total energy of the model; sterics, steric overlap for the model; H-bond, pharmacophoric concordance; Mo-Qry, the agreement between the query tuplet and the pharmacophoric tuplet for the ligands as a group.

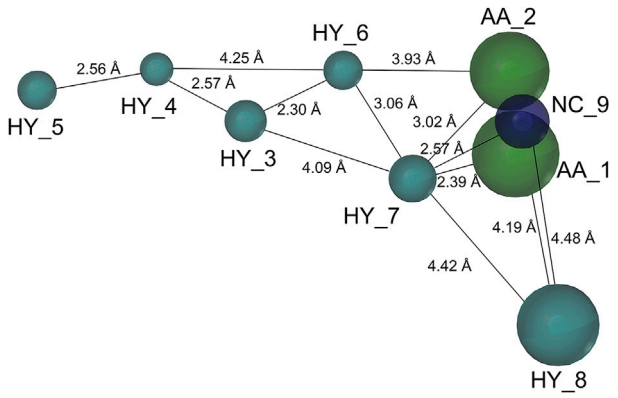

FIGURE 1
Map of a common feature pharmacophore model. AA, the atom center of the hydrogen bond acceptor; HY, hydrophobic group; and NC, negative center.

analyzing the matching degree with the pharmacophore model through the Qfit value. The values of all derivatives were over 50 and **FA-8** possessed the highest Qfit value of 82.66, which indicated that the design of the derivative was reasonable and the designed **FA** derivatives possessed potential antimicrobial activity. The structures, molecular surface lipophilic potential photographs, and Qfit values of derivatives are shown in Table 2. There was still high hydrophobic potential maintained in the C-25 position when methyl was converted into an object of low-size profile, such as hydrogen, chlorine, and bromine. Additionally, strong negative electrical potential in the C-21 position field was not significantly altered by the creation of the lactonic ring. The aim of modification at C-3 was to maintain and even strengthen the lipophilic tendency within this range of the **FA** skeleton frame.

2.3 Molecular docking

The previous study reported that **FA** was considered as an antibiotic by interfering with the EF-G of *S. aureus* (Chen et al., 2010). Therefore, it was applied therapeutically to treat Gram-positive bacterial infections, such as *S. aureus* (Lannergård et al., 2009). As shown in Figure 2, the target derivatives **FA-8**, **9**, **20**, and **22** were docked to the EF-G to investigate the action between the molecular and the receptor protein. The results showed that the interactions between the carboxyl groups of **FA** derivatives and the binding pockets existed. Compound **FA-8** could engender good affinities to Ala655, Tyr668, Glu455, and Phe88 in the active site by a hydrogen bond (Figure 2A). This kind of action of the hydrogen bond existed likewise in the mode of **FA-20** and **FA-22** fitting to the protein pocket (Figures 2C, D). However, FA-9 docking results saw a massive loss of these key interactions (Figure 2B), which corresponded to the low pharmacophore score. In addition, brominated **FA-8** had a halogen bond with Asp87, and the azide group in **FA-20** formed a salt bridge with Glu93, which may be positive features to obtain better activities. The results illustrated that the molecular docking model and the pharmacophore model could not be unanimous. It was not surprising that many epactal interactions, such as hydrogen bond and halogen bond interactions, predicted by the binding model may well compensate for some losses of key interactions.

2.4 Chemistry

The previous studies put forward some enlightenment that the modification at C-25 of **FA** could be beneficial for maintaining the antibacterial effect (Riber et al., 2006; Zhao et al., 2013). A group of target **FA** derivatives (**FA-6** to **FA-8**) was synthesized, as shown in Scheme 1. The C-25 position of **FA** had been modified successfully according to the literature reports; however, there were very few modifications with simple and small-sized atoms with functional characteristics at this position that have been carried out to estimate the antibacterial activity. We have commenced with this route by preparing several vital intermediate **FA** derivatives. The **FA** triethylamine, as an acid-binding agent, and chloromethyl pivalate were dissolved in DMF and stirred overnight at 50°C. Thus, the **FA-1** was procured with protected carboxyl groups. The **FA-2** was produced by oxidation of **FA-1** with N-methyl morpholine N-oxide (NMO) in the presence of ozone at 0°C (Schwartz et al., 2006). The derivatives **FA-6**, **FA-7**, and **FA-8** were obtained through the next simple steps such as Wittig's reaction and de-esterification. To clarify the stability of the ester group at C-16 under different alkaline conditions, potassium carbonate and sodium hydroxide were used to promote the lactone reaction of **FA** and the intermediate **FA-1,** respectively. As a result, the lactone derivative **FA-9** was generated by the esterification of **FA** with sodium hydroxide. The syntheses of the derivatives (**FA-6~9**) are outlined in Scheme 1. The new **FA** derivatives were determined by using NMR, HRMS, and CHNS-O elemental analyzer.

Scheme 2 shows the syntheses of FA-17~22 and FA-24. Briefly, FA-1 was treated with the methane sulfonyl chloride and the pyridine in dichloromethane and afforded product FA-10. Subsequently, on one hand, the methane sulfonyloxy in FA-10 was replaced by the azide group, phenylamino group, and halogens to afford FA-11~16, respectively. On the other hand, methane sulfonyloxy was reduced into a double bond in the positions of C-3 and C-4 to give FA-23. Finally, all the culminating products (FA-17~22 and FA-24) were obtained by deblocking the protected ester at the C-21 position with potassium carbonate as the base reagent according to the ester stability experiment of FA derivatives. In this procedure, the related derivatives were identified mainly by HRMS.

2.5 Biological evaluation

2.5.1 Inhibition zone test

As shown in Table 3, the antibacterial activities of the **FA** derivatives were assessed using the inhibition zone test. Compound **FA-6** possessed remarkable activity against Gram-positive germs with the corresponding inhibition zone diameters of 18.89 ± 0.03, 19.72 ± 0.12, and 14.96 ± 1.21 mm in a relatively low dosage (0.83 nmol). As the dosage increased, **FA-17~22** and **FA-24** displayed obvious inhibition zones against Gram-positive bacteria. However, there was no sign for all target derivatives to inhibit Gram-negative germs in this test.

2.5.2 The minimum inhibitory concentration (MIC) test

Thenceforward, the MIC test was carried out to evaluate the antibacterial effect of the **FA** derivatives. As shown in Table 4, the C-25 positions of the **FA** derivatives were altered chemically with the halogen and hydrogen groups and the derivatives maintained the bioactivity against Gram-positive bacteria. **FA-7** with a chlorine group as the substituent group at C-25 displayed the best medicinal property

10.3389/fchem.2022.1094841

TABLE 2 Structure of the designed derivatives and the Qfit values.

Compound	Chemical structure	Molecular surface lipophilic potential	Qfit
FA-6	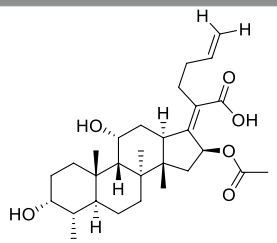	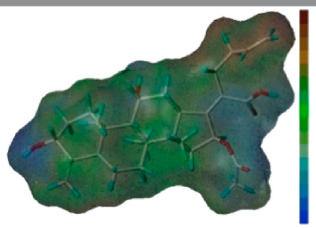	81.83
FA-7	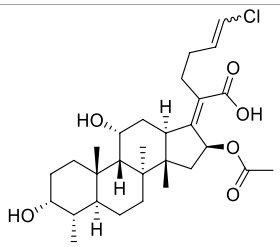	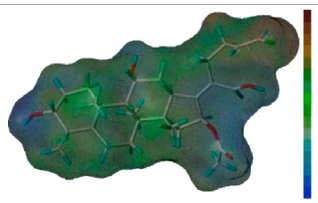	81.92
FA-8	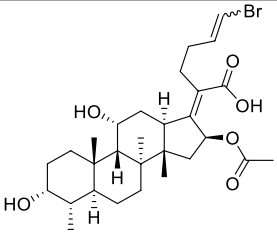	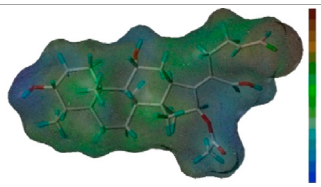	82.66
FA-9	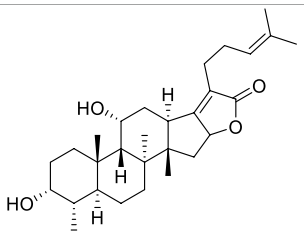		54.45
FA-20	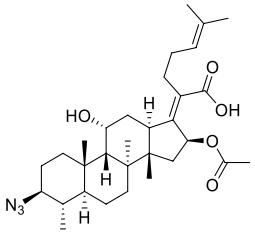	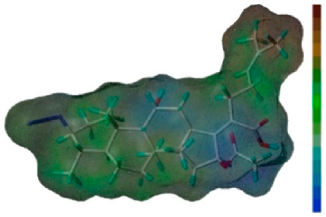	79.98
FA-22	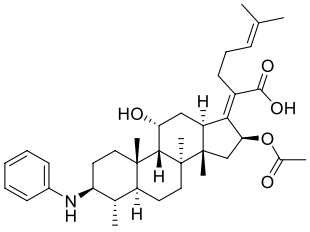	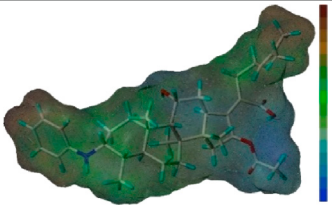	50.67

(Continued on following page)

10.3389/fchem.2022.1094841

TABLE 2 (*Continued*) **Structure of the designed derivatives and the Qfit values.**

Compound	Chemical structure	Molecular surface lipophilic potential	Qfit
FA-24	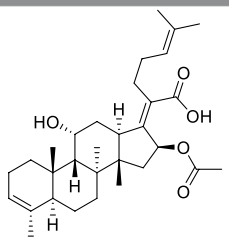	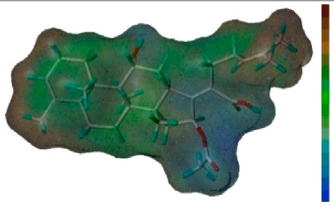	56.29

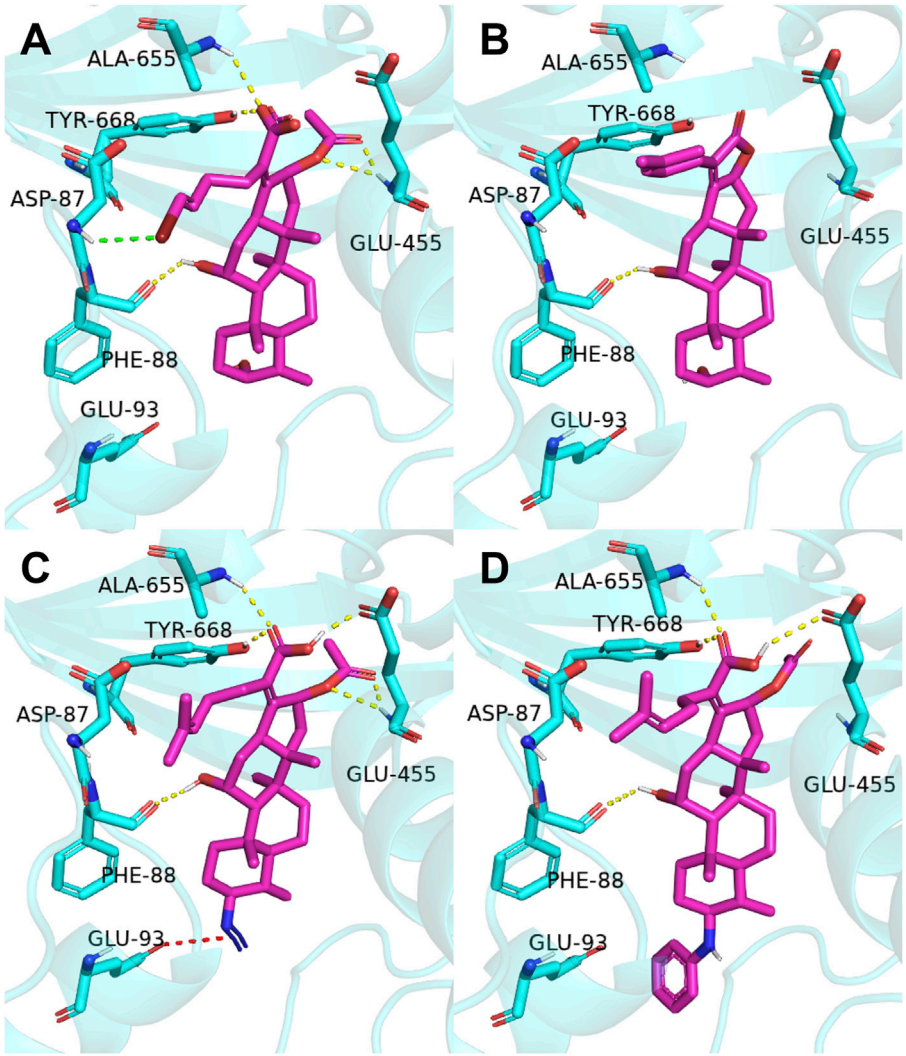

FIGURE 2
Binding mode of four derivatives in the *S. aureus* EF-G pocket: **(A) FA-8**; **(B) FA-9**; **(C) FA-20;** and **(D) FA-22**. The relevant ligand molecules were colored by magenta, and the vital amino acid was colored by cyan. The red color dash indicated the salt bridge force; the yellow color dash indicated the hydrogen bond; and the green color indicated the halogen bond interaction.

with a MIC of 3.125 μM. None of the intermediates showed any antibacterial activity in this assay. Simultaneously, it was noteworthy that esterification at C-21 resulted in the complete loss of activity. Therefore, the integrity of carboxyl at C-21 was indispensable for the preservation of activity. Additionally, the results of the bioassay showed that **FA-20**, **FA-21**, and **FA-22** possessed weaker antimicrobial activity than those owned by the halogen groups. Therefore, the existence of the halogen groups was much more conducive to antibacterial activity.

10.3389/fchem.2022.1094841

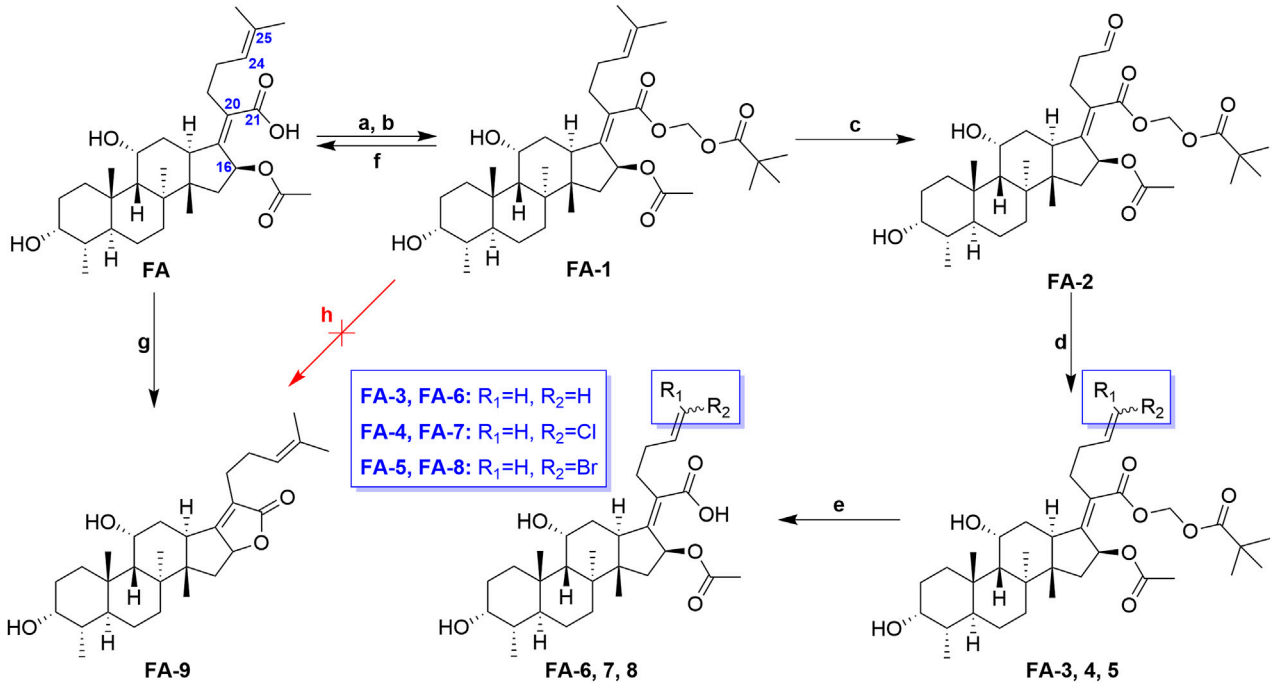

SCHEME 1
Synthetic route of **FA-6~9**. Reagents and conditions: **(A)** DMF, Et_3N (1.3 eq.), 30 min; **(B)** $tBuCO_2CH_2Cl$, overnight, 50°C; **(C)** O_3, NMO (1 eq.), DCM, 0°C; **(D)** Wittig's reaction; **(E)** K_2CO_3 (2 eq.), methanol, r. t., 1 h; **(F)** K_2CO_3 (2 eq.), methanol, r. t., overnight; **(G)** 2 N NaOH (5 eq.), ethanol, refluxed, overnight; and **(H)** K_2CO_3 (2 eq.), methanol, r. t., overnight.

2.6 Quantitative structure–activity relationship (QSAR)

Based on the pMIC (negative logarithm of the MIC) values of the synthesized **FA** derivatives, a comparative molecular similarity index analysis (CoMSIA) model was constructed to explore the structure–activity relationship of the constructed **FA** derivatives against *S. aureus*. Cross-validated coefficients (q2), non-cross-validated correlation coefficients (r^2), standard error of estimates, and F-test values F) were 0.55, 0.921, 0.167, and 110.547 in the constructed CoMSIA model, respectively. The obtained q^2 and r^2 values were in the range of the internal validations ($q^2 > 0.5$ and $r^2 > 0.8$), which indicated that the predictive accuracy of the constructed 3D-QSAR models was credible. The results displayed a linear relationship between the experimental and predicted values as shown in the scatter plot (Figure 3A). As shown in Figure 3B, the aligned compounds were imported into Phase to make partial least-squares (PLS). The model was then used to correlate the activities of these compounds with the Phase field data calculated from their 3D structures. The steric contour map of CoMSIA is given in Figure 3C, and the result suggested that the larger the size of substituents at C-3, C-21, and C-25 positions, the stronger will be the antibacterial activity of derivatives. The electrostatic contour map in Figure 3D shows that the introduction of the atom with high electrostatic potential at C-21 and C-25 would be beneficial to improve the antibacterial activity of derivatives. In addition, the hydrophobic group and the group of hydrogen bond acceptors at C-3 and C-21 positions would contribute to enhanced antibacterial activities, as shown in Figures 3E, F. Overall, the presences of halogen groups at the positions C-3 and C-25 were more advantageous for maintaining antibacterial activity than **FA**.

3 Materials and methods

3.1 Generation of the pharmacophore model and design of derivatives

The pharmacophore model was constructed using the Genetic Algorithm with Linear Assignment of Hypermolecular Alignment of Database (GALAHAD) module of SYBYL-X 2.1 software (Tripos Inc., St. Louis, MO, United States), and two similar models with varied parameters including specificity, N-hits, feats, and energy were first generated by setting 2, 5, and 4 for the parameters of population size, maximum generation, and mols, respectively. The pharmacophore model that was suitable for screening should basically meet the following requirements: specificity >4, N-hits (the number of compounds used for the construction), and relatively low energy that indicated stability. A decoy set method was then applied to evaluate the quality of the model. The decoy set in this study was composed of 19 **FA** derivatives with notable antibacterial activities taken from the published literature reports, as shown in Table 5. Following the creation of the pharmacophore models, the most effective model was carried out and a 3D search query was applied for the designed derivatives. Then, a column of Qfit parameters was loaded with the **FA** derivatives. Qfit is a value between 0 and 100, where 100 is the best. It represents how close the ligand atoms of the compounds match the query target coordinates. Meanwhile, the Qfit values for derivatives were shown to assess the degree of correlation with antibacterial activity. In this study, the minimum standard value of Qfit was first set to 50, and seven compounds with Qfit values of more than 50 were obtained.

10.3389/fchem.2022.1094841

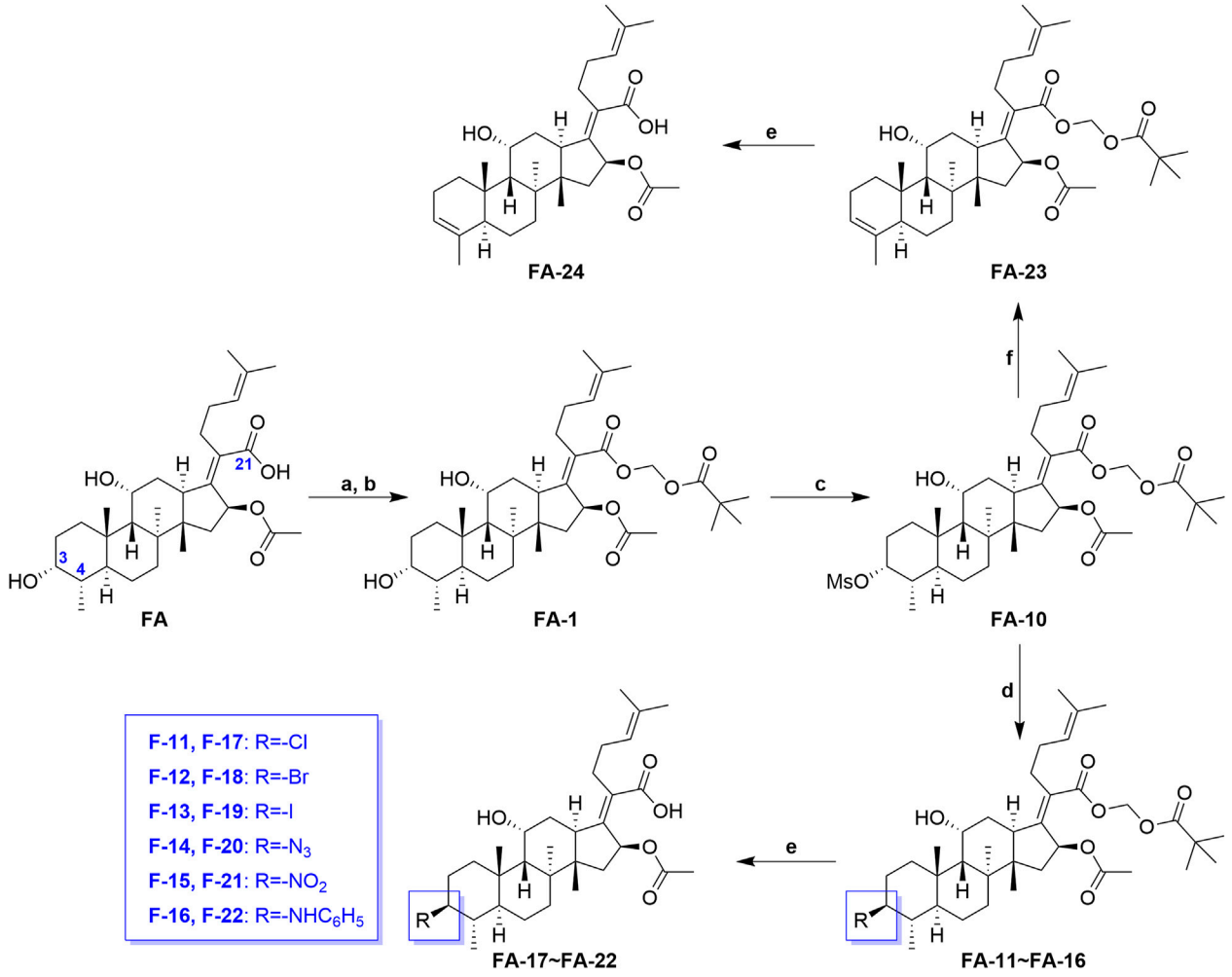

SCHEME 2
Synthetic route of **FA-17~22** and **FA-24**. Reagents and conditions: **(A)** DMF, Et_3N (1.3 seq.), 30 min; **(B)** $tBuCO_2CH_2Cl$, overnight, 50°C; **(C)** pyridine (2 eq.), methane sulfonyl chloride (5 eq.), DCM, overnight; **(D)** tetrabutylammonium chloride/bromide/iodide/nitrite/sodium azide (2 eq.), THF, reflux, overnight; **(E)** K_2CO_3 (2 eq.), methanol, r. t., 1 h; **(F)** 2,6-lutidine, 130°C, 2 h.

3.2 Molecular docking

To anticipate the ligand–receptor interactions, molecular docking experiments were conducted using SYBYL-X 2.0 software. The target protein EF-G (PDB: 2XEX) of *S. aureus* was selected as a receptor to bind the derivatives, and several significant residues were identified as the active protein pocket. The **FA**-binding site was bordered by Arg464, His457, Leu456, Thr436, Asp434, and Phe88, which created a specific cavity. All the hydrogens were added to EF-G in the structural model to improve the quality of the model. The Tripos force field and Gasteiger–Huckel charges were assigned for the EF-G and **FA** derivatives, respectively. After docking, the ligand–receptor complexes were opened in PyMol software for the visualizer to analyze the interaction.

3.3 Materials

All reagents were purchased from commercial suppliers of Adamas Reagent Ltd. (Shanghai, China) in analytical reagent grade and were used directly without further purification. Flash chromatography was carried out with silica gel (200–300 mesh) which was supplied by Innochem Co., Ltd. (Beijing, China). Analytical TLC was performed on pre-coated silica gel F254 plates (0.25 mm; E. Merck), and the products were visualized by UV detection or treated with an ethanolic solution of p-anisaldehyde spray followed by heating. The derivatives of **FA** were characterized by ^{1}H NMR, ^{13}C NMR, HRMS, and elemental analysis. The antibacterial activity was assayed by using a multi-model plate reader (Infinite 200).

3.4 Synthesis chemistry

3.4.1 21-Fusidic acid (pivaloyloxymethyl) ester (FA-1, $C_{37}H_{58}O_8$)

First, chloromethyl pivalate (1.52 ml; 9.062 mmol) was added to the solution of **FA** (2 g; 4.513 mmol) in dry N, N-dimethylformamide (30 ml) at room temperature for 10 min. This was followed by drop-wise addition of triethylamine (0.7 mL; 5.890 mmol). The resulting reaction mixture was stirred at 50°C overnight. After completion of the reaction (TLC), the mixture was diluted with EtOAc and washed with

TABLE 3 The inhibition zone test of FA and its derivatives against bacterial strains.

Compound	Dosage (nmol)	Diameters of inhibition zones (mm)[a]				
		Staphylococcus aureus ATCC 6538	*Staphylococcus albus* ATCC 29213	*Staphylococcus epidermidis* ATCC 12228	*Escherichia coli* CMCC 44102	*Salmonella typhimurium* CMCC 50115
FA	0.12	20.31 ± 0.34	19.43 ± 0.42	19.91 ± 0.20	<6	<6
FA-1~2	100	<6	<6	<6	<6	<6
FA-3~5	—[b]	—	—	—	—	—
FA-6	0.83	18.89 ± 0.03	19.72 ± 0.12	14.96 ± 1.21	<6	<6
FA-7	5	26.00 ± 1.24	24.64 ± 0.56	25.89 ± 0.99	<6	<6
FA-8	5	25.68 ± 1.04	25.84 ± 0.88	27.27 ± 0.81	<6	<6
FA-9~16	25	<6	<6	<6	<6	<6
FA-17	25	13.63 ± 0.10	16.91 ± 0.38	15.38 ± 0.60	<6	<6
FA-18	25	19.65 ± 0.05	21.69 ± 0.27	20.49 ± 0.50	<6	<6
FA-19	25	18.55 ± 1.86	18.79 ± 1.23	19.25 ± 0.68	<6	<6
FA-20	25	11.55 ± 0.02	12.88 ± 0.21	10.19 ± 0.57	<6	<6
FA-21	25	9.63 ± 0.45	9.20 ± 0.26	8.05 ± 0.21	<6	<6
FA-22	25	14.42 ± 1.32	16.80 ± 1.23	12.22 ± 0.89	<6	<6
FA-23	—	—	—	—	—	—
FA-24	25	12.64 ± 1.16	15.56 ± 0.89	16.23 ± 0.98	<6	<6
Gatifloxacin	1	19.12 ± 0.73	17.13 ± 0.64	18.67 ± 0.25	NT[c]	NT

[a]No diameter of diffusion was determined.
[b]Not detected.
[c]Not tested. Gatifloxacin was used as a positive control.

water. The EtOAc layer was then dried over anhydrous sodium sulfate, filtered, and concentrated *in vacuo*. The crude product was purified by column chromatography using n-hexane: ethyl acetate = 1: 4 as the eluent, affording the target compound as a white solid (1.62 g; 81%). Mp: 76°C–78°C. ^{1}H NMR (400 MHz, $CDCl_3$) δ 7.27 (s, 1H), 5.86 (d, J = 8.3 Hz, and 1H), 5.74 (dd, 2H), 5.08 (t, J = 7.0 Hz, and 1H), 4.34 (s, 1H), 3.74 (d, J = 8.3 Hz, and 1H), 3.05 (d, J = 11.1 Hz, and 1H), 2.54–2.36 (m, 2H), 2.31 (d, J = 14.1 Hz, and 1H), 2.25–2.06 (m, 4H), 1.98 (s, 3H), 1.93–1.79 (m, 2H), 1.79–1.70 (m, 2H), 1.67 (s, 3H), 1.61–1.47 (m, 8H), 1.37 (s, 3H), 1.29 (t, J = 16.0, 7.6 Hz, and 2H), 1.21 (s, 9H), 1.18–1.02 (m, 2H), 0.97 (s, 3H), 0.90 (d, J = 16.7, 7.5 Hz, and 6H). ^{13}C NMR (100 MHz, $CDCl_3$) δ 176.0, 171.3, 169.1, 151.9, 131.6, 128.3, 123.9, 79.8, 74.3, 71.4, 68.2, 49.2, 48.8, 44.3, 39.4, 39.0, 38.8, 37.1, 36.2, 36.2, 35.6, 32.4, 30.3, 30.0, 28.8, 28.2, 26.9, 25.7, 24.2, 22.8, 20.8, 20.8, 17.9, 17.8, 15.9. Anal. calcd. for $C_{37}H_{58}O_8$: C 70.44, H 9.27; found: C 69.81, H 9.32. HRMS (ESI): $C_{37}H_{58}O_8Na$ (653.4029) $[M + Na]^+$ = 653.4027.

3.4.2 24-Oxo-21-fusidic acid (pivaloyloxymethyl) ester (FA-2, $C_{34}H_{52}O_9$)

In a 50-mL round-bottom flask, **FA-1** (100 mg; 0.166 mmol) was dissolved in dichloromethane (5 mL). Then NMO (18.56 mg; 0.249 mmol) and OsO_4 (0.9 μL, 0.0166 mmol, and 0.1 eq.) in MeCN were added, respectively. The solution of 2% O_3/O_2 (nominal output of 1 mmol O_3/min) was introduced directly above the solution *via* a glass pipet for 6.6 min (nominally 2.2 equiv ozone relative to alkene) at 0°C for 1 h. The reaction was then quenched by the addition of 10 mL of saturated sodium thiosulfate. The reaction was stirred for an additional 45 min and then concentrated *in vacuo* to remove dichloromethane. Subsequently, EtOAc and brine were added, and the layers were separated. The aqueous layer was extracted with EtOAc. The combined organic layers were dried over anhydrous sodium sulfate, filtered, and concentrated *in vacuo*. The crude product was purified by flash chromatography using an eluent (n-hexane: ethyl acetate = 3: 2, V: V). **FA-2** as a white solid was obtained. Yield: 90%. ^{1}H NMR (400 MHz, $CDCl_3$) δ 9.76 (s, 1H), 5.96 (d, J = 8.4 Hz, 1H), 5.74 (dd, J = 28.0, 5.4 Hz, 2H), 4.35 (s, 1H), 3.71 (d, J = 2.0 Hz, 1H), 3.10 (d, J = 10.6 Hz, 1H), 2.75–2.46 (m, 5H), 2.39–2.24 (m, 2H), 2.18 (d, J = 3.9 Hz, 2H), 1.98 (s, 3H), 1.90–1.40 (m, 8H), 1.36 (s, 3H), 1.28 (dd, J = 12.2, 11.0 Hz, 2H), 1.21 (s, 9H), 1.17–1.03 (m, 2H), 0.97 (s, 3H), 0.90 (d, J = 6.4 Hz, 6H). ^{13}C NMR (100 MHz, $CDCl_3$) δ 201.2, 177.1, 170.1, 167.4, 153.2, 127.1, 79.9, 74.2, 71.4, 67.9, 49.4, 48.8, 44.6, 43.8, 39.5, 38.8, 38.7, 36.8, 36.6, 35.5, 35.3, 31.3, 30.9, 29.8, 26.8, 23.6, 23.4, 21.3, 21.1, 20.8, 17.7, and 16.0. HRMS (ESI): $C_{34}H_{52}O_9Na$ (627.3509) $[M + Na]^+$ = 627.3503.

3.4.3 24-Ene-21-fusidic acid (pivaloyloxymethyl) ester (FA-3, $C_{35}H_{54}O_8$)

A solution of methyltriphenylphosphonium bromide (389.04 mg; 1.09 mmol) and potassium tert-butoxide (122.2 mg, 1.09 mol) was added to the mixture of **FA-2** (441.49 mg, 0.73 mol) in 20 mL of toluene under nitrogen. The reaction was kept refluxed overnight and monitored by TLC. After completion of the reaction (TLC), the mixture was diluted with EtOAc and washed with water. The EtOAc layer was

TABLE 4 MICs of FA and its derivatives against the bacterial strains.

Compound	MICs (μM)[a]				
	S. aureus ATCC 6538	S. *albus* ATCC 29213	S. *epidermidis* ATCC 12228	*E. coli* CMCC 44102	*S. typhimurium* CMCC 50115
FA	3.125	3.125	3.125	>200	>200
FA-1~FA-2	>200	>200	>200	>200	>200
FA-3~FA-5	—[b]	—	—	—	—
FA-6	20.84	10.41	20.84	>200	>200
FA-7	6.25	3.125	3.125	>200	>200
FA-8	12.5	12.5	6.25	>200	>200
FA-9~16	>200	>200	>200	>200	>200
FA-17	25	12.5	25	>200	>200
FA-18	25	6.25	6.25	>200	>200
FA-19	25	12.5	25	>200	>200
FA-20	100	100	100	>200	>200
FA-21	100	100	100	>200	>200
FA-22	100	50	50	>200	>200
FA-23	>200	>200	>200	>200	>200
FA-24	50	25	50	>200	>200
Gatifloxacin	0.2	0.2	0.2	NT[c]	NT

[a]MIC values in the experiment were performed in triplicate.
[b]Not detected.
[c]Not tested. Gatifloxacin was used as a positive control.

then dried over anhydrous sodium sulfate, filtered, and concentrated *in vacuo*. The crude product was purified by flash chromatography using an eluent (n-hexane: ethyl acetate = 3: 2, V: V). **FA-3** as a white solid was obtained. Yield: 75%. Anal. calcd. for $C_{35}H_{54}O_8$: C 69.74, H 9.03; found: C 68.93, H 8.96. HRMS (ESI): $C_{35}H_{54}O_8Na$ (625.3716) $[M + Na]^+$ = 625.3709 (Zhao et al., 2016).

3.4.4 (E)-25-chlorohexa-24-ene-21-fusidic acid (pivaloyloxymethyl)ester (FA-4, $C_{35}H_{53}ClO_8$)

A solution of **FA-2** (200 mg, 0.34 mmol) and (chloromethyl) triphenylphosphonium chloride (212 mg, 0.68 mmol) in anhydrous tetrahydrofuran (15 mL) was cooled to 0°C under nitrogen for 15 min, and then n-butyllithium (416.7 μL) dissolved in n-hexane (0.68 mmol, 1.6 mol/L) was added drop-wise above the solution and stirred at 0°C for 30 min. After completion of the reaction (TLC), the mixture was diluted with EtOAc and washed with water. The EtOAc layer was then dried over anhydrous sodium sulfate, filtered, and concentrated *in vacuo*. The crude product was purified by flash chromatography using an eluent (n-hexane: ethyl acetate = 3: 2, V: V). **FA-4** as a white solid was obtained. Yield: 43% (Zhao et al., 2016).

3.4.5 (E)-25-bromohexa-24-ene-21-fusidic acid (pivaloyloxymethyl)ester (FA-5, $C_{35}H_{53}BrO_8$)

A solution of **FA-2** (200 mg, 0.34 mmol) and (bromomethyl) triphenylphosphonium bromide (296.7 mg, 0.68 mmol) in anhydrous tetrahydrofuran (15 mL) was cooled to 0°C under nitrogen for 15 min, and then, n-butyllithium (416.7 μL) dissolved in n-hexane (0.68 mmol, 1.6 mol/L) was added drop-wise above the solution and stirred at 0°C for 30 min. After completion of the reaction (TLC), the mixture was diluted with EtOAc and washed with water. The EtOAc layer was then dried over anhydrous sodium sulfate, filtered, and concentrated *in vacuo*. The crude product was purified by flash chromatography using an eluent (n-hexane: ethyl acetate = 3: 2, V: V). **FA-5** as a white solid was obtained. Yield: 32%. ^{1}H NMR (400 MHz, $CDCl_3$) δ 6.22–6.11 (m, 1H), 6.11–6.00 (m, 1H), 5.93–5.84 (m, 1H), 5.80 (dd, J = 8.9, 5.4 Hz, 1H), 5.70 (d, J = 5.4 Hz, 1H), 4.34 (s, 1H), 3.75 (s, 1H), 3.07 (t, J = 12.2 Hz, 1H), 2.64–2.44 (m, 2H), 2.42–2.05 (m, 6H), 1.98 (d, J = 1.6 Hz, 3H), 1.93–1.69 (m, 4H), 1.65–1.48 (m, 4H), 1.37 (s, 3H), 1.35–1.23 (m, 3H), 1.21 (s, 9H), 1.27–1.03 (m, 2H), 0.99 (s, 3H), and 0.92 (d, J = 6.4 Hz, 6H). ^{13}C NMR (100 MHz, $CDCl_3$) δ 177.1, 170.2, 167.7, 152.5, 136.4, 133.2, 128.2, 108.7, 105.5, 79.8, 74.3, 71.4, 68.2, 49.2, 48.9, 44.5, 39.5, 39.0, 38.8, 37.1, 36.2, 36.2, 35.7, 32.5, 30.3, 30.0, 29.8, 27.0, 26.9, 24.2, 22.7, 20.8, 20.7, 18.0, and 15.9. HRMS (ESI): $C_{35}H_{53}BrNaO_8$ (703.2822) $[M + Na]^+$ = 703.2606.

3.4.6 General procedures to produce FA-6, FA-7, and FA-8

A solution of derivatives (**FA-3**, **FA-4,** and **FA-5**, respectively; 0.0924 mmol) and potassium carbonate (25.55 mg, 0.185 mmol) in methanol was stirred at room temperature for 1 h and monitored by TLC. After completion of the reaction, the mixture was diluted with EtOAc and washed with water. The EtOAc layer was then dried over anhydrous sodium sulfate, filtered, and concentrated *in vacuo*. The crude product was

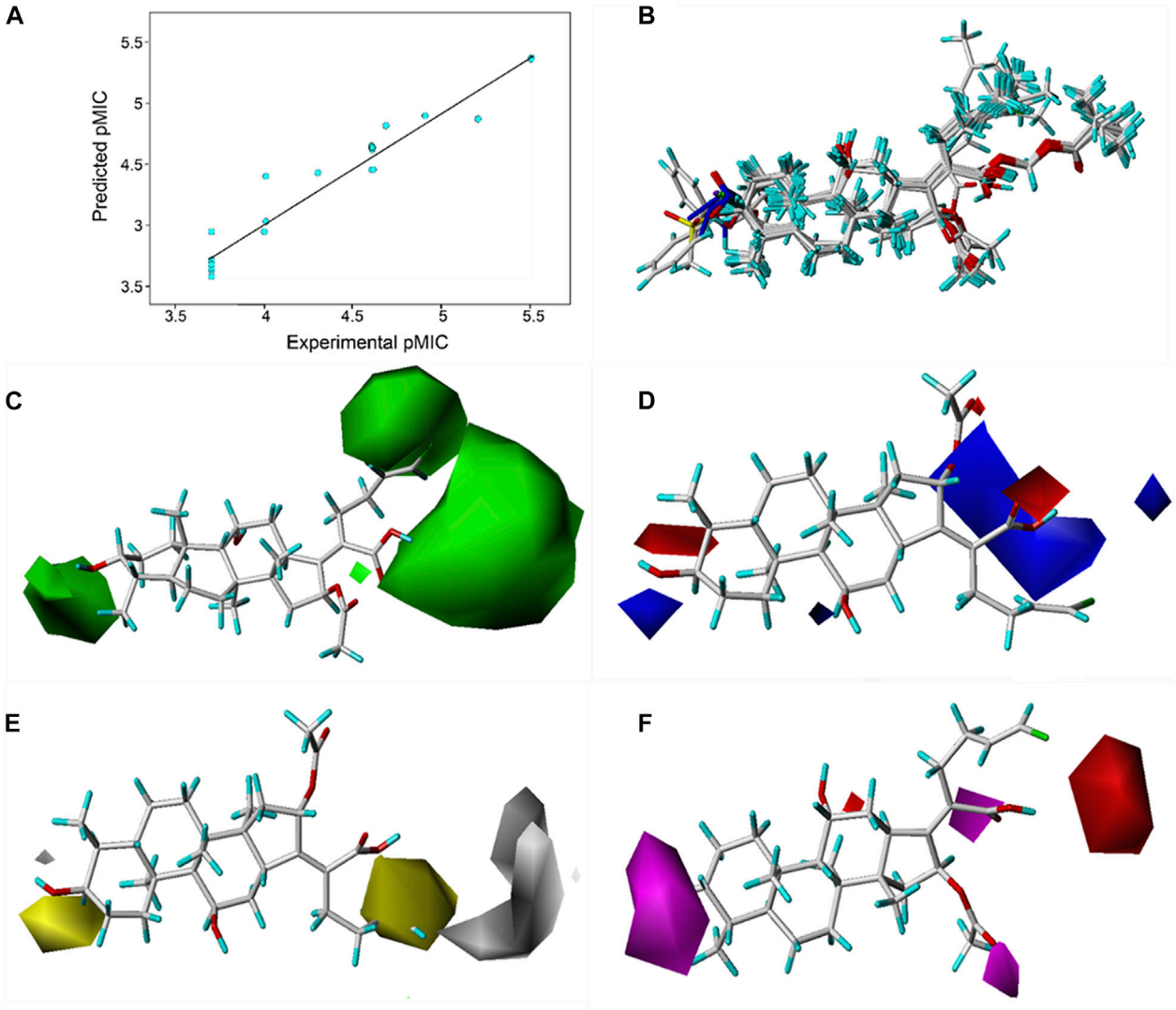

FIGURE 3
(A) Relationship between the experimental and predicted antibacterial activities by the QSAR model, pMIC = -lg MIC, showing R^2 = 0.921; **(B)** flexible alignment of derivatives shown in the stick model; **(C)** steric fields, green favorable and yellow disfavored; **(D)** Phase electrostatic fields, blue favorable and red disfavored; **(E)** hydrophobic fields, yellow favorable and white disfavored; and **(F)** H-bond acceptor fields, magenta favorable and red disfavored.

purified by flash chromatography using an eluent (n-hexane: ethyl acetate = 3: 2, V: V). **FA-6**, **FA-7**, and **FA-8** were obtained, respectively.

24-ene-Fusidic acid (**FA-6**). White solid. Yield: 55%. ^{1}H NMR (400 MHz, $CDCl_3$) δ 5.88 (d, J = 8.3 Hz, 1H), 5.86–5.73 (m, 1H), 5.04 (d, J = 17.1 Hz, 1H), 4.97 (d, J = 10.1 Hz, 1H), 4.34 (s, 1H), 3.73 (s, 1H), 3.05 (d, J = 12.0 Hz, 1H), 2.45–2.41 (m, 2H), 2.29 (d, J = 13.8 Hz, 1H), 2.24–2.03 (m, 5H), 1.99 (s, 3H), 1.84 (t, J = 13.2 Hz, 2H), 1.78–1.66 (m, 2H), 1.66–1.53 (m, 3H), 1.49 (d, J = 12.8 Hz, 1H), 1.43 (s, 1H), 1.38 (s, 3H), 1.29 (d, J = 5.6 Hz, 1H), 1.26 (s, 1H), 1.18–1.05 (m, 2H), 0.98 (s, 3H), and 0.92 (s, 6H). ^{13}C NMR (100 MHz, $CDCl_3$) δ 172.4, 171.4, 148.6, 137.6, 130.1, 115.1, 74.4, 71.4, 68.2, 49.4, 48.8, 43.9, 39.6, 38.9, 36.8, 36.6, 35.8, 35.5, 33.8, 31.8, 30.0, 29.8, 28.0, 23.6, 23.3, 21.1, 20.6, 17.6, and 15.9. Anal. calcd. for $C_{29}H_{44}O_6$: C 71.28, H 9.08; found: C 70.42, H 9.12. HRMS (TOF): $C_{29}H_{43}O_6$ (487.3060) $[M\text{-}H]^-$ = 487.3058.

(E)-25-chlorohexa-24-ene-fusidic acid (**FA-7**). White solid. Yield: 55%. ^{1}H NMR (400 MHz, $CDCl_3$) δ 6.02 (dd, J = 19.0, 10.2 Hz, 1H), 5.95–5.70 (m, 2H), 4.36 (s, 1H), 3.76 (s, 1H), 3.08 (t, J = 10.3 Hz, 1H), 2.65–2.48 (m, 2H), 2.48–2.21 (m, 3H), 2.21–2.06 (m, 3H), 1.97 (s, 3H), 1.92–1.67 (m, 4H), 1.67–1.46 (m, 4H), 1.38 (s, 3H), 1.31 (d, J = 14.3 Hz, 1H), 1.28–1.18 (m, 2H), 1.18–1.03 (m, 2H), 0.98 (s, 3H), and 0.92 (d, J = 5.4 Hz, 6H). ^{13}C NMR (100 MHz, $CDCl_3$) δ 173.9 [173.7 (for the second diastereoisomer)], 170.7, 152.44 [152.39 (for the second diastereoisomer)], 132.5 [130.2 (for the second diastereoisomer)], 128.6 [128.3 (for the second diastereoisomer)], 118.9 [118.0 (for the second diastereoisomer)], 74.44 [74.40 (for the second diastereoisomer)], 71.6, 68.2 [68.1 (for the second diastereoisomer)], 49.27 [49.26 (for the second diastereoisomer)], 48.78 [48.77 (for the second diastereoisomer)], 44.50 [44.45 (for the second diastereoisomer)], 39.5, 38.90 [38.88 (for the second diastereoisomer)], 36.9, 36.4, 36.0 [35.9 (for the second diastereoisomer)], 35.6 [35.5 (for the second diastereoisomer)], 32.08 [32.06 (for the second diastereoisomer)], 31.2 [27.9 (for the

TABLE 5 Known FA derivatives with notable antibacterial activities used to generate a pharmacophore model.

Chemical structure	MIC (reference)	Chemical structure	MIC (reference)
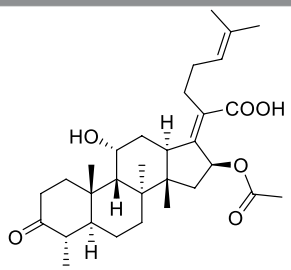	1 μg/mL (Garcia Chavez et al., 2021)	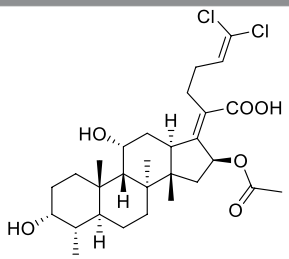	0.25 μg/mL (Garcia Chavez et al., 2021)
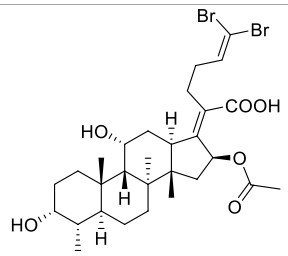	0.125 μg/mL (Garcia Chavez et al., 2021)	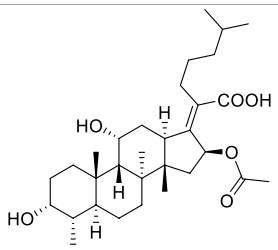	0.25 μg/mL (Garcia Chavez et al., 2021)
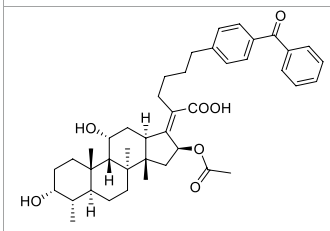	1–4 μg/mL (Riber et al., 2006)	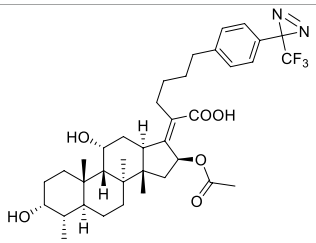	1–4 μg/mL (Riber et al., 2006)
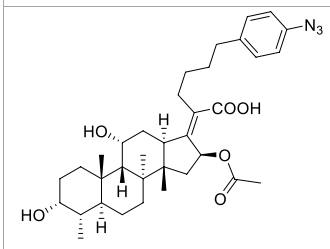	1–4 μg/mL (Riber et al., 2006)	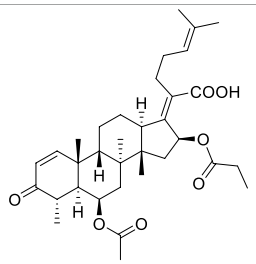	16 μg/mL (Kong et al., 2018)
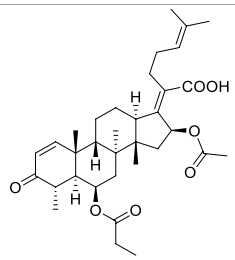	2 μg/mL (Kong et al., 2018)	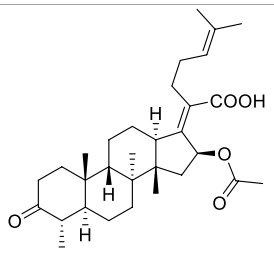	2 μg/mL (Lv et al., 2017)
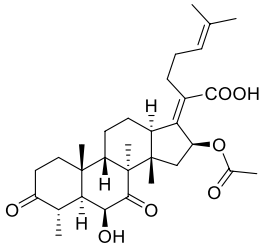	1 μg/mL (Lv et al., 2017)	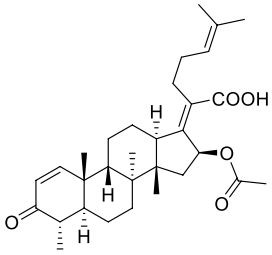	1 μg/mL (Lv et al., 2017)

(Continued on following page)

TABLE 5 (*Continued*) Known FA derivatives with notable antibacterial activities used to generate a pharmacophore model.

Chemical structure	MIC (reference)	Chemical structure	MIC (reference)
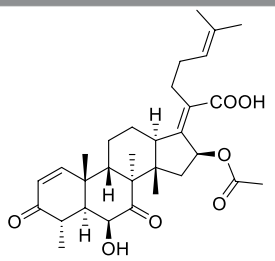	0.5 μg/mL (Lv et al., 2017)	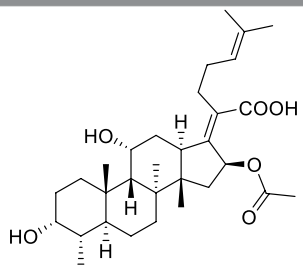	0.125 μg/mL (Garcia Chavez et al., 2021)
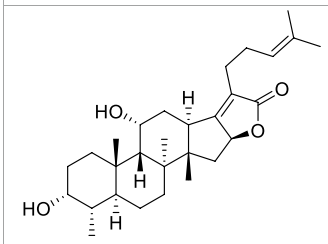	4.0μg/mL (Godtfredsen et al., 1966	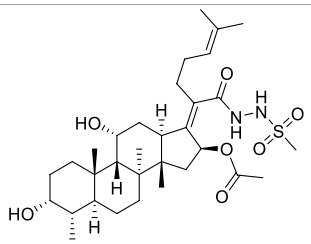	10 μM (Singh et al., 2020)
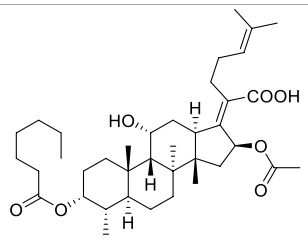	5 μM (Singh et al., 2020)	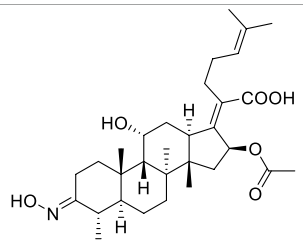	2.5 μM (Singh et al., 2020)
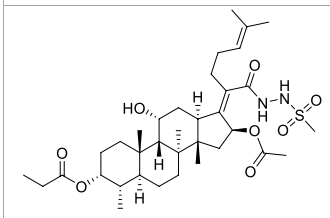	7.81 μM (Singh et al., 2020)		

second diastereoisomer)], 30.3 [30.1 (for the second diastereoisomer)], 29.8 [27.4 (for the second diastereoisomer)], 27.2 [27.0 (for the second diastereoisomer)], 24.0, 23.06 [23.03 (for the second diastereoisomer)], 20.9, 20.6, 17.9, and 16.0. Anal. calcd. for $C_{29}H_{43}ClO_6$: C 66.59, H 8.29; found: C 65.21, H 8.34. HRMS (ESI): $C_{29}H_{42}ClO_6$ (521.2670) $[M\text{-}H]^-$ = 521.2656.

(E)-25-bromohexa-24-ene-fusidic acid (**FA-8**). White solid. Yield: 80%. ^{1}H NMR (400 MHz, $CDCl_3$) δ 6.22–6.15 (m, 1H), 6.15–6.03 (m, 1H), 5.92 (d, J = 8.3 Hz, 1H), 4.35 (s, 1H), 3.76 (s, 1H), 3.08 (t, J = 12.0 Hz, 1H), 2.62–2.46 (m, 2H), 2.46–2.06 (m, 6H), 1.98 (s, 3H), 1.93–1.67 (m, 4H), 1.67–1.46 (m, 4H), 1.38 (s, 3H), 1.35–1.23 (m, 2H), 1.21 (t, J = 7.0 Hz, 1H), 1.18–1.03 (m, 2H), 0.98 (s, 3H), and 0.95–0.88 (m, 6H). ^{13}C NMR (100 MHz, $CDCl_3$) δ 173.7, 170.9, 152.3, 136.8 [133.6 (for the second diastereoisomer)], 128.9, 108.7 [105.6 (for the second diastereoisomer)], 74.5, 71.7, 68.4, 49.4, 49.0, 44.6, 39.6, 39.1, 37.1, 36.4, 36.2, 35.8, 33.2, 32.4 [30.3 (for the second diastereoisomer)], 30.2, 30.0, 27.2, 24.2, 23.0, 21.0, 20.8, 18.1, and 16.1. Anal. calcd. for $C_{29}H_{43}BrO_6$: C 61.37, H 7.64; found: C 60.41, H 7.66. HRMS (ESI): $C_{29}H_{42}{}^{79}BrO_6$ (565.2165) $[M\text{-}H]^-$ = 565.2147; $C_{29}H_{42}{}^{81}BrO_6$ (567.2144) $[M\text{-}H]^-$ = 567.2146.

3.4.7 Fusidic acid [b]furan-21-one (FA-9, $C_{29}H_{44}O_4$)

A solution of **FA** (200 mg, 0.32 mmol) and sodium hydroxide (1.95 mmol, 1.2 mL) in methanol was refluxed overnight and monitored by TLC. After completion of the reaction, 1 N hydrochloric acid was added to adjust the pH to 2–3. The mixture was diluted with EtOAc and washed with water. The EtOAc layer was then dried over anhydrous sodium sulfate, filtered, and concentrated *in vacuo*. The crude product was purified by flash chromatography using an eluent (n-hexane: ethyl acetate = 1: 1, V: V). **FA-9** as a white solid was obtained. Yield: 74%. ^{1}H NMR (400 MHz, $CDCl_3$) δ 5.11 (t, J = 6.0 Hz, 1H), 4.95 (dd, J = 10.9, 4.2 Hz, 1H), 4.39 (s, 1H), 3.75 (s, 1H), 3.53 (d, J = 11.7 Hz, 1H), 2.41–2.15 (m, 6H), 2.15–1.96 (m, 4H), 1.90–1.78 (m, 2H), 1.75 (d, J = 13.3 Hz, 1H), 1.68 (s, 3H), 1.66–1.62 (m, 1H), 1.60 (s, 3H), 1.57–1.46 (m, 6H), 1.32–1.07 (m, 4H), 0.97 (s, 3H), 0.94 (d, J = 6.7 Hz, 3H), and 0.82 (s, 3H). ^{13}C NMR (100 MHz, $CDCl_3$) δ 176.8, 169.1, 132.9, 123.6, 123.4, 82.0, 71.5, 68.0, 55.3, 50.6, 40.9, 38.3, 37.2, 36.9, 36.0, 34.2, 31.8, 31.6, 30.2, 30.0, 27.6, 25.8, 24.2, 23.5, 23.2, 21.2, 20.1, 17.9, and 16.1. Anal. calcd. for $C_{29}H_{44}O_4$: C 76.27, H 9.71; found: C 74.91, H 9.57. HRMS (TOF): $C_{29}H_{44}O_4Na$ (479.3137) $[M + Na]^+$ = 479.3136.

3.4.8 3β-(Methylsulfonyloxy)-21-fusidic acid (pivaloyloxymethyl) ester (FA-10, $C_{38}H_{60}O_{10}S$)

A solution of **FA-1** (615 mg, 0.98 mmol) and pyridine (236.8 μL, 2.4 mmol) in anhydrous dichloromethane (20 mL) was stirred at 0°C for 15 min and methane sulfonyl chloride (1.95 mmol, 151.23 μL) was added drop-wise. The reaction was stirred overnight and monitored by TLC. After completion of the reaction, 1 N hydrochloric acid was added to adjust pH to 2–3. The mixture was diluted with EtOAc and washed with water. The EtOAc layer was then dried over anhydrous sodium sulfate, filtered, and concentrated *in vacuo*. The crude product was purified by flash chromatography. **FA-10** as a white solid was obtained. Yield: 60%. HRMS (TOF): $C_{38}H_{60}O_{10}NaS$ (731.3805) $[M + Na]^+$ = 731.3812.

3.4.9 3α-Chloro-21-fusidic acid (pivaloyloxymethyl) ester (FA-11, $C_{37}H_{57}ClO_7$)

A solution of **FA-10** (100 mg, 0.141 mmol) and tetrabutylammonium chloride (78.5 mg, 0.282 mmol) in tetrahydrofuran (5 mL) was stirred at 80°C for 1 h and monitored by TLC. After completion of the reaction, the mixture was diluted with EtOAc and washed with water. The EtOAc layer was then dried over anhydrous sodium sulfate, filtered, and concentrated *in vacuo*. The crude product was purified by flash chromatography. **FA-11** as a white solid was obtained. Yield: 49.1%. HRMS (TOF): $C_{37}H_{57}O_7NaCl$ (671.3691) $[M + Na]^+$ = 671.3678.

3.4.10 3α-Bromo-21-fusidic acid (pivaloyloxymethyl) ester (FA-12, $C_{37}H_{57}BrO_7$)

A solution of **FA-10** (100 mg, 0.141 mmol) and tetrabutylammonium bromine (91.0 mg, 0.282 mmol) in dimethyl sulfoxide (5 mL) was stirred at room temperature overnight and monitored by TLC. After completion of the reaction, the mixture was diluted with EtOAc and washed with water. The EtOAc layer was then dried over anhydrous sodium sulfate, filtered, and concentrated *in vacuo*. The crude product was purified by flash chromatography. **FA-12** as a white solid was obtained. Yield: 51.0%. HRMS (ESI): $C_{37}H_{57}O_7Na^{79}Br$ (715.3171) $[M + Na]^+$ = 715.3185; $C_{37}H_{57}O_7Na^{81}Br$ (717.3177) $[M + Na]^+$ = 717.3165.

3.4.11 3α-Iodo-21-fusidic acid (pivaloyloxymethyl) ester (FA-13, $C_{37}H_{57}IO_7$)

A solution of **FA-10** (100 mg, 0.141 mmol) and tetrabutylammonium iodide (104.3 mg, 0.282 mmol) in tetrahydrofuran (5 mL) was stirred at room temperature for 6 h and monitored by TLC. After completion of the reaction, the mixture was diluted with EtOAc and washed with water. The EtOAc layer was then dried over anhydrous sodium sulfate, filtered, and concentrated *in vacuo*. The crude product was purified by flash chromatography. **FA-13** as a white solid was obtained. Yield: 40.5%. HRMS (ESI): $C_{37}H_{57}O_7NaI$ (763.3047) $[M + Na]^+$ = 763.3053.

3.4.12 3α-Azido-21-fusidic acid (pivaloyloxymethyl) ester (FA-14, $C_{37}H_{57}N_3O_7$)

A solution of **FA-10** (100 mg, 0.141 mmol) and sodium azide (18.3 mg, 0.282 mmol) in dimethyl sulfoxide (5 mL) was stirred at 90°C overnight and monitored by TLC. After completion of the reaction, the mixture was diluted with EtOAc and washed with water. The EtOAc layer was then dried over anhydrous sodium sulfate, filtered, and concentrated *in vacuo*. The crude product was purified by flash chromatography. **FA-14** as a white solid was obtained. Yield: 15.7%. HRMS (ESI): $C_{37}H_{57}N_3O_7Na$ (678.4094) $[M + Na]^+$ = 678.4101.

3.4.13 3α-Nitrohexadecahydro-21-fusidic acid (pivaloyloxymethyl) ester (FA-15, $C_{37}H_{57}NO_9$)

A solution of **FA-10** (100 mg, 0.141 mmol) and tetrabutylammonium nitrate (85.9 mg, 0.282 mmol) in dimethyl sulfoxide (5 mL) was stirred at 70°C overnight and monitored by TLC. After completion of the reaction, the mixture was diluted with EtOAc and washed with water. The EtOAc layer was then dried over anhydrous sodium sulfate, filtered, and concentrated *in vacuo*. The crude product was purified by flash chromatography. **FA-15** as a white solid was obtained. HRMS (ESI): $C_{37}H_{57}NO_9Na$ (682.3931) $[M + Na]^+$ = 682.3917.

3.4.14 3α-Phenylamino-21-fusidic acid (pivaloyloxymethyl) ester (FA-16, $C_{43}H_{63}NO_7$)

A solution of **FA-10** (100 mg, 0.141 mmol), triethylamine (28.6 mg, 0.282 mmol), and aniline (26.3 mg, 0.282 mmol) in tetrahydrofuran (5 mL) was stirred at 90°C overnight and monitored by TLC. After completion of the reaction, the mixture was diluted with EtOAc and washed with water. The EtOAc layer was then dried over anhydrous sodium sulfate, filtered, and concentrated *in vacuo*. The crude product was purified by flash chromatography. **FA-16** as a white solid was obtained. Yield: 45.2%. HRMS (ESI): $C_{43}H_{64}NO_7$ (706.4683) $[M + H]^+$ = 706.4667.

3.4.15 3-Ene-21-fusidic acid (pivaloyloxymethyl) ester (FA-23, $C_{37}H_{56}O_7$)

A solution of **FA-10** (0.759 g, 1.32 mmol, 1.0 equiv) in 2,6-lutidine (5.00 mL) was heated to 130°C and stirred at the same temperature for 2 h and monitored by TLC. Upon completion, the reaction mixture was cooled to 23°C and then concentrated directly. A white solid was obtained. Yield: 95.5%. HRMS (ESI): $C_{37}H_{56}O_7Na$ (635.3924) $[M + Na]^+$ = 635.3918.

3.4.16 General procedures to produce FA-17~FA-22 and FA-24

A solution of the derivatives (**FA-11**~**FA-16** and **FA-23**, respectively; 0.185 mmol) and potassium carbonate (25.55 mg, 0.185 mmol) in methanol (5 mL) was stirred at room temperature for 1 h and monitored by TLC. After completion of the reaction, the mixture was diluted with EtOAc and washed with water. The EtOAc layer was then dried over anhydrous sodium sulfate, filtered, and concentrated *in vacuo*. The crude product was purified by flash chromatography using an eluent (n-hexane: ethyl acetate = 1: 1, V: V). The derivatives (**FA-17~24**) were obtained, respectively.

3α-Chloro-21-fusidic acid (**FA-17**, $C_{31}H_{47}O_5Cl$). White solid, Yield: 97%. HRMS (ESI): $C_{31}H_{47}O_5NaCl$ (557.3010) $[M + Na]^+$ = 557.2997.
3α-Bromo-21-fusidic acid (**FA-18**, $C_{31}H_{47}O_5Br$). White solid. Yield: 85.5%. HRMS (ESI): $C_{31}H_{46}O_5{}^{79}Br$ (577.2529) $[M-H]^-$ = 577.2534; $C_{31}H_{46}O_5{}^{81}Br$ (579.2508) $[M-H]^-$ = 579.2522.
3α-Iodo-21-fusidic acid (**FA-19**, $C_{31}H_{47}O_5I$). White solid. Yield: 97.6%. HRMS (ESI): $C_{31}H_{46}O_5I$ (625.2390) $[M-H]^-$ = 625.2380.
3α-Azido-21-fusidic acid (**FA-20**, $C_{31}H_{47}N_3O_5$). White solid. Yield: 58.0%. HRMS (ESI): $C_{31}H_{46}N_3O_5$ (540.3437) $[M-H]^-$ = 540.3428.

3α-Nitrohexadecahydro-21-fusidic acid (**FA-21**, $C_{31}H_{48}NO_7$). White solid. Yield: 58.0%.
3α-Phenylamino-21-fusidic acid (**FA-22**, $C_{37}H_{53}NO_5$). White solid. Yield: 65.5%. HRMS (ESI): $C_{37}H_{52}NO_5$ (590.3845) $[M-H]^-$ = 590.3838.
3-Ene-21-fusidic acid (**FA-24**, $C_{31}H_{46}O_5$). White solid. Yield: 98.3%. HRMS (ESI): $C_{31}H_{46}O_5Na$ (521.3243) $[M + Na]^+$ = 521.3235.

3.5 Biological evaluation

3.5.1 Inhibition zone test

The standard agar diffusion method with a slight modification was used for the determination of the antibacterial efficacy of the **FA** derivatives (Luangtongkum et al., 2007; Gaudreau et al., 2008; Benamrouche et al., 2014). *S. aureus* (ATCC 6538), S. albus (ATCC 29213), S. epidermidis (ATCC 12228), *S. typhimurium* (CMCC 50115), and *E. coli* (CMCC 44102) were cultured in a liquid medium, Mueller–Hinton Agar (MHA), at 37°C. Bacterial suspensions of 1.5×10^6 CFU/mL with 400 μL prepared were uniformly inoculated onto MHA solidified in 60-mm Petri dishes. Sterile filter paper disks of 6 mm diameter containing 5 μL different concentrations of compounds were pressed gently against the surface of the agar. A disk containing Gatifloxacin was used as a positive control, while DMSO was used as the negative control. Then the disks were incubated in a constant temperature incubator at 37°C for 24 h and the bacteriostatic circles were observed. The inhibition zone (IZ) diameter was measured using a vernier caliper. All the experiments were performed in triplicate.

3.5.2 Minimum inhibitory concentration (MIC) assay

The MIC was determined by a microdilution method in 96-well plates according to the Clinical and Laboratory Standards Institute (CLSI) with a slight modification. (Sader et al., 2006). Liquid media were used to cultivate the test bacteria at 37°C. Then, 195-μL bacterial suspensions containing 1.5×10^5 CFU/mL with 5 μL different derivative concentrations were added to 96-cell plates and the plates were incubated at 37°C for 24 h. In each well, OD values of derivatives were measured at 600 nm and compared with blank controls without bacteria and negative controls with bacteria. The lowest concentration of compounds, which did not show any visible growth of the test organisms after macroscopic evaluation, was determined as the MIC. Gatifloxacin served as the positive control and DMSO served as the negative control.

3.5.3 Quantitative structure–activity relationship (QSAR) study

The MIC values (μM) of the constructed 22 derivatives (**FA**, **FA-1**, **FA-2**, and **FA-6~24)** were converted into their corresponding negative logarithms (pMIC) for the 3D-QSAR model analysis by SYBYL-X 2.0 software (Shanghai Tri-I. Biotech. Inc., China) (Wang et al., 2019; Chen et al., 2020). Three-dimensional molecular conformations were successively optimized using the Gasteiger–Huckel charge, Tripos force field, and Powell conjugate gradient algorithm until the obtained convergence criteria were minimized in molecular energies. Three-dimensional structures of derivatives were aligned on the common scaffold of the template molecule **FA-7** that exhibited the best *in vitro* antibacterial activity against Gram-positive bacteria among the 22 synthesized derivatives. A partial least-squares (PLS) technique was applied for optimizing the obtained 3D-QSAR model. Subsequently, the obtained PLS coefficients and standard descriptor values were used to generate their corresponding contour maps including steric, electrostatic, hydrophobic, and hydrogen bond acceptors.

4 Conclusion

In this study, a ligand-based pharmacophore model was constructed and seven **FA** derivatives were designed according to the reported structure–activity relationship and the pharmacophore characteristics. The designed **FA** derivatives were applied to analyze the matching degree with the pharmacophore model through Qfit values, and partially designed **FA** derivatives were docked onto the EF-G of *S. aureus* to study the bonding with the target protein. Finally, the designed **FA** derivatives were synthesized and their antibacterial activities were evaluated by the inhibition zone test and the MIC test. Afterward, 3D-QSAR was carried out on all the derivatives, and the results indicated that the substituents at the C-3, C-21, and C-25 positions would exert an influence on the antibacterial activity of derivatives. In summary, this study provides a promising computational approach to design **FA** derivatives with highly potent antibacterial activity.

Data availability statement

The original contributions presented in the study are included in the article/Supplementary Material; further inquiries can be directed to the corresponding authors.

Author contributions

Writing—original draft, software, formal analysis, and methodology: WZ and BT; writing—original draft, resources, and methodology: ZZ; software, formal analysis, and investigation: JL; methodology and investigation: ZY; validation and investigation: KS; formal analysis and investigation: DD; methodology and investigation: YS; validation and investigation: XW; project administration and resources: BZ; funding acquisition, supervision, and project administration: KZ and W-LW; writing—review and editing, supervision, project administration, and data curation: PW and WH; and writing—review and editing, methodology, project administration, and funding acquisition: SA. All authors read and agreed to the published version of the manuscript.

Funding

This study was supported by the National Natural Science Foundation of China (Nos. 81803390 and 22077020), Natural Science Foundation of Guangdong Province (No. 2021A1515010221), Hong Kong and Macao Joint Research and Development Foundation of 2021 (No. 2021WGALH09), Special Funds for the Cultivation of Guangdong College Students' Scientific and Technological Innovation ("Climbing Program" Special Funds, No.

pdjh 2022a0523), and Special Fund Project of Science and Technology Innovation Strategy of Guangdong Province 2018 and 2020 [Nos. Jiangke (2018)352 and Jiangke (2020)182]. The authors acknowledge the Foundation of the Department of Education of Guangdong Province (Nos. 2020KZDZX1202 and 2022KTSCX144).

Conflict of interest

The authors declare that the research was conducted in the absence of any commercial or financial relationships that could be construed as a potential conflict of interest.

The handling editor declared a shared affiliation with the author BZ at the time of review.

Publisher's note

Supplementary material

The Supplementary Material for this article can be found online at: https://www.frontiersin.org/articles/10.3389/fchem.2022.1094841/full#supplementary-material

References

Belardinelli, R., and Rodnina, M. V. (2017). Effect of fusidic acid on the kinetics of molecular motions during EF-G-induced translocation on the ribosome. *Sci. Rep.* 7, 10536. doi:10.1038/s41598-017-10916-8

Benamrouche, N., Lazri, M., Hassiba, T. M., and Rahal, K. (2014). Comparison of Corynebacterium diphtheriae susceptibility testing to antibiotics by the broth dilution and diffusion (E-test and disk) methods. *Med. Maladies Infect.* 44, 392–393. doi:10.1016/j.medmal.2014.07.007

Bodley, J. W., Zieve, F. J., Lin, L., and Zieve, S. T. (1969). Formation of the ribosome-G factor-GDP complex in the presence of fusidic acid. *Biochem. Biophysical Res. Commun.* 37, 437–443. doi:10.1016/0006-291X(69)90934-6

Borg, A., Holm, M., Shiroyama, I., Hauryliuk, V., Pavlov, M., Sanyal, S., et al. (2015). Fusidic acid targets elongation factor G in several stages of translocation on the bacterial ribosome. *J. Biol. Chem.* 290, 3440–3454. doi:10.1074/jbc.M114.611608

Cardoso, M. H., Orozco, R. Q., Rezende, S. B., Rodrigues, G., Oshiro, K. G. N., Candido, E. S., et al. (2019). Computer-aided design of antimicrobial peptides: Are we generating effective drug candidates? *Front. Microbiol.* 10, 3097. doi:10.3389/fmicb.2019.03097

Cerqueira, N. M. F. S. A., Gesto, D., Oliveira, E. F., Santos-Martins, D., Brás, N. F., Sousa, S. F., et al. (2015). Receptor-based virtual screening protocol for drug discovery. *Archives Biochem. Biophysics* 582, 56–67. doi:10.1016/j.abb.2015.05.011

Chen, J., Luo, Y., Wei, C., Wu, S., Wu, R., Wang, S., et al. (2020). Novel sulfone derivatives containing a 1, 3, 4-oxadiazole moiety: Design and synthesis based on the 3D-QSAR model as potential antibacterial agent. *Pest Manag. Sci.* 76, 3188–3198. doi:10.1002/ps.5873

Chen, Y., Koripella, R. K., Sanyal, S., and Selmer, M. (2010). Staphylococcus aureus elongation factor G – structure and analysis of a target for fusidic acid. *FEBS J.* 277, 3789–3803. doi:10.1111/j.1742-4658.2010.07780.x

Chen, Z., Li, H., Zhang, Q., Bao, X., Yu, K., Luo, X., et al. (2009). Pharmacophore-based virtual screening versus docking-based virtual screening: A benchmark comparison against eight targets. *Acta Pharmacol. Sin.* 30, 1694–1708. doi:10.1038/aps.2009.159

Collignon, P., and Turnidge, J. (1999). Fusidic acid *in vitro* activity. *Int. J. Antimicrob. Agents* 12, S45–S58. doi:10.1016/S0924-8579(98)00073-9

Duvold, T., Sørensen, M. D., Björkling, F., Henriksen, A. S., and Rastrup-Andersen, N. (2001). Synthesis and conformational analysis of fusidic acid side chain derivatives in relation to antibacterial activity. *J. Med. Chem.* 44, 3125–3131. doi:10.1021/jm010899a

Fjell, C. D., Hiss, J. A., Hancock, R. E. W., and Schneider, G. (2012). Designing antimicrobial peptides: Form follows function. *Nat. Rev. Drug Discov.* 11, 37–51. doi:10.1038/nrd3591

Garcia Chavez, M., Garcia, A., Lee, H. Y., Lau, G. W., Parker, E. N., Komnick, K. E., et al. (2021). Synthesis of fusidic acid derivatives yields a potent antibiotic with an improved resistance profile. *ACS Infect. Dis.* 7, 493–505. doi:10.1021/acsinfecdis.0c00869

Gaudreau, C., Girouard, Y., Gilbert, H., Gagnon, J., and Bekal, S. (2008). Comparison of disk diffusion and agar dilution methods for erythromycin, ciprofloxacin, and tetracycline susceptibility testing of campylobacter coli and for tetracycline susceptibility testing of campylobacter jejuni subsp jejuni. *Antimicrob. Agents Chemother.* 52, 4475–4477. doi:10.1128/AAC.00767-08

Godtfredsen, W. O., Albrethsen, C., Daehne, W. V., Tybring, L., and Vangedal, S. (1965). Transformations of fusidic acid and the relationship between structure and antibacterial activity. *Antimicrob. Agents Chemother. (Bethesda)* 5, 132–137. doi:10.1021/jm00319a004

Godtfredsen, W. O., Von Daehne, W., Tybring, L., and Vangedal, S. (1966). Fusidic acid derivatives. I. Relationship between structure and antibacterial activity. *J. Med. Chem.* 9, 15–22. doi:10.1021/jm00319a004

Kong, F., Huang, X., Ma, Q., Xie, Q., Wang, P., Chen, P., et al. (2018). Helvolic acid derivatives with antibacterial activities against Streptococcus agalactiae from the marine-derived fungus Aspergillus fumigatus HNMF0047. *J. Nat. Prod.* 81, 1869–1876. doi:10.1021/acs.jnatprod.8b00382

Lannergård, J., Norström, T., and Hughes, D. (2009). Genetic determinants of resistance to fusidic acid among clinical bacteremia isolates of Staphylococcus aureus. *Antimicrob. Agents Chemother.* 53, 2059–2065. doi:10.1128/AAC.00871-08

Lu, J., Ni, J., Wang, J., Liu, Z., Shang, K., and Bi, Y. (2019). Integration of multiscale molecular modeling approaches with the design and discovery of fusidic acid derivatives. *Future Med. Chem.* 11, 1427–1442. doi:10.4155/fmc-2018-0567

Luangtongkum, T., Morishita, T. Y., El-Tayeb, A. B., Ison, A. J., and Zhang, Q. (2007). Comparison of antimicrobial susceptibility testing of Campylobacter spp. by the agar dilution and the agar disk diffusion methods. *J. Clin. Microbiol.* 45, 590–594. doi:10.1128/JCM.00986-06

Lv, J.-M., Hu, D., Gao, H., Kushiro, T., Awakawa, T., Chen, G.-D., et al. (2017). Biosynthesis of helvolic acid and identification of an unusual C-4-demethylation process distinct from sterol biosynthesis. *Nat. Commun.* 8, 1644. doi:10.1038/s41467-017-01813-9

Mouchlis, V. D., Melagraki, G., Zacharia, L. C., and Afantitis, A. (2020). Computer-aided drug design of β-secretase, γ-secretase and anti-tau inhibitors for the discovery of novel alzheimer's therapeutics. *Int. J. Mol. Sci.* 21, 703. doi:10.3390/ijms21030703

Niu, Y., Ma, C., Jin, H., Xu, F., Gao, H., Liu, P., et al. (2012). The discovery of novel beta-secretase inhibitors: Pharmacophore modeling, virtual screening, and docking studies. *Chem. Biol. Drug Des.* 79, 972–980. doi:10.1111/j.1747-0285.2012.01367.x

Petrosillo, N., Granata, G., and Cataldo, M. A. (2018). Novel antimicrobials for the treatment of clostridium difficile infection. *Front. Med.* 5, 96. doi:10.3389/fmed.2018.00096

Ragab, A. E., Ibrahim, A.-R. S., and Leon, F. (2020). 3-O-formyl -27-hydroxyfusidic acid: A new metabolite of fusidic acid by cunninghamella echinulata. *Rec. Nat. Prod.* 14, 292–296. doi:10.25135/rnp.168.19.12.1505

Riber, D., Venkataramana, M., Sanyal, S., and Duvold, T. (2006). Synthesis and biological evaluation of photoaffinity labeled fusidic acid analogues. *J. Med. Chem.* 49, 1503–1505. doi:10.1021/jm050583t

Sader, H. S., Fritsche, T. R., and Jones, R. N. (2006). Daptomycin bactericidal activity and correlation between disk and broth microdilution method results in testing of Staphylococcus aureus strains with decreased susceptibility to vancomycin. *Antimicrob. Agents Chemother.* 50, 2330–2336. doi:10.1128/AAC.01491-05

Salimova, E. V., Mamaev, A. G., Tret'yakova, E. V., Kukovinets, O. S., Mavzyutov, A. R., Shvets, K. Y., et al. (2018). Synthesis and biological activity of cyanoethyl derivatives of fusidic acid. *Russ. J. Org. Chem.* 54, 1411–1418. doi:10.1134/S1070428018090245

Sangeetha, K., Sasikala, R. P., and Meena, K. S. (2017). Pharmacophore modeling, virtual screening and molecular docking of ATPase inhibitors of HSP70. *Comput. Biol. Chem.* 70, 164–174. doi:10.1016/j.compbiolchem.2017.05.011

Schwartz, C., Raible, J., Mott, K., and Dussault, P. H. (2006). Fragmentation of carbonyl oxides by N-oxides: An improved approach to alkene ozonolysis. *Org. Lett.* 8, 3199–3201. doi:10.1021/ol061001k

Sharma, T., Harioudh, M. K., Kuldeep, J., Kumar, S., Banerjee, D., Ghosh, J. K., et al. (2020). Identification of potential inhibitors of cathepsin-B using shape & pharmacophore-based virtual screening, molecular docking and explicit water thermodynamics. *Mol. Inf.* 39, 1900023. doi:10.1002/minf.201900023

Singh, K., Kaur, G., Shanika, P. S., Dziwornu, G. A., Okombo, J., and Chibale, K. (2020). Structure-activity relationship analyses of fusidic acid derivatives highlight crucial role of the C-21 carboxylic acid moiety to its anti-mycobacterial activity. *Bioorg. Med. Chem.* 28, 115530. doi:10.1016/j.bmc.2020.115530

Talambedu, U., Dhivya, S., Arvind Kumar, G., Chinaga Suresh, K., and Sushil Kumar, M. (2017). Recent updates on computer-aided drug discovery: Time for a paradigm shift. *Curr. Top. Med. Chem.* 17, 3296–3307. doi:10.2174/1568026618666180101163651

Tanaka, N., Kinoshita, T., and Masukawa, H. (1968). Mechanism of protein synthesis inhibition by fusidic acid and related antibiotics. *Biochem. Biophysical Res. Commun.* 30, 278–283. doi:10.1016/0006-291X(68)90447-6

Turnidge, J. (1999). Fusidic acid pharmacology, pharmacokinetics and pharmacodynamics. *Int. J. Antimicrob. Agents* 12, S23–S34. doi:10.1016/S0924-8579(98)00071-5

Von Daehne, W., Godtfredsen, W., and Rasmussen, P. (1979). Structure-activity relationships in fusidic acid-type antibiotics. *Adv. Appl. Microbiol.* 25, 95–146. doi:10.1016/s0065-2164(08)70148-5

Wang, M., Zhu, H., Wang, P., Zeng, D., Wu, Y., Liu, L., et al. (2019). Synthesis of thiazolium-labeled 1, 3, 4-oxadiazole thioethers as prospective antimicrobials: *In vitro* and *in vivo* bioactivity and mechanism of action. *J. Agric. Food Chem.* 67, 12696–12708. doi:10.1021/acs.jafc.9b03952

Zhao, M., Godecke, T., Gunn, J., Duan, J. A., and Che, C. T. (2013). Protostane and fusidane triterpenes: A mini-review. *Molecules* 18, 4054–4080. doi:10.3390/molecules18044054

Zhao, S., Wu, P., Zhang, K., Hong, W., Jiang, Z., Cui, X., et al. (2016). *Chemically modified fusidic acid, preparation method and application*. Guangdong: China National Intellectual Property Administration, C. N. Patent No 105,924,488.

Zhu, C., Li, X. W., Zhao, B. Y., Peng, W. Q., Li, W., and Fu, W. (2020). Discovery of aryl-piperidine derivatives as potential antipsychotic agents using molecular hybridization strategy. *Eur. J. Med. Chem.* 193, 112214. doi:10.1016/j.ejmech.2020.112214

frontiers | Frontiers in Chemistry

TYPE Original Research
PUBLISHED 17 January 2023
DOI 10.3389/fchem.2023.1121724

OPEN ACCESS

EDITED BY
Xuetao Xu,
Wuyi University, China

REVIEWED BY
Rohan Kalyan Rej,
University of Michigan, United States
Clemens Zwergel,
Sapienza University of Rome, Italy

*CORRESPONDENCE
Bo Jiang,
jiangboqdy@126.com
Sichuan Hou,
housichuandoctor@126.com
Shumin Ma,
mashumin@ouc.edu.cn
Chong Qin,
qc@ouc.edu.cn

SPECIALTY SECTION
This article was submitted to Medicinal and Pharmaceutical Chemistry, a section of the journal Frontiers in Chemistry

RECEIVED 12 December 2022
ACCEPTED 04 January 2023
PUBLISHED 17 January 2023

CITATION
Wang Q, Li B, Zhang W, Li Z, Jiang B, Hou S, Ma S and Qin C (2023), Lethal activity of BRD4 PROTAC degrader QCA570 against bladder cancer cells.
Front. Chem. 11:1121724.
doi: 10.3389/fchem.2023.1121724

Lethal activity of BRD4 PROTAC degrader QCA570 against bladder cancer cells

Qiang Wang[1,2], Baohu Li[2], Wenkai Zhang[2], Zhuoyue Li[2], Bo Jiang[1]*, Sichuan Hou[1]*, Shumin Ma[2]* and Chong Qin[2,3]*

[1]Department of Urology, Qingdao Municipal Hospital, Qingdao University, Qingdao, China, [2]Key Laboratory of Marine Drugs, Chinese Ministry of Education, School of Medicine and Pharmacy, Ocean University of China, Qingdao, China, [3]Laboratory for Marine Drugs and Bioproducts, Qingdao National Laboratory for Marine Science and Technology, Qingdao, China

Bladder cancer is the most common malignancy of the urinary system. Efforts to identify innovative and effective therapies for bladder cancer are urgently needed. Recent studies have identified the BRD4 protein as the critical factor in regulation of cell proliferation and apoptosis in bladder cancer, and it shows promising potential for pharmacologic treatment against bladder cancer. In this study, we have evaluated the biological function of QCA570, a novel BET degrader, on multiple bladder cancer cells and explore its underlying mechanisms. QCA570 potently induces degradation of BRD4 protein at nanomolar concentrations, with a DC_{50} of ~ 1 nM. It decreases EZH2 and c-MYC levels by transcriptional suppression and protein degradation. Moreover, the degrader significantly induces cell apoptosis and cycle arrest and shows antiproliferation activity against bladder cancer cells. These findings support the potential efficacy of QCA570 on bladder cancer.

KEYWORDS

QCA570, BRD4, PROTAC, bladder cancer, targeted therapy

Introduction

Bladder cancer (BC) remains the most common malignancy of the urinary tract with an estimated 500,000 new cases and 200,000 deaths worldwide each year (Lenis et al., 2020; Dobruch and Oszczudłowski, 2021). Clinically, bladder cancer is classified as either a non-muscle-invasive bladder cancer (NMIBC), in which the muscle tissue was not affected, or a muscle-invasive bladder cancer (MIBC) (Witjes et al., 2021). MIBC has a high rate of metastasis and is more likely to lead to death (Liu et al., 2022a). Although common treatments, such as transurethral resection and systemic chemotherapy, are effective for some MIBC patients, the recurrence and distant metastasis remains at approximately 50% and the 5-year survival rate is 50%–65% (Wu et al., 2016; Xie et al., 2020). Hence, development of novel treatment strategies is necessary to improve the clinical results of treatment of patients with bladder cancer.

The bromodomain and extraterminal domain (BET) proteins including BRD2, BRD3, BRD4 and the testis-specific protein (BRDT) are known to be important epigenome readers which interact with the acetylated histones, recruit chromatin-modifying enzymes to target promoters and function as coactivators or corepressors in a context-dependent manner (Filippakopoulos et al., 2010; Yan et al., 2014; Donati et al., 2018). By regulating gene transcription both at the initiation and elongation steps, these proteins play key roles during embryogenesis and cancer development (Wang et al., 2017). As the most widely studied member, BRD4 has emerged as an attractive therapeutic target for cancer therapy (Jung et al., 2015; Duan et al., 2018). Dysregulation of BRD4 has been involved in a variety of cancers including hematological and several solid malignancies (Ozer et al., 2018; Wu et al., 2019). For

example, BRD4 is significantly upregulated in melanoma tissues and treatment with BET inhibitors impairs melanoma cell proliferation and metastatic behavior (Segura et al., 2013). In acute myeloid leukemia (AML), BRD4 has been reported to be critical for disease maintenance and suppression of BRD4 led to significant antileukemic effects *in vitro* and *in vivo* (Zuber et al., 2011).

Yan reported for the first time that BRD4 is upregulated in bladder cancer tissues, and its high expression is closely associated with a more malignant clinical feature and poor patient prognosis (Yan et al., 2014). Recently, Wu revealed BRD4 as a novel promising target for pharmacologic treatment against bladder cancer and reported that BRD4 regulates proliferation and apoptosis of bladder cancer cells by positively regulating EZH2 transcription through upregulation of c-MYC (Wu et al., 2016). The Liu group showed that BRD4 promoted the migration, invasion, and DDP (cisplatin) resistance of BCa cells (Liu et al., 2022b). Multiple BRD4 protein small-molecule inhibitors, such as JQ1, have been developed and have shown promising anticancer results in experimental and clinical cancer studies (White et al., 2019). However, limitations of these BRD4 inhibitors were also displayed (Zhang et al., 2022). Some studies have shown that the accumulation of BRD4 protein is a key factor which confers resistance to BET inhibitors (Janouskova et al., 2017; Jin et al., 2018).

Recently, a target protein degradation strategy based on the concept of proteolysis targeting chimeric (PROTAC) molecules has been developed and has received increasing attention in the past decade (Neklesa et al., 2017; Burslem and Crews, 2020). These are heterobifunctional small molecules consisting of two ligands linked by a linker: one ligand binds to the protein of interest while the other binds to an E3 ubiquitin ligase, leading to ubiquitination and degradation of the target protein by the ubiquitin-proteasome system (UPS) (Békés et al., 2022). The novel pan BET degrader, QCA570 exerts potent degradation efficiency on BET proteins in leukemia cells and achieved complete and durable tumor regression in xenograft models at well-tolerated dose-schedules (Qin et al., 2018). In this study, we tested the potential anticancer activity and underlying signalling mechanisms of QCA570 on bladder cancer cells.

Materials and methods

Reagents

QCA570 was synthesized as reported previously (Qin et al., 2018). JQ1, MLN4924 and MG132 were purchased from Med Chem Express (Monmouth Junction, NJ).

Cell lines

The human bladder cancer cell lines T24 and SV-HUC-1 was purchased from Procell Life Science & Technology Co., Ltd. (Wuhan, China). The 5637, J82, UMUC-3 and EJ-1 cells were obtained from Yuhuangding Hospital (Yantai, China). 5637, EJ-1, UM-UC-3 cells were cultured in RPMI1640 media (Procell, PM150110); J82 cells were cultured in MEM (NEAA) media (Procell, PM150410), and T24 cells were cultured in McCoy's 5A media (PM150710). A total of 10% FBS (Gibco,1099141C) and 1% antibiotics (penicillin and streptomycin, Procell, PB180120) were added to the basic media. All the cells were cultured at 37°C with 5% CO_2.

Western blotting

Cells were lysed in RIPA lysis buffer (Beyotime Biotechnology, Jiangsu, China) with protease inhibitor (Roche, 11697498001) and phosphatase inhibitor (Roche, 4906837001) for 10 min on ice and shaken every 5 min on a vortex mixer for 30 s. Lysates were centrifuged at 12,000 rpm at 4°C for 10 min and the supernatant fraction was retained. Protein concentrations were quantified with BCA Protein Assay Kit (Thermo Fisher Scientific, A53226). Protein samples were separated *via* 10% SDS-PAGE and then transferred onto PVDF membrane. The membrane was blocked in 5% milk containing TBST (Tris-buffered Saline with Tween 20) at room temperature for 1 h, and this was followed by incubation with indicated primary antibodies overnight at 4°C. The membrane was then washed 3 times with TBST and incubated with secondary antibody for 1 h at room temperature before its development with the ECL kit (Thermo Fisher Scientific, 34,578). Primary antibodies to the following proteins were used: BRD4 (Bethyl Laboratories, A301-985A100), BRD3 (Bethyl Laboratories, A302-368A), BRD2 (Bethyl Laboratories, A302-583A), EZH2 (D2C9) (Cell Signaling Technology Inc, #5246), c-MYC (Abcam, ab32072), caspase-3 (Cell Signaling Technology Inc, #9662) GAPDH (ABclonal, AC033), β-Actin (ABclonal, AC006).

Quantitative reverse transcriptase-polymerase chain reaction (qPCR)

Total RNA was extracted using the RNA-easy Isolation Reagent (Vazyme, R701) according to the manufacturer's instructions. Complementary DNAs (cDNAs) were synthesized using HiScript III RT Super Mix for qPCR (+gDNA wiper) (Vazyme, R323). qPCR was performed using ChamQ Universal SYBR qPCR Master Mix (Vazyme, Q711) and detected with a LightCycler® 96 Detection System (Roche, Switzerland). The PCR amplification was performed following the program: 95°C for 5 min of initial denaturation, then 40 cycles at 95°C for 30 s, 60°C for 30 s, and 72°C for 10 s, followed by a final melting curve step. The relative abundance of transcripts was calculated based on normalization to the GAPDH gene. The primers are shown in Table 1.

TABLE 1 The data sets collected from public GDSC database.

Primer	Sequence (5′—3′)
GAPDH-F	TCAAGAAGGTGGTGAAGCAG
GAPDH-R	CGTCAAAG GTGGAGGAGTG
c-MYC-F	AGGGATCGCGCTGAGTATAA
c-MYC-R	TGCCTCTCGCTGGAATTACT
EZH2-F	CCCTGACCTCTGTCTTACTTGTGGA
EZH2-R	ACGT CAGATGGTGCCAGCAATA

Cell viability by CCK-8 assay

5637, T24, EJ-1 at 3,000 cells/well and J82, UMUC-3 at 5,000 cells/well were seeded into 96-well plates. Cell viability and proliferation were measured with CCK-8 (Biosharp, BS350) at designated times after drug treatment. Briefly, 10 μL of CCK-8 solution was added to each well and incubated at 37°C for 2 h before reading the absorbance at 450 nm. The results were analyzed using GraphPad software. All experiments were repeated at least three times.

Wound healing assay

Collect cells, seed them in 12-well plates, culture until the cells are completely confluent, and use a 200 μL sterilized pipette tip to make scratches perpendicular to the bottom of the culture dish. The original medium was discarded, washed twice with PBS, and the medium containing the compound was added again, and cultured in the incubator for 48 h. They were placed under a microscope and photographed at 8, 12, 24, and 48 h respectively.

Flow cytometry assays for the cell cycle

Cells were harvested two days after treatment with compounds or DMSO, washed twice with PBS, and fixed with 70% ethanol overnight at 4°C. Then cells were centrifuged at 3,000 rpm for 5 min, washed twice with PBS, and resuspended in PBS. After incubating with 20 μg/mL RNase A (Solarbio Beijing, China), cells were stained with 20 μg/mL propidium iodide (PI) (Solarbio Beijing, China). A Beckman Coulter flow cytometer was used for detection and FlowJo-V10 software was used to analyze the data.

Annexin V-FITC/PI apoptosis assay by flow cytometry

We harvested cells after a 2-day treatment with compounds or DMSO and washed them twice with cold PBS before resuspending them in 1x binding buffer. An Annexin V-FITC/PI Apoptosis Assay Kit (abs50001, Absin) was used to stain cells. After incubation for 15 min in the dark, we analyzed cell apoptosis on a flow cytometer (Beckman Coulter). Data were analyzed with FlowJo-V10 software.

Terminal deoxyribonucleotide transferase-mediated dUTP nick-end labeling and staining

For this experiment, 5×10^5 cells were grown on coverslips. Cell apoptosis was determined using the one-step TUNEL apoptosis assay kit (Roche, 12156792910) according to the manufacturer's instructions. Following TUNEL staining, the slides were stained with DAPI (Solarbio Beijing, C0060) to highlight the nuclei with fluorescence. Slides were observed under an LSM 510 META Olympus Confocal Laser Scanning Microscope using 488-nm excitation and 530-nm emission, and the images were captured and quantified by image analysis software, ImageJ.

Online analysis

The BRD4 and EZH2 gene expression across tumor and normal samples was analyzed online from TCGA clinical data on the UALCAN database (ualcan.path.uab.edu/home, accessed on may 3, 2022). TPM (transcripts per million) values were employed for the generation of boxplots and to estimate the significance between groups by *t*-test. Besides, BRD4 and EZH2 gene expression data were also downloaded from the publicly available GEO website (Home - GEO - NCBI (nih.gov), accessed on may 3, 2022) and included GSE48276 and GSE13507 datasets containing the raw RNA microarray data of 208 samples, comprised of 43 control and 165 BC patients. The Kaplan–Meier survival analysis was generated from the OncoLnc database (OncoLnc, accessed on May 3, 2022) which performs in-depth analyses of TCGA gene expression data. A Log-rank test was used for survival comparison.

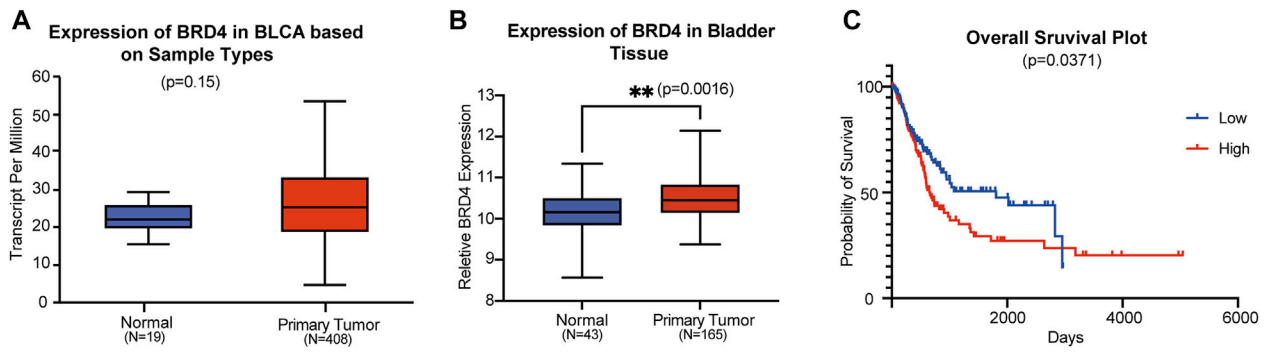

FIGURE 1
Association of BRD4 expression and bladder cancer risk **(A)** The BRD4 mRNA expression level of bladder tissues were analyzed in TGCA cohorts. The *p*-value was examined by Mann–Whitney U-test. **(B)** The relative expression level of BRD4 was determined in GEO database (GSE48276 and GSE13507). The remove Batch Effect function in the limma package was used to remove batches. The *p*-value was examined by Welch's *t*-test. **(C)** The risk of BRD4 expression for survival analysis in 240 well-defined BC cases derived from TCGA databases was performed by the Kaplan-Meier plotter online. The *p*-value was calculated by a log-rank test.

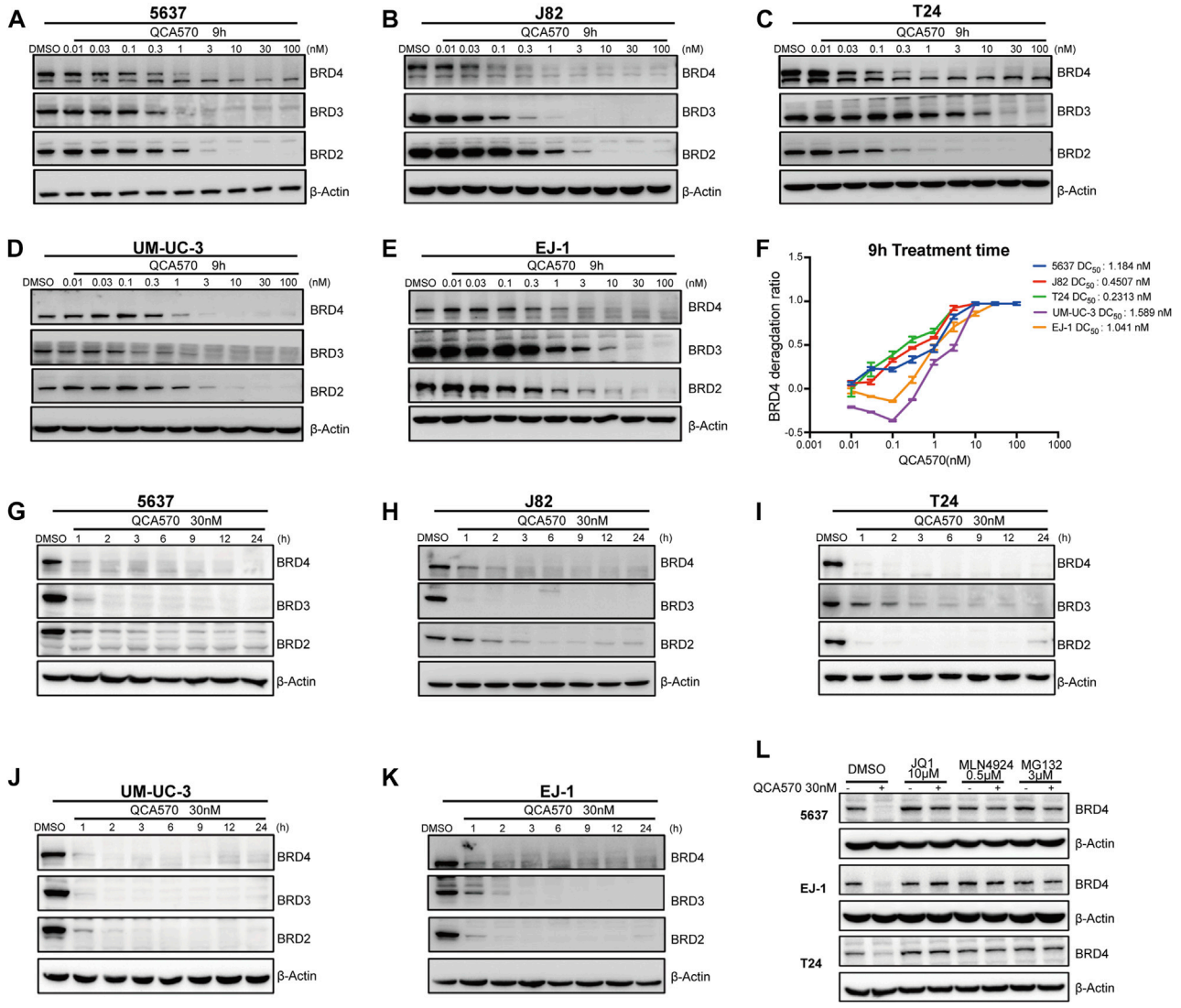

FIGURE 2
QCA570 potently induces BRD4 degradation in multiple BC cell lines **(A–F)** with a treatment of QCA570 at varied concentrations for 9 h in BC cells, the BET family proteins were detected by Western blotting. GAPDH was used as loading control. Protein levels were quantified with ImageJ and the degradation curve was plotted with GraphPad Prism 9. **(G–K)** BC cells were treated with 30 nM of QCA570 for indicated time points. BET family protein levels were determined by Western blotting and GAPDH was used as loading control. **(L)** Cells were pretreated with BETi JQ1, neddylation activating E1 enzyme inhibitor MLN4924 and proteasome inhibitor MG132 for 6 h, followed by treatment of QCA570 for a further 3 h. BRD4 protein levels were detected by Western blotting and β-Actin was used as a loading control.

Results

BRD4 is overexpressed in patients with BC and is associated with poor prognosis

To explore the role of BRD4 in BC progression, we analyzed the mRNA expression data from the TCGA database. In bladder tissues from 408 patients, BRD4 was upregulated compared with normal samples (Figure 1A). Data from the GEO website further confirmed that BRD4 was overexpressed in BC tissues (Figure 1B) from these patients. Kaplan-Meier survival analysis of 240 well-defined BC cases derived from the TCGA database showed that high BRD4 expression was associated with poor overall survival (OS) of BC patients (Figure 1C). These results showed the association between BRD4 expression with BC risk and suggest that BRD4 may be involved in a potential therapy target for BC patients.

QCA570 is a potent BET degrader in cell lines of BC model

The PROTAC molecule QCA570 ($C_{39}H_{33}N_7O_4S$, CAS number 2207569-08–0) developed by Qin et al. showed effective degradation of BET proteins BRD2, BRD3, and BRD4 at low picomolar concentrations and showed more potent proliferation inhibitory activity than other BET degraders such as dBET1, ARV-

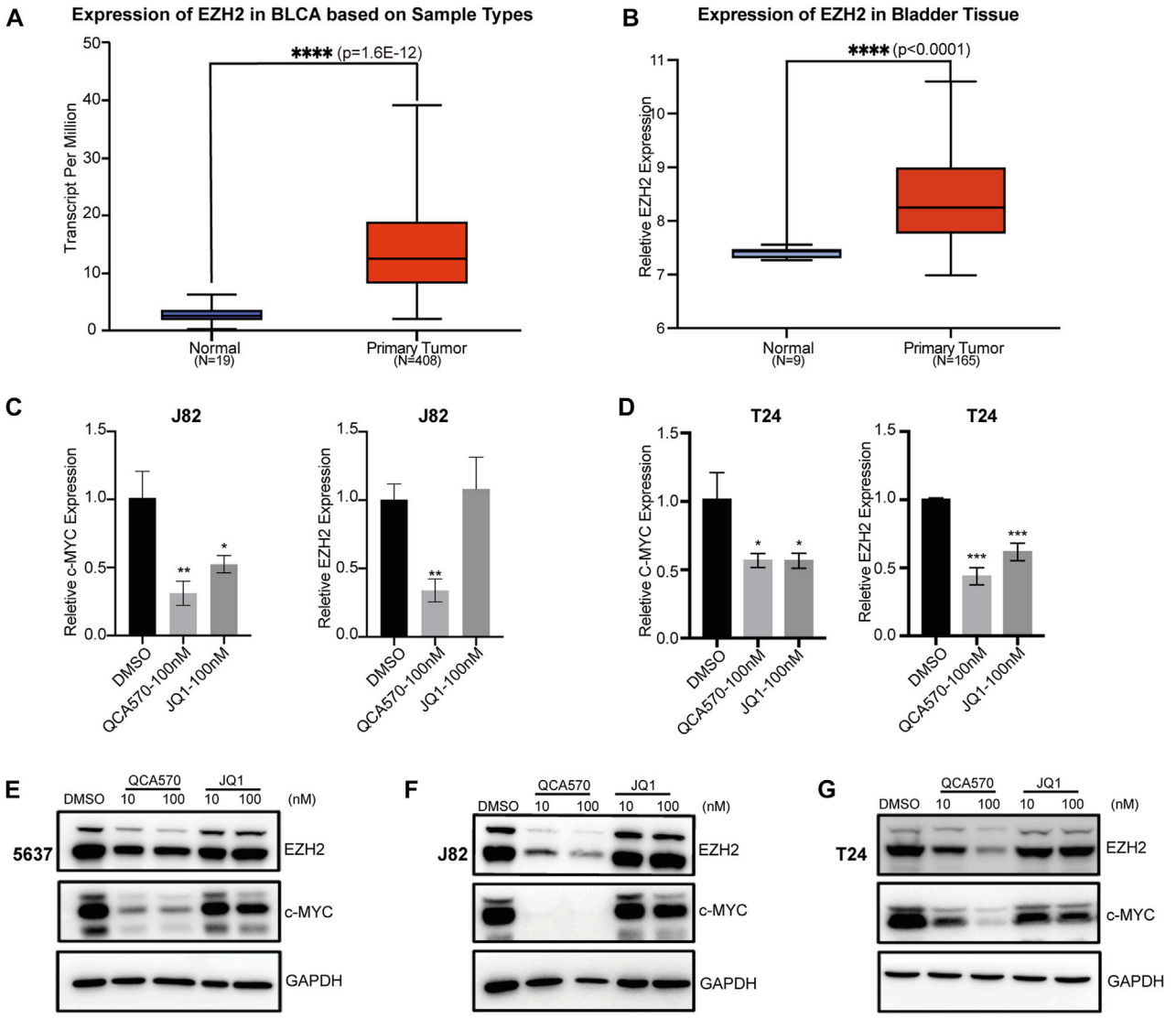

FIGURE 3
BRD4 target genes are downregulated by QCA570 **(A)** The EZH2 mRNA expression level of bladder tissues was analyzed in TGCA cohorts. The *p*-value was examined by the Mann–Whitney U-test. **(B)** The relative expression level of EZH2 was determined in GEO database (GSE13507). Using the remove Batch Effect function in the limma package to removes batches. The *p*-value was examined by Welch's *t*-test. **(C, D)** RT-qPCR analysis of c-MYC and EZH2 gene expression in J82 and T24 cells. Values are the means ± SEM, $*p < 0.05$, $**p < 0.01$, $***p < 0.001$, two-tailed Student's t-test. **(E–G)** The protein level of c-MYC and EZH2 were detected by Western blotting. GAPDH was used as loading control.

825, ARV-771, and ZBC260 in human leukemia cell lines. The degradation ability of QCA570 was also validated by Liu et al. in human lung cancer cells. In this study, we evaluated the activity of QCA570 on BC cell lines. As shown in Figures 2A-F, QCA570 induces degradation of BET proteins BRD2, BRD3 and BRD4 in a dose-dependent manner with a treatment of 9 h. BRD4 at 3 nM was largely depleted in each of these five BC cell lines with a DC_{50} around 1 nM. We next explored the degradation kinetics of QCA570 at 30 nM concentration at various duration times ranging from 1 to 24 h (Figures 2G-K). The BRD4 degradation peaked within 1 h in 5637, T24, UM-UC-3 cells and within 3 h in J82 and EJ-1 cell lines. A time-dependent degradation was also observed with BRD2 and BRD3 proteins.

Based on its PROTAC design, QCA570 forms a ternary complex dependent upon its binding to the target protein and E3 ubiquitin ligase CRBN. Similarly, QCA570 should also be proteasome-dependent. The mechanism used by QCA570 for the degradation of BET proteins was previously validated in RS4; 11 cells. In our study, we also confirmed the degradation mechanism in BC cells (Figure 2L). The Western blotting (WB) result showed that BRD4 degradation was almost completely abolished by pre-treatment with the proteasome inhibitor MG-132, the E1 neddylation inhibitor MLN4924, and the BRD4 ligand, JQ1 in BC cells. These data together provide evidence pertaining to the mechanism for ligands and proteasome-dependent degradation of BET proteins, consistent with its PROTAC character.

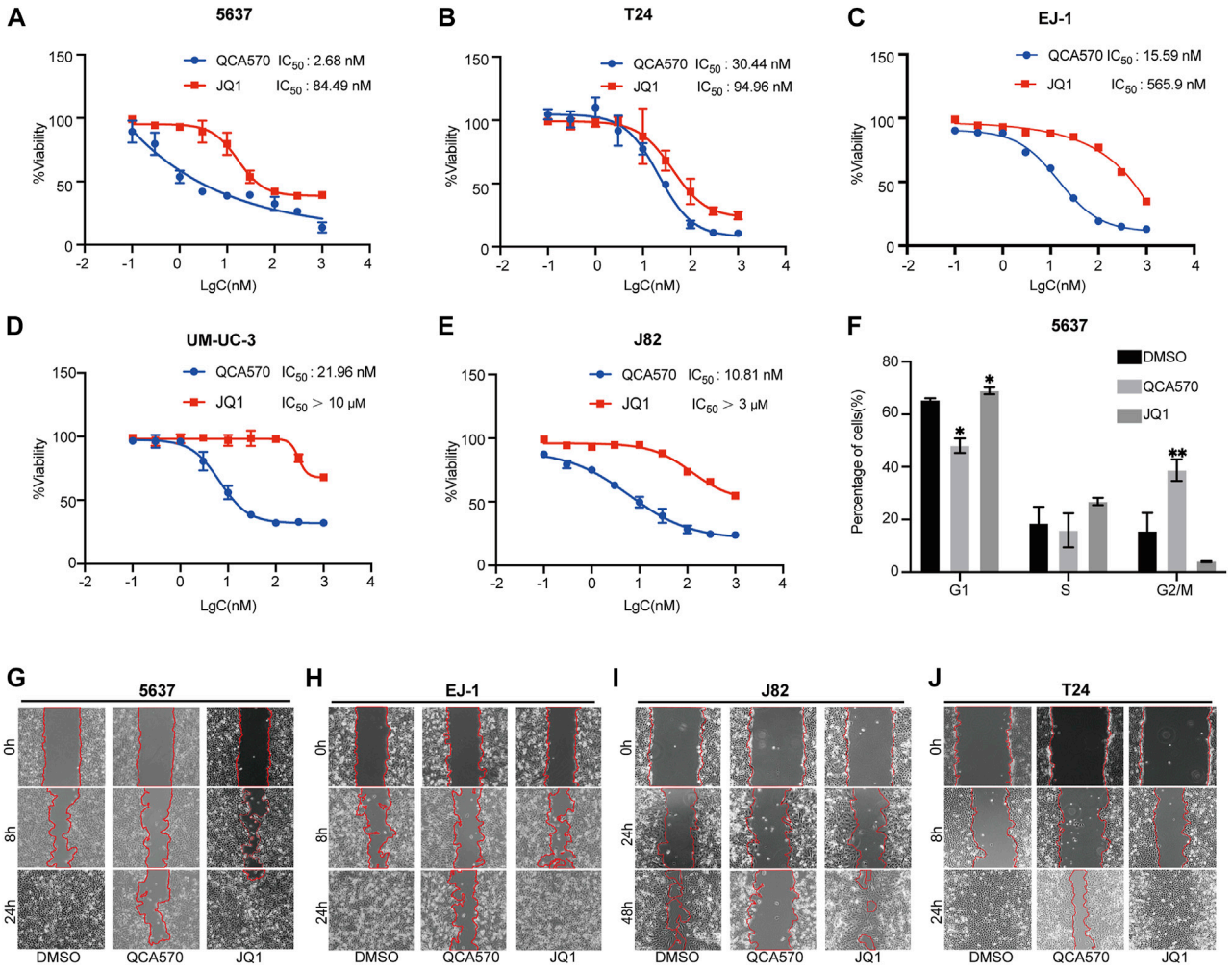

FIGURE 4
QCA570 treatment inhibits BC cell proliferation and migration **(A–E)** Antiproliferative effect of QCA570 or JQ1 in BC cell lines after 72 h treatment. Cell numbers were measured at the indicated time points with the CCK-8 assay and represented as absorbance at 450 nm. Values are the means ± SEM, $*p < 0.05$; $**p < 0.01$, two-tailed Student's t-test. **(F)** 5637 cells were exposed to QCA570 (10 nM) or JQ1 (10 nM) for 72 h then collected for analysis using flow cytometry. Data was analyzed using Flowjo software and the quantified result was plotted with GraphPad Prism9.0. Values are the means ± SEM, $*p < 0.05$; $**p < 0.01$, two-tailed Student's t-test. **(G-J)** Wound-healing assay was performed on 5637, EJ1, J82 and T24 cells with a treatment of QCA570 (100 nM) or JQ1 (100 nM) at indicated time points. The dotted line represents the wound healing boundary.

QCA570 suppresses the expression of BRD4 target genes in BC cells

Previous studies have reported that BET inhibition blocks expression of certain key oncogenes, such as c-MYC in many cancers (Filippakopoulos et al., 2010; Sahai et al., 2016). The Jiang group recently showed that BRD4 can promote EZH2 gene transcription through upregulation of c-MYC which functions as a transcription factor supporting BC progression (Xie et al., 2020; Wu et al., 2016). The mRNA expression data from TCGA and GEO database shows that EZH2 is upregulated in BC tissues, which suggests that the EZH2 gene is significantly associated with BC cancer risk (Figure 3A, B). To investigate whether BRD4 degradation down-regulates the expression level of EZH2, we determined the mRNA levels of these two genes in BC cell lines J82 and T24. In response to treatment with QCA570, the expression of c-MYC and EZH2 was significantly reduced with BRD4 degradation while the BET inhibitor JQ1 showed less suppression activity (Figures 3C, D). The protein level was also consistent with the qPCR results (Figures 3E-G).

QCA570 inhibits the cancer phenotype of BC cells

We next examined the antitumor effect of QCA570 on BC cell proliferation. As shown in Figure 4A-E, QCA570 effectively decreased the survival of the five BC cell lines tested, with IC_{50} values ranging from 2 to 30 nM. Notably, 5637 cells and J82 cells were particularly sensitive to QCA570 treatment, with IC_{50} values of 2.6 and 10.8 nM. In contrast, JQ1 is much less potent than QCA570 in each BC cell line tested. We also observed that QCA570 induced G2/M phase arrest of the cell cycle in 5637 cells (Figure 4F), further confirming the functional effect of

10.3389/fchem.2023.1121724

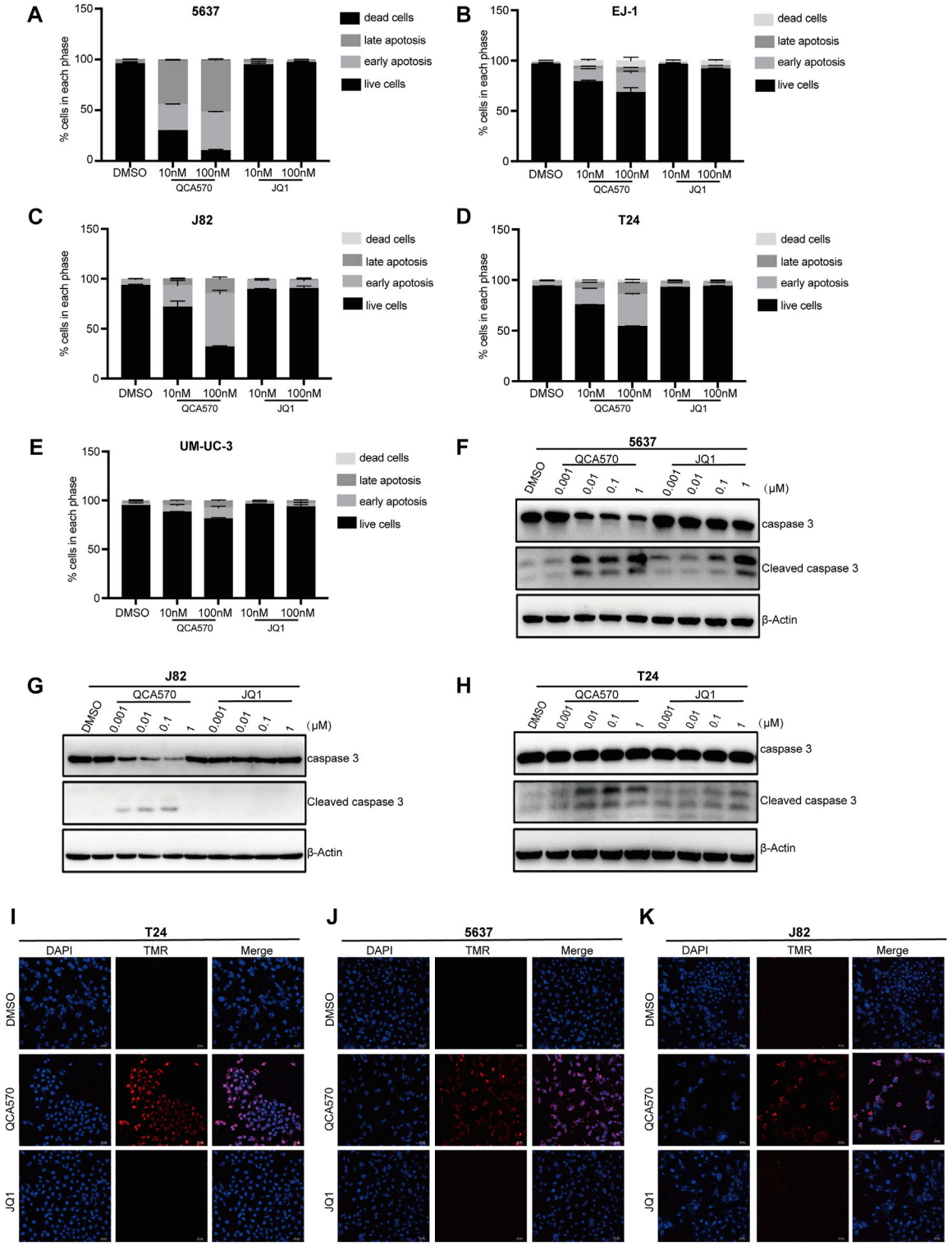

FIGURE 5
QCA570 induced cell apoptosis and cell cycle arrest **(A–E)** EJ-1, 5637, J82, UMUC-3 and T24 cells were treated with QCA570 or JQ1 for 72 h, and cell apoptosis was determined by Annexin V-FITC/PI staining and flow cytometry. Percentages of apoptosis cells were plotted using GraphPad Prism 9.0. Data were presented as means ± SEM. **(F–H)** 5637, J82 and T24 cells were treated with different concentrations of QCA570 or JQ1 for 72 h. Western blot analysis of the expression of cleaved caspase-3. **(I–K)** Apoptosis was analyzed by TUNEL staining. The red dots represented apoptotic cells, and DAPI (blue) indicated cell nuclei. Magnification, × 10.

QCA570. We investigated cell migration ability that represents another cancer-related feature which has been associated by wound healing assays with tumor metastasis. The results showed that with a 24 h treatment in 5637, EJ-1, J82 and T24 cells, QCA570 significantly suppressed cell migration ability (Figures 4G-J).

QCA570 induces BC cell apoptosis

To better understand the antiproliferation mechanism of QCA570, we investigated the effect of QCA570 on cell apoptosis in BC cell lines. Flow cytometry results demonstrated that QCA570 increased cell apoptosis in a dose-dependent manner (Figures 5A-E). In J82 and 5637 cell lines, apoptosis was induced in more than 50% of cells by QCA570 treatment. As a comparison, JQ1 had minimal effect on cell apoptosis. Consistent with the flow cytometry data, WB with cleaved Caspase-3 detection (Figures 5F-H) and a TUNEL assay of DNA break staining (Figures 5I-K) further confirmed that QCA570 induced greater cell apoptosis than in JQ1 in BC cells.

Discussion

BRD4 is the most extensively studied member of the BET family, and has emerged as an attractive therapeutic target for cancer therapy. It is widely considered to be a driver of transcriptional activation and is involved in a variety of cancers by mediating the expression of oncogenes such as c-MYC, bcl-xL and bcl-6 (Lovén et al., 2013; Donati, Lorenzini, and Ciarrocchi 2018). It has been reported that BRD4 knockdown leads to cell cycle arrest, cell apoptosis and tumor growth inhibition in bladder cancer both *in vitro* and *in vivo*. In the current study, we observed after analyzing data from TGCA and GEO, that BRD4 was upregulated in BC tissues as compared to the corresponding normal bladder tissues. Furthermore, high expression of BRD4 was correlated with the poor prognosis of BC patients as shown by the Kaplan-Meier survival curve. These findings indicate that BRD4 might play a tumor-activator role in bladder cancer progression and targeting this protein could be an effective therapy for bladder cancer.

Recently, several potent small-molecule BRD4 inhibitors such as JQ1 and I-BET, which disrupt BET proteins binding to acetylated histones, have been discovered and have shown promising therapeutic potential in preclinical models of multiple cancers (Filippakopoulos et al., 2010; Filippakopoulos and Knapp 2014; Boi et al., 2015). However, due to drug resistance and lack of sustained transcriptional inhibition of targets, these agents showed limited clinical activity (Piya et al., 2019). For example, in Burkitt's lymphoma cells, high concentrations and continuous exposure to BRD4 inhibitors were required to suppress the expression of c-MYC (Lu et al., 2015). In prostate cancer, mutated Speckle type POZ protein (SPOP) leads to impaired degradation and upregulation of BRD4 protein which confers intrinsic resistance to BET inhibitors (Janouskova et al., 2017; Dai et al., 2017; Zhang et al., 2017). In addition, several studies have revealed that BRD4 inhibitors cause the feedback elevation of BRD4 and less suppression of c-MYC expression (Fu et al., 2015; Hajmirza et al., 2018; White, Fenger, and Carson 2019). More recently, BET degraders, known as proteolysis targeting chimeric molecules (PROTACs), have been developed and exert more rapid, potent and durable inhibition of targets (Raina et al., 2016). The novel pan BET degrader, QCA570 showed more potent cell growth inhibitory activity in leukemia cell lines than previously published BET degraders such as dBET1,43 ARV-825,37 ARV-771,47 and ZBC26044 (Qin et al., 2018). The PROTAC molecule also displayed suppression of the survival of several human lung cancer cell lines with induction of apoptosis (C. Liu et al., 2022a). Therefore, in order to provide more potential therapies for bladder cancer, we employed this BET degrader, QCA570 to evaluate its antitumor effect on bladder cancer cells.

In our study, we observed a significant degradation of BET proteins induced by QCA570 in multiple BC cell lines and confirmed the PROTAC mechanism of QCA570 in BC cells. Wu has recently reported that BRD4 can positively regulate EZH2 gene expression through upregulation of c-MYC and that the BRD4/c-MYC/EZH2 axis plays a vital role in the regulation of bladder cancer progression. Therefore, we analyzed the expression of target genes under conditions of BRD4 depletion. Compared with BET inhibitor JQ1, QCA570 treatment resulted in much more suppression at the mRNA and protein levels of c-MYC and EZH2. Next, we explored the antitumoral activity of QCA570 on BC cells, as compared with JQ1. In multiple BC cell lines, QCA570 showed higher inhibition of cell proliferation and migration than JQ1. Meanwhile, we found that the G2/M cell cycle in 5637 cells was significantly arrested by QCA570, and further exploration with multiple detection methods showed that QCA570 efficiently induces cell apoptosis.

In conclusion, we have demonstrated that the high expression of BRD4 is correlated with the progression of BC patients and we tested the activity of the potent BRD4 degrader QCA570 on multiple BC cell models. We validated the suppression of c-MYC and EZH2 genes by QCA570 and its antitumor effect on BC cell lines. In view of the promising effects of the QCA570 against BC cells, we are providing a new approach to an effective therapy of human BC patients.

Data availability statement

Publicly available datasets were analyzed in this study. This data can be found here: https://www.ncbi.nlm.nih.gov/geo/ - GSE48276 and GSE13507.

Author contributions

QW: data curation, formal analysis, investigation; BL, WZ, and ZL: data curation and formal analysis; BJ, SH: writing, review and editing; SM, CQ: supervision, resources, writing, review and editing. All authors have read and agreed with the published version of the manuscript.

Funding

This work was supported by the grants from National Natural Science Foundation of China (22107095), Natural Science Foundation of Shandong Province, China (ZR2021YQ53).

Conflict of interest

The authors declare that the research was conducted in the absence of any commercial or financial relationships that could be construed as a potential conflict of interest.

Publisher's note

All claims expressed in this article are solely those of the authors and do not necessarily represent those of their affiliated organizations, or those of the publisher, the editors and the reviewers. Any product that may be evaluated in this article, or claim that may be made by its manufacturer, is not guaranteed or endorsed by the publisher.

Supplementary material

The Supplementary Material for this article can be found online at: https://www.frontiersin.org/articles/10.3389/fchem.2023.1121724/full#supplementary-material

References

Békés, M., Langley, D. R., and Crews, C. M. (2022). PROTAC targeted protein degraders: The past is prologue. *Nat. Rev. Drug Discov* 21 (3), 181–200. doi:10.1038/s41573-021-00371-6

Boi, M., Gaudio, E., Bonetti, P., Kwee, I., Elena, B., and Tarantelli, C., (2015). The BET bromodomain inhibitor OTX015 affects pathogenetic pathways in preclinical B-cell tumor models and synergizes with targeted drugs. *Clin. Cancer Res. Official J. Am. Assoc. Cancer Res* 21 (7), 1628–1638. doi:10.1158/1078-0432.CCR-14-1561

Burslem, G. M., and Crews, C. M. (2020). Proteolysis-targeting chimeras as therapeutics and tools for biological discovery. *Cell* 181 (1), 102–114. doi:10.1016/j.cell.2019.11.031

Dai, X., Gan, W., Li, X., Wang, S., Zhang, W., and Huang, L., (2017). Prostate cancer-associated SPOP mutations confer resistance to BET inhibitors through stabilization of BRD4. *Nat. Med* 23 (9), 1063–1071. doi:10.1038/nm.4378

Dobruch, J., and Oszczudłowski, M. (2021). Bladder cancer: Current challenges and future directions. *Med. Kaunas. Lith* 57 (8), 749. doi:10.3390/medicina57080749

Donati, B., Lorenzini, E., and Ciarrocchi, A. (2018). BRD4 and cancer: Going beyond transcriptional regulation. *Mol. Cancer* 17 (1), 164. doi:10.1186/s12943-018-0915-9

Duan, Y., Guan, Y., Qin, W., Zhai, X., Yu, B., and Liu, H. (2018). Targeting Brd4 for cancer therapy: Inhibitors and degraders. *MedChemComm* 9 (11), 1779–1802. doi:10.1039/c8md00198g

Filippakopoulos, P., and Knapp, S. (2014). Targeting bromodomains: Epigenetic readers of lysine acetylation. *Nat. Rev. Drug Discov* 13 (5), 337–356. doi:10.1038/nrd4286

Filippakopoulos, P., Qi, J., Picaud, S., Shen, Y., Smith, W. B., and Fedorov, O., (2010). Selective inhibition of BET bromodomains. *Nature* 468 (7327), 1067–1073. doi:10.1038/nature09504

Fu, L.-l., Tian, M., Xiang, L., Li, J. J., Huang, J., and Ouyang, L., (2015). Inhibition of BET bromodomains as a therapeutic strategy for cancer drug discovery. *Oncotarget* 6 (8), 5501–5516. doi:10.18632/oncotarget.3551

Hajmirza, A., Emadali, A., Gauthier, A., Casasnovas, O., Gressin, R., and MaryCallanan, B. (2018). BET family protein BRD4: An emerging actor in NFκB signaling in inflammation and cancer. *Biomedicines* 6 (1), 16. doi:10.3390/biomedicines6010016

Janouskova, H., Geniver El, T., Bellini, E., Udeshi, N. D., Anna, R., and Ulbricht, A., (2017). Opposing effects of cancer-type-specific SPOP mutants on BET protein degradation and sensitivity to BET inhibitors. *Nat. Med* 23 (9), 1046–1054. doi:10.1038/nm.4372

Jin, X., Yan, Y., Wang, D., Ding, D., Ma, T., and Ye, Z., (2018). DUB3 promotes BET inhibitor resistance and cancer progression by deubiquitinating BRD4. *Mol. Cell* 71 (4), 592–605. doi:10.1016/j.molcel.2018.06.036

Jung, M., Gelato, K. A., Fernández-Montalván, A., Siegel, S., and Haendler, B. (2015). Targeting BET bromodomains for cancer treatment. *Epigenomics* 7 (3), 487–501. doi:10.2217/epi.14.91

Lenis, A. T., Lec, P. M., Chamie, K., and Mshs, M. D. (2020). Bladder cancer: A review. *JAMA* 324 (19), 1980–1991. doi:10.1001/jama.2020.17598

Liu, C., Qian, L., Vallega, K. A., Ma, G., Zong, D., and Chen, L., (2022). The novel BET degrader, QCA570, is highly active against the growth of human NSCLC cells and synergizes with osimertinib in suppressing osimertinib-resistant EGFR-mutant NSCLC cells. *Am. J. Cancer Res* 12 (2), 779–792.

Liu, T., Zhang, Z., Wang, C., Huang, H., and Li, Y. (2022). BRD4 promotes the migration and invasion of bladder cancer cells through the sonic hedgehog signaling pathway and enhances cisplatin resistance. *Biochem. Cell Biol. = Biochimie Biol. Cell* 100 (2), 179–187. doi:10.1139/bcb-2021-0552

Lovén, J., Hoke, H. A., Lin, C. Y., Lau, A., Orlando, D. A., and Vakoc, C. R., (2013). Selective inhibition of tumor oncogenes by disruption of super-enhancers. *Cell* 153 (2), 320–334. doi:10.1016/j.cell.2013.03.036

Lu, J., Qian, Y., Altieri, M., Dong, H., Wang, J., and Raina, K., (2015). Hijacking the E3 ubiquitin ligase cereblon to efficiently target BRD4. *Chem. Biol* 22 (6), 755–763. doi:10.1016/j.chembiol.2015.05.009

Neklesa, T. K., Winkler, J. D., and Crews, C. M. (2017). Targeted protein degradation by PROTACs. *Pharmacol. Ther* 174 , 138–144. doi:10.1016/j.pharmthera.2017.02.027

Ozer, H. G., El-Gamal, D., Powell, B., Hing, Z. A., Blachly, J. S., and Harrington, B., (2018). BRD4 profiling identifies critical chronic lymphocytic leukemia oncogenic circuits and reveals sensitivity to PLX51107, a novel structurally distinct BET inhibitor. *Cancer Discov* 8 (4), 458–477. doi:10.1158/2159-8290.CD-17-0902

Piya, S., Mu, H., Bhattacharya, S., Lorenzi, P. L., Eric Davis, R., and Teresa, M. Q., (2019). BETP degradation simultaneously targets acute myelogenous leukemic stem cells and the microenvironment. *J. Clin. Investigation* 129 (5), 1878–1894. doi:10.1172/JCI120654

Qin, C., Hu, Y., Zhou, B., Fernandez-Salas, E., Yang, C.-Y., and Liu, L., (2018). Discovery of QCA570 as an exceptionally potent and efficacious proteolysis targeting chimera (PROTAC) degrader of the bromodomain and extra-terminal (BET) proteins capable of inducing complete and durable tumor regression. *J. Med. Chem* 61 (15), 6685–6704. doi:10.1021/acs.jmedchem.8b00506

Raina, K., Lu, J., Qian, Y., Altieri, M., Gordon, D., Ann marie, K. R., and jing, W. (2016). PROTAC-induced BET protein degradation as a therapy for castration-resistant prostate cancer. *Proceedings. Natl. Acad. Sci. USA* 113 (26), 7124–7129. doi:10.1073/pnas.1521738113

Sahai, V., Redig, A. J., Collier, K. A., Eckerdt, F. D., and Munshi, H. G. (2016). Targeting BET bromodomain proteins in solid tumors. *Oncotarget* 7 (33), 53997–54009. doi:10.18632/oncotarget.9804

Segura, M. F., Fontanals-Cirera, B., Gaziel-Sovran, A., Guijarro, M. V., Hanniford, D., and Zhang, G., (2013). BRD4 sustains melanoma proliferation and represents a new target for epigenetic therapy. *Cancer Res* 73 (20), 6264–6276. doi:10.1158/0008-5472.CAN-13-0122-T

Wang, S., Pike, A. M., Lee, S. S., Strong, M. A., Connelly, C. J., and Greider, C. W. (2017). BRD4 inhibitors block telomere elongation. *Nucleic Acids Res* 45 (14), 8403–8410. doi:10.1093/nar/gkx561

White, M. E., Fenger, J. M., and Carson, W. E. (2019). Emerging roles of and therapeutic strategies targeting BRD4 in cancer. *Cell. Immunol* 337, 48–53. doi:10.1016/j.cellimm.2019.02.001

Witjes, J. A., Bruins, H. M., Cathomas, R., Compérat, E. M., Cowan, N. C., and Gakis, G., (2021). European association of urology guidelines on muscle-invasive and metastatic bladder cancer: Summary of the 2020 guidelines. *Eur. Urol* 79 (1), 82–104. doi:10.1016/j.eururo.2020.03.055

Wu, X., Dong, L., Tao, D., Xiang, W., Xiao, X., and Wang, M., (2016). BRD4 regulates EZH2 transcription through upregulation of C-myc and represents a novel therapeutic target in bladder cancer. *Mol. Cancer Ther* 15 (5), 1029–1042. doi:10.1158/1535-7163.MCT-15-0750

Wu, Y., Wang, Y., Diao, P., Zhang, W., Jin, L., and Han, G., (2019). Therapeutic targeting of BRD4 in head neck squamous cell carcinoma. *Theranostics* 9 (6), 1777–1793. doi:10.7150/thno.31581

Xie, F., Xiao, X., Tao, D., Huang, C., Wang, L., and Liu, F., (2020). CircNR3C1 suppresses bladder cancer progression through acting as an endogenous blocker of BRD4/C-myc complex. *Mol. Ther. Nucleic Acids* 22 , 510–519. doi:10.1016/j.omtn.2020.09.016

Yan, Y., Yang, F.-Q., Zhang, H.-M., Li, J., Li, W., and Wang, G.-C., (2014). Bromodomain 4 protein is a predictor of survival for urothelial carcinoma of bladder. *Int. J. Clin. Exp. Pathology* 7 (7), 4231–4238.

Zhang, P., Wang, D., Zhao, Y., Ren, S., Gao, K., and Ye, Z.,(2017). Intrinsic BET inhibitor resistance in SPOP-mutated prostate cancer is mediated by BET protein stabilization and AKT-MTORC1 activation. *Nat. Med* 23 (9), 1055–1062. doi:10.1038/nm.4379

Zhang, X., Zheng, Y.-Y., Hu, C.-M., Wu, X.-Z., Lin, J., and Xiong, Z., (2022). Synthesis and biological evaluation of coumarin derivatives containing oxime ester as α-glucosidase inhibitors. *Arabian J. Chem* 15 (9), 104072. doi:10.1016/j.arabjc.2022.104072

Zuber, J., Shi, J., Wang, E., Rappaport, A. R., Herrmann, H., and Sison, E. A., (2011). RNAi screen identifies Brd4 as a therapeutic target in acute myeloid leukaemia. *Nature* 478 (7370), 524–528. doi:10.1038/nature10334

frontiers | Frontiers in Chemistry

TYPE Original Research
PUBLISHED 13 February 2023
DOI 10.3389/fchem.2023.1097027

OPEN ACCESS

EDITED BY
Xuetao Xu,
Wuyi University, China

REVIEWED BY
Xinhui Su,
Zhejiang University, China
Edson Roberto Silva,
University of São Paulo, Brazil

*CORRESPONDENCE
Qiangqiang Jia,
jia1108029@163.com
Shoude Zhang,
shoude.zhang@qhu.edu.cn

†These authors have contributed equally to this work

SPECIALTY SECTION
This article was submitted to Medicinal and Pharmaceutical Chemistry, a section of the journal Frontiers in Chemistry

RECEIVED 13 November 2022
ACCEPTED 30 January 2023
PUBLISHED 13 February 2023

CITATION
Ma Y, Zhang F, Zhong Y, Huang Y, Yixizhuoma, Jia Q and Zhang S (2023), A label-free LC/MS-based enzymatic activity assay for the detection of PDE5A inhibitors. *Front. Chem.* 11:1097027.
doi: 10.3389/fchem.2023.1097027

A label-free LC/MS-based enzymatic activity assay for the detection of PDE5A inhibitors

Yufeng Ma[1,2†], Fengsen Zhang[1,2†], Yijing Zhong[2], Yongchun Huang[2], Yixizhuoma[1], Qiangqiang Jia[1*] and Shoude Zhang[1,2*]

[1]State Key Laboratory of Plateau Ecology and Agriculture, Qinghai University, Xining, China, [2]Department of Pharmacy, Medical College of Qinghai University, Xining, China

Phosphodiesterase type 5 (PDE5), a cyclic nucleotide phosphodiesterase, controls the duration of the cyclic guanosine monophosphate (cGMP) signal by hydrolyzing cGMP to GMP. Inhibiting the activity of PDE5A has proven to be an effective strategy for treating pulmonary arterial hypertension and erectile dysfunction. Current enzymatic activity assay methods for PDE5A mainly use fluorescent or isotope-labeled substrates, which are expensive and inconvenient. Here, we developed an LC/MS-based enzymatic activity assay for PDE5A without labeling, which detects the enzymatic activity of PDE5A by quantifying the substrate cGMP and product GMP at a concentration of 100 nM. The accuracy of this method was verified by a fluorescently labeled substrate. Moreover, a new inhibitor of PDE5A was identified by this method and virtual screening. It inhibited PDE5A with an IC_{50} value of 870 nM. Overall, the proposed strategy provides a new method for screening PDE5A inhibitors.

KEYWORDS

PDE5A, LC/MS, cGMP, enzyme activity, inhibitor

1 Introduction

cGMP is a unique second messenger that is commonly involved in the opening of cell membrane ion channels (Biel and Michalakis 2009), glycogen decomposition (Zhang et al., 2022), apoptosis (Kim et al., 1999), and relaxation of smooth muscle (Ignarro and Kadowitz 1985). It is produced by soluble guanosine cyclase (sGC) and granular guanosine cyclase (pGC) after combining with nitric oxide (NO) and natriuretic peptides (NPs), respectively (Cerra and Pellegrino 2007; Hofmann 2020; Friebe et al., 2020). cGMP mediates NO biological signals through three major cellular targets, including cGMP-dependent protein kinase G (PKG), cyclized nucleotide cation-gated channels (CNG), and PDEs (Francis et al., 2010). The main target molecule of cGMP action is PKG, and the activation of PKG is usually associated with the regulation of processes such as calcium homeostasis (Chen et al., 2009), smooth muscle contraction (Rybalkin et al., 2003), platelet activation, and adhesion (Li et al., 2003). The intracellular homeostasis of cGMP is mainly regulated by PDE5A and GC (Mullershausen et al., 2004). The PDE superfamily can be divided into 11 families, namely, PDE1-11, according to their sequence homology, substrate specificity, and regulatory characteristics (Omori and Kotera 2007). PDE5A is the most well-studied phosphodiesterase in this family and is expressed in lung, brain, kidney, cardiomyocytes, gastrointestinal tissues, vascular smooth muscle cells, platelets, penile spongy body, and many other tissues (Kotera et al., 2000; Daniela et al., 2001). As shown in Figure 1, PDE5A converts cGMP to 5′-GMP, an inactive form, by hydrolyzing the phosphodiester bond (Lin 2004; Lugnier 2006). Preventing the degradation of cGMP by PDE5A inhibitors, such as sildenafil and vardenafil, has become a strategy for the treatment of

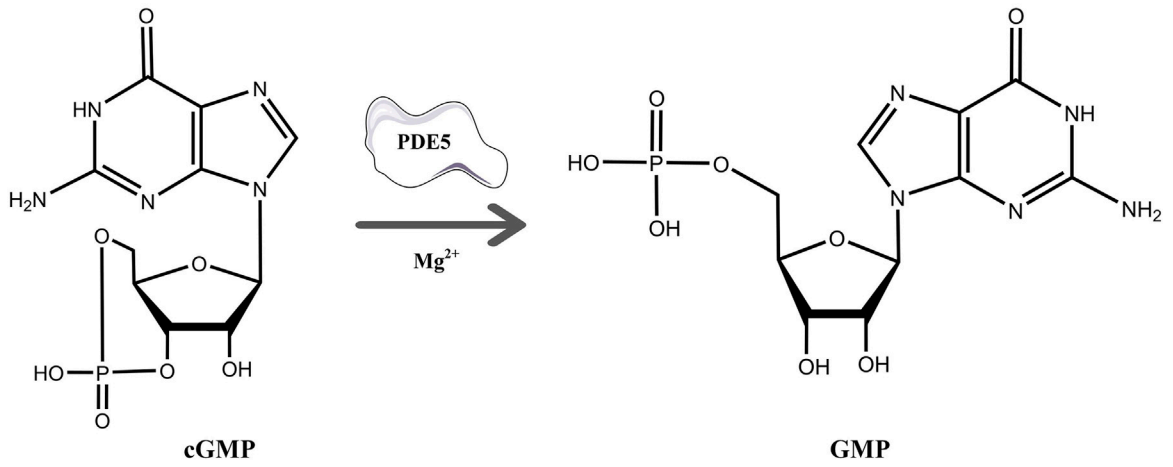

FIGURE 1
The process of hydrolysis of cGMP to GMP by PDE5A and differences in the chemical structures of cGMP and GMP.

diseases such as pulmonary hypertension and erectile dysfunction (Corbin et al., 2005; Sandner et al., 2007). However, due to the high homology among family members, the clinical application of drugs is limited (Setter et al., 2005; Ueda et al., 2019), so the development of selective PDE5A inhibitors is of great importance.

Fluorescent or isotope-labeled substrates are widely used in current inhibitor screening for PDE5A (Xu et al., 2011; Li et al., 2013; Shibata et al., 2020) and are expensive or inconvenient. Here, we developed a novel PDE5A enzymatic activity assay method based on LC/MS. In this method, free-labeled cGMP and GMP are separated by UHPLC with high resolution and quantified by mass spectrometry at the nanomolar level. The enzymatic activity of PDE5A treated with inhibitor or without inhibitor could be detected by analyzing the quantity change in cGMP or GMP. In this work, we not only confirmed the accuracy of this method with a fluorescent labeling method but also verified a virtual screening result of PDE5A inhibitors with this method. Finally, a new PDE5A inhibitor was identified with this method.

2 Materials and methods

2.1 Materials

The following materials were obtained from Sigma–Aldrich (St. Louis, MO, United States): guanosine 3′,5′-cyclic monophosphate sodium salt (cGMP, HPLC, 99%), zirconyl chloride octahydrate ($ZrOCl_2$, reagent grade, 98%), and bovine serum albumin (BSA, ≥98%). Guanosine monophosphate (GMP), sildenafil citrate (HPLC), and vardenafil HCl trihydrate (HPLC) were purchased from Aladdin (Shanghai, China). Deionized water was purified by a Milli-Q purification system (Millipore, Bedford, MA, United States). HPLC grade acetonitrile, HPLC formic acid, HPLC methanol, and HisPur™ Ni-NTA Resin were purchased from Thermo Fisher Scientific (Vilnius, Lithuania). Dimethyl sulfoxide (DMSO≥99%), ultrafiltration spin columns (0.5 mL, 10 kDa MWCO, PES, Sartorius), and 96-well black opaque plates were purchased from Beyotime Biotechnology (Shanghai, China). Proanthocyanidins and nine other standards were purchased from Baoji Herbest Bio-Tech Co., Ltd, and 2′-O-(6-[tetramethylrhodaminyl]aminopentylcarbamoylethylcarbonyl) guanosine-3′,5′-cyclic monophosphate trifluoroacetate salt (96%) was purchased from AAT Bioquest, Inc. (TAMRA-R-cGMP, Sunnyvale, CA, United States). All other reagents were of analytical grade and obtained from Sinopharm Chemical Reagent Co., Ltd. (Shanghai China).

2.2 Protein expression and purification

The catalytic domain of PDE5A (residues 535-862; GenBank accession number BC126233.1) was subcloned into the T7 promoter-driven expression vector pET21b with a 6 × His-tag at the C-terminus (Hsieh et al., 2020). The recombinant plasmid was transformed into *E. coli* strain BL21 (DE3) and grown in an autoinducing medium (Studier 2005) containing 50 μg/mL ampicillin at 37 C until OD600 = 0.6–0.7, then induced protein expression at 15°C for 40 h. The PDE5A protein was purified through the Ni-NTA column (Thermo Scientific) and further purified by the HiPrep™26/60 Sephacryl™-S-200HR column (GE Healthcare). A typical batch cell yielded over 10 mg of the PDE5A protein from 1 L of autoinducing medium with a purity >95% based on SDS–PAGE. The protein was concentrated to a certain concentration using centrifugal filters and stored in a storage buffer (50 mM NaCl, 20 mM Tris-HCl pH 7.5, 1 mM β-mercaptoethanol, 1 mM EDTA, and 5% glycerol).

2.3 LC/MS method

2.3.1 LC/MS condition

The chromatographic separation of cGMP and GMP was achieved on a Hypersil GOLD™ aQ C18 column (1.9 μm, 100 mm × 2.1 mm, Thermo Scientific) using phase A (100% LC/MS grade acetonitrile) and phase B (0.1% LC/MS grade formic acid in water), followed by 0.00 min: 1% A, 3 min: 1% A, 6 min: 90% A, 8 min: 90% A, 10 min: 1% A, 12 min:

1% A, at a consistent flow rate of 0.3 mL/min. The injection volume was set at 2 μL, and the column temperature was controlled at 35°C.

MS analysis was performed on a Thermo Fisher Q Exactive Plus mass spectrometer (Waltham, MA, United States; Thermo, Bremen, Germany) with a heated electrospray ionization (HESI) ion source. The separated samples from UHPLC were injected into the system and analyzed by positive ion swing with full MS and SIM scans. The HESI parameters in positive polarity were as follows: spray voltage 3.5 kV; capillary temperature 320°C; auxiliary gas heater temperature 300 C; sheath gas flow rate 35 μL/min; auxiliary gas flow rate 10 μL/min; S-lens RF level was 50 V; full MS scan resolution of primary parent ions was 70,000 full width at half maximum (FWHM); scan range was 100–1,500 m/z; the automated gain control (AGC) target was 1 E^6; SIM scan resolution of daughter ion was 35,000 FWHM; maximum IT was 50 m; isolation window in quadrupole was 3.0 m/z, and specific normalized collision energy (NCE) for each precursor m/z in 35.

During analyzation, Xcalibur 4.1 (Thermo Fisher Scientific, San Jose, CA, United States) was used to determine and integrate peak areas. After that, the linear correlation between the peak area and concentration of GMP was calculated based on the above condition and gradient concentration of GMP.

2.3.2 Method validations

Method validation was performed from the aspects of linearity, range, precision accuracy, reproducibility, stability according to our previous research (Jia et al., 2020). Briefly, the linearity was expressed by linear regression between the peak area and the analyte concentration. LOD was defined as the concentration when the signal intensity was three times than that of noise (S/N = 3) and LOQ was defined as the concentration when S/N = 10. To determine the accuracy, reaction samples were spiked with standards solution of cGMP and GMP with a concentration of 5 μg/mL and analyzed six times for each standard and the recovery rate was calculated by comparing the changes of amounts. The precision was detected in a day (intra-day) and in 3 days (inter-day) with the cGMP and GMP standards at the concentration 5 μg/mL. The stability was evaluated by analyzing the 5 μg/mL mixed standard solution at 0, 12, 24, 36, and 48 h, and the variations were expressed as RSDs. The cGMP and GMP standards at the concentration of 5 μg/mL were used to determine the repeatability.

2.4 Enzymatic activity assay method

Enzyme activity refers to the ability of an enzyme to catalyze a certain chemical reaction. The enzyme activity of PDE5A can be calculated by the increase in the product GMP per unit time (U/mg, where 1 U is the amount of enzyme that consumes 1 μmol of cGMP per minute). Plots of GMP production vs. time and amount of enzyme vs. reaction speed were fit by linear regression using GraphPad Prism 9. The absolute value of the slope of the production vs. time curves is defined as the activity of PDE5A. Relationships between substrate concentration [S] and PDE5A activity (v) were fit by non-linear regression using GraphPad Prism 9 according to the Michaelis and Menten equation (Bisswanger 2014),

$$v = v_{max}[S]/(Km + [S]) \quad (1)$$

where v_{max} is the maximum reaction rate and K_m the concentration of substrate [S] at which the enzymatic reaction reaches half the maximum velocity v_{max}. The total reaction volume was set to 200 μL, and the substrate and enzyme were each 100 μL. The reaction was terminated by boiling for 5 min at 100°C. After cooling, the protein was removed by ultrafiltration membrane (0.5 mL, 10 KD, Merck Millipore) filtration, and the filtrate was detected by LC/MS.

2.5 Assay for measuring PDE5A inhibition

Each assay was performed in a 150 μL reaction volume containing PDE5A (50 nM), various concentrations of compounds, and cGMP (10 μM), each 50 μl PDE5A was placed at room temperature for 30 min with the small molecule, cGMP was added, and the reaction mixture was left to settle at room temperature for 15 min. For the compound inhibition study on PDE5A, stock solutions of the compounds were prepared in 100% DMSO and diluted in reaction buffer (10 mM Tris–HCl pH 7.5, 0.1 mg/mL BSA, 10 mM $MgCl_2$, and 1 mM β-ME) to the appropriate concentrations to give a final concentration of <2% DMSO. After the reaction, the mixed solution was filtered by an ultrafiltration membrane to remove the protein, the filtrated solution was tested by LC/MS using established methods, and the GMP peak release was recorded. Relative PDE5A activity (%) was calculated by normalizing the activity of negative controls (background factors need to be excluded). PDE5A inhibitory activity was calculated from the equation below (background subtraction for each group: $C_{negative.GMP}$).

$$\%\text{PDE5A inhibition} = \left(C_{positive.GMP} - C_{compound.GMP}\right) \times \Big/ C_{positive.GMP} \times 100\% \quad (2)$$

In this equation, $C_{negative.GMP}$ represents the production of GMP (without enzyme); $C_{positive.GMP}$ indicates the amount of product after hydrolysis of cGMP by PDE5A; and $C_{compound.GMP}$ represents the amount of hydrolysate after the compound inhibits PDE5A.

2.6 Virtual screening method

An in-house compound database containing 1,427 natural products was used for virtual screening. The structures and X-ray crystal structure of PDE5A (PDB: 1TBF) were prepared by MGLTools developed by the Scripps Research Institute. The grid box of the receptor was centered on the ligand sildenafil in the refined crystal structure and defined to enclose the residues located within 40 points from the ligand. The docking process was performed using AutoDock Vina with the default docking parameter (Trott and Olson 2010). Ten conformers were generated in the docking process for every compound, and only the top conformer for each compound was retained. Finally, the top 50 compounds were reserved for further visual observation, and 10 compounds were selected for experimental testing.

2.7 Enzyme activity assay based on fluorescently labeled substrate

TAMRA-R-cGMP is a derivative of cGMP linked with a red fluorescence group. It can bind to cGMP binding site of PDE5A and has been used for enzyme activity determination and inhibitor screening according to changes in fluorescence intensity (Santillo and Mapa 2018). Assays were performed in 96-well black opaque plates with a volume of 100 μL per well. Then, 200 nM PDE5A (25 μL) was

mixed with various concentrations of compounds (25 μL) in reaction buffer (10 mM Tris–HCl pH 7.5, 0.1 mg/mL BSA, 10 mM $MgCl_2$ and 1 mM β-ME). After incubation for 30 min at room temperature, an equal volume of 100 μM $ZrOCl_2$ (25 μL) and 5 μM TAMRA-R-cGMP (25 μL) was added to the solution. Check for fluorescence quenching after 15 min. Incubations for negative control (no PDE5A), positive control (PDE5A), and background (assay buffer) were tested in triplicate wells for each assay run. The inhibition activity of the compounds was initially screened at 20 μM and the IC_{50} values for the active compounds were calculated at various concentrations. Fluorescence intensity was measured with Filter Max F5 Multi-Mode Microplate Readers (Molecular Devices) at an excitation wavelength of 535 nm and an emission wavelength of 590 nm. Each measurement was repeated at least 3 times, and IC_{50} values were calculated by non-linear regression in GraphPad Prism 9. PDE5A inhibitory activity was calculated from the equation below:

$$\%\text{PDE5A inhibition} = \left(FI_{compound} - FI_{positive}\right) \Big/ \times \left(FI_{negative} - FI_{positive}\right) \times 100\% \quad (3)$$

In this equation, $FI_{negative}$ represents the reaction system containing only fluorescent substrates (without enzyme); $FI_{positive}$ indicates the fluorescence value of the substrate after hydrolysis of cGMP by PDE5A; and $FI_{compound}$ represents the fluorescence value of the remaining substrate after the compound inhibits PDE5A.

3 Results and discussion

3.1 Establishment of the LC/MS-based enzymatic activity assay for the detection of PDE5A inhibitors

3.1.1 Strategy of LC/MS-based enzymatic activity assay for the detection of PDE5A

As shown in Figure 1, cGMP and GMP have different structures and molecular weights, which lead to different retention times in liquid chromatography. Based on our established liquid chromatography conditions, cGMP and GMP can be separated with high resolution, and the retention times were 3.09 min and 1.39, respectively (Figure 2A). After separation, cGMP and GMP can be further quantified by mass spectrometry. Based on this principle, we developed a new strategy to detect quantitative changes in cGMP and GMP in the catalytic reaction of PDE5A (Figure 2B). Both the decrease in cGMP and the increase in GMP are related to the activity of PDE5A. After the quantified PDE5A and cGMP were incubated with the compounds, PDE5A was removed from the reaction buffer by an ultrafiltration tube, and the filtrate was used to detect the changes in the cGMP and GMP contents. The ion peaks of cGMP and GMP could be extracted by Xcalibur 4.1 software and quantified by the standard curve between the GMP concentration and peak. The inhibition rate was calculated by Equation (B). Next, this method is used not only for the determination of the enzyme activity of PDE5A but also for the screening of new inhibitors in combination with virtual screening.

3.1.2 Method validation

The results of method validation are summarized in Table 1. Within the concentration range, the calibration curves of the GMP and cGMP showed good linearity, with correlation coefficients greater than 0.9960. The LOD and LOQ ranges of the GMP and cGMP are 0.03–0.10 μg/mL and 0.02–0.05 μg/mL, respectively, which indicates that the detection of the GMP and cGMP by this method is sufficiently sensitive. The recovery range of accuracy for GMP and cGMP are 98.67% and 96.94, respectively, with RSD less than 3.79%. The RSDs of inter-day and intra-day precision ranged from 3.86% to 4.33% and from 2.01% to 3.89%, respectively. The RSD values in stability are less than 1.96%, which implied that GMP and cGMP in solution are stable for 48 h at room temperature. The RSD values of the repeatability ranged from 2.19% to 2.95%, which indicated that the developed method is reliable.

3.1.3 Detection of the relative enzyme activity of PDE5A based on a LC/MS strategy

In the process of enzyme activity determination, to ensure whether the boiling termination process affects cGMP stability, a reaction system containing only substrate was set up, and GMP was detected after boiling at 95°C for 5 min. Simultaneously, to ensure that the boiling process could completely terminate the enzyme activity, a reaction system containing only PDE5A was set up. GMP was detected after PDE5A was boiled for 5 min at 95°C and incubated with cGMP for 15 min. Finally, no GMP was detected by the LC/MS method, indicating that the boiling process not only did not affect the stability of cGMP but also completely terminated the enzymatic activity of PDE5A. To quantify the product GMP in the enzyme-catalyzed reaction, a linear standard curve of peak area and concentration was first established using the GMP standard (R^2 = 0.9967).

To find an optimal reaction time and quantify the enzymatic activity of PDE5A, the change in GMP was detected over time in 33 min, and a linear fit was made to the change in amount and time (Figure 3A). Finally, the optimal reaction time was selected as 15 min within the linear response range, and the absolute values of these slopes were defined as PDE5A activity. To select the appropriate enzyme concentration, we determined the initial reaction velocity (V_0) of PDE5A at different concentrations (Figure 3B), and a concentration of 50 nM was selected within the linear range to ensure the fastest reaction rate. The specific activity was calculated by dividing the enzyme activity by the amount of enzyme, and the result was 0.3 U/mg. According to the Michaelis and Menten analysis, the half-maximum concentration (K_m) of GMP was 3.87 ± 0.12 μM (Figures 3C,D), which is consistent with the reference value of the literature (Kouvelas et al., 2009). Therefore, the substrate concentration was selected to be 10 μm to ensure the enzyme binding site as much as possible (Acker and Douglas, 2014).

3.1.4 Feasibility analysis of the LC/MS-based method in PDE5A inhibitor screening

To show the feasibility of the developed LC/MS-based method in PDE5A inhibitor screening, this method was used to assay the inhibitory activity of sildenafil and vardenafil, which are two known inhibitors of PDE5A with high affinity for PDE5A (Shabsigh et al., 2006) and are widely used in erectile dysfunction and pulmonary hypertension. The established LC/MS-based method was used to detect the quantitative change in GMP after the addition of two inhibitors, and the inhibition rate was calculated using Equation

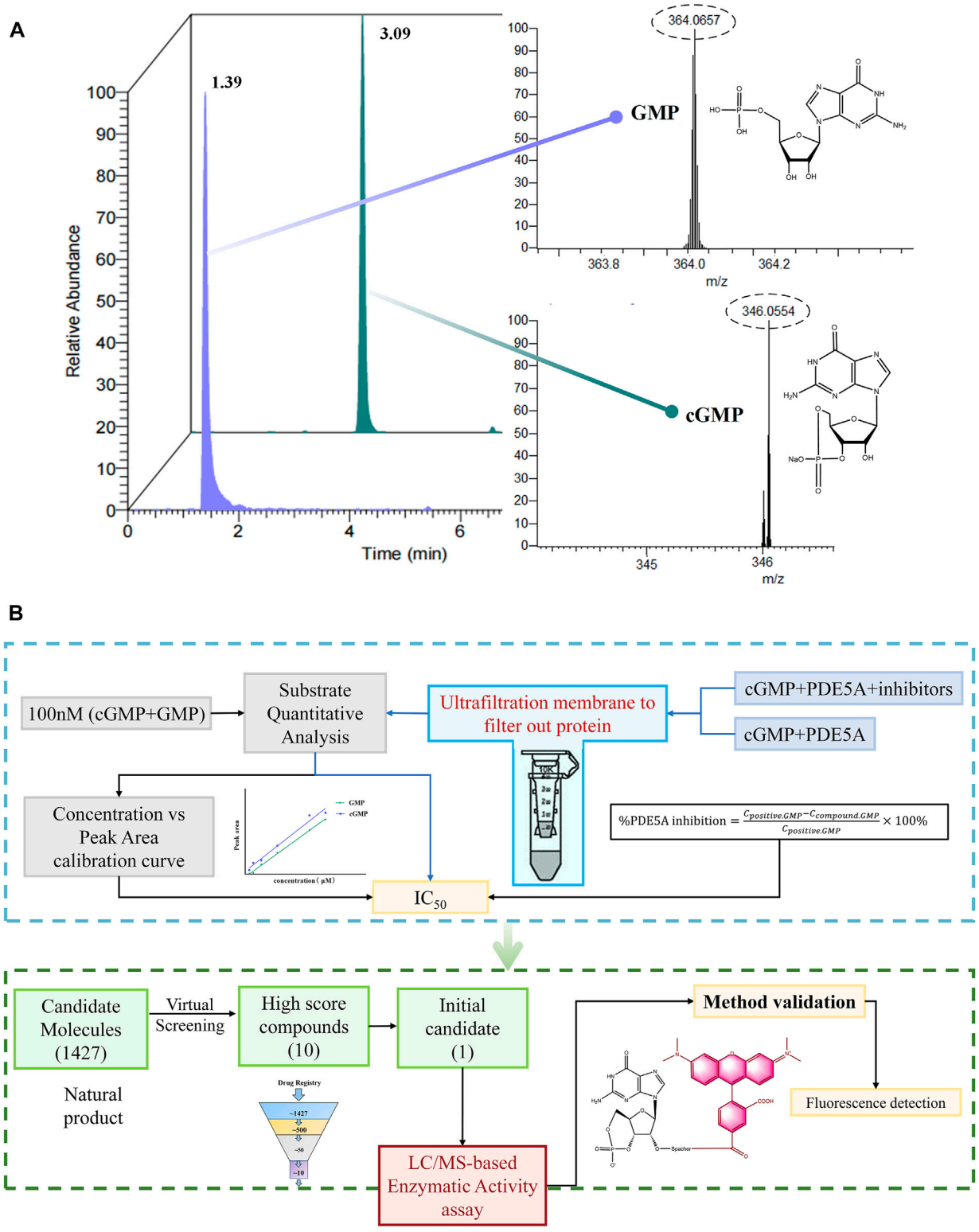

FIGURE 2
Enzyme activity assay and inhibitor screening strategy for PDE5A based on LC/MS. **(A)** The analyzed results of GMP and cGMP by LC/MS at 100 nM. **(B)** Routes for the determination of enzyme activity and new inhibitors of PDE5A by this method.

B). Finally, sildenafil and vardenafil inhibited the enzymatic activity of PDE5A with IC_{50} values of 78.72 ± 1.7 nM and 1.47 ± 0.02 nM, respectively (Figures 4A,B), which were consistent with previous reports (Rotella 2002; Dell'Agli et al., 2005).

3.2 Screening of new inhibitors of PDE5A

All reported PDE5A inhibitors are competitive inhibitors, which bind to the catalytic site of PDE5A (Kim et al., 2001). Therefore, we performed a

TABLE 1 Linearity, LOD and LOQ, accuracy, precision, stability and repeatability of the LC/MS method (n = 6).

Analytes	Linearity			LOD (μg/L)	LOQ (μg/L)	Accuracy		Precision		Stability	Repeatability
	Calibration curves	Range (μg/mL)	R^2			Recovery (%)	RSD (%)	Inter-day RSD (%)	Intra-day RSD (%)	RSD (%)	RSD (%)
GMP	Y = 784184X-187112	0.1135–7.264	0.9967	0.03	0.10	98.67	2.31	4.33	2.42	1.96	2.19
cGMP	Y = 562405X+12921	0.057–7.344	0.9969	0.02	0.05	96.94	3.79	3.86	2.01	1.75	2.95

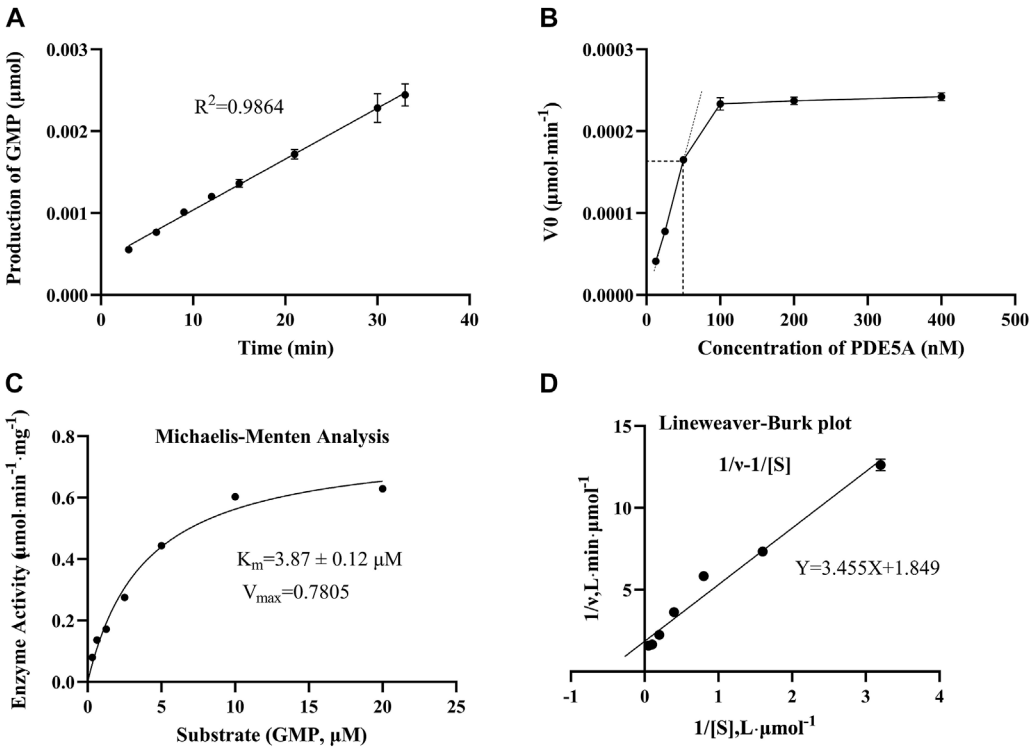

FIGURE 3
The results of the enzymatic activity assay of PDE5A. **(A)** Enzyme reaction progress curve. The linear portion of the reaction progress curve was fitted according to the throughput of GMP. **(B)** Enzyme concentration curve. The change in the initial reaction velocity (V_0) was determined at different enzyme concentrations (C_{cGMP} = 10 μM). **(C, D)** Michaelis-Menten analysis curve and Lineweaver Burk plot. K_m and V_{max} were determined using progression curve analysis by varying substrate concentrations (20–0.3125 μM).

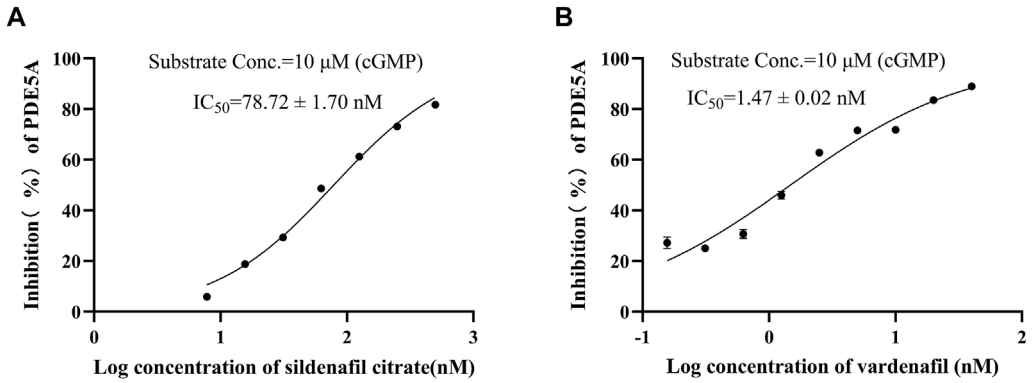

FIGURE 4
Positive drug inhibitory activity results were detected by LC/MS strategy. **(A)** Inhibitory activity of sildenafil citrate on PDE5A. **(B)** Inhibitory activity of vardenafil on PDE5A.

TABLE 2 Virtual screening results and essential information.

No	Name	Structure	CAS No	Docking Score (kcal/mol)
Positive	Sildenafil	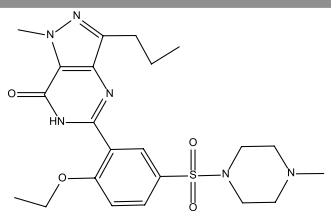	171599-83-0	−9.1
	Vardenafil	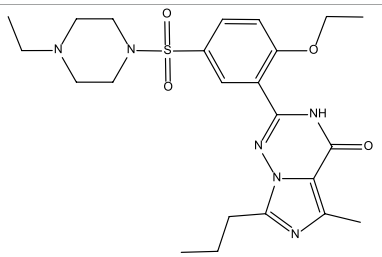	330808-88-3	−8.5
1	Kuwanon G	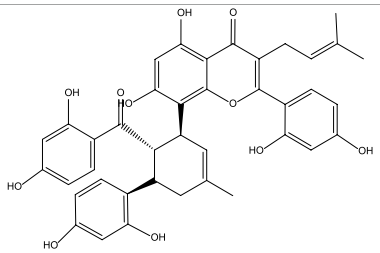	75629-19-5	−8.5
2	Proanthocyanidins	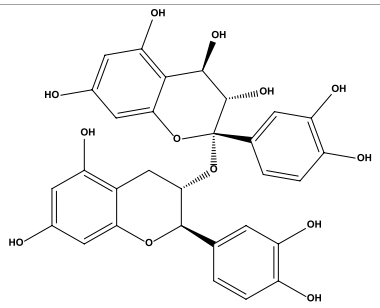	4852-22-6	−8.3
3	Daurisoline	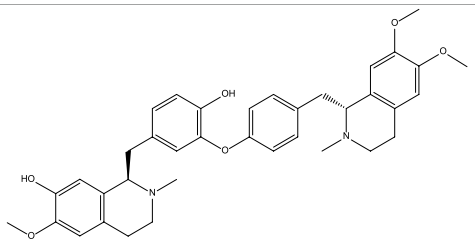	70553-76-3	−9.7
4	Isoliensinine	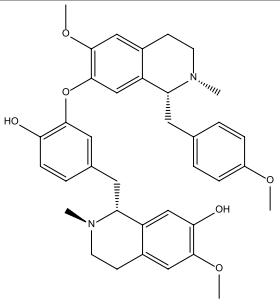	6817-41-0	−8.7

(Continued on following page)

10.3389/fchem.2023.1097027

TABLE 2 (*Continued*) Virtual screening results and essential information.

No	Name	Structure	CAS No	Docking Score (kcal/mol)
5	Ginkgetin	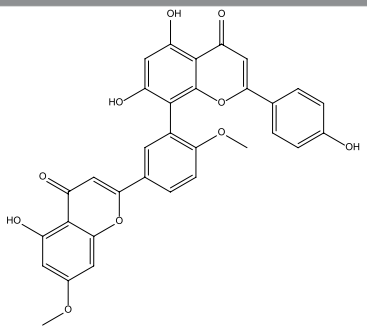	481-46-9	−10.2
6	7-O-Methylaloeresin A	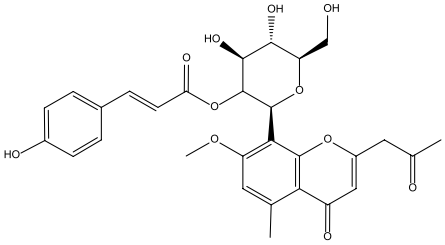	329361-25-3	−8.2
7	Silychristin	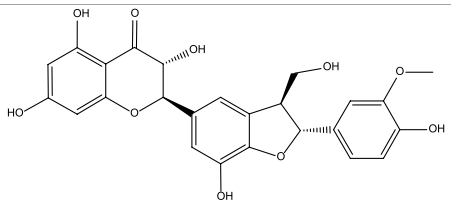	33889-69-9	−8.6
8	Isosilybin	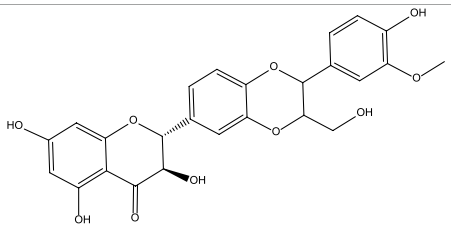	72581-71-6	−7.9
9	Cordycepin	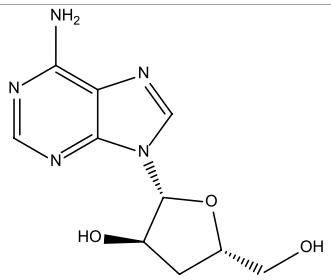	73-03-0	−7.0
10	Methylophiopogonone A	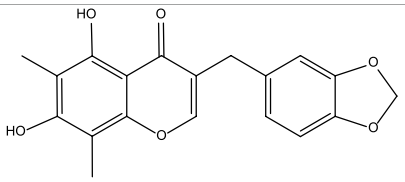	74805-90-6	−8.6

new competitive inhibitor screening based on the catalytic site of PDE5A. A total of 1,427 compounds were docked into the ligand binding site of PDE5A, and 10 compounds were finally selected for the activity assay based on the affinity score (Table 2) and visual selection. The inhibitory activities of these 10 compounds for PDE5A were determined by the LC/MS-based method and fluorescent-labeled substrates.

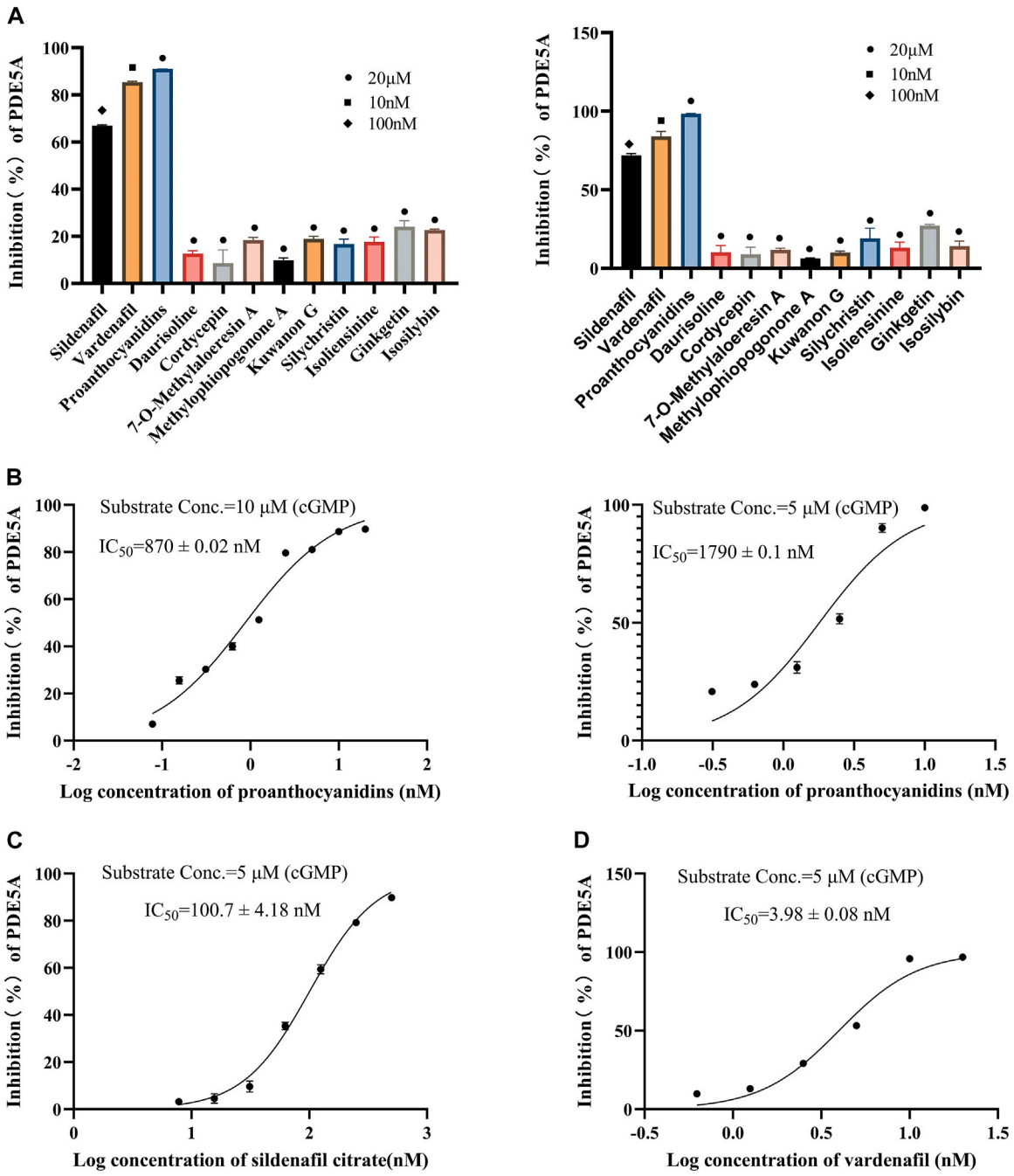

FIGURE 5
Inhibitory activity of 10 compounds for PDE5A based on the LC/MS-based method and luorescent-labeled substrate-based method. **(A)** Inhibitory activity of 10 compounds for PDE5A at 20 μM, and sildenafil and vardenafil were set to 100 nM and 10 nM, respectively (left: LC/MS-based method; right: luorescent-labeled substrate-based method). **(B)** Inhibition curve of proanthocyanidins. Left: LC/MS-based method; right: luorescent-labeled substrate-based method. **(C, D)** Inhibition curves of sildenafil, vardenafil (luorescent-labeled substrate-based method).

3.2.1 Results of the LC/MS-based method

All 10 compounds from virtual screening were initially assayed at a concentration of 20 μM, and sildenafil and vardenafil were selected as positive controls. The active compounds with significant inhibition rates at this concentration were selected to further test the IC_{50}. Among them, sildenafil and vardenafil exhibited 66% and 85% inhibition at 100 nM and 10 nM, respectively. Fortunately, one of the 10 compounds, named proanthocyanidins, showed significant inhibitory activity against PDE5A, with an inhibition rate of 91% at 20 μM. Other compounds were all less than 25% inhibitory (Figure 5A left). The IC_{50} of proanthocyanidins was calculated by setting gradient concentrations and was 870 ± 0.02 nM (Figure 5B left).

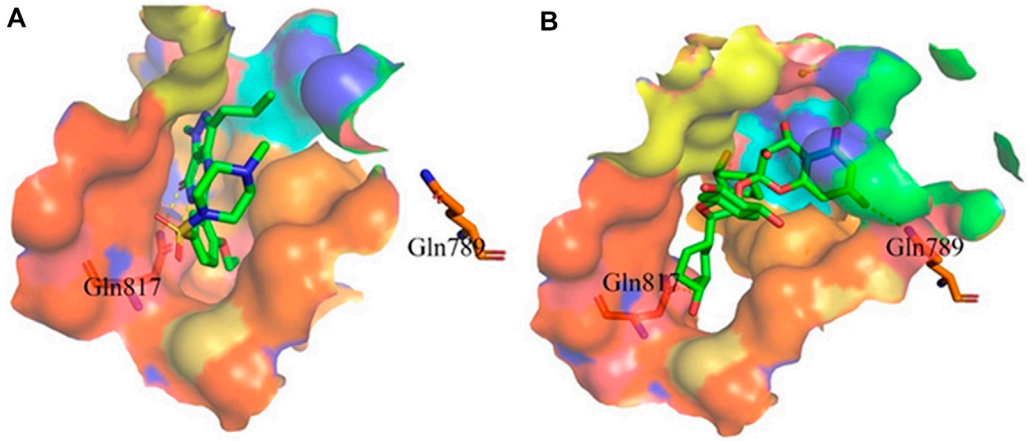

FIGURE 6
Binding mode between inhibitor and PDE5A. **(A)** Binding mode between sildenafil and PDE5A. **(B)** Binding mode between proanthocyanidins and PDE5A. Compounds are shown as a stick model with carbon atoms colored green, and PDE5A (PDB: 1TBF) is shown as the surface. Hydrogen bonds are represented by yellow dashed lines.

3.2.2 The results of the fluorescent-labeled substrate-based method

To verify the accuracy of the LC/MS-based method, a known method based on a fluorescently labeled substrate was used to test the activity of 10 compounds. As shown in Figure 5A Right, sildenafil (100 nM) and vardenafil (10 nM) showed more than 70% inhibitory activity against PDE5A, and the inhibitory activity of proanthocyanidins (20 μM) remained the strongest among the 10 compounds and reached 98%, which was consistent with the results measured by the LC/MS-based method. The IC_{50} values of and proanthocyanidins (1790 ± 0.09 nM) were still consistent with the results measured by the LC/MS-based method (Figure 5B right), sildenafil (100.7 ± 4.18 nM), vardenafil (3.98 ± 0.08 nM, Figures 5C,D).

3.2.3 Binding mode of proanthocyanidins and PDE5A

Proanthocyanidins, oligomeric compound formed by catechin and epicatechin molecules, are present in the flowers, nuts, fruits, bark, and seeds of various plants (Ou and Gu 2014). Here, proanthocyanidins was identified as a new inhibitor of PDE5A. To understand the inhibitory activity of proanthocyanidins, we checked the binding mode between proanthocyanidins and PDE5A based on the molecular docking result. Compared to the binding mode of sildenafil (Figure 6A), proanthocyanidins not only occupied the sildenafil site well but also a part of the structure extends to the active site on the right side and interacts with PDE5A in a hydrophobic manner (Figure 6B). Sildenafil forms a hydrogen bond with the residue Gln817, but proanthocyanidins formed another hydrogen bond with the residue Gln789 in addition to Gln817. Overall, the two-part structures of proanthocyanidins, catechin and epicatechin, not only occupy the binding site of sildenafil but also increase the binding range to the active site of PDE5, while the formation of two hydrogen bonds enhances its affinity to PDE5.

4 Conclusion

In conclusion, we established a new method for enzyme activity testing for PDE5A based on LC/MS, which has the advantages of being label-free, safe, and economical. Based on the high sensitivity of this method, it can detect not only the *in vitro* activity of PDE5A but also the enzyme activity of *in vivo* samples. Meanwhile, this method also provides an assay idea for enzyme activity testing based on similar substrates, such as cAMP. Moreover, proanthocyanidins was identified as a new inhibitor of PDE5A with high affinity by the LC/MS-based method.

Data availability statement

The datasets presented in this study can be found in online repositories. The names of the repository/repositories and accession number(s) can be found in the article.

Author contributions

YM: Data curation and writing of the original draft. FZ: Data curation and validation. YZ: Software. YH: Data curation. Yixizhuoma: Review and editing. QJ: Supervision and validation. SZ: Supervision, funding acquisition, and manuscript editing.

Funding

This work was supported by the Project of Qinghai Science and Technology Department (2021-QY-203).

Conflict of interest

The authors declare that the research was conducted in the absence of any commercial or financial relationships that could be construed as a potential conflict of interest.

Publisher's note

References

Acker, M. G., and Douglas, S. A. (2014). Considerations for the design and reporting of enzyme assays in high-throughput screening applications. *Perspect. Sci.* 1 (1-6), 56–73. doi:10.1016/j.pisc.2013.12.001

Biel, M., and Michalakis, S. (2009). Cyclic nucleotide-gated channels. *Handb. Exp. Pharmacol.* 191, 111–136. doi:10.1007/978-3-540-68964-5_7

Bisswanger, H. (2014). Enzyme assays. *Perspect. Sci.* 1 (1-6), 41–55. doi:10.1016/j.pisc.2014.02.005

Cerra, M. C., and Pellegrino, D. (2007). Cardiovascular cGMP-generating systems in physiological and pathological conditions. *Curr. Med. Chem.* 14 (5), 585–599. doi:10.2174/092986707780059715

Chen, H. P., Liao, Z. P., Huang, Q. R., and He, M. (2009). Sodium ferulate attenuates anoxia/reoxygenation-induced calcium overload in neonatal rat cardiomyocytes by NO/cGMP/PKG pathway. *Eur. J. Pharmacol.* 603 (1-3), 86–92. doi:10.1016/j.ejphar.2008.12.003

Corbin, J. D., Beasley, A., Blount, M. A., and Francis, S. H. (2005). High lung PDE5: A strong basis for treating pulmonary hypertension with PDE5 inhibitors. *Biochem. biophysical Res. Commun.* 334 (3), 930–938. doi:10.1016/j.bbrc.2005.06.183

Daniela, G., Maria, E., De, S., and Gennaro, C. (2001). Expression of cGMP-binding cGMP-specific phosphodiesterase (PDE5) in mouse tissues and cell lines using an antibody against the enzyme amino-terminal domain. *Biochimica Biophysica Acta (BBA) - Mol. Cell Res.* 1539 (1-2), 16–27. doi:10.1016/s0167-4889(01)00086-6

Dell'Agli, M., V Galli, G., Vrhovsek, U., Mattivi, F., and Bosisio, E. (2005). *In vitro* inhibition of human cGMP-specific phosphodiesterase-5 by polyphenols from red grapes. *J. Agric. food Chem.* 53 (6), 1960–1965. doi:10.1021/jf048497+

Francis, S. H., Jennifer, L., and Jackie, D. C. (2010). cGMP-dependent protein kinases and cGMP phosphodiesterases in nitric oxide and cGMP action. *Pharmacol. Rev.* 62 (3), 525–563. doi:10.1124/pr.110.002907

Friebe, A., Sandner, P., and Schmidtko, A. (2020). cGMP: A unique 2nd messenger molecule–recent developments in cGMP research and development. *Naunyn-schmiedeberg's Archives Pharmacol.* 393 (2), 287–302. doi:10.1007/s00210-019-01779-z

Hofmann, F. (2020). The cGMP system: Components and function. *Biol. Chem.* 401 (4), 447–469. doi:10.1515/hsz-2019-0386

Hsieh, C. M., Chen, C. Y., Chern, J. W., and Chan, N. L. (2020). Structure of human phosphodiesterase 5A1 complexed with avanafil reveals molecular basis of isoform selectivity and guidelines for targeting alpha-helix backbone oxygen by halogen bonding. *J. Med. Chem.* 63 (15), 8485–8494. doi:10.1021/acs.jmedchem.0c00853

Ignarro, L. J., and Kadowitz, P. J. (1985). The pharmacological and physiological role of cyclic GMP in vascular smooth muscle relaxation. *Annu. Rev. Pharmacol. Toxicol.* 25 (1), 171–191. doi:10.1146/annurev.pa.25.040185.001131

Jia, Q., Zhang, S., Zhang, H., Yang, X., Cui, X., Su, Z., et al. (2020). A comparative study on polyphenolic composition of berries from the Tibetan plateau by UPLC-Q-orbitrap MS system. *Chem. Biodivers.* 17 (4), e2000033. doi:10.1002/cbdv.202000033

Kim, N. N., Huang, Y., Goldstein, I., Bischoff, E., and Abdulmaged, M. T. (2001). Inhibition of cyclic GMP hydrolysis in human corpus cavernosum smooth muscle cells by vardenafil, a novel, selective phosphodiesterase type 5 inhibitor. *Life Sci.* 69 (19), 2249–2256. doi:10.1016/s0024-3205(01)01308-x

Kim, Y. M., Chung, H. T., Kim, S. S., Han, J. A., Yoo, Y. M., Kim, K. M., et al. (1999). Nitric oxide protects PC12 cells from serum deprivation-induced apoptosis by cGMP-dependent inhibition of caspase signaling. *J. Neurosci.* 19 (16), 6740–6747. doi:10.1523/jneurosci.19-16-06740.1999

Kotera, J., Fujishige, K., and Omori, K. (2000). Immunohistochemical localization of cGMP-binding cGMP-specific phosphodiesterase (PDE5) in rat tissues. *J. Histochem. Cytochem.* 48 (5), 685–693. doi:10.1177/002215540004800512

Kouvelas, D., Goulas, A., Papazisis, G., Sardeli, C., and Pourzitaki, C. (2009). PDE5 inhibitors: *In vitro* and *in vivo* pharmacological profile. *Curr. Pharm. Des.* 15 (30), 3464–3475. doi:10.2174/138161209789206971

Li, Z., Xi, X., Gu, M., Feil, R., Richard, D. Y., Eigenthaler, M., et al. (2003). A stimulatory role for cGMP-dependent protein kinase in platelet activation. *Cell* 112 (1), 77–86. doi:10.1016/s0092-8674(02)01254-0

Li, Z., Cai, Y. H., Cheng, Y. K., Lu, X., Shao, Y. X., Li, X., et al. (2013). Identification of novel phosphodiesterase-4D inhibitors prescreened by molecular dynamics-augmented modeling and validated by bioassay. *J. Chem. Inf. Model* 53 (4), 972–981. doi:10.1021/ci400063s

Lin, C. S. (2004). Tissue expression, distribution, and regulation of PDE5. *Int. J. Impot. Res.* 16 (1), S8–S10. doi:10.1038/sj.ijir.3901207

Lugnier, C. (2006). Cyclic nucleotide phosphodiesterase (PDE) superfamily: A new target for the development of specific therapeutic agents. *Pharmacol. Ther.* 109 (3), 366–398. doi:10.1016/j.pharmthera.2005.07.003

Mullershausen, F., Russwurm, M., Koesling, D., and Friebe, A. (2004). *In vivo* reconstitution of the negative feedback in nitric oxide/cGMP signaling: Role of phosphodiesterase type 5 phosphorylation. *Mol. Biol. Cell* 15 (9), 4023–4030. doi:10.1091/mbc.e03-12-0890

Omori, K., and Kotera, J. (2007). Overview of PDEs and their regulation. *Circulation Res.* 100 (3), 309–327. doi:10.1161/01.res.0000256354.95791.f1

Ou, K., and Gu, L. (2014). Absorption and metabolism of proanthocyanidins. *J. Funct. Foods* 7, 43–53. doi:10.1016/j.jff.2013.08.004

Rotella, D. P. (2002). Phosphodiesterase 5 inhibitors: Current status and potential applications. *Nat. Rev. Drug Discov.* 1 (9), 674–682. doi:10.1038/nrd893

Rybalkin, S. D., Yan, C., Bornfeldt, K. E., and Beavo, J. A. (2003). Cyclic GMP phosphodiesterases and regulation of smooth muscle function. *Circulation Res.* 93 (4), 280–291. doi:10.1161/01.res.0000087541.15600.2b

Sandner, P., Hütter, J., Tinel, H., Ziegelbauer, K., and Bischoff, E. (2007). PDE5 inhibitors beyond erectile dysfunction. *Int. J. Impot. Res.* 19 (6), 533–543. doi:10.1038/sj.ijir.3901577

Santillo, M. F., and Mapa, M. S. T. (2018). Phosphodiesterase (PDE5) inhibition assay for rapid detection of erectile dysfunction drugs and analogs in sexual enhancement products. *Drug Test. Anal.* 10, 1315–1322. doi:10.1002/dta.2375

Setter, S. M., Iltz, J. L., Fincham, J. E., Campbell, R. K., and Baker, D. E. (2005). Phosphodiesterase 5 inhibitors for erectile dysfunction. *Ann. Pharmacother.* 39 (7-8), 1286–1295. doi:10.1345/aph.1E487

Shabsigh, R., Seftel, A. D., Rosen, R. C., Porst, H., Ahuja, S., Deeley, M. C., et al. (2006). Review of time of onset and duration of clinical efficacy of phosphodiesterase type 5 inhibitors in treatment of erectile dysfunction. *Urology* 68 (4), 689–696. doi:10.1016/j.urology.2006.05.009

Shibata, S., Sugiyama, T., Uekusa, Y., Masui, R., Narukawa, Y., and Kiuchi, F. (2020). Five new 2-(2-phenylethyl)chromone derivatives from agarwood. *J. Nat. Med.* 74 (3), 561–570. doi:10.1007/s11418-020-01410-z

Studier, F. W. (2005). Protein production by auto-induction in high-density shaking cultures. *Protein Expr. Purif.* 41 (1), 207–234. doi:10.1016/j.pep.2005.01.016

Trott, O., and Olson, A. J. (2010). AutoDock Vina: Improving the speed and accuracy of docking with a new scoring function, efficient optimization, and multithreading. *J. Comput. Chem.* 31 (2), 455–461. doi:10.1002/jcc.21334

Ueda, Y., Johnson, L. R., Ontiveros, E. S., Visser, L. C., Gunther-Harrington, C. T., and Stern, J. A. (2019). Effect of a phosphodiesterase-5A (PDE5A) gene polymorphism on response to sildenafil therapy in canine pulmonary hypertension. *Sci. Rep.* 9 (1), 6899. doi:10.1038/s41598-019-43318-z

Xu, Z., Liu, Z., Chen, T., Chen, T., Wang, Z., Tian, G., et al. (2011). Utilization of halogen bond in lead optimization: A case study of rational design of potent phosphodiesterase type 5 (PDE5) inhibitors. *J. Med. Chem.* 54 (15), 5607–5611. doi:10.1021/jm200644r

Zhang, X., Pan, L., Tong, R., Li, Y., Si, L., Chen, Y., et al. (2022). Effects of crustacean hyperglycaemic hormone RNA interference on regulation of glucose metabolism in Litopenaeus vannamei after ammonia-nitrogen exposure. *Br. J. Nutr.* 127 (6), 823–836. doi:10.1017/s0007114521001574

frontiers | Frontiers in Chemistry

TYPE Mini Review
PUBLISHED 16 February 2023
DOI 10.3389/fchem.2023.1132025

OPEN ACCESS

EDITED BY
Xi Zheng,
Rutgers, The State University of New Jersey, United States

REVIEWED BY
Jiean Chen,
Shenzhen Bay Laboratory, China
Bivas Mondal,
National University of Singapore, Singapore

*CORRESPONDENCE
Jia-Lei Yan,
yanjialei@wyu.edu.cn

†These authors have contributed equally to this work

SPECIALTY SECTION
This article was submitted to Medicinal and Pharmaceutical Chemistry, a section of the journal Frontiers in Chemistry

RECEIVED 26 December 2022
ACCEPTED 10 January 2023
PUBLISHED 16 February 2023

CITATION
Liu J, Chen H, Wang M, He W and Yan J-L (2023), Organocatalytic asymmetric synthesis of P-stereogenic molecules. *Front. Chem.* 11:1132025. doi: 10.3389/fchem.2023.1132025

Organocatalytic asymmetric synthesis of P-stereogenic molecules

Junyang Liu[1,2†], Hang Chen[3†], Min Wang[1], Wangjin He[1] and Jia-Lei Yan[1*]

[1]Innovation Center of Marine Biotechnology and Pharmaceuticals, School of Biotechnology and Health Sciences, Wuyi University, Jiangmen, China, [2]State Key Laboratory of Chemical Oncogenomics, Key Laboratory of Chemical Genomics, Peking University Shenzhen Graduate School, Shenzhen, China, [3]Division of Chemistry and Biological Chemistry, School of Chemistry, Chemical Engineering and Biotechnology, Nanyang Technological University, Singapore, Singapore

P-chirality broadly appears in natural and synthetic functional molecules. The catalytic synthesis of organophosphorus compounds bearing P-stereogenic centers is still challenging, due to the lack of efficient catalytic systems. This review summarizes the key achievements in organocatalytic methodologies for the synthesis of P-stereogenic molecules. Different catalytic systems are emphasized for each strategy class (desymmetrization, kinetic resolution, and dynamic kinetic resolution) with examples cited to illustrate the potential applications of the accessed P-stereogenic organophosphorus compounds.

KEYWORDS

organocatalysis, asymmetric synthesis, desymmetrization, kinetic resolution, P-chirality

Introduction

Organophosphorus compounds bearing P-stereogenic centers have widely emerged in biological molecules and natural products (Figure 1A)(Kolodiazhnyi, 2021), and they also serve as broadly useful ligands and catalysts in asymmetric synthesis (Dutartre et al., 2016; Xu et al., 2019; Imamoto, 2021) (Figure 1B). Nowadays, P-stereogenic scaffolds show an increasing presence in bioactive molecules for medical uses (Figure 1C). For example, remdesivir is used to treat coronavirus disease (Wang et al., 2020a). Tenofovir alafenamide is an antiviral prescription medicine for the treatment of HIV (Ray et al., 2016) and chronic hepatitis B infection (Scott and Chan, 2017); phostine serves as an anti-malignant proliferation agent (Bousseau et al., 2019). Cyclophostin is an inhibitor of acetylcholinesterase (Martin et al., 2015). It is worth noting that the absolute stereochemistry of phosphorus is often directly associated with the biological activity of these molecules (Pradere et al., 2014; Nocentini et al., 2019; Babbs et al., 2020; Nocentini et al., 2020). Thus, developing efficient strategies to access P-stereogenic organophosphorus compounds is of great importance.

In the early years, optically pure P-stereogenic compounds were obtained by relying on the resolution of organophosphorus enantiomers or the related diastereomeric mixtures (Meisenheimer and Lichtenstadt, 1911). The pioneering asymmetric strategy to access P-stereogenic molecules is chiral auxiliary-assisted synthesis, in which the auxiliary is bound to the P-atom to control the stereochemistry (Farnham et al., 1970; Berger and Montchamp, 2013). Similarly, using stoichiometric chiral reagents to influence the enantiomeric outcome of the P-stereogenic center is also a viable approach (Muci et al., 1995; Bergin et al., 2007; Kortmann et al., 2014). However, stoichiometric amounts of chiral reagents are essential in all the aforementioned strategies. In parallel, catalytic asymmetric strategies to access P-stereogenic molecules are more succinct and economic. These catalytic strategies have had an impressive breakthrough in the past two decades, especially in transition metal catalytic systems (Lemouzy et al., 2020; Ye et al., 2021). In contrast, organocatalytic asymmetric strategies were not so

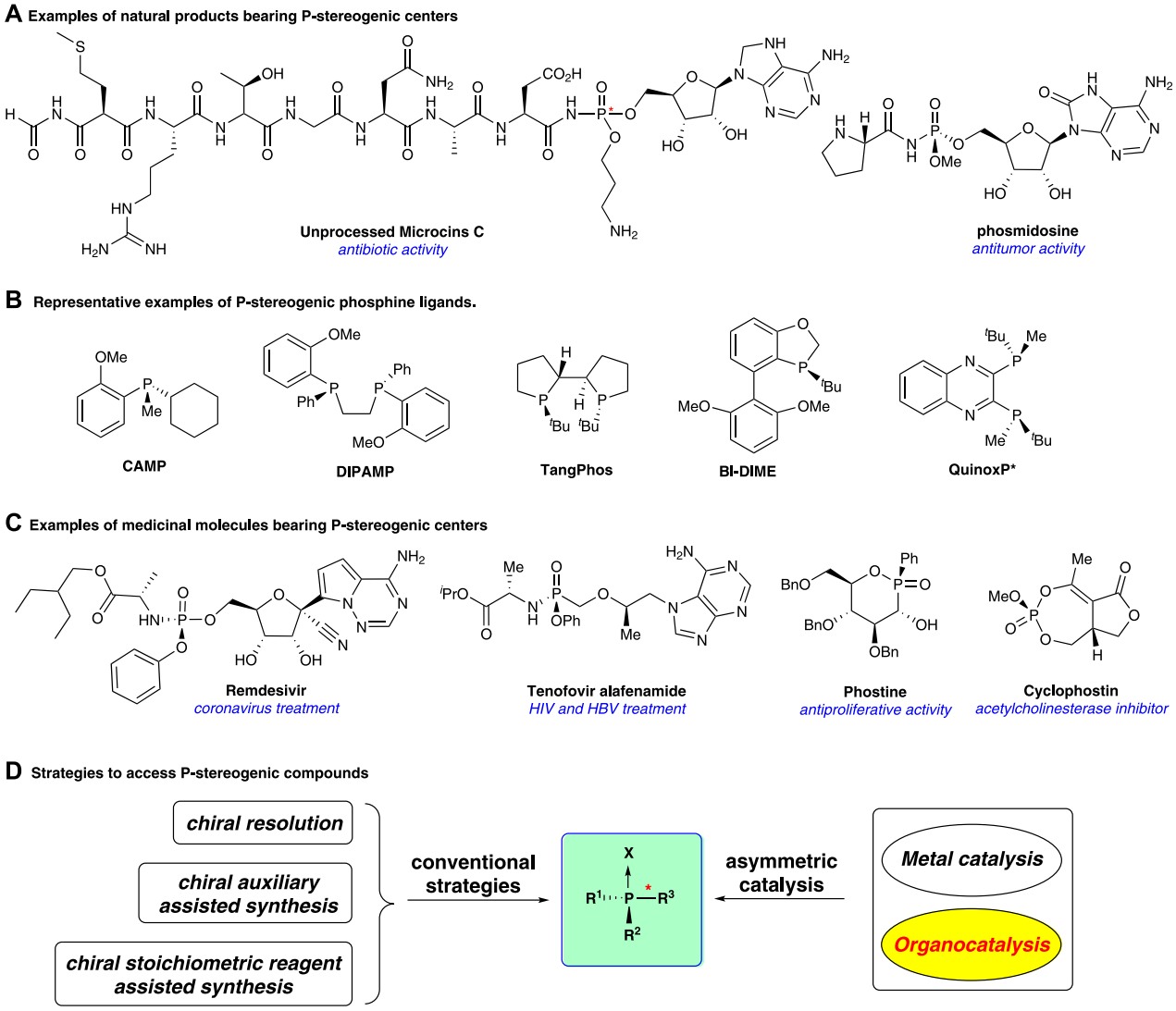

FIGURE 1
P-stereogenic compounds and the existing synthetic strategies. **(A)**: Examples of natural products; **(B)**: Examples of P-stereogenic phosphine ligands; **(C)**: Examples of medicinal molecules; **(D)**: Strategies to access P-stereogenic compounds.

developed until recent years. In order to guide a better understanding, this review will focus on organocatalytic strategies and introduces the most recent developments of stereoselective access to P-stereogenic compounds.

Asymmetric desymmetrization strategies

A powerful strategy to access P-stereogenic compounds is the desymmetrization of symmetrical achiral organophosphorus compounds, which has accounted for a large part of the catalytic synthesis of P-stereogenic compounds. This pioneering work was reported by Lebel et al. (2003), in which catalytic alkylation of phosphine–boranes for constructing P-stereogenic phosphine borane **2** was demonstrated using a *Cinchona* alkaloid-derived catalyst **C1** as a phase-transfer catalyst (Figure 2A; Supplementary Scheme S1). Although enantioselectivity was not satisfying (17% ee), this work greatly encouraged the synthesis of P-stereogenic phosphorus compounds through asymmetric organocatalysis.

In 2014, Johnston and co-workers reported a chiral Brønsted acid-catalyzed diastereo- and enantio-selective iodocyclization of phosphoramidic acid for the construction of C- and P-stereogenic cyclic phosphoramidates (Toda et al., 2014) (Figure 2B; Supplementary Scheme S2). Utilizing this strategy, a range of cyclic products (**4a**–**4f**) was prepared with high levels of absolute and relative stereocontrol (up to >20:1 dr, 98% ee). The resulting phosphoramidate products acted as precursors for enantio-enriched epoxy allylamines (**5**) upon treatment with alkoxy anions. Thus, this method could be regarded as a formal asymmetric epoxidation of allylamine derivatives.

With the diverse development of organocatalysis, more investigations on P-stereogenic constructions were performed. In 2016, the Chi group reported *N*-heterocyclic carbene (NHC)-catalyzed desymmetric acylation of pro-chiral bisphenol phosphine oxides for the synthesis of P-stereogenic phosphinates, phosphinamides, and triarylphosphine oxides (Figure 2C; Supplementary Scheme S3) (Huang et al., 2016). Good to excellent

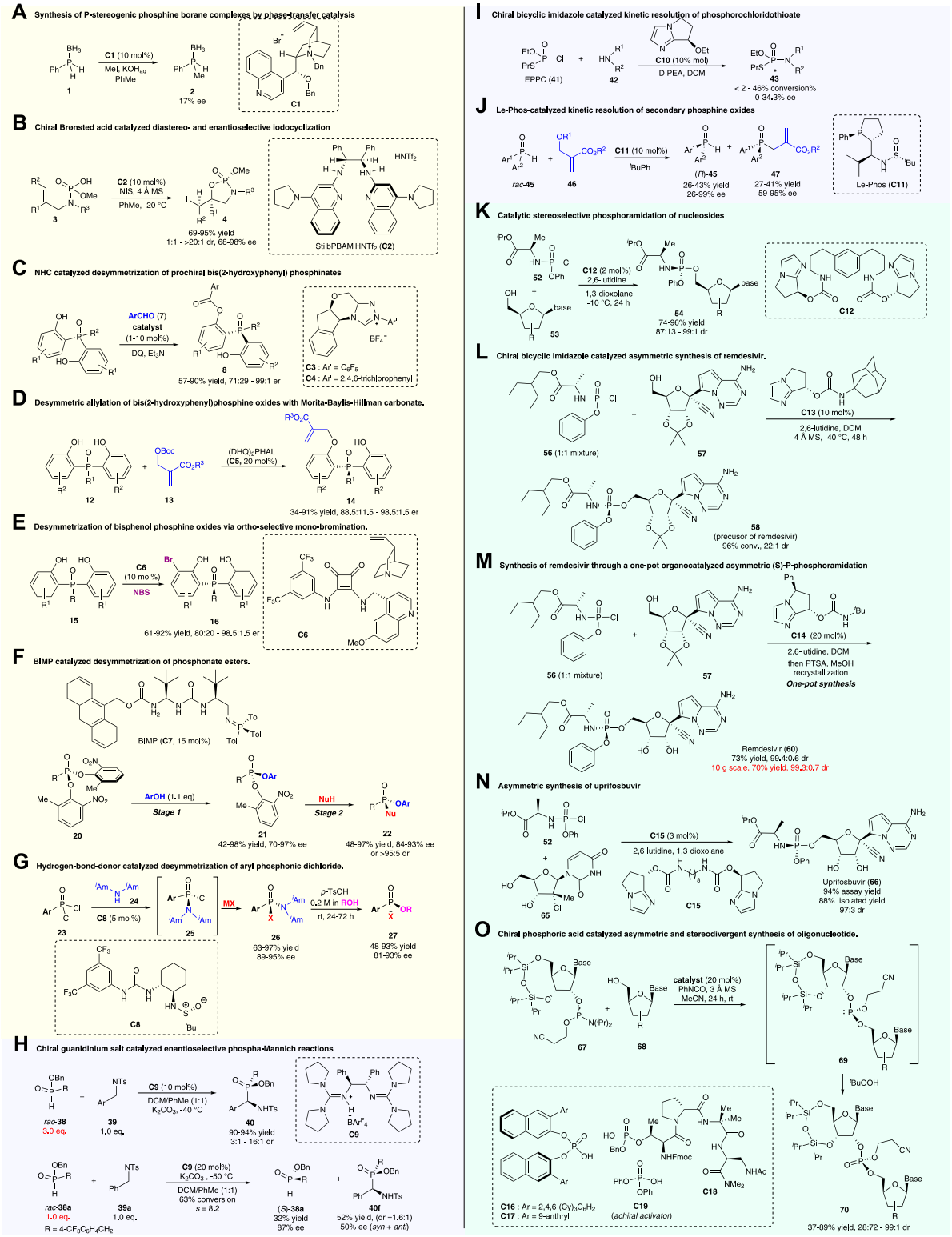

FIGURE 2
Organocatalytic asymmetric strategies for access to P-stereogenic compounds. **(A–G)**: Desymmetrization strategies; **(H–J)**: Kinetic resolution; **(K–O)**: Dynamic kinetic resolution strategies.

yields and enantioselectivities were realized in this work. Moreover, this reaction possesses a wide substrate scope and could be performed on a gram-scale with low catalyst loading (1 mol%). To further demonstrate the utility of this methodology, the P-stereogenic product **8a** was converted to the chiral bidentate Lewis base **10** and the precursor of the chiral ligand DiPAMP *via* simple transformations. The newly

synthesized bidentate Lewis base **10** could be directly used as a catalyst in asymmetric reductive aldol reactions of enones and aldehydes.

Based on the bis(2-hydroxyphenyl) phosphine oxides, the Li group demonstrated a biscinchona alkaloid-catalyzed desymmetric allylation reaction with the Morita–Baylis–Hillman carbonate to produce P-stereogenic phosphine oxides (Figure 2D; Supplementary Scheme S4) (Yang et al., 2019). Multiple functional groups were tolerated under mild reaction conditions, with a wide range of chiral P-stereogenic phosphine oxides prepared with good yields (up to 99%) and high enantioselectivities (up to 98.5:1.5 er). Additionally, large-scale reactions and synthetic transformations were also conducted in the study. Mechanically, theoretical calculations revealed that the $\Delta\Delta G^{\ddagger}$ value between **TS1** and **TS2** was 2.2 kcal mol^{-1} (Supplementary Scheme S4b), and the stabilization effect of the C–H $\cdots$ π interaction between the catalyst and substrate (as shown in **TS1**), as well as the destabilization steric effect of bulky *tert*-butyl (as shown in **TS2**), were the key factors that contributed to the energy difference of the two transition states, which were crucial for the excellent enantioselectivity control.

Recently, the Li group reported an alternative strategy for the desymmetrization of bisphenol phosphine oxides using chiral squaramide-catalyzed ortho-selective mono-bromination (Figure 2E; Supplementary Scheme S5) (Huang et al., 2021). This reaction could provide a series of chiral bisphenol phosphine oxides and phosphinates with good to excellent yields (up to 92%) and enantioselectivities (up to 98.5:1.5 er). Furthermore, this reaction could be scaled up to 1.0 mmol without the loss of the er value for **16a**. The *ortho*-brominated P-stereogenic product can be further transformed into functional molecules, which retained the optical purities, *via* reactions including metal-catalyzed cross-couplings, *O*-alkylations, or nucleophilic substitutions in P-centers (Supplementary Scheme S5b). This asymmetric *ortho*-bromination strategy provided an alternative route for the desymmetrization of bisphenol phosphine oxides.

In contrast to the desymmetric functionalization of bisphenol phosphine oxides, direct nucleophilic desymmetrization at the P-center, with the formation of a new P–X bond, is a more challenging but powerful strategy. In 2021, Dixon's group published a preprint work, in which a novel bifunctional iminophosphorane (BIMP, **C7**) catalytic two-stage desymmetrization strategy for the construction of P-stereogenic compounds was reported (Figure 2F; Supplementary Scheme S6) (Formica et al., 2021). This process involves BIMP-catalyzed asymmetrically nucleophilic substitution of one phenolic leaving group at the P-center (first stage) and subsequent enantiospecific displacement of the other phenolic leaving group *via* SN2 substitution (second stage), which allows quick access to a diverse range of chiral P(V) compounds including those with *O*-, *N*-, and *S*-linkages. Notably, nucleophilic phenols with an *ortho*-substituent were essential for the first stage. Also, the *O*-, *S*-, and *N*-centered nucleophiles were all suitable for the second stage, which gave rise to a range of chiral phosphonate esters, phosphorothioates, and phosphonamidite esters, with good yields and high enantioselectivities or diastereoselectivities.

Pro-chiral phosphonic dichlorides are also suitable substrates for the acquisition of P-stereogenic molecules *via* asymmetric desymmetrization. Forbes and Jacobsen (2022) reported hydrogen bond donor **C8**-catalyzed desymmetrization of pro-chiral phosphonic dichloride *via* enantioselective substitutions at the P-center for the preparation of aryl chlorophosphonamidates, which were developed as versatile P(V)-stereogenic building blocks. After the first desymmetric substitution step, the remaining two leaving groups (chloro and amino groups) on chlorophosphonamidates (**25**) can be displaced sequentially and stereospecifically to give a diverse range of P(V)-stereogenic compounds through substitutions with different nucleophiles (e.g., alkoxides, phenoxides, thiolates, deprotonated carbamates, and Grignard reagents) (Figure 2G; Supplementary Scheme S7a). A series of P(V)-stereogenic compounds were obtained in good yields and high optical purities, except for reactions using alkyl phosphonic dichlorides as substrates. The phosphonamidite product **26** could further be converted to a wide range of phosphonates, phosphonate thioesters, phosphinates, and phosphonamidates with retained enantioselectivities or slight loss via acid-promoted nucleophilic substitution of the diisoamyl amino group (Supplementary Scheme S7b).

To further demonstrate the synthetic utility of this hydrogen bond donor catalytic strategy, Forbes and Jacobsen have achieved three-step synthesis of the utrophin modulator (+)-SMT022332 (**31**) and formal synthesis of a matrix metalloproteinase (MMP) inhibitor (**37**) (Supplementary Scheme S8). The subjection of phosphonic dichloride **28** to the optimized conditions for catalytic enantioselective substitution produced phosphonamidate **29** (68% yield; 95% ee). After sequential methanolysis and phenol displacement, phosphonamidate **30** was converted to (+)-SMT022332 (**31**) with 94% ee, 100% es, and 43% overall yield over the three steps. In the formal synthesis of the matrix metalloproteinase inhibitor (**37**), *N*-allyl benzylamine (**33**) was used in the substitution reaction of phosphonic dichloride **32** under modified conditions, with high enantioselectivity obtained as well. The subsequent ring closing-metathesis and related transformations generated the target MMP inhibitor (**37**). It is anticipated that *N*-allyl benzylamine's versatility as a masked "–NH_2" equivalent may enable access to a wide variety of other phosphonamidate targets.

Asymmetric kinetic resolution strategies

The catalytic kinetic resolution of racemic P-stereogenic compounds represents a practical and efficient approach in the preparation of enantio-enriched P-stereogenic compounds, especially when racemic forms are readily available whereas enantiopure forms are not. Compared to desymmetrization strategies, catalytic kinetic resolution protocols are less developed for accessing P-stereogenic chirality.

In 2009, Tan and co-workers reported a pioneering work, in which a chiral guanidinium salt (**C9**)-catalyzed phospha-Mannich reaction of imine (**39**) with secondary phosphine oxides or H-phosphinates producing P-stereogenic α-amino phosphinates was reported (Fu et al., 2009). With the use of 3.0 equiv. racemic H-phosphinates (*rac*-**38**) as nucleophiles, the reaction realized an enantioselective construction of P-stereogenic α-amino phosphinates (**40**) with good to excellent enantio- and diastereo-selectivities as representative examples, as shown in Figure 2H and Supplementary Scheme S9a. When using 1.0 equiv. H-phosphinate *rac*-**38a** as a nucleophile, the Mannich reaction with imine **39a** resulted in the kinetic resolution of H-phosphinate *rac*-**38a**, producing enantio-enriched H-phosphinate (*S*)-**38a** (32% yield;

87% ee) and α-amino phosphinate **40f** (*syn* and *anti*, 52% yield, 1.6: 1 dr, and 50% ee) (Figure 2H; Supplementary Scheme S9b).

In 2012, Zhang and co-workers reported chiral bicyclic imidazole **C10**-catalyzed kinetic resolution of phosphorochloridothioate to generate P-stereogenic phosphoramides (Liu et al., 2012). As shown in Figure 2I and Supplementary Scheme S10, under the catalytic system, the reaction of *O*-ethyl *S*-propyl phosphorochloridothioate (EPPC, **41**) with amides or amines gave rise to the corresponding phosphoramides with P-chirality, although both the conversion rate and enantioselectivity were poor. It was speculated that the catalytic process involved (1) the selective formation of two diastereoisomers of ammonium intermediates *via* the reaction of phosphoryl chloride **41** and the chiral catalyst **C10**, and (2) diastereoselective attack of the amino compound **42** on these two active intermediates (**44** and *epi*-**44**) producing the optically enriched product **43**, with the release of the catalyst. The second step was rate-determining, and both steps contributed to the enantioselectivity of the products.

Secondary phosphine oxides are electron-rich in the "P" center and are usually used as nucleophiles and ligands in synthetic chemistry (Shaikh et al., 2012). In 2020, Zhang and co-workers reported Le-Phos (**C11**)-catalyzed kinetic resolution of secondary phosphine oxides (*rac*-**45**) *via* the asymmetric allylation reaction with Morita–Baylis–Hillman carbonates (Figure 2J; Supplementary Scheme S11) (Qiu et al., 2020). A variety of optically pure secondary phosphine oxides (*R*)-**45** and tertiary P-stereogenic phosphine oxides (**47**) were prepared utilizing this method with good yields and high enantioselectivities. Moreover, this reaction could be performed on a gram-scale without the loss of enantioselectivity. The resulting P-stereogenic products were suitable for further transformations to obtain optimal P-stereogenic catalysts and ligands (Supplementary Scheme S11b).

Asymmetric dynamic kinetic resolution strategies

Although the kinetic resolution strategy can provide optically pure products, it is limited to a maximum theoretical yield of 50%. Thus, dynamic kinetic resolution (DKR) has drawn more attention for preparing P-stereogenic phosphorus compounds as the yield can be theoretically increased to as much as 100%.

Phosphoramidate prodrugs (mostly containing P-stereogenic centers) are a key component of pronucleotide (ProTide) therapies for the treatment of viral diseases and cancer. In 2017, DiRocco and co-workers reported a bicyclic imidazole-derived multifunctional catalyst (**C12**) and applied it to the synthesis of ProTide MK-3682 (**54a**), which is in late-stage clinical trials for the treatment of HCV disease (DiRocco et al., 2017). As shown in Figure 2K and Supplementary Scheme S12, **C12** mimicked the complex function of enzyme catalysis *via* a distinctive activation mode. In the catalytic system, chlorophosphoramidate (**52**) is in rapid equilibrium with activated species **55a** and **55b**, and P–O bond formation is the turnover-limiting step. Despite the fact that the catalyst was designed for preparing MK-3682 (**54a**), the catalytic system was suitable for asymmetric phosphoramidation of multiple nucleoside analogs.

Dynamic kinetic asymmetric transformation (DyKAT) showed its potential in the synthesis of the anti-SARS-CoV-2 drug remdesivir. Shortly after the breakout of COVID-19, Wang et al (2020b) responded rapidly to report a chiral bicyclic imidazole (**C13**)-catalyzed coupling of P-racemic phosphoryl chloride (**56**), with a protected nucleoside GS-441524 (**57**), which promoted asymmetric access to the P-stereogenic structure of remdesivir (Figure 2L; Supplementary Scheme S13). This process involves a smoothly dynamic kinetic asymmetric transformation (DyKAT) with high reactivity and excellent stereoselectivity (96% conv., 22:1 S_P:R_P).

Gannedi et al. (2021) have also reported chiral bicyclic imidazole (**C14**)-catalyzed asymmetric (*S*)-P-phosphoramidation for the synthesis of remdesivir (Figure 2M; Supplementary Scheme S14). Under optimized reaction conditions, the desired (*S*)-P-phosphoramidate **60** was obtained with 73% yield and a 99.4:0.6 dr ratio (after recrystallization), when 20 mol% of the catalyst **C14** was employed as a catalyst. Furthermore, a 10-g-scale one-pot synthesis *via* a combination of (*S*)-P-phosphoramidation and protecting group removal, followed by one-step recrystallization, produced remdesivir with a 70% yield and 99.3:0.7 dr.

Additionally, chiral bicyclic imidazole-catalyzed asymmetric P-phosphoramidation was applied in the total synthesis of the antiviral agent uprifosbuvir by Klapars et al. (2021). A five-step synthesis of uprifosbuvir with 50% overall yield, from readily available uridine (**61**), was reported (Figure 2N; Supplementary Scheme S15). The synthetic route features the following: (1) complexation-driven selective acyl migration/oxidation; (2) BSA-mediated cyclization to anhydrouridine; (3) hydrochlorination using $FeCl_3$/TMDSO; and (4) dynamic stereoselective P-phosphoramidation. The key stereoselective P-phosphoramidation of alcohol **65** with chlorophosphoramidate **52** employed only 3 mol% loading of the bicyclic imidazole catalyst **C15**, providing uprifosbuvir (**66**) with a ratio of 97:3 dr, 94% assay yield, and 88% isolated yield of uprifosbuvir after crystallization. This asymmetric P-phosphoramidation-based route achieved a 50-fold improvement in the overall yield of uprifosbuvir over the previous manufacturing process.

In addition to the aforementioned bicyclic imidazole-type catalysts, chiral phosphoric acid has also emerged as a powerful catalyst for constructing P-stereogenic molecules. Recently, Featherston et al. (2021) demonstrated the chiral phosphoric acid (CPA)-catalyzed formation of stereogenic phosphorous centers during phosphoramidite transfer (Figure 2O; Supplementary Scheme S16). Both peptide-embedded phosphothreonine-derived CPAs (**C18**) and C2-symmetric BINOL-derived CPAs (**C16–C17**) were investigated in the study, which gave rise to unprecedented levels of diastereodivergence, enabling access to either phosphite diastereomers. Diastereodivergent catalysis can be applied to other nucleobase pairs, demonstrating the broad fundamental significance and utility.

Conclusion and outlook

Organocatalytic methods to access P-stereogenic scaffolds have made great progress during the last decade. Strategies based on desymmetrization and (dynamic) kinetic resolution

have attracted most of the work and are still mainstreamed in the development. Multiple catalytic systems were developed, with numerous optically enriched P-stereogenic molecules prepared. Nevertheless, investigations on new catalytic modes and diversified substrates are still highly demanded. In the coming years, we expect to see an expansion in new-type organocatalytic methodologies and applications of these strategies in the creation of medicines, natural products, and other functional P-stereogenic molecules.

Author contributions

JL and HC contributed equally to this work and drafted the manuscript. MW and WH participated in writing some parts of the manuscript and checking. J-LY conceptualized and directed the whole project. All authors contributed to scientific discussions.

Funding

The authors acknowledge funding support from the Guangdong Department of Education (2021ZDJS097), the Guangdong Basic and Applied Basic Research Foundation (2021A1515010188, 2022A1515110592, and 2023A1515012715), and Wuyi University (507170050407).

Conflict of interest

The authors declare that the research was conducted in the absence of any commercial or financial relationships that could be construed as a potential conflict of interest.

Publisher's note

All claims expressed in this article are solely those of the authors and do not necessarily represent those of their affiliated organizations, or those of the publisher, the editors, and the reviewers. Any product that may be evaluated in this article, or claim that may be made by its manufacturer, is not guaranteed or endorsed by the publisher.

Supplementary material

The Supplementary Material for this article can be found online at: https://www.frontiersin.org/articles/10.3389/fchem.2023.1132025/full#supplementary-material

References

Babbs, A., Berg, A., Chatzopoulou, M., Davies, K. E., Davies, S. G., Edwards, B., et al. (2020). Synthesis of SMT022357 enantiomers and *in vivo* evaluation in a Duchenne muscular dystrophy mouse model. *Tetrahedron* 76 (2), 130819. doi:10.1016/j.tet.2019.130819

Berger, O., and Montchamp, J.-L. (2013). A general strategy for the synthesis of P-stereogenic compounds. *Angew. Chem. Int. Ed.* 52 (43), 11377–11380. doi:10.1002/anie.201306628

Bergin, E., O'Connor, C. T., Robinson, S. B., McGarrigle, E. M., O'Mahony, C. P., and Gilheany, D. G. (2007). Synthesis of P-stereogenic phosphorus compounds. Asymmetric oxidation of phosphines under appel conditions. *J. Am. Chem. Soc.* 129 (31), 9566–9567. doi:10.1021/ja072925l

Bousseau, S., Marchand, M., Soleti, R., Vergori, L., Hilairet, G., Recoquillon, S., et al. (2019). Phostine 3.1a as a pharmacological compound with antiangiogenic properties against diseases with excess vascularization. *FASEB J.* 33 (5), 5864–5875. doi:10.1096/fj.201801450RRR

DiRocco, D. A., Ji, Y., Sherer, E. C., Klapars, A., Reibarkh, M., Dropinski, J., et al. (2017). A multifunctional catalyst that stereoselectively assembles prodrugs. *Science* 356 (6336), 426–430. doi:10.1126/science.aam7936

Dutartre, M., Bayardon, J., and Jugé, S. (2016). Applications and stereoselective syntheses of P-chirogenic phosphorus compounds. *Chem. Soc. Rev.* 45 (20), 5771–5794. doi:10.1039/C6CS00031B

Farnham, W. B., Murray, R. K., and Mislow, K. (1970). Stereospecific alkylation of menthyl phenylphosphinate. *J. Am. Chem. Soc.* 92 (19), 5809–5810. doi:10.1021/ja00722a083

Featherston, A. L., Kwon, Y., Pompeo, M. M., Engl, O. D., Leahy, D. K., and Miller, S. J. (2021). Catalytic asymmetric and stereodivergent oligonucleotide synthesis. *Science* 371 (6530), 702–707. doi:10.1126/science.abf4359

Forbes, K. C., and Jacobsen, E. N. (2022). Enantioselective hydrogen-bond-donor catalysis to access diverse stereogenic-at-P (V) compounds. *Science* 376 (6598), 1230–1236. doi:10.1126/science.abp8488

Formica, M., Rogova, T., Shi, H., Sahara, N., Farley, A. J., Christensen, K. E., et al. (2021). Catalytic enantioselective nucleophilic desymmetrisation of phosphonate esters. *ChemRxiv* 2021, 5714. doi:10.26434/chemrxiv-2021-5714s-v2

Fu, X., Loh, W.-T., Zhang, Y., Chen, T., Ma, T., Liu, H., et al. (2009). Chiral guanidinium salt catalyzed enantioselective phospha-mannich reactions. *Angew. Chem. Int. Ed.* 48 (40), 7387–7390. doi:10.1002/anie.200903971

Gannedi, V., Villuri, B. K., Reddy, S. N., Ku, C.-C., Wong, C.-H., and Hung, S.-C. (2021). Practical remdesivir synthesis through one-pot organocatalyzed asymmetric (S)-P-phosphoramidation. *J. Org. Chem.* 86 (7), 4977–4985. doi:10.1021/acs.joc.0c02888

Huang, Q.-H., Zhou, Q.-Y., Yang, C., Chen, L., Cheng, J.-P., and Li, X. (2021). Access to P-stereogenic compounds via desymmetrizing enantioselective bromination. *Chem. Sci.* 12 (12), 4582–4587. doi:10.1039/D0SC07008D

Huang, Z., Huang, X., Li, B., Mou, C., Yang, S., Song, B.-A., et al. (2016). Access to P-stereogenic phosphinates via N-heterocyclic carbene-catalyzed desymmetrization of bisphenols. *J. Am. Chem. Soc.* 138 (24), 7524–7527. doi:10.1021/jacs.6b04624

Imamoto, T. (2021). Synthesis and applications of high-performance P-chiral phosphine ligands. *Proc. Jpn. Acad. Ser. B* 97 (9), 520–542. doi:10.2183/pjab.97.026

Klapars, A., Chung, J. Y. L., Limanto, J., Calabria, R., Campeau, L.-C., Campos, K. R., et al. (2021). Efficient synthesis of antiviral agent uprifosbuvir enabled by new synthetic methods. *Chem. Sci.* 12 (26), 9031–9036. doi:10.1039/D1SC01978C

Kolodiazhnyi, O. I. (2021). Phosphorus compounds of natural origin: Prebiotic, stereochemistry, application. *Symmetry* 13 (5), 889. doi:10.3390/sym13050889

Kortmann, F. A., Chang, M.-C., Otten, E., Couzijn, E. P. A., Lutz, M., and Minnaard, A. J. (2014). Consecutive dynamic resolutions of phosphine oxides. *Chem. Sci.* 5 (4), 1322–1327. doi:10.1039/C3SC52913D

Lebel, H., Morin, S., and Paquet, V. (2003). Alkylation of phosphine boranes by phase-transfer catalysis. *Org. Lett.* 5 (13), 2347–2349. doi:10.1021/ol0347139

Lemouzy, S., Giordano, L., Hérault, D., and Buono, G. (2020). Introducing chirality at phosphorus atoms: An update on the recent synthetic strategies for the preparation of optically pure P-stereogenic molecules. *Eur. J. Org. Chem.* 2020 (23), 3351–3366. doi:10.1002/ejoc.202000406

Liu, S., Zhang, Z., Xie, F., Butt, N. A., Sun, L., and Zhang, W. (2012). First catalytic enantioselective synthesis of P-stereogenic phosphoramides via kinetic resolution promoted by a chiral bicyclic imidazole nucleophilic catalyst. *Tetrahedron Asymmetry* 23 (5), 329–332. doi:10.1016/j.tetasy.2012.02.018

Martin, B. P., Vasilieva, E., Dupureur, C. M., and Spilling, C. D. (2015). Synthesis and comparison of the biological activity of monocyclic phosphonate, difluorophosphonate and phosphate analogs of the natural AChE inhibitor cyclophostin. *Biorg. Med. Chem.* 23 (24), 7529–7534. doi:10.1016/j.bmc.2015.10.044

Meisenheimer, J., and Lichtenstadt, L. (1911). Über optisch-aktive Verbindungen des Phosphors. *Berichte Dtsch. Chem. Ges.* 44 (1), 356–359. doi:10.1002/cber.19110440154

Muci, A. R., Campos, K. R., and Evans, D. A. (1995). Enantioselective deprotonation as a vehicle for the asymmetric synthesis of C2-symmetric P-chiral diphosphines. *J. Am. Chem. Soc.* 117 (35), 9075–9076. doi:10.1021/ja00140a028

Nocentini, A., Alterio, V., Bua, S., Micheli, L., Esposito, D., Buonanno, M., et al. (2020). Phenyl(thio)phosphon(amid)ate benzenesulfonamides as potent and selective inhibitors of human carbonic anhydrases II and VII counteract

allodynia in a mouse model of oxaliplatin-induced neuropathy. *J. Med. Chem.* 63 (10), 5185–5200. doi:10.1021/acs.jmedchem.9b02135

Nocentini, A., Gratteri, P., and Supuran, C. T. (2019). Phosphorus versus sulfur: Discovery of benzenephosphonamidates as versatile sulfonamide-mimic chemotypes acting as carbonic anhydrase inhibitors. *Chem. Eur. J.* 25 (5), 1188–1192. doi:10.1002/chem.201805039

Pradere, U., Garnier-Amblard, E. C., Coats, S. J., Amblard, F., and Schinazi, R. F. (2014). Synthesis of nucleoside phosphate and phosphonate prodrugs. *Chem. Rev.* 114 (18), 9154–9218. doi:10.1021/cr5002035

Qiu, H., Dai, Q., He, J., Li, W., and Zhang, J. (2020). Access to P-chiral sec-and tert-phosphine oxides enabled by Le-Phos-catalyzed asymmetric kinetic resolution. *Chem. Sci.* 11 (36), 9983–9988. doi:10.1039/D0SC04041J

Ray, A. S., Fordyce, M. W., and Hitchcock, M. J. M. (2016). Tenofovir alafenamide: A novel prodrug of tenofovir for the treatment of human immunodeficiency virus. *Antivir. Res.* 125, 63–70. doi:10.1016/j.antiviral.2015.11.009

Scott, L. J., and Chan, H. L. Y. (2017). Tenofovir alafenamide: A review in chronic hepatitis B. *Drugs* 77 (9), 1017–1028. doi:10.1007/s40265-017-0754-9

Shaikh, T. M., Weng, C.-M., and Hong, F.-E. (2012). Secondary phosphine oxides: Versatile ligands in transition metal-catalyzed cross-coupling reactions. *Coord. Chem. Rev.* 256 (9), 771–803. doi:10.1016/j.ccr.2011.11.007

Toda, Y., Pink, M., and Johnston, J. N. (2014). Brønsted acid catalyzed phosphoramidic acid additions to alkenes: Diastereo- and enantioselective halogenative cyclizations for the synthesis of C- and P-chiral phosphoramidates. *J. Am. Chem. Soc.* 136 (42), 14734–14737. doi:10.1021/ja5088584

Wang, M., Cao, R., Zhang, L., Yang, X., Liu, J., Xu, M., et al. (2020a). Remdesivir and chloroquine effectively inhibit the recently emerged novel coronavirus (2019-nCoV) *in vitro*. *Cell Res.* 30 (3), 269–271. doi:10.1038/s41422-020-0282-0

Wang, M., Zhang, L., Huo, X., Zhang, Z., Yuan, Q., Li, P., et al. (2020b). Catalytic asymmetric synthesis of the anti-COVID-19 drug remdesivir. *Angew. Chem. Int. Ed.* 59 (47), 20814–20819. doi:10.1002/anie.202011527

Xu, G., Senanayake, C. H., and Tang, W. (2019). P-chiral phosphorus ligands based on a 2,3-Dihydrobenzo[d] [1,3]oxaphosphole motif for asymmetric catalysis. *Acc. Chem. Res.* 52 (4), 1101–1112. doi:10.1021/acs.accounts.9b00029

Yang, G.-H., Li, Y., Li, X., and Cheng, J.-P. (2019). Access to P-chiral phosphine oxides by enantioselective allylic alkylation of bisphenols. *Chem. Sci.* 10 (15), 4322–4327. doi:10.1039/C8SC05439H

Ye, X., Peng, L., Bao, X., Tan, C.-H., and Wang, H. (2021). Recent developments in highly efficient construction of P-stereogenic centers. *Green Synthesis Catal.* 2 (1), 6–18. doi:10.1016/j.gresc.2020.12.002

Frontiers in Chemistry

Explores all fields of chemical science across the periodic table

Advances our understanding of how atoms, ions, and molecules come together and come apart. It explores the role of chemistry in our everyday lives - from electronic devices to health and wellbeing.

Discover the latest Research Topics

See more →

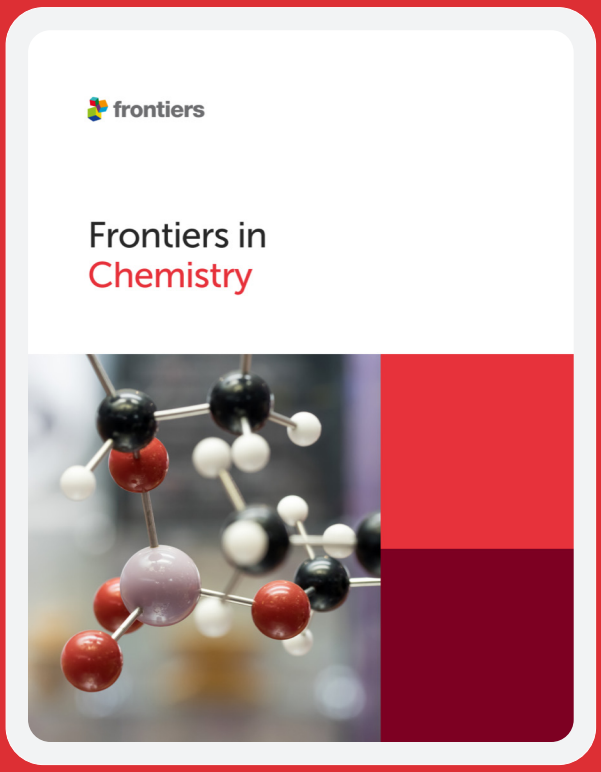

Frontiers

Avenue du Tribunal-Fédéral 34
1005 Lausanne, Switzerland
frontiersin.org

Contact us

+41 (0)21 510 17 00
frontiersin.org/about/contact